

# Nanomechanical resonators with low dissipation for quantum optomechanics

Présentée le 6 octobre 2023

Faculté des sciences et techniques de l'ingénieur  
Laboratoire de photonique et mesures quantiques (STI/SB)  
Programme doctoral en photonique

pour l'obtention du grade de Docteur ès Sciences

par

**Alberto BECCARI**

Acceptée sur proposition du jury

Prof. L. G. Villanueva Torrijo, président du jury  
Prof. T. Kippenberg, directeur de thèse  
Prof. S. Schmid, rapporteur  
Prof. G. Steele, rapporteur  
Prof. Y. Chu, rapporteuse





## ACKNOWLEDGEMENTS

---

I had the luck of being surrounded by some competent, inspiring and selfless people during the last five years, to whom I should give credit for completing this thrilling and exhausting journey. Tobias Kippenberg, our group leader, with his inexhaustible energy and optimism (even when facing bleak prospects) and his “athletic” approach to science certainly has something to teach to all of his collaborators. Nils and Sergey have been incredible sources of inspiration; Nils for his patience, carefulness and the joy with which he mentored all of his students, Sergey for his scientific genius, his fantastic creativity, and his moral revulsion towards taking any compromise about the quality of his scientific work. Thanks Nils for proofreading the thesis manuscript; in a future life I will learn to read as fast as you! Mohammad, for mysteriously combining passion and tireless work with being the “sane”, down-to-earth guy. Amirali, for the countless *Ciao Darwin* marathons in our apartment. Guanhao, for generously “purging” my coffee cup in my absence, as well as for being a brilliant and cryptic guy. Alessio, for the herculean energies and motivation, that will serve him well in his microfabrication adventures! Itay, for his hilarious, dry irony and for leaving behind in his former office one of his most precious keepsakes of his life in Switzerland. Andrea, for shooting and recording hours of comedy gold, and being acutely aware of the hilarious/crazy side of K-Lab and its denizens. Diego and Robin, for being some of the most skilled, hard-working master students in EPFL. You have been sorely missed after your departure! Antonella, for being insanely qualified for her job, a tremendous Stakhanovite, and somehow still deeply caring for the K-Lab blue collars, and always enjoying a good chat. I am also grateful to many of the technicians of the CMi cleanroom at EPFL, whose stellar work keeps the facility a productive place to work in and learn, as well as a constantly-growing hub for microfabrication. I am especially indebted to Zdenek, Joffrey, Giovanni, Vivigan and Adrien for their help.

Outside of the lab, Edoardo and I shared *everything* during his years in Switzerland, including one lockdown during a pandemic. Alessio, Andrea, Aurora and Maria have been precious friends with whom to share a meal and crack a few jokes, or move the occasional piece of furniture around the Lemanic Arc. Gianmaria and Michele provided so many good reasons for visiting Milan (or San Francisco) as often as possible. With my friends of the Majno clique (Mattia, Pietro, Tommaso, Daniele), we have maintained a beautiful friendship over the past years, and they always gifted me a refreshing perspective on the existence of conscious life outside of academia.

I am deeply grateful to Aslıhan for all the fun, companionship and love I experienced in the last months. I am humbled by your selflessness in supporting me whenever I showed the slightest sign of need. To my sister, mom and dad goes my warmest affection. I hope I will manage to hold on to your spirit of self-sacrifice and to your unconditional affection as paradigms for my future life. Dad, your everyday courage and love of life are a beautiful mystery to me.



## ABSTRACT

---

Fields of technology as diverse as microwave filter construction, characterization of material interfaces with atomic precision, and detection of gravitational waves from astronomical sources employ mechanical resonators at their core. The utility of mechanical resonators can be explained by their sensitivity to a multitude of force fields and actuation mechanisms, and the existence of extremely precise position measurement techniques.

The possibility of faithful, real-time reconstruction of mechanical motion, especially when the resonator is monitored interferometrically or with cavity spectroscopy, has enabled the creation and engineering of quantum states of macroscopic mechanical resonators, in the fields of quantum optomechanics, levitodynamics and quantum acoustodynamics. These experiments must however overcome the large thermal occupation of mechanical oscillators in typical conditions, due to contact with high-temperature baths. A fruitful path to counteract the thermal fluctuations governing the motion of mechanical oscillators has been the engineering of the quality factor ( $Q$ ) of the mechanical mode of interest, which coincides with the control of dissipation and isolation from its environment. The class of methods termed *dissipation dilution*, implemented in strained, high-aspect-ratio nanoresonators, allow the control of the mechanical  $Q$  through mode shape engineering, and underpinned in the last decade an astounding growth in mechanical coherence levels.

In this thesis, I report on the development of new types of ultracoherent mechanical resonators leveraging dissipation dilution, united by a common goal of preparing quantum states of such resonators at room temperature. We improved the mechanical performance of dissipation-diluted resonators by utilizing single-crystal materials with high strain and aspect ratio, and investigated the performance of strained silicon as a material for nanomechanics. Combining soft clamping in phononic crystal (PnC) structures with the low friction of crystalline materials, we witnessed record-high mechanical quality factors beyond  $10^{10}$  at MHz frequencies, at temperatures around 7 K, corresponding to phonon lifetimes of several hours.

We have also endeavoured towards observing quantum optomechanics at room temperature, by exploiting mechanical resonators with high dissipation dilution. We assembled a room temperature membrane-in-the-middle experiment, where a soft clamped PnC membrane interacts dispersively with the optical modes of a Fabry-Pérot cavity. In our first studies of this system, we witnessed an intensity noise mechanism vastly exceeding the magnitude of quantum noise of the employed light field, and understood it to be due to the sizeable thermal motion of the membrane resonator, distorted by the nonlinear cavity transduction. We termed this noise source “Thermomechanical Intermodulation Noise” (TIN), and devised methods to reduce its magnitude below the vacuum fluctuations of the light field.

The limitations of our room temperature optomechanics experiment could also be overcome with new types of mechanical resonators. I report on the development of hierarchical membrane resonators with a partially soft clamped fundamental mode, exploiting the notion of wave amplitude suppression over a three-beam joint, and PnC

membrane resonators with density modulation, which offer enticing performance for ground state cooling from room temperature in our experiment.

**Keywords:** nanomechanical resonators, dissipation dilution, tensile structures, nanofabrication, cavity optomechanics, precision measurements.

## RÉSUMÉ

---

Les résonateurs mécaniques sont au cœur d'applications technologiques aussi diverses que la construction de filtres micro-ondes, la caractérisation d'interfaces entre matériaux avec une précision atomique et la détection d'ondes gravitationnelles provenant de sources astronomiques. L'utilité des résonateurs mécaniques s'explique par leur sensibilité à une multitude de champs de force et de mécanismes d'actionnement, ainsi que par l'existence de techniques de mesure de position extrêmement précises.

La possibilité de reconstruire fidèlement et en temps réel le mouvement mécanique, en particulier lorsque le résonateur est contrôlé par interférométrie ou par spectroscopie de cavité, a permis la création d'états quantiques artificiels de résonateurs mécaniques macroscopiques, dans les domaines de l'optomécanique quantique, de la lévito-dynamique et de l'acoustodynamique quantique. Ces expériences doivent cependant surmonter l'énorme occupation thermique des oscillateurs mécaniques dans les conditions ambiantes, en raison du contact avec des bains à haute température. Une voie fructueuse pour contrer les fluctuations thermiques régissant le mouvement des oscillateurs mécaniques a été l'amélioration du facteur de qualité ( $Q$ ) du mode mécanique concerné, qui coïncide avec le contrôle de la dissipation et de l'isolation par rapport à son environnement. La classe de méthodes appelée *dilution de dissipation*, mise en œuvre dans des nanorésonateurs sous tension, à rapport de forme élevé, permet le contrôle du facteur de qualité mécanique par la maîtrise de la forme du mode, et les niveaux de cohérence quantique démontrés au cours de la dernière décennie ont cru de manière stupéfiante.

Dans cette thèse, je présente le développement de nouveaux types de résonateurs mécaniques ultracohérents tirant parti de la dilution de dissipation, dans le but commun de préparer des états quantiques de ces résonateurs à température ambiante. Nous avons amélioré les performances mécaniques des résonateurs à dilution de dissipation en utilisant des matériaux mono-cristallins avec une tension et un rapport de forme élevés, et nous avons étudié les performances du silicium déformé en tant que matériau pour la nanomécanique. En combinant le *soft clamping* dans les structures à cristal phononique (PnC) avec la faible friction des matériaux cristallins, nous avons observé des facteurs de qualité mécanique record supérieurs à  $10^{10}$  aux fréquences MHz, à des températures d'environ 7 K, correspondant à des durées de vie des phonons de plusieurs heures.

Nous nous sommes également intéressés à l'optomécanique quantique à température ambiante, exploitant des résonateurs mécaniques à forte dilution de dissipation. Nous avons réalisé une expérience de *membrane-in-the-middle* à température ambiante, dans laquelle une membrane PnC souple interagit de manière dispersive avec les modes optiques d'une cavité Fabry-Pérot. Nos premières études de ce système ont révélé un mécanisme de bruit d'intensité dépassant largement l'ampleur du bruit quantique du champ lumineux utilisé, et nous avons découvert qu'il était dû à l'important mouvement thermique du résonateur de la membrane, déformé par la transduction non linéaire de la cavité. Nous avons baptisé ce phénomène "bruit d'intermodulation thermomécanique" (abr. TIN pour "thermal intermodulation noise") et avons déve-

loppé des méthodes pour réduire son amplitude en dessous des fluctuations du vide du champ lumineux.

Les difficultés de notre expérience d'optomécanique à température ambiante pourraient également être surmontées grâce à de nouveaux types de résonateurs mécaniques. Je présente le développement de résonateurs à membrane hiérarchiques avec un mode fondamental partiellement "soft clamped", exploitant la notion de suppression de l'amplitude de l'onde sur une triple jointure, et de résonateurs à membrane PnC avec modulation de densité, offrant des performances intéressantes pour le refroidissement de l'état fondamental à partir de la température ambiante dans notre expérience.

**Mots-clés:** résonateurs nanomécaniques, dilution de dissipation, structures sous tension, nanofabrication, optomécanique en cavité, mesures de précision.

# CONTENTS

1	INTRODUCTION	1
1.1	This thesis	5
2	FUNDAMENTALS OF NANOMECHANICAL RESONATORS	7
2.1	Quantization of the equations of elasticity	7
2.1.1	Strain, stress and elastic energy	7
2.1.2	Kirchoff-Love membrane theory	9
2.1.3	Modal expansion	13
2.2	Fluctuations and dissipation	16
2.2.1	Correlations and spectral densities	16
2.2.2	Oscillator linearly coupled with a thermal bath	18
2.2.3	The fluctuation-dissipation theorem	19
2.3	Dissipation dilution in resonators with tensile stress	22
2.3.1	Loss angle and quality factor	22
2.3.2	Dissipation dilution in a square drum	27
2.3.3	Soft clamping via dispersion engineering and phononic bandgaps	32
2.3.4	Dissipation dilution of torsional modes	36
2.3.5	Finite element simulations of strained nanomechanical resonators	37
2.3.6	Mechanical dissipation sources	39
2.3.6.1	Anelastic relaxation	40
2.3.6.2	Thermoelastic damping	41
2.3.6.3	Interaction with two level systems	43
2.3.6.4	Surface losses	48
2.3.6.5	Gas damping	49
2.3.6.6	Phonon radiation	52
2.3.7	Anharmonicity from geometric nonlinearity	54
3	STRAINED SILICON, SOFT CLAMPED NANOSTRINGS	57
3.1	Microfabrication of strained silicon nanostrings	58
3.1.1	Device layer patterning	59
3.1.2	Dielectric film encapsulation	61
3.1.3	Plasma undercut	61
3.1.4	Wet release	62
3.2	Strain imaging	65
3.2.1	Dark field electron holography	65
3.2.2	Raman spectroscopy	66
3.3	Soft clamped PnC nanostrings	69
3.3.1	Buckling in large corrugations	73
3.4	Quality factor temperature dependence	75
3.4.1	Gas damping of the localized mode at room temperature	77
3.5	Quality factors of additional samples	78
3.6	Optical heating	81
3.7	Characterization methods	83
3.7.1	Low-vibration cryostat	83
3.7.2	Optical interferometer	84

3.7.3	Ringdown characterization . . . . .	90
3.7.4	Displacement calibration with interferometric nonlinearity . . . . .	91
3.7.5	Light-induced damping and antidamping . . . . .	94
3.8	Outlook for sSi nanomechanics . . . . .	98
4	MEMBRANE-IN-THE-MIDDLE OPTOMECHANICS . . . . .	101
4.1	Rudiments of Cavity Optomechanics . . . . .	102
4.1.1	Dynamic backaction . . . . .	104
4.1.2	Displacement measurement in cavity optomechanics . . . . .	105
4.1.3	Ponderomotive squeezing . . . . .	108
4.1.4	Feedback cooling . . . . .	109
4.2	MiM dispersive optomechanics . . . . .	111
4.3	Design and assembly of the Fabry-Pérot cavity . . . . .	112
4.4	Stress-modulated PnC membranes . . . . .	116
4.4.1	Microfabrication walk-through . . . . .	118
4.4.1.1	Device layer and membrane windows patterning . . . . .	120
4.4.1.2	KOH deep etching . . . . .	121
4.4.1.3	Chip-scale undercut . . . . .	122
4.5	Observation of thermal intermodulation noise . . . . .	124
4.5.1	Theory of TIN . . . . .	125
4.5.2	Brownian intermodulation noise . . . . .	127
4.5.3	Experimental observation with uniform membranes . . . . .	128
4.5.4	TIN with a soft clamped PnC membrane . . . . .	132
4.6	Membranes with a soft clamped fundamental mode . . . . .	135
4.6.1	Displacement gradient suppression over a three-beam branch . . . . .	138
4.6.2	Trampoline membranes with branching tethers . . . . .	139
4.6.2.1	Buckling and static deformations . . . . .	143
4.7	Density-modulated PnC membranes . . . . .	144
4.7.1	Design principles . . . . .	147
4.7.2	Microfabrication process . . . . .	150
4.7.2.1	Nanopillars definition . . . . .	151
4.7.2.2	Nanopillars encapsulation . . . . .	153
4.7.2.3	Membrane release and encapsulation removal . . . . .	154
4.7.3	Mechanical characterization . . . . .	155
4.8	Outlook for MiM optomechanics . . . . .	157
4.8.1	Room temperature ponderomotive squeezing . . . . .	157
4.8.2	Tailoring the optical properties of a PnC membrane with photonic structures . . . . .	159
5	CONCLUDING REMARKS . . . . .	161
A	APPENDIX: CAVITY-LESS LASER COOLING IN A CRYOGENIC ENVIRONMENT . . . . .	163
	BIBLIOGRAPHY . . . . .	167
B	Curriculum Vitae . . . . .	182



## LIST OF FIGURES

---

Figure 1.1	Cavendish apparatus. . . . .	2
Figure 1.2	Prototype gravitational wave detector. . . . .	3
Figure 1.3	LIGO mirror suspensions. . . . .	4
Figure 2.1	Thin plate illustration. . . . .	10
Figure 2.2	Bending eigenmodes of a tensioned plate. . . . .	14
Figure 2.3	Johnson noise in an RL circuit. . . . .	21
Figure 2.4	Thermomechanical displacement spectral density. . . . .	25
Figure 2.5	Dilution factors of square membrane eigenmodes. . . . .	30
Figure 2.6	PnC density modulation band diagrams. . . . .	32
Figure 2.7	Localized mode in a density-modulated membrane. . . . .	35
Figure 2.8	Finite element simulation of a tensioned resonator. . . . .	38
Figure 2.9	Illustration of thermoelastic damping. . . . .	42
Figure 2.10	Illustration of two-level-systems damping. . . . .	44
Figure 2.11	Gas damping illustration and experimental evidence. . . . .	51
Figure 2.12	Elastic radiation pattern. . . . .	53
Figure 2.13	Mechanical resonant frequency noise and thermomechanical spectrum of $X^2 + Y^2$ . . . . .	56
Figure 3.1	Scanning transmission electron micrograph of the cross-section of a processed sSOI sample. . . . .	58
Figure 3.2	Simplified fabrication process. . . . .	59
Figure 3.3	Utility of a stress-compensation layer. . . . .	60
Figure 3.4	Determination of intrinsic stress through wafer bow. . . . .	62
Figure 3.5	Exposure of sSi strings to buffered HF and diluted HF. . . . .	63
Figure 3.6	Drawing of PTFE chip holder for wet etching. . . . .	64
Figure 3.7	False-color SEM micrograph of a high aspect ratio PnC nanostring. . . . .	65
Figure 3.8	Strain map with dark-field electron holography. . . . .	66
Figure 3.9	Raman Stokes spectrum. . . . .	66
Figure 3.10	Micro Raman map over the unit cell of a corrugated nanostring. . . . .	67
Figure 3.11	Micro-Raman scans with variable laser power. . . . .	69
Figure 3.12	Phononic band diagrams associated with string corrugation. . . . .	70
Figure 3.13	Localized mode displacement and curvature. . . . .	71
Figure 3.14	Quality factors and frequencies of the flexural modes of the 6.0 mm-long nanostring. . . . .	72
Figure 3.15	Gated ringdown of the localized mode. . . . .	73
Figure 3.16	Buckling instability in the unit cell. . . . .	74
Figure 3.17	Variation of Q with temperature for different modes of a soft-clamped nanostring. . . . .	75
Figure 3.18	Temperature sweep around the dissipation maximum. . . . .	77
Figure 3.19	Gas damping of the localized mode at room temperature. . . . .	78
Figure 3.20	Quality factors of shorter sSi nanostrings. . . . .	79
Figure 3.21	Heating effect on the string resonant frequencies. . . . .	80
Figure 3.22	Cryostat temperature records during a cooldown. . . . .	83

Figure 3.23	Calculation of the displacement sensitivity of a Mach-Zehnder interferometer. . . . .	85
Figure 3.24	Simplified scheme of the mechanical characterization setup. . . . .	86
Figure 3.25	Photographs of the interferometric, high vacuum characteriza- tion setup. . . . .	87
Figure 3.26	Interferometric nonlinearity in records of driven motion of a me- chanical resonator. . . . .	92
Figure 3.27	MATLAB app for fitting interferometric nonlinearity and ob- taining displacement calibration. . . . .	93
Figure 3.28	Comparison of ringdowns with continuous and gated acquisition. . . . .	95
Figure 3.29	Optical antidamping of a trampoline resonator. . . . .	96
Figure 3.30	Schematic illustration of a mechanical resonator oscillating in an optical standing wave. . . . .	97
Figure 4.1	Contributions to displacement sensitivity in resonant optome- chanics. . . . .	108
Figure 4.2	Optical cavity design specifications. . . . .	113
Figure 4.3	Schematic illustration of the compact MiM assembly. . . . .	115
Figure 4.4	Low $m_{\text{eff}}$ PnC membrane designs. . . . .	117
Figure 4.5	Thermomechanical spectra of the PnC membrane designs. . . . .	118
Figure 4.6	Edge modes in PnC soft clamped membranes. . . . .	119
Figure 4.7	Simplified fabrication process of $\text{Si}_3\text{N}_4$ membrane resonators. . . . .	119
Figure 4.8	Truncated pyramid holes formed by KOH wet etching under square apertures. . . . .	121
Figure 4.9	Torn PnC membrane sample after partial double-sided undercut. . . . .	121
Figure 4.10	Photographs of chip-scale membrane release in KOH. . . . .	123
Figure 4.11	Optical microscope image of a suspended triangular-defect PnC membrane. . . . .	124
Figure 4.12	Cavity reflection signal with different optomechanical coupling. . . . .	129
Figure 4.13	Linear frequency fluctuations and nonlinear TIN measured at different cavity detuning. . . . .	130
Figure 4.14	Scaling of RIN with $g_0$ and optical power. . . . .	130
Figure 4.15	Comparison of theoretical and experimental frequency and res- onant intensity noises. . . . .	132
Figure 4.16	Frequency spectrum and detuning dependence of TIN with a phononic crystal membrane. . . . .	133
Figure 4.17	Frequency noise at the magic detuning compared with fre- quency noise from an empty cavity. . . . .	136
Figure 4.18	Undercut nanostrings for MiM experiments. . . . .	136
Figure 4.19	Simulated cavity-transduced thermomechanical displacement of a uniform membrane and a trampoline resonator. . . . .	137
Figure 4.20	Suppression of the displacement over a three-beam branch. . . . .	138
Figure 4.21	Scanning electron micrograph of a binary-tree beam with three branching levels. . . . .	140
Figure 4.22	Microscope images of trampoline membranes with partial soft clamping. . . . .	141
Figure 4.23	FEM-simulated displacement profiles of the trampoline and steering wheel fundamental modes. . . . .	142

Figure 4.24	Measured quality factors of self-similar and steering wheel trampolines. . . . .	142
Figure 4.25	Thermomechanical noise spectrum of a trampoline with branching tethers. . . . .	143
Figure 4.26	Buckling in a steering wheel resonator. . . . .	145
Figure 4.27	Density modulated membrane after the method of [67]. . . . .	146
Figure 4.28	Losses induced by bending of nanopillars. . . . .	147
Figure 4.29	Effect of tuning the radius of the high density regions closest to the PnC defect. . . . .	149
Figure 4.30	Simplified fabrication process for density-modulated membrane resonators. . . . .	150
Figure 4.31	False-colored SEM micrograph of a nanopillar cross section. . . .	152
Figure 4.32	SEM micrograph of nanopillars covered with a PECVD $\text{Si}_x\text{N}_y$ film.	153
Figure 4.33	A density-modulated PnC membrane shown at different scales. .	154
Figure 4.34	Density-modulated membranes characterization data. . . . .	155
Figure 4.35	Thermomechanical spectrum of a density-modulated PnC membrane. . . . .	156
Figure 4.36	Vibrational noise of PnC cavity mirrors. . . . .	157
Figure 4.37	Room temperature ponderomotive squeezing spectrum. . . . .	158
Figure 4.38	Optical resonance in nanopillar metasurfaces. . . . .	159
Figure A.1	Feedback cooling of a mechanical resonator with interferometric detection. . . . .	164



## INTRODUCTION

---

In 1797, Henry Cavendish was finally able to operate his apparatus to "weigh the world", i.e., estimate the average density of Earth [1]. At the time, the law of universal gravitation was not formulated in the same form as it is today, and the gravitational constant  $G$  had not been defined. However, with knowledge of the radius of the Earth and the gravitational acceleration  $g$ , the estimation of the density of Earth also yielded a well-defined value of the gravitational constant. Cavendish' instrument was a delicate *torsion balance*, a rigid rod with two lead spheres on its ends (each weighing about 730 g), suspended by a slender wire from its center of mass. In the vicinity of the lead spheres, Cavendish placed a couple of much larger lead balls (weighing about 158 kg), which could be lowered and raised by a pulley to change the distance from the spheres, imparting a significant gravitational attraction on them (the apparatus is portrayed in Fig. 1.1). The rod started rotating, until the restoring force from the twisted suspension wire compensated the gravitational pull. By measuring the equilibrium deflection, the rotational period of the balance and the distances between masses, the density of Earth could be readily estimated. The torsion balance of Cavendish is an example of a mechanical resonator, and it was used to carry out a remarkably sensitive measurement of force for the time: the magnitude of the attractive force between each pair of lead spheres was only around 150  $\mu\text{N}$ . Torsion balances with optical detection are still used today for refining the precision of our  $G$  measurements, and to probe the gravitational field generated by ever smaller source masses [2].

While Cavendish's experiments confirmed and improved the Newtonian theory of gravitation, more sensitive mechanical sensors also provided crucial experimental evidence supporting its successor, Einstein's general relativity. Gravitational waves are emitted, according to general relativity, by source masses with time-varying acceleration, whose motion does not exhibit spherical symmetry. The energy carried by such waves is immensely large for astronomic sources such as black holes and neutron stars binary mergers, rendering them observable even when extremely distant from Earth (as far as  $3 \times 10^6$  light years for neutron star mergers [3]). When a gravitational wave impinges on an elastic body, it generates measurable, time-varying stress and strain states [4]. If the displacement of such a test mass can be measured with a sufficient sensitivity, it can be used as a detector of the arrival of gravitational waves, and to infer the properties of the generating astronomical event. Early attempts and prototypes tried to exploit the resonant enhancement of the displacement response provided by a high-Q mechanical oscillator (see Fig. 1.2), but lacked the necessary sensitivity. In 2015, the first direct observations of gravitational waves were made using kilometer-scale interferometers, where the detection light is circulated in high-finesse cavities (intracavity circulating power around  $2 \times 10^5$  W), in which *mirror suspensions* provide the test masses, deforming at the arrival of a gravitational wave. These observatories are sensitive to minuscule displacements, as small as  $2 \times 10^{-20}$  m within one second of integration time [3, 5], in a broad frequency band between  $10^1$  and  $10^3$  Hz. The sensitivity band is no longer limited to a single resonance, but building high-Q mirror

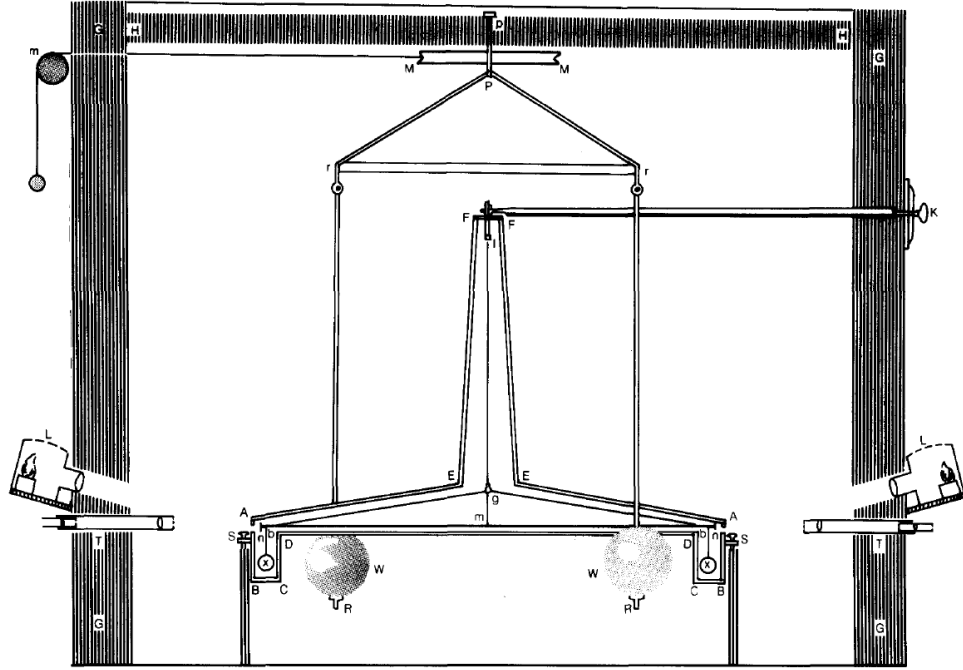


Figure 1.1: Cross section through the Cavendish apparatus. The mobile lead spheres are marked with  $x$ , while the heavy lead spheres are marked with  $W$ . Image adapted from [1].

suspensions has remained extremely important, in order to reduce the off-resonant Brownian motion contributing to the displacement noise floor [6].

Another ubiquitous and celebrated example of a precision sensor based on a mechanical resonator is the *atomic force microscope* (AFM) [8]. An offshoot of the development of the scanning tunneling microscope, the AFM was invented by Binnig in 1986, and proved to be much more practical and versatile, as it does not require conductive samples and can be operated at atmospheric pressure and even in liquid environments. As such, AFMs are now widely commercially available and employed for material growth characterization, surface science, and nanobiology, among other applications. In an AFM, a mechanical resonator with a sharp tip (typically a cantilever) is brought in the vicinity of the surface of a sample to be investigated, and the forces acting between the surface and the tip deflect and perturb the mechanical parameters of the resonator, such as its stiffness, which are monitored in real-time with optical detection (based on deflection or interferometry). By monitoring, for example, the oscillation frequency of the driving feedback loop as the tip is scanned on the sample surface, a map of the nanoscale forces is obtained. Atomic resolution with the AFM was achieved soon after its invention [9], and the extremely sensitive nature of this instrument was highlighted by achievements such as the detection of the magnetic force exerted by a single electron spin [10] (in the attonewton range) and the direct imaging of DNA in aqueous environments [11]. The nature of the interactions probed with atomic force microscopy is extremely diverse: van der Waals, electrostatic, magnetic and adhesion forces can all measurably affect the AFM cantilever.

As this short overview aims to highlight, mechanical resonators are particularly attractive for realizing very precise measurements, due to their extreme versatility in



Figure 1.2: Joseph Weber installing strain gauges on a resonant bar detector for gravitational waves. Image adapted from [7].

coupling with different force fields. Precision measurements are also valued in applied quantum mechanics, where mechanical resonators have been employed for their strong interaction with systems with genuine quantum behaviour, such as superconducting qubits [12, 13] and atomic clouds [14, 15], realizing hybrid quantum systems. Due to the same versatility, mechanical resonators are exploited to mediate interactions between different quantum systems, or to transduce information with high efficiency and low added noise between different frequency domains. In the quantum mechanics of open systems, the interaction strength with a measurement field has to be compared with the coupling rate to the environment, which is typically hot and overflowing with thermal fluctuations. The theory of decoherence, in fact, shows that a system must be very well-isolated from the environment in order to prepare states with nonclassical behaviour, such as those exhibiting Wigner function negativity [16], and to retain quantum coherence, and entanglement over time. This requirement becomes harder to fulfill as the system becomes more macroscopic [17]. Mechanical resonators are, however, particularly attractive for the high degree of isolation from the environment that they can achieve, which is reflected by the damping rate or, equivalently, by the quality factor  $Q = \Omega_m / \Gamma_m$  ( $\Omega_m$  is the angular eigenfrequency and  $\Gamma_m$  the damping rate in angular units). The low dissipation of carefully-manufactured mechanical oscillators was perfected in the Muscovite research group of Vladimir Braginsky, starting from the 1960s, that was responsible for astounding progress in the technological aspects of gravitational wave detectors and precision sensors. For example, in [18], a 13.7 cm-long cylinder made of crystalline sapphire (high purity  $\text{Al}_2\text{O}_3$ ), with a fundamental elongational mode resonating at 38 kHz was reported to have a quality factor of about  $3 \cdot 10^7$  at 200 K and  $5 \cdot 10^9$  at 4 K. Such mechanical coherence required great care in the manufacturing and assembly of the resonator, which was polished, annealed and chemically etched to reduce its surface losses, and suspended with a silk thread by its center of mass in a cryogenic vacuum chamber (the residual pressure was smaller than  $1 \times 10^{-5}$  mbar), to reduce elastic energy radiation and gas damping. Braginsky and



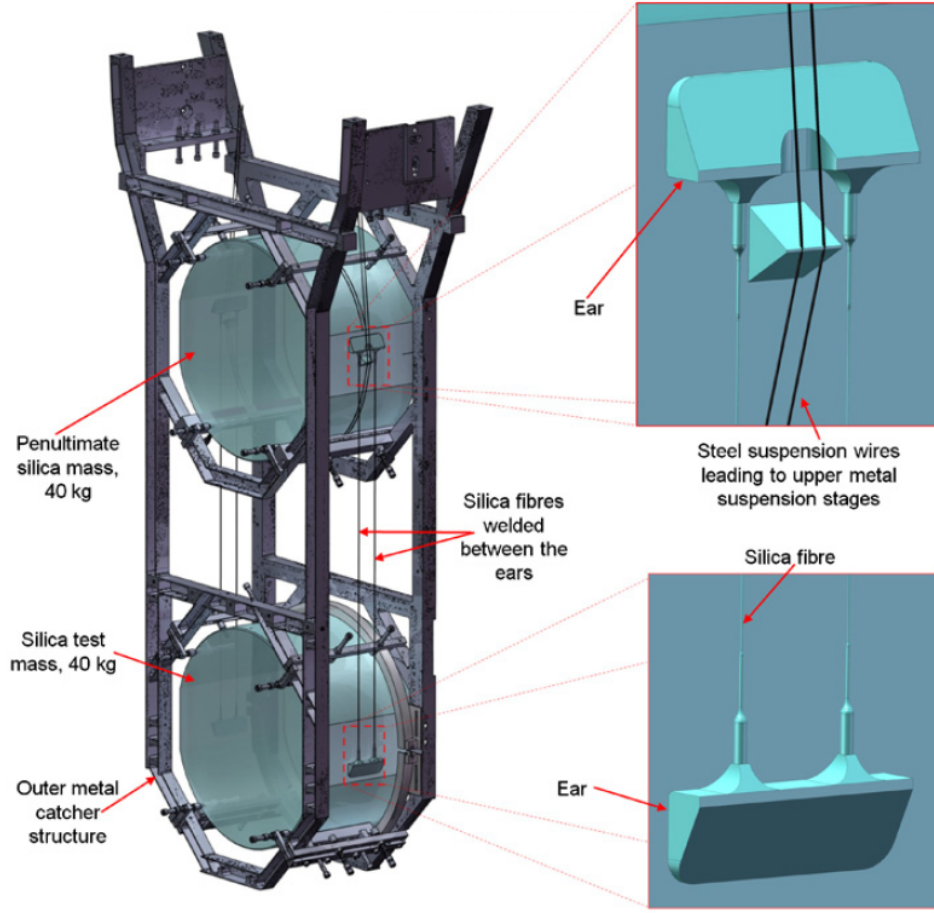


Figure 1.3: Simplified suspension schematics of the LIGO detector mirrors; the test masses are suspended by four tensioned fused silica fibers. Image adapted from [21].

his colleagues were also aware that their high- $Q$  mechanical oscillators would behave quantum mechanically even at relatively high temperatures, and contributed crucially to the study of the impact of quantum fluctuations of the radiation pressure force of a light field in continuous displacement measurements of a mechanical oscillators, and to the development of quantum measurement techniques to circumvent the resulting sensitivity limitations [19]. These findings laid the foundations for the field of *quantum optomechanics* [20].

The previous example of a high- $Q$  sapphire resonator shows that most of our current knowledge about the microscopic causes of mechanical dissipation was already consolidated by the 1970s (the two-level defects model for describing mechanical and electromagnetic losses in glasses was proposed in the same decade [22]). A new method for the enhancement of mechanical quality factors was discovered, however, in the 1990s, independent of the precise microscopic mechanism that induces friction in the material. Researchers investigated theoretically and experimentally the Brownian motion of the mirror suspensions that would become the sensing element for the LIGO gravitational wave interferometer, i.e. thin steel or fused silica fibers supporting the weight of the massive cavity end-mirrors (about 40 kg) [23] (see Fig. 1.3). They noticed that some classes of eigenmodes of the silica fibers, tensioned by the strong gravitational pull,



would exhibit particularly low mechanical dissipation (and thermomechanical noise), in particular the ‘violin’ fiber vibrational patterns and, to a greater extent, the ‘pendulum’ resonance of the mirror suspension. Compared to those dictated by the intrinsic material friction, the dissipation rates were suppressed by about two orders of magnitude. This was attributed to the storage of the majority of mechanical energy, during resonant oscillations, in the lossless gravitational potential, compared to the fraction stored in the dissipative elastic deformation. In the last 15 years, the phenomenon was rediscovered independently in the field of nanomechanics, where strings and membranes under high tensile stress due to thin-film synthesis processes were observed to support similarly long-lived flexural resonances at kHz to MHz frequencies. Due to the negligible contribution of gravitational potential energy, the *dissipation dilution* effect was again scrutinized and a more general criterion for dilution of mechanical loss was formulated: the phenomenon will exist when there is *tension* in the mechanical resonator at rest, and when the vibrational pattern exhibits *geometric nonlinearity*, i.e. when the elongation of its elements is quadratic in the amplitude of the mechanical mode [24], as we will discuss in Chapter 2. The latter condition, in particular, favours resonators shapes with a high aspect ratio (just like the silica fiber suspensions of Fig. 1.3), a requirement which mechanical resonators can fulfill naturally.

Remarkably, in the last years the implicit dependence of the dilution on the resonator geometry was exploited to engineer ultracoherent resonators, by tailoring the displacement field curvature of vibrational patterns. The discovery of *soft clamping* [25, 26], in its various incarnations, has brought forward a remarkable growth of mechanical quality factors, with values beyond  $10^9$  [27] and  $10^{10}$  [28] demonstrated at room temperature and at liquid Helium temperature, reaching and surpassing the performance of macroscopic resonators (despite the much more severe surface losses affecting nanomechanical resonators, due to a large surface-to-volume ratio). A multitude of experimental results in cavity optomechanics have stemmed from these highly-diluted mechanical resonators, among which are high-fidelity ground state cooling [29], strong-coupled hybrid atom-mechanical systems [14], and microwave-to-optics converters that permitted optical readout of superconducting qubits [30], with many more applications envisioned by physicists, ranging from dark matter detection [31] to fundamental tests of the mechanisms underlying wavefunction collapse in quantum mechanics [32].

## 1.1 THIS THESIS

Within this thesis project, I have contributed to the development of low-dissipation, highly-diluted nanomechanical resonators for optomechanics experiments, especially for demonstrations of quantum optomechanics at room temperature, where the oscillator is required to be particularly well-isolated from the sizeable thermal fluctuations of the hot environment in order for radiation pressure to be the dominant drive of its dynamics. In Chapter 2 I provide an introduction to the most important parameters of micromechanical oscillators, to the spectral properties of Brownian motion, to the known intrinsic and extrinsic mechanical damping sources and an overview of the estimation and manipulation of dissipation dilution. The description of the experimental results of this thesis will start in Chapter 3, reporting on the development of crystalline nanostrings with phononic crystal (PnC) soft clamping and state-of-the-art mechanical dissipation at liquid Helium cryogenic temperatures. Chapter 4 will describe our room

temperature optomechanical system: a membrane-in-the-middle system (MiM) with an ultracoherent resonator embedded in a high-finesse Fabry-Pérot cavity. I will describe the details of the apparatus, and report on a strong thermal noise source we encountered and characterized since the first investigations of our optomechanical cavity – thermomechanical intermodulation noise (TIN). Finally, I will present our recent efforts in suppressing TIN and results on feedback cooling in the MiM experiment, as well as the design and fabrication of new membrane resonators that could significantly simplify the requirements for ground-state cooling from room temperature, i.e. hierarchical trampoline resonators and density-modulated phononic crystal membranes.

## FUNDAMENTALS OF NANOMECHANICAL RESONATORS

---

In this chapter, I introduce the language, the observables and the most important figures of merit pertaining to mechanical resonators, with particular focus on nanomechanical structures under high tension. First, the fundamental fields and equations that describe the vibrations of a bi-dimensional, elastic thin structure will be presented. I will then introduce the most important parameters for a mechanical resonator, such as the spring constant and effective mass, used for mapping to a one-dimensional harmonic oscillator model. I will discuss the Brownian motion induced by the interaction of the oscillator with a thermal reservoir, and its formal treatment with the fluctuation-dissipation theorem. The discussion will then focus on the energy dissipation mechanisms in mechanical oscillators, and I will introduce the principles and rules for computing the dissipation dilution for resonators under tension. Finally, I will review some secondary consequences of dissipation dilution, such as the anharmonicity due to geometric nonlinearity and the resonant frequency fluctuations.

### 2.1 QUANTIZATION OF THE EQUATIONS OF ELASTICITY

#### 2.1.1 Strain, stress and elastic energy

The deformations of a solid-state, continuous body are described by the theory of elasticity [33]. A *displacement field* (or deformation field)  $\vec{u}$  maps the position of the elements of the body before and after the deformation:

$$\vec{r}' = \vec{r} + \vec{u}(\vec{r}) \quad (2.1)$$

The distance  $ds$  between closely-spaced points in the deformed body can be expressed in terms of the original coordinates (by a Taylor expansion of  $\vec{u}$  to the first order):

$$\begin{aligned} ds^2 &= (dr_i + du_i)(dr_i + du_i) \\ &= dr_i dr_i + \left( \frac{\partial u_i}{\partial r_j} + \frac{\partial u_j}{\partial r_i} \right) dr_i dr_j + \frac{\partial u_k}{\partial r_i} \frac{\partial u_k}{\partial r_j} dr_i dr_j, \end{aligned} \quad (2.2)$$

where summation over repeated indices is implied (Einstein convention, adopted for the remainder of this chapter). We can now define a *strain tensor*, that will provide a definition of metric in the deformed body:

$$\epsilon_{ij} = \frac{1}{2} \left( \frac{\partial u_i}{\partial r_j} + \frac{\partial u_j}{\partial r_i} + \frac{\partial u_k}{\partial r_i} \frac{\partial u_k}{\partial r_j} \right), \quad (2.3)$$

such that  $ds^2 = (\delta_{ij} + 2\epsilon_{ij}) dr_i dr_j$  ( $\delta_{ij}$  is the Kronecker delta). Note that the strain tensor is symmetric by construction (an antisymmetric component would represent rigid

motion, which does not change distances within the body). In equation 2.3, the strain tensor consists of two contributions: the first summand is linear in the displacement amplitude, while the second is quadratic,

$$\epsilon_{ij}^{(\text{lin})} = \frac{1}{2} \left( \frac{\partial u_i}{\partial r_j} + \frac{\partial u_j}{\partial r_i} \right) \quad (2.4)$$

$$\epsilon_{ij}^{(\text{nl})} = \frac{1}{2} \frac{\partial u_k}{\partial r_i} \frac{\partial u_k}{\partial r_j} \quad (2.5)$$

The second contribution is called *geometrically nonlinear* and is simply due to the Euclidean definition of distance. It is generally neglected in the study of small deformations, but can imply very tangible consequences for vibrations, as we will see in the treatment of dissipation dilution.

In order to write equations of motion for the reversible deformations of an elastic body, we need an expression for the elastic energy density,  $w$  (the total elastic energy is obtained by integrating  $w$  over the volume of the body). Rigid deformations do not store elastic energy, therefore the strain tensor is an appropriate variable for constructing the energy. The simplest such scalar, that respects basic assumptions of temporal and spatial invariance, is:

$$w = \frac{1}{2} C_{ijkl} \epsilon_{ij} \epsilon_{kl}, \quad (2.6)$$

where  $C_{ijkl}$  is the third-rank stiffness tensor, whose elements have the dimensions of pressure. Equation 2.6 models the simplest case of *physically linear* elastic bodies, which is an appropriate treatment for all the mechanical resonators described in this thesis. Note however that for some materials, like rubbers or polymers undergoing very large deformations, the model of 2.6 is no longer sufficient, and more complicated expressions have to be postulated [34]. Elastic forces within the body are expressed through the *stress tensor* (symmetric in turn):

$$\sigma_{ij} = \frac{\partial w}{\partial \epsilon_{ij}}, \quad (2.7)$$

such that the elastic energy density can be expressed as:

$$w = \frac{1}{2} \sigma_{ij} \epsilon_{ij} \quad (2.8)$$

Stress and strain components are linearly related with the elastic energy defined in 2.6, and their dependence determines the elements of the stiffness tensor. This relation is a generalization of Hooke's law for continuum elasticity. The stiffness tensor is generally greatly simplified by symmetries of the solid-state material (e.g., crystal lattice symmetries, as we will see in Chapter 3). Indeed, for an isotropic material the relation between stress and strain is determined by just two independent elastic constants, Young's modulus  $E$  and Poisson's ratio  $\nu$ :

$$\begin{pmatrix} \sigma_{11} \\ \sigma_{22} \\ \sigma_{33} \\ \sigma_{23} \\ \sigma_{13} \\ \sigma_{12} \end{pmatrix} = \frac{E}{(1+\nu)(1-2\nu)} \begin{pmatrix} 1-\nu & \nu & \nu & 0 & 0 & 0 \\ \nu & 1-\nu & \nu & 0 & 0 & 0 \\ \nu & \nu & 1-\nu & 0 & 0 & 0 \\ 0 & 0 & 0 & \frac{1-2\nu}{2} & 0 & 0 \\ 0 & 0 & 0 & 0 & \frac{1-2\nu}{2} & 0 \\ 0 & 0 & 0 & 0 & 0 & \frac{1-2\nu}{2} \end{pmatrix} \cdot \begin{pmatrix} \epsilon_{11} \\ \epsilon_{22} \\ \epsilon_{33} \\ \epsilon_{23} \\ \epsilon_{13} \\ \epsilon_{12} \end{pmatrix} \quad (2.9)$$

(the stress and strain tensor components have been here collected in a compact vector form, and their symmetric nature exploited in order to reduce the number of elements).

We consider the vibrations of a solid object with pre-stress, i.e. a body which has internal strains and stresses at rest. In order to simplify the elastic energy expressions, we split the stress and strain fields into their static and time-dependent parts:

$$\begin{aligned} \sigma_{ij} &= \bar{\sigma}_{ij}(\vec{r}) + \Delta\sigma_{ij}(t, \vec{r}) \\ \epsilon_{ij} &= \bar{\epsilon}_{ij}(\vec{r}) + \Delta\epsilon_{ij}(t, \vec{r}) \end{aligned} \quad (2.10)$$

Additionally, we explicitly decompose the time-dependent strain field into its linear and quadratic components,  $\Delta\epsilon_{ij} = \Delta\epsilon_{ij}^{(\text{lin})} + \Delta\epsilon_{ij}^{(\text{nl})}$ . We insert this expansion in 2.8, and find the time-varying part of the elastic energy density (the one which governs vibrational dynamics). Retaining only the terms up to the second order in the displacement gradient, we obtain:

$$\begin{aligned} \Delta w &\approx \bar{\sigma}_{ij}\Delta\epsilon_{ij}^{(\text{nl})} + \bar{\sigma}_{ij}\Delta\epsilon_{ij}^{(\text{lin})} + \frac{1}{2}\Delta\sigma_{ij}^{(\text{lin})}\Delta\epsilon_{ij}^{(\text{lin})} \\ &= \bar{\sigma}_{ij}\Delta\epsilon_{ij}^{(\text{nl})} + \frac{1}{2}\Delta\sigma_{ij}^{(\text{lin})}\Delta\epsilon_{ij}^{(\text{lin})} \\ &= \Delta w^{(\text{nl})} + \Delta w^{(\text{lin})} \end{aligned} \quad (2.11)$$

where we used the identity  $\bar{\sigma}_{ij}\Delta\epsilon_{ij} = \bar{\epsilon}_{ij}\Delta\sigma_{ij}$  to write the first summand, and, to write the second equality, we used the equilibrium condition  $\partial\bar{\sigma}_{ij}/\partial r_j = 0$ , valid for the static strain tensor [33].

### 2.1.2 Kirchhoff-Love membrane theory

With the expression of elastic energy density of 2.11, we can write a Lagrangian functional  $\mathcal{L}$  and apply the principle of least action to find the dynamical equations for the displacement field. This procedure can be used, for example, to derive the wave equations for excitations travelling within a medium with no pre-stress. However, for our case of interest, it is more useful to simplify 2.11 by considering a pre-stressed, high-aspect-ratio plate, i.e. a generic quasi-bidimensional body whose thickness  $h$  is much smaller than its other dimensions (see Fig. 2.1).

For a thin plate, we can parameterize flexure (bending) by a displacement field  $u_z = \psi(x, y)$ , approximately independent of  $z$ , the coordinate running along the plate thickness. The plate cannot support large forces at its interfaces and, being thin, some components of the stress tensor will approximately vanish in its interior:  $\Delta\sigma_{xz} =$

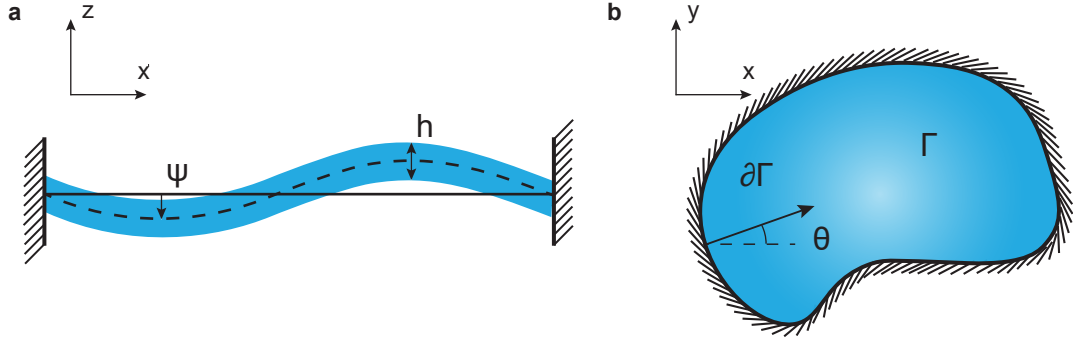


Figure 2.1: **a**, Cross-sectional view of a thin plate undergoing bending, with the neutral plane marked with a dashed line. **b**, Top-down view of the plate, with clamped boundaries marked by hatches.

$\Delta\sigma_{yz} = \Delta\sigma_{zz} = 0$ . Expressing these components with Hooke's law (2.9), and assuming an isotropic material, we derive conditions that define the remaining components of the displacement field:

$$\begin{aligned}\frac{\partial u_x}{\partial z} &= -\frac{\partial \psi}{\partial x} \\ \frac{\partial u_y}{\partial z} &= -\frac{\partial \psi}{\partial y} \\ \frac{\partial u_x}{\partial x} + \frac{\partial u_y}{\partial y} &= -\frac{\nu}{1-\nu} \frac{\partial \psi}{\partial z}\end{aligned}\tag{2.12}$$

Integrating these differential equations and choosing the integration constants such that strains vanish at the midpoint of the plate  $z = 0$  (neutral plane approximation) gives all the components of the strain tensor in terms of the displacement  $\psi$ :

$$\begin{aligned}\Delta\epsilon_{xx}^{(\text{lin})} &= -z \frac{\partial^2 \psi}{\partial x^2} \\ \Delta\epsilon_{yy}^{(\text{lin})} &= -z \frac{\partial^2 \psi}{\partial y^2} \\ \Delta\epsilon_{zz}^{(\text{lin})} &= z \frac{\nu}{1-\nu} \left( \frac{\partial^2 \psi}{\partial x^2} + \frac{\partial^2 \psi}{\partial y^2} \right) \\ \Delta\epsilon_{xy}^{(\text{lin})} &= -z \frac{\partial^2 \psi}{\partial x \partial y} \\ \Delta\epsilon_{xz}^{(\text{lin})} &= \Delta\epsilon_{yz}^{(\text{lin})} = 0\end{aligned}\tag{2.13}$$

Notice that strains change sign between the different sides of the plate, as is expected for bending. Using again 2.9, we can now calculate the linear, time-varying part of the elastic energy density:

$$\Delta w^{(\text{lin})} = z^2 \frac{E}{2(1-\nu^2)} \left( \left( \frac{\partial^2 \psi}{\partial x^2} + \frac{\partial^2 \psi}{\partial y^2} \right)^2 + 2(1-\nu) \left( \left( \frac{\partial^2 \psi}{\partial x \partial y} \right)^2 - \frac{\partial^2 \psi}{\partial x^2} \frac{\partial^2 \psi}{\partial y^2} \right) \right) \tag{2.14}$$

We can calculate similarly the geometrically-nonlinear dynamic strain components. By keeping derivatives of  $\psi$  up to first order:

$$\begin{aligned}\Delta\epsilon_{xx}^{(nl)} &= \frac{1}{2} \left( \frac{\partial\psi}{\partial x} \right)^2 \\ \Delta\epsilon_{yy}^{(nl)} &= \frac{1}{2} \left( \frac{\partial\psi}{\partial y} \right)^2 \\ \Delta\epsilon_{xy}^{(nl)} &= \frac{1}{2} \frac{\partial\psi}{\partial x} \frac{\partial\psi}{\partial y}\end{aligned}\tag{2.15}$$

The remaining components are irrelevant for the purpose of computing the geometrically-nonlinear component of the elastic energy density, which is expressed as <sup>1</sup>:

$$\Delta w^{(nl)} = \frac{1}{2} \left( \bar{\sigma}_{xx} \left( \frac{\partial\psi}{\partial x} \right)^2 + \bar{\sigma}_{yy} \left( \frac{\partial\psi}{\partial y} \right)^2 + 2\bar{\sigma}_{xy} \frac{\partial\psi}{\partial x} \frac{\partial\psi}{\partial y} \right)\tag{2.16}$$

With these expressions for the elastic potential energy, we are equipped to derive the plate equation of motion from the least action principle. First, we write the plate Lagrangian:

$$\mathcal{L} = \frac{\rho}{2} \left( \frac{\partial\psi}{\partial t} \right)^2 - \Delta w^{(lin)} - \Delta w^{(nl)},\tag{2.17}$$

where the first term provides the kinetic energy density, and  $\rho$  is the material density (we neglected the smaller components of the displacement field along  $x$  and  $y$ ). We then require the action

$$\mathcal{S} = \int dt \int_{\Omega} dV \mathcal{L},\tag{2.18}$$

to be stationary, i.e.  $\delta\mathcal{S} = 0$  (here  $\Omega$  represents the plate spatial domain). The  $\delta$  symbol here represents a functional variation in an arbitrary direction, which can be propagated to variations of the displacement field  $\psi$  and its time derivative,  $\dot{\psi}$ . We split the different terms of the action integral in order to separately analyze each of them, i.e.  $\delta\mathcal{S} = \int dt (\delta K - \delta W^{(lin)} - \delta W^{(nl)})$ . For the kinetic energy variation, we obtain:

$$\int dt \delta K = h \int dt \int_{\Gamma} dS \rho \psi \delta\psi = \left[ \int_{\Gamma} dS \rho h \psi \delta\psi \right]_{t=0}^{t=\infty} - \int dt \int_{\Gamma} dS \delta\psi \rho h \dot{\psi},\tag{2.19}$$

where the second equation was obtained with an integration by parts, a procedure which is always necessary in order to express the equations of motion in differential form and obtain boundary and initial conditions. Moreover,  $h$  is the plate thickness, assumed uniform, and  $\Gamma$  is the plate surface. We similarly vary the linear part of the elastic energy, which is repeated here, after integration over the  $z$  coordinate:

<sup>1</sup> The static shear stress  $\bar{\sigma}_{xy}$  is generally negligible in thin film materials used for nanomechanical resonators, but can arise after the thin film is patterned and suspended through microfabrication techniques.

$$\Delta W^{(\text{lin})} = \frac{D}{2} \int_{\Gamma} dS \left( \left( \frac{\partial^2 \psi}{\partial x^2} + \frac{\partial^2 \psi}{\partial y^2} \right)^2 + 2(1-\nu) \left( \left( \frac{\partial^2 \psi}{\partial x \partial y} \right)^2 - \frac{\partial^2 \psi}{\partial x^2} \frac{\partial^2 \psi}{\partial y^2} \right) \right), \quad (2.20)$$

where the factor  $D = \frac{Eh^3}{12(1-\nu^2)}$ , with units of torque, is called the *bending* or *flexural rigidity* of the plate. We start by differentiating the first integral:

$$\begin{aligned} \delta \left( \frac{1}{2} \int_{\Gamma} dS \nabla^4 \psi \right) &= \int_{\Gamma} dS \nabla^2 \psi \nabla^2 (\delta \psi) \\ &= \int_{\Gamma} dS \operatorname{div}(\nabla(\delta \psi) \nabla^2 \psi) - \int_{\Gamma} dS \nabla(\delta \psi) \cdot \nabla(\nabla^2 \psi) \\ &= \int_{\partial \Gamma} dl \nabla^2 \psi \frac{\partial(\delta \psi)}{\partial n} - \int_{\Gamma} dS \operatorname{div}(\delta \psi \nabla(\nabla^2 \psi)) + \int_{\Gamma} dS \delta \psi \nabla^4 \psi \\ &= \int_{\partial \Gamma} dl \left( \nabla^2 \psi \frac{\partial(\delta \psi)}{\partial n} - \delta \psi \frac{\partial(\nabla^2 \psi)}{\partial n} \right) + \int_{\Gamma} dS \delta \psi \nabla^4 \psi, \end{aligned} \quad (2.21)$$

where to expand the integrals we used the vector calculus identity  $\operatorname{div}(a\vec{b}) = a \operatorname{div}(\vec{b}) + \vec{b} \cdot \nabla a$ , and we used the divergence theorem to switch from surface integrals to flux integrals over the plate boundary  $\partial \Gamma$  ( $\partial/\partial n$  represents the derivative in the normal direction to the boundary). The second integral of 2.20 can be immediately converted to a line integral over the plate contour by writing it in terms of the divergence of a vector field. A straightforward but lengthy calculation gives:

$$\begin{aligned} \delta \left( \int_{\Gamma} dS \left( \frac{\partial^2 \psi}{\partial x \partial y} \right)^2 - \frac{\partial^2 \psi}{\partial x^2} \frac{\partial^2 \psi}{\partial y^2} \right) &= \\ \int_{\partial \Gamma} dl \frac{\partial(\delta \psi)}{\partial n} \left( 2\sin\theta \cos\theta \frac{\partial^2 \psi}{\partial x \partial y} - \sin^2\theta \frac{\partial^2 \psi}{\partial x^2} - \cos^2\theta \frac{\partial^2 \psi}{\partial y^2} \right) &+ \\ \int_{\partial \Gamma} dl \delta \psi \frac{\partial}{\partial l} \left[ \sin\theta \cos\theta \left( \frac{\partial^2 \psi}{\partial y^2} - \frac{\partial^2 \psi}{\partial x^2} \right) + (1 - 2\sin^2\theta) \frac{\partial^2 \psi}{\partial x \partial y} \right], \end{aligned} \quad (2.22)$$

where  $\partial/\partial l$  is a derivative carried out in the direction parallel to the contour and  $\theta$  is the angle formed locally between the  $x$  axis and the normal to the contour (see the definition in Fig. 2.1b). Finally, we differentiate the geometrically-nonlinear component of the elastic strain energy:

$$\Delta W^{(\text{nl})} = \frac{h}{2} \int_{\Gamma} dS \left( \bar{\sigma}_{xx} \left( \frac{\partial \psi}{\partial x} \right)^2 + \bar{\sigma}_{yy} \left( \frac{\partial \psi}{\partial y} \right)^2 + 2\bar{\sigma}_{xy} \frac{\partial \psi}{\partial x} \frac{\partial \psi}{\partial y} \right) \quad (2.23)$$

Applying the same divergence identity and integration by parts rules as in 2.21, we get the following expression for the energy variation:

$$\begin{aligned} \delta W^{(\text{nl})} &= -h \int_{\Gamma} dS \delta \psi \left( \bar{\sigma}_{xx} \frac{\partial^2 \psi}{\partial x^2} + \bar{\sigma}_{yy} \frac{\partial^2 \psi}{\partial y^2} + 2\bar{\sigma}_{xy} \frac{\partial^2 \psi}{\partial x \partial y} \right) + \\ h \int_{\partial \Gamma} dl \delta \psi \left( \bar{\sigma}_{xx} \frac{\partial \psi}{\partial x} \cos\theta + \bar{\sigma}_{yy} \frac{\partial \psi}{\partial y} \sin\theta + \bar{\sigma}_{xy} \left( \frac{\partial \psi}{\partial x} \sin\theta + \frac{\partial \psi}{\partial y} \cos\theta \right) \right), \end{aligned} \quad (2.24)$$



where we used  $\partial \bar{\sigma}_{ij} / \partial r_j = 0$  for the static stress field to simplify the surface integral.

The sum of the surface integrals in 2.19, 2.21 and 2.24 must vanish for the action to be stationary. Since the functional variation  $\delta\psi$  is arbitrary within the domain, the following differential equation must hold:

$$\rho \frac{\partial^2 \psi}{\partial t^2} + \frac{D}{h} \nabla^4 \psi - \bar{\sigma}_{xx} \frac{\partial^2 \psi}{\partial x^2} - \bar{\sigma}_{yy} \frac{\partial^2 \psi}{\partial y^2} - 2\bar{\sigma}_{xy} \frac{\partial^2 \psi}{\partial x \partial y} = 0, \quad (2.25)$$

which is the general equation for bending vibrations of a thin, isotropic plate with in-plane stresses, in the limit of small vibration amplitude (as we neglected terms of third order and higher in the displacement field gradient in writing the elastic strain energy). The boundary integrals in 2.19, 2.21, 2.22, 2.24, on the other hand, provide initial and boundary conditions for the differential problem. We can immediately see that all the boundary integrals vanish by the choice of displacement fields with a vanishing amplitude and normal derivative on the plate contours:

$$\psi|_{\partial\Gamma} = \frac{\partial \psi}{\partial n}|_{\partial\Gamma} = 0 \quad (2.26)$$

These are *clamped boundary conditions* for the plate, implying that the displacement vanishes at the plate edges and is locally horizontal close to them. On the other hand, the boundary integrals can be nullified by other conditions on the displacement field, such as those appropriate for simply supported or free edges. Since the analytical expressions of these boundary conditions are quite cumbersome, we refer to [33] for explicit expressions.

### 2.1.3 Modal expansion

We define now an inner product on the plate surface  $\Gamma$ :<sup>2</sup>

$$\langle \phi, \chi \rangle = \int_{\Gamma} dS \, \phi^* \chi \quad (2.27)$$

and rewrite the plate equation of motion as:

$$\rho h \frac{\partial^2 \psi}{\partial t^2} = \hat{O} \psi, \quad (2.28)$$

identifying with  $\hat{O}$  the differential operator containing all the spatial derivatives in 2.25:

$$\hat{O} \psi = -D \nabla^4 \psi + h \bar{\sigma}_{xx} \frac{\partial^2 \psi}{\partial x^2} + h \bar{\sigma}_{yy} \frac{\partial^2 \psi}{\partial y^2} + 2h \bar{\sigma}_{xy} \frac{\partial^2 \psi}{\partial x \partial y} \quad (2.29)$$

<sup>2</sup> Complex conjugation in the inner product definition is not strictly necessary as we are for the moment dealing with real functions, but we include it nevertheless in order to maintain the validity of the definition when we will later consider complex eigenmodes with Euler's notation.

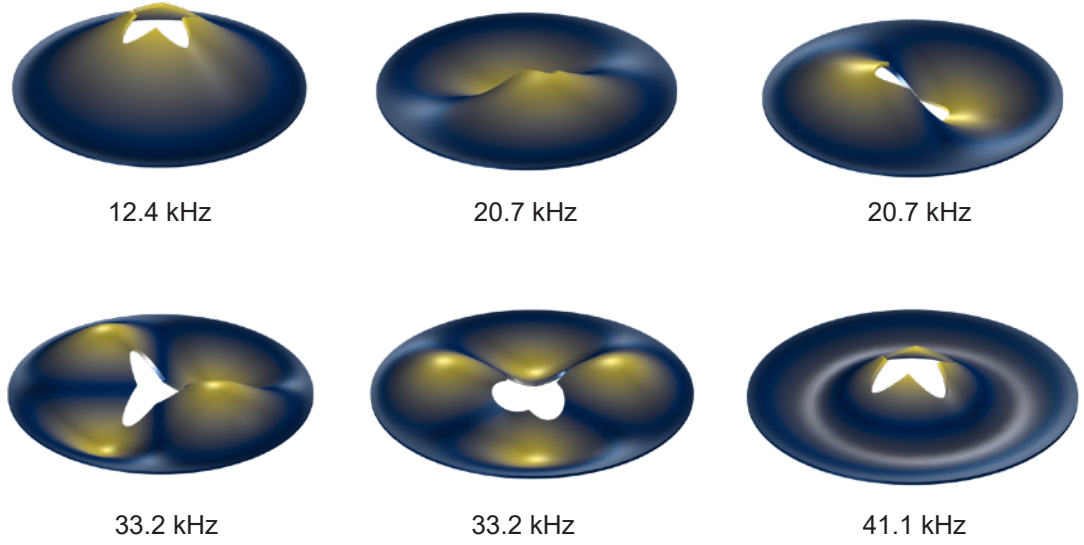


Figure 2.2: The six lowest-frequency bending eigenmodes of a tensioned plate, clamped on the outer rim and free at the inner contour.

$\hat{O}$  is a hermitian operator with the definition of inner product in 2.27, provided that all displacement fields satisfy the aforementioned boundary conditions on the plate contour <sup>3</sup>. Therefore, its eigenfunctions (see an example in Fig. 2.2) form a complete basis  $\phi_n(x, y)$  for the set of displacement fields with a fixed choice of boundary conditions, i.e. we can write any displacement field as:

$$\psi(x, y, t) = x_n(t) \cdot \sum_n \phi_n(x, y), \quad (2.30)$$

where the time-dependent amplitudes  $x_n$  have units of length (and the  $\phi_n$  are adimensional) <sup>4</sup>. The eigenfunctions are also orthogonal, i.e.  $\int_{\Gamma} dS \phi_n^* \phi_m = 0$  if  $m \neq n$ . We can then reduce 2.28 to a single-variable differential equation by inserting the modal expansion of 2.30, multiplying with an arbitrary eigenfunction from the left and integrating over the plate domain <sup>5</sup>. We obtain:

$$m_{\text{eff},n} \ddot{x}_n(t) = -k_n x_n(t), \quad (2.31)$$

the equation of motion of a simple harmonic oscillator with angular resonant frequency  $\Omega = \sqrt{k_n/m_{\text{eff},n}}$  and no dissipation, in which we have identified an effective mass [35] and spring constant for the eigenmode  $\phi_n$ , given by the following integral definitions:

<sup>3</sup> The proof of this statement is essentially analogous to the integration by parts carried out in 2.21.

<sup>4</sup> An expansion in the form of sum over discrete eigenmodes is guaranteed by the finite size of the plate domain.

<sup>5</sup> When this procedure is applied to an expansion over an arbitrary basis, it is termed a ‘‘Galerkin method’’ for the discretization of the partial differential equations. This method is common in the formulation of finite element problems.

$$\begin{aligned}
m_{\text{eff},n} &= \rho h \int_{\Gamma} dS |\phi_n^2| \\
k_n &= - \int_{\Gamma} dS \phi_n^* \hat{O} \phi_n = D \int_{\Gamma} dS \phi_n^* \nabla^4 \phi_n - \\
&\quad h \int_{\Gamma} dS \phi_n^* \left( \bar{\sigma}_{xx} \frac{\partial^2 \phi_n}{\partial x^2} + \bar{\sigma}_{yy} \frac{\partial^2 \phi_n}{\partial y^2} + 2\bar{\sigma}_{xy} \frac{\partial^2 \phi_n}{\partial x \partial y} \right) = k_n^{(\text{lin})} + k_n^{(\text{nl})}
\end{aligned} \tag{2.32}$$

In the expression of the spring constant we distinguished the two components originating from linear and nonlinear dynamic strains. Using the same rules of integration by parts applied when varying the action, we note that  $k_n^{(\text{lin})} = 2\Delta W^{(\text{lin})}(\phi_n)$  and  $k_n^{(\text{nl})} = 2\Delta W^{(\text{nl})}(\phi_n)$ , with the expressions of the elastic energy components given in 2.20 and 2.23. We insert the linear expansion of 2.30 in the Lagrangian:

$$L = \int_{-h/2}^{h/2} dz \int_{\Gamma} dS \mathcal{L} = \frac{\rho h}{2} \langle \dot{\psi}, \dot{\psi} \rangle + \frac{1}{2} \langle \psi, \hat{O} \psi \rangle = \sum_n \frac{m_{\text{eff},n}}{2} \dot{x}_n^2(t) - \frac{k_n}{2} x_n^2(t) \tag{2.33}$$

This Lagrangian represents infinite non-interacting harmonic oscillators, each corresponding to one eigenmode of the bidimensional structure. Exploiting the canonic quantization rules [36], we associate with the conjugated variables  $x_n$  and  $m_{\text{eff},n} \dot{x}_n$  the operators  $\hat{x}_n$  and  $\hat{p}_n$ , such that their commutator at  $t = 0$  is  $[\hat{x}_n(0), \hat{p}_n(0)] = i\hbar$ . Following the treatment of the quantum harmonic oscillator, we can also introduce the annihilation operator  $\hat{b}_n$  (and its hermitian-conjugated creation operator,  $\hat{b}_n^\dagger$ ):

$$\hat{b}_n(t) = \frac{1}{2} \left( \frac{\hat{x}_n(t)}{x_{\text{zpf},n}} + i \frac{\hat{p}_n(t)}{p_{\text{zpf},n}} \right), \tag{2.34}$$

with  $x_{\text{zpf},n} = \sqrt{\hbar/2m_{\text{eff},n}\Omega_n}$  and  $p_{\text{zpf},n} = \sqrt{\hbar m_{\text{eff},n}\Omega_n/2}$ . Using these operators we can express the quantum Hamiltonian of the mechanical resonator as:

$$\hat{H} = \sum_n \frac{\hat{p}_n^2}{m} - \hat{L} = \sum_n \hbar \Omega_n \left( \hat{b}_n^\dagger \hat{b}_n + \frac{1}{2} \right), \tag{2.35}$$

expressed in terms of the number of phonons populating each mechanical mode (the phonon number operator is  $\hat{n}_n = \hat{b}_n^\dagger \hat{b}_n$ ). The  $\hbar \Omega_n/2$  zero-point energy is given by vacuum fluctuations, and similarly  $x_{\text{zpf}}$ ,  $p_{\text{zpf}}$  can be shown to be the root mean square widths of the vacuum state wavefunction in its position and momentum representations.

By knowing the frequency eigenvalue and the effective mass of mechanical resonances in the frequency band of interest, one can disregard the distributed nature of the resonator for many practical aims, and treat it as a collection of independent harmonic oscillators. One case in which this simplification is crucial is the description and calculation of thermomechanical noise, which will be summarized in the next section.

## 2.2 FLUCTUATIONS AND DISSIPATION

### 2.2.1 Correlations and spectral densities

We want to consider fluctuations of the observables of an eigenmode of a mechanical resonator, excited by the interaction with an external environment. The environment is assumed to have a large heat capacity such that it is not measurably perturbed by the coupling. In order to deal with time-varying observables, it is convenient to formulate their quantum mechanical evolution in the *Heisenberg picture*, i.e. the system is presumed to remain in the initial state, while operators evolve according to the rule:

$$\hat{X}(t) = e^{i\hat{H}t/\hbar} \hat{X}(0) e^{-i\hat{H}t/\hbar} = \hat{U}^\dagger(t) \hat{X}(0) \hat{U}(t) \quad (2.36)$$

(valid if the Hamiltonian does not explicitly vary with time), where  $\hat{H}$  is the Hamiltonian and we defined  $\hat{U}$ , the time evolution operator. This picture is completely equivalent to the more traditional Schrödinger evolution of the wavefunction. Under the harmonic oscillator Hamiltonian of 2.35, for example, the position and momentum observables swap every quarter of the mechanical oscillation period:

$$\begin{aligned} \hat{x}_n(t) &= \hat{x}_n(0) \cos(\Omega_n t) + \frac{\hat{p}_n(0)}{m_{\text{eff},n} \Omega_n} \sin(\Omega_n t) \\ \hat{p}_n(t) &= \hat{p}_n(0) \cos(\Omega_n t) - m_{\text{eff},n} \Omega_n \hat{x}_n(0) \sin(\Omega_n t) \end{aligned} \quad (2.37)$$

The temporal fluctuations around the expectation value of an observable are expressed as:

$$\delta\hat{X}(t) = \hat{X}(t) - \langle \hat{X}(t) \rangle = \hat{X}(t) - \text{Tr}(\hat{\rho} \hat{X}(t)), \quad (2.38)$$

where  $\hat{\rho}$  is the density matrix representation of the state, which can be pure or mixed.

Fluctuations are more conveniently described in the frequency domain, and in order to do so we introduce an analogue of the *spectral density* of a classical random process for quantum-mechanical observables. With the definition of Fourier transform:

$$\hat{X}(\omega) = \int_{-\infty}^{\infty} dt \hat{X}(t) e^{i\omega t} \quad (2.39)$$

the spectral density is given by:

$$S_{XX}(\omega) = \lim_{T \rightarrow \infty} \langle \hat{X}_T^\dagger(\omega) \hat{X}_T(\omega) \rangle, \quad (2.40)$$

where the subscript  $T$  indicates that the Fourier transform does not extend between  $\pm\infty$ , but has been limited to a temporal window of duration  $T$  between  $\pm T/2$  (this definition is rendered necessary to deal with random processes carrying infinite energy). The Wiener-Khinchin theorem holds like in the case of classical random variables, and guarantees that the spectral density is the Fourier transform of the process autocorrelation (here we assume that processes are stationary, i.e. their moments do not change with time):

$$S_{XX}(\omega) = \int_{-\infty}^{\infty} dt \langle \hat{X}(t) \hat{X}(0) \rangle e^{i\omega t} = \frac{1}{2\pi} \int_{-\infty}^{\infty} d\omega' \langle \hat{X}(\omega) \hat{X}(\omega') \rangle, \quad (2.41)$$

where the second equality descends from the definition of Fourier transform and its inverse. Note that, by the definition of inverse transform, the integral of the spectral density gives the variance of the fluctuating observable:

$$\text{Var}(\delta\hat{X}(t)) = \langle \delta\hat{X}^2(0) \rangle = \frac{1}{2\pi} \int_{-\infty}^{\infty} d\omega S_{XX}(\omega), \quad (2.42)$$

implying the interpretation of  $S_{XX}$  as the power that the random process exerts in a unitary frequency band.

This definition of spectral density does not always correspond to an experimentally-observable quantity. An important difference with the case of classical random variables is that the spectral density is not necessarily symmetric in frequency, i.e.  $S_{XX}(\omega) \neq S_{XX}(-\omega)$ , irrespective of  $\hat{X}(t)$  being an hermitian operator. In order for the spectral density to be symmetric, the hermitian operator should commute with itself at different times, i.e.  $[\hat{X}(t), \hat{X}(t')] = 0$ , a condition which is not even respected in the case of the simple harmonic evolution of 2.37. Observable spectra are always symmetric around the zero frequency, and in order to define quantities that match more closely the empirical observables, a frequency-symmetrized version of the spectral density is sometimes introduced:

$$\bar{S}_{XX}(\omega) = \frac{1}{2} (S_{XX}(\omega) + S_{XX}(-\omega)) = \bar{S}_{XX}(-\omega) \quad (2.43)$$

In this case, spectral information at positive and negative frequencies is redundant, and it is customary to define a single-sided spectral density,  $\bar{S}_X(\omega) = 2\bar{S}_{XX}(\omega)$  for  $\omega > 0$ , such that signal powers obtained by integration are the same when computed only over positive frequencies.

Despite a frequency-asymmetric spectrum not being directly accessible, frequency asymmetries can be measured with appropriately-conceived measurement schemes [37], and they carry an interesting physical meaning. Consider a quantum harmonic oscillator coupled linearly to a reservoir with a fluctuating force that induces transitions between its energy levels, i.e. an interaction described by an interaction Hamiltonian  $\hat{H}_{\text{bath}} \propto \hat{x}\hat{F}$ . Using time-dependent perturbation theory and the Fermi golden rule, it can be shown that negative and positive frequency components of the force noise spectral density are proportional to the ascending and descending transition rates between adjacent eigenstates of the harmonic oscillator ladder [38], i.e.:

$$\frac{\gamma_{n \rightarrow n+1}}{\gamma_{n+1 \rightarrow n}} = \frac{S_{FF}(-\Omega)}{S_{FF}(\Omega)}, \quad (2.44)$$

with  $\Omega$  being the oscillator frequency. In particular, in thermal equilibrium *detailed balance* imposes that each total transition rate (i.e. weighted by the occupation factor) between eigenstates is individually balanced by its reverse, such that:

$$\frac{S_{FF}(-\Omega)}{S_{FF}(\Omega)} = \frac{\gamma_{n \rightarrow n+1}}{\gamma_{n+1 \rightarrow n}} = \frac{P_{n+1}}{P_n} = e^{-\beta \hbar \Omega} = \frac{\bar{n}}{\bar{n} + 1}, \quad (2.45)$$

where we noted with  $P_n = \langle n | \hat{\rho} | n \rangle$  the occupation probability of the eigenstate with  $n$  phonons, with  $\bar{n} = \langle \hat{n} \rangle$  the average phonon occupation,

$$\bar{n} = \frac{1}{e^{\beta \hbar \Omega} - 1}, \quad (2.46)$$

and with  $\beta = (k_B T)^{-1}$  the inverse thermal energy, where  $T$  is the equilibrium temperature. To write the last two equalities we used Bose-Einstein occupation statistics:

$$P_n = \exp\left(-\frac{\hbar \Omega n}{k_B T}\right) \left(1 - \exp\left(-\frac{\hbar \Omega}{k_B T}\right)\right) \quad (2.47)$$

We see that in the case of thermal equilibrium, the frequency asymmetry is simply given by the Boltzmann factor, and that in the ‘classical’ limit of high temperature,  $\bar{n} \rightarrow \infty$ , a symmetric spectral density is recovered.

### 2.2.2 Oscillator linearly coupled with a thermal bath

We focus now on the problem of a single harmonic oscillator (with angular frequency  $\Omega_m$  and effective mass  $m_{\text{eff}}$ ), kept in a thermal state by its contact with a bath at temperature  $T$ . The equilibrium is maintained by a linear interaction with the bath, i.e. described by the aforementioned Hamiltonian  $\hat{H}_{\text{bath}} = \hat{X}_i \hat{F}_i$ , with  $\hat{F}_i$  a stochastic force induced by the bath and  $\hat{X}_i$  its conjugated variable. Using perturbative theory, Ryogo Kubo derived an important result (valid both for quantum and classical mechanics), that relates the fluctuations induced in an observable by the random force coupled from the bath to the linear response of the system to a coherent drive [38, 39]. In a thermal state and under linear coupling with the bath, fluctuations in a system observable  $\hat{X}_j$  are given by the linear, delayed response

$$\begin{aligned} \delta \hat{X}_j(t) &= \int_{-\infty}^{\infty} dt' \chi_{jk}(t-t') \delta \hat{F}_k(t') \\ \delta \hat{X}_j(\omega) &= \chi_{jk}(\omega) \delta \hat{F}_k(\omega), \end{aligned} \quad (2.48)$$

where  $\chi_{jk}(t)$  is the time-domain force *susceptibility*, that can be computed from the free-evolution of the system observable:

$$\chi_{jk}(t) = -\frac{i}{\hbar} \langle [\hat{X}_j(t), \hat{X}_k(0)] \rangle \Theta(t), \quad (2.49)$$

where  $\Theta(t)$  is the Heaviside step function and  $\hat{X}_j(t)$  is the time evolution induced by the system Hamiltonian (without bath coupling).  $\chi(t)$  represents the system response to an impulsive force applied at  $t = 0$ , and by virtue of this theorem, describes also the incoherent response to fluctuations. As an example, we can compute the harmonic

oscillator susceptibility to a force coupling with position,  $\hat{H}_{\text{bath}} = \hat{x}\hat{F}$ , by inserting the time evolution  $\hat{x}(t)$  from 2.37 in 2.49:

$$\chi(t) := \chi_{xx}(t) = -\Theta(t) \frac{\sin(\Omega_m t)}{m_{\text{eff}} \Omega_m} \quad (2.50)$$

and Fourier-transform it to obtain the frequency-domain susceptibility:

$$\chi(\omega) = \frac{1}{m_{\text{eff}}(\Omega_m^2 - \omega^2)} + i \frac{\pi}{2m_{\text{eff}} \Omega_m} (\delta(\omega - \Omega_m) - \delta(\omega + \Omega_m)), \quad (2.51)$$

in which the real part coincides with the susceptibility of a classical harmonic oscillator with no dissipation, i.e. described by the equation of motion of 2.31 ( $\delta(x)$  is the Dirac delta function). The imaginary part is usually associated with dissipation (being time-delayed with respect to the force), but in this case is simply a consequence of the causality of the impulse response ( $\chi(t) = 0$  if  $t < 0$ ), or of the Kramers-Kronig relations.

### 2.2.3 The fluctuation-dissipation theorem

The density matrix of a thermal equilibrium state is given by the canonical ensemble:

$$\hat{\rho} = \frac{\exp(-\beta \hat{H}_0)}{Z}, \quad (2.52)$$

with  $\hat{H}_0$  being the system Hamiltonian (e.g. the harmonic oscillator model of 2.35).  $Z$  is the partition function that ensures correct normalization of the state:  $Z = \text{Tr}(\exp(-\beta \hat{H}_0))$ . Note that this state is mixed ( $\hat{\rho}^2 \neq \hat{\rho}$ ) and has zero off-diagonal elements in the basis of Fock states, i.e. it represents a classical mixture with no quantum coherence. Before proving the fluctuation-dissipation theorem, we state a useful, formal identity on self-correlations of operators in the thermal state. We consider the correlator of an observable with itself at a different time,

$$\begin{aligned} \langle \hat{X}(0) \hat{X}(t) \rangle &= \frac{1}{Z} \text{Tr} \left( \exp^{-\beta \hat{H}_0} \hat{X}(0) \hat{X}(t) \right) \\ &= \frac{1}{Z} \text{Tr} \left( \hat{X}(t) \exp^{-\beta \hat{H}_0} \hat{X}(0) \right) \\ &= \frac{1}{Z} \text{Tr} \left( \exp^{-\beta \hat{H}_0} \left( \exp^{\beta \hat{H}_0} \hat{X}(t) \exp^{-\beta \hat{H}_0} \right) \hat{X}(0) \right) \\ &= \frac{1}{Z} \text{Tr} \left( \exp^{-\beta \hat{H}_0} \hat{X}(t - i\hbar\beta) \hat{X}(0) \right) = \langle \hat{X}(t - i\hbar\beta) \hat{X}(0) \rangle \end{aligned} \quad (2.53)$$

where we used the cyclic property of the trace to go from the second to the third equality and the time evolution of operators in the Heisenberg picture (cfr. 2.36) to obtain the fifth from the fourth equation. In particular, 2.53 implies the following identity after Fourier-transforming and using the Wiener-Khinchin theorem:

$$S_{XX}(-\omega) = S_{XX}(\omega) e^{-\hbar\omega\beta}, \quad (2.54)$$

that coincides with the detailed balance criterion 2.45, as we are considering a thermal equilibrium state.

We want to derive a thermal equilibrium relation between the imaginary part of the susceptibility (providing, as we mentioned, the dissipative response to forces) and the spectral density of the fluctuations induced by the bath in the observable whose incoherent response is set by the susceptibility. To do this, we express the imaginary part of the self-susceptibility ( $\chi(t) := \chi_{xx}(t)$ , with  $x$  being a generic observable coupled to the thermal bath random force) in the frequency domain:

$$\text{Im}(\chi(\omega)) = \frac{\chi(\omega) - \chi^*(\omega)}{2i} \xrightarrow{\text{inverse FT}} \frac{\chi(t) - \chi^*(-t)}{2i} \quad (2.55)$$

Using the perturbative expression of susceptibility (2.49), the invariance under time-translations of the momenta of stationary processes and the properties of hermitian operators, we obtain a simple expression in terms of correlators:

$$\begin{aligned} \frac{\chi(t) - \chi^*(-t)}{2i} &= \frac{1}{2\hbar} (\Theta(t)(\langle \hat{X}(t)\hat{X}(0) \rangle - \langle \hat{X}(0)\hat{X}(t) \rangle) + \Theta(-t)(\langle \hat{X}(t)\hat{X}(0) \rangle - \langle \hat{X}(0)\hat{X}(t) \rangle)) \\ &= \frac{1}{2\hbar} (\langle \hat{X}(t)\hat{X}(0) \rangle - \langle \hat{X}(0)\hat{X}(t) \rangle) \\ &= \frac{1}{2\hbar} (\langle \hat{X}(t)\hat{X}(0) \rangle - \langle \hat{X}(t - i\hbar\beta)\hat{X}(0) \rangle), \end{aligned} \quad (2.56)$$

where we used 2.53 to derive the last equality. Taking the Fourier transform of both sides, and recalling that the Wiener-Khinchin theorem connects the self-correlation with the spectral density, we get the desired relationship between the fluctuations of the observable and the dissipative part of its susceptibility:

$$S_{XX}(\omega) = \frac{2\hbar}{1 - e^{-\hbar\omega\beta}} \text{Im}(\chi(\omega)) \quad (2.57)$$

A more familiar form is obtained by switching to frequency-symmetrized spectra, using the detailed balance relation 2.54 to expand the negative-frequency part:

$$\begin{aligned} \bar{S}_{XX}(\omega) &= (1 + e^{-\beta\hbar\omega}) \frac{S_{XX}(\omega)}{2} \\ &= \hbar \coth\left(\frac{\hbar\omega}{2k_B T}\right) \text{Im}(\chi(\omega)) \\ &= (2\bar{n}(\omega) + 1) \hbar \text{Im}(\chi(\omega)), \end{aligned} \quad (2.58)$$

with  $\bar{n}(\omega)$  being the average phonon occupation for an oscillator with frequency  $\omega$ . In the limit of high temperature  $\bar{n} \approx k_B T/(\hbar\omega) \gg 1$ , 2.58 can be approximated by <sup>6</sup>:

$$\bar{S}_{XX}(\omega) = \frac{2k_B T}{\omega} \text{Im}(\chi(\omega)) \quad (2.59)$$

<sup>6</sup> An approximation that is accurate when evaluating fluctuation frequencies below the THz range at  $T = 300$  K and up to several GHz at  $T = 1$  K.



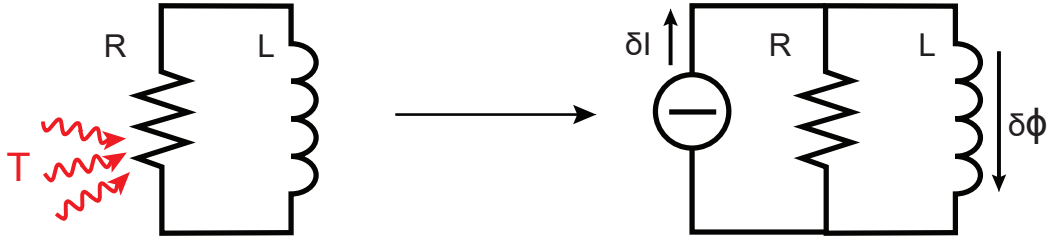


Figure 2.3: Johnson noise in an RL circuit. The passive circuit in thermal equilibrium at temperature  $T$  is equivalent to a noiseless RL with a noisy current source in parallel with the resistor.

The opposite limit,  $\beta \rightarrow \infty$ , implies that the system lies in the vacuum state, i.e.  $\hat{\rho} = |0\rangle\langle 0|$ . We then obtain the spectral density of zero-point fluctuations:

$$\bar{S}_{XX}^{\text{zpf}}(\omega) = \hbar \text{Im}(\chi(\omega)) \quad (2.60)$$

Finally, to refer the fluctuations of the system observable  $\delta\hat{X}(t)$  to an effective spectrum of the random force  $\bar{S}_{FF}$ , the linear response theory prescribes that 2.58 should simply be divided by  $|\chi(\omega)|^2$ :

$$\bar{S}_{FF}(\omega) = -(2\bar{n}(\omega) + 1) \hbar \text{Im}(\chi(\omega)^{-1}) \quad (2.61)$$

The expressions in 2.58, 2.59, 2.61 are the best-known forms of the fluctuation-dissipation theorem [39, 40]. They hold for classical stochastic processes as well as in quantum mechanics, and their scope of application goes well beyond the case of a mechanical resonator mode in thermal equilibrium, that we are mostly interested in. Consider for example the electric circuit illustrated in Fig. 2.3, where an inductor is connected in parallel with a resistor. In thermal equilibrium, the environment will induce voltage and current fluctuations in the inductor through the resistor dissipative contact, and the noisy resistor can be modelled as an ideal, noiseless resistor with a stochastic current source in parallel. The conjugate variable of the current is the flux threaded through the inductor, hence we can write the susceptibility as:

$$\chi = \phi/I = \frac{RL}{R - i\omega L} \quad (2.62)$$

So that the inductor flux noise is given by 2.58:

$$\bar{S}_{\phi\phi} = \hbar \coth\left(\frac{\hbar\omega}{2k_B T}\right) \frac{\omega L^2/R}{1 + \omega^2 L^2/R^2} \quad (2.63)$$

and the spectral density of the resistor current noise is obtained by considering the circuit current partition:

$$\bar{S}_{II} = \left| \frac{R - i\omega L}{R} \right|^2 \frac{\bar{S}_{\phi\phi}}{L^2} = \frac{\hbar\omega}{R} \coth\left(\frac{\hbar\omega}{2k_B T}\right) \xrightarrow{k_B T \gg \hbar\omega} \frac{2k_B T}{R}, \quad (2.64)$$

which is the expression of thermal Johnson current noise in a resistor, derived well before the fluctuation-dissipation theorem had been formulated in its general form [41]. Similarly, the theorem explains the connection found by Einstein between the frictional damping (dissipation) and the diffusion constant (fluctuation) of a particle undergoing Brownian motion in a viscous medium [42].

## 2.3 DISSIPATION DILUTION IN RESONATORS WITH TENSILE STRESS

### 2.3.1 Loss angle and quality factor

The fluctuation-dissipation theorem relates thermomechanical fluctuations with the damping properties, but our description of a plate mechanical resonator in section 2.1 did not include mechanical dissipation. If the dissipation rate is small compared to the mechanical frequency ( $Q \gg 1$ ), it is appropriate to introduce and compute it perturbatively, after formally solving the equations of elasticity and obtaining the displacement, strains and stresses.

The mechanical power dissipated by friction in a vibrating body can be written as:

$$P = - \int dV \sigma_{ij}^{(\text{diss})} \frac{\partial \epsilon_{ij}}{\partial t}, \quad (2.65)$$

where  $\sigma_{ij}^{(\text{diss})}$  is a tensor of dissipative stresses. If the material deformations are reversible and within the elastic regime, the dissipative stresses only depend on the dynamic strains and not on the static pre-strain. In order to treat the simplest-possible case, the stresses are postulated to depend only on the *local* strain field at the same point in space<sup>7</sup>, with a linear relation analogous to a dissipative version of Hooke's law. If we introduce a dissipative stiffness tensor  $\eta_{ijkl}(t)$ , explicitly time-dependent in order to model a delayed response to strain, the dissipated power simplifies to:

$$P(t) = - \int dV \int_{-\infty}^t d\tau \eta_{ijkl}(t - \tau) \Delta \epsilon_{kl}^{(\text{lin})}(\tau) \frac{\partial \Delta \epsilon_{ij}^{(\text{lin})}(t)}{\partial t}, \quad (2.66)$$

where we made the approximation  $\Delta \epsilon_{ij} \approx \Delta \epsilon_{ij}^{(\text{lin})}$ , as the linear strain terms are dominant. This expression is more conveniently written in the frequency domain, for vibrations at the frequency  $\omega$ :

$$P(\omega) = i\omega \int dV \eta_{ijkl}(\omega) \Delta \epsilon_{kl}^{(\text{lin})}(\omega) \Delta \epsilon_{ij}^{(\text{lin})}(\omega) \quad (2.67)$$

<sup>7</sup> This assumption is violated for some known mechanical dissipation mechanisms. In thermoelastic damping, for example, the dissipative stresses are mediated by a temperature field that is generated by expansion and compression, which has a finite extent governed by heat diffusion.

A great simplification is obtained by assuming a specific form of  $\eta(\omega)$ : it is suggestive to model the energy dissipation with an imaginary component of the material stiffness constants (e.g. the Young's modulus, in the isotropic case), since in the time domain this will bring forth a time-delayed response. Limiting ourselves to the isotropic case, we write the Young's modulus as  $E^{(\text{lossy})}(\omega) = Ee^{-i\phi(\omega)} \approx E(1 - i\phi(\omega))$ . The phase term  $\phi(\omega) \ll 1$  is called *loss angle* in treatments of friction in solids [43] and its introduction allows an alternative expression of the dissipative stiffness:  $\eta_{ijkl}(\omega) \approx -i\phi(\omega)C_{ijkl}$ . By comparison with 2.11, we can then write the dissipated power in terms of the linear elastic strain energy:

$$P(\omega) = 2\omega\phi(\omega)\Delta W^{(\text{lin})} \quad (2.68)$$

We want to relate this expression of the dissipated power to an effective damping rate for the one-dimensional harmonic oscillator model. Using the normal mode expansion of 2.30, and recalling that the dissipated power for a particle moving in one dimension is  $P(t) = -F\dot{x}$ , or  $P(\omega) = i\omega Fx$ , with  $F$  a generic dissipative force, we obtain:

$$F(\omega) = -2i\phi(\omega)\Delta W^{(\text{lin})}(\phi_n)x_n(\omega), \quad (2.69)$$

Note that the energy functional evaluated on a normalized eigenfunction,  $\Delta W^{(\text{lin})}(\phi_n)$ , has dimensions of N/m. We can add the dissipative force to our equation of motion for the eigenmode amplitude in the frequency domain (we drop the eigenmode index for brevity) and obtain the familiar form of a damped-driven harmonic oscillator,

$$\begin{aligned} (-m_{\text{eff}}\omega^2 + k - i\omega m_{\text{eff}}\Gamma(\omega))x(\omega) &= F_{\text{drive}}(\omega) \\ \chi(\omega) &= \frac{1}{m_{\text{eff}}((\Omega^2 - \omega^2) - i\omega\Gamma(\omega))} \end{aligned} \quad (2.70)$$

The damping rate  $\Gamma$  is expressed by comparison with the previous expression for the dissipative force:

$$\Gamma(\omega) = \frac{2\phi(\omega)}{m_{\text{eff}}\omega}\Delta W^{(\text{lin})}, \quad (2.71)$$

and the quality factor is evaluated as the ratio of the resonant frequency to the damping rate:

$$Q = \frac{\Omega}{\Gamma} \approx \frac{m_{\text{eff}}\Omega^2}{2\phi(\Omega)\Delta W^{(\text{lin})}} = \frac{k^{(\text{lin})} + k^{(\text{nl})}}{2\phi(\Omega)\Delta W^{(\text{lin})}} = \frac{1}{\phi(\Omega)} \frac{\Delta W^{(\text{nl})} + \Delta W^{(\text{lin})}}{\Delta W^{(\text{lin})}}, \quad (2.72)$$

where we assumed  $\Gamma \ll \Omega$ , thus  $\omega \approx \Omega$  to write the second equality. This expression for  $Q$  contains the loss angle, which is a property of the internal friction of the material, and an enhancement factor in terms of a ratio of geometrically nonlinear and linear strain energies. It is customary to identify an intrinsic quality factor  $Q_{\text{int}} = \phi(\Omega)^{-1}$ , and a *dilution factor* provided by the coexistence of static stress in the structure and dynamic nonlinear strain in the vibrational mode, that ensure  $\Delta W^{(\text{nl})} \neq 0$ :

$$Q = D_Q \cdot Q_{\text{int}}, \quad (2.73)$$

$$D_Q = 1 + \frac{\Delta W^{(\text{nl})}}{\Delta W^{(\text{lin})}} = 1 + \frac{k^{(\text{nl})}}{k^{(\text{lin})}} \quad (2.74)$$

The expression of  $D_Q$  was obtained for bidimensional, high aspect ratio mechanical resonators, but it is useful to remember that they hold also for generic three-dimensional elastic bodies [24]. However,  $D_Q$  is heavily dependent on the resonator geometry and strained high-aspect-ratio structures were the only ones that so far exhibited measurable and significant dissipation dilution. It is useful to remark the conditions that allowed us to express the quality factor in the simple form of 2.73, as a direct enhancement over the intrinsic properties of the material:

- Dissipation should be governed by coupling of the linear strains produced during the dynamic deformation of the material with internal degrees of freedom, and not by interaction with external entities separated from the mechanical resonator.
- Dissipation manifests locally, as a simple temporal lag between dissipative stresses and strain at the same location in space, which is set by the loss angle  $\phi$ .
- The oscillation amplitude is small and lies in the linear regime.
- The diluted quality factor should be high,  $Q \gg 1$ .

An historical excursus on the discovery of dissipation dilution in nanomechanical resonators is instructive. Dissipation dilution was first observed in strings of silicon nitride ( $\text{Si}_3\text{N}_4$ ) in the mid 2000s, when Verbridge et al. measured quality factors ( $Q$ ) over one million at room temperature [44, 45], 100 times higher than the expectation from intrinsic material losses in amorphous media. Similarly, very high  $Q$ s were observed in  $\text{Si}_3\text{N}_4$  membranes intended for transmission electron microscopy sample holders (grids) [46]. Silicon nitride does not a priori appear to be a good material for high- $Q$  mechanical resonators, as amorphous materials are known to have high intrinsic mechanical losses ( $Q_{\text{int}} \sim 10^3$ ). The appeal of silicon nitride stems from a technical advantage: thin films can be deposited with high strain through low pressure chemical vapor deposition (LPCVD). In the context of nanomechanical oscillators it was evident that strain played a crucial role in the high quality factors that were observed. Nevertheless, the origin of the observed low dissipation was not immediately obvious, as evidenced by it being described as a ‘crack in the universal dissipation of glasses’ [47]. Later, strain and geometric nonlinearity of deformations were recognized as the cause of the phenomenon [24, 48]. The first link to the work on mirror suspensions in gravitational wave interferometers from Saulson and González [23] was made by Wu and Yu in 2011 [49] and, around the same time, Unterreithmeier et al. [48] and Schmid et al. [50] provided a complete theoretical modeling of the dissipation dilution in a doubly-clamped beam. Yu et al. later extended the theory to the case of a clamped rectangular membrane [51]. After these findings early in the last decade, it became fully appreciated that dissipation dilution occurs both in macroscopic mirror suspensions and in nanomechanical resonators.

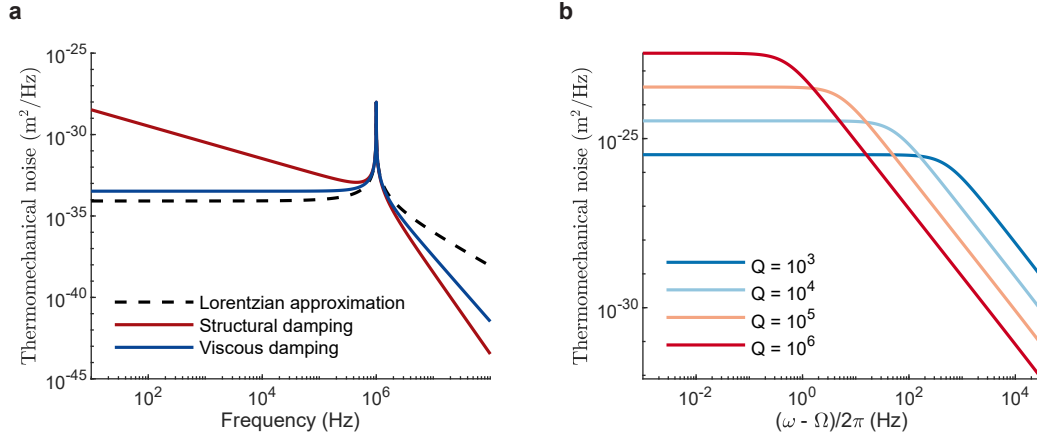


Figure 2.4: **a**, Thermomechanical displacement spectral density  $\bar{S}_{xx}(f)$ , for different mechanical susceptibility models. The modelled oscillator has  $m_{\text{eff}} = 1 \text{ ng}$ ,  $\Omega = 1 \text{ MHz}$  and  $Q = 10^5$ , and the temperature is assumed to be  $T = 300 \text{ K}$ . **b**, Effect of the quality factor on the thermomechanical noise close to resonance. For increasing  $Q$ , the resonant peak becomes sharper and higher, and the background noise decreases. The oscillator is assumed to be structurally-damped.

Let us discuss in greater detail the intrinsic friction described by  $\phi$ . In 2.70, a damping rate  $\Gamma$  that does not depend on frequency implies a frictional force proportional to velocity, which is analogous to the well known case of drag during motion within a liquid or a gas (viscous damping). From 2.71, we note that this case coincides with a loss angle proportional to the frequency. While gas or liquid damping is a frequent dissipation source in mechanical resonators, it does not resemble intrinsic friction occurring within the material, it cannot be diluted by tension, and indeed a linearly-varying loss angle is not observed in measurements of mechanical energy lost to friction. Since the pioneering work of Kimball and Lovell in 1927 [52]<sup>8</sup>, it has been observed that the loss angle of solid-state objects is, to a good approximation, frequency independent [53], although no clear theoretical explanation has been provided so far. An oscillator model with  $\partial\phi/\partial\omega \approx 0$  or  $\Gamma(\omega) = \Omega^2/(Q\omega)$  is said to be affected by *structural damping* [6].

The main consequence of the loss angle dependence on frequency is on the spectral shape of thermomechanical noise: evaluating the high-temperature fluctuation dissipation relation 2.59 for the damped harmonic oscillator susceptibility of 2.70, we obtain

$$\bar{S}_{xx} \approx \frac{2k_B T m_{\text{eff}} \Gamma(\omega)}{m_{\text{eff}}^2} \frac{1}{(\omega^2 - \Omega^2)^2 + \omega^2 \Gamma^2(\omega)} = 2k_B T m_{\text{eff}} \Gamma(\omega) \cdot |\chi^2(\omega)| \quad (2.75)$$

and the corresponding well-known equation of thermomechanical force noise coupled from the environment,

<sup>8</sup> The method applied by Kimball and Lovell to measure material friction is particularly clever: a slender bar of the analyzed material is bent by applying a weight to its end, and set into rotation on its axis at the desired frequency. Upon rotation, the alternating tension and compression of the material elements induces frictional forces that manifest with an overall deflection of the bar. Interestingly, the loss angle correspond exactly to the angle of this deflection from the vertical.

$$\bar{S}_{\text{FF}} = (2\bar{n} + 1)\hbar m_{\text{eff}}\Gamma(\omega)\omega \approx 2k_{\text{B}}T m_{\text{eff}}\Gamma(\omega), \quad (2.76)$$

where the last equality holds for the high temperature, classical limit. The spectrum of 2.75 has a different frequency dependence according to  $\Gamma(\omega)$  representing a viscous or structural damping relation, as represented in Fig. 2.4a for a generic oscillator. Close to resonance, the lineshape does not exhibit a significant difference in the two cases, but the frequency scaling at low and high frequencies is dramatically different: structural damping thermal noise rolls off faster ( $\propto \omega^{-5}$ ) beyond the resonant frequency, and diverges as  $\propto \omega^{-1}$  at low frequency, while for viscous damping the scaling is  $\propto \omega^4$  and  $\propto \omega^0$  at high and low frequencies. A Lorentzian approximation (dashed black line), given by:

$$\chi(\omega) \approx \frac{1}{2\Omega m_{\text{eff}}((\omega - \Omega) - i\Gamma/2)} \quad (2.77)$$

fits well the resonant peak, but fails to describe the off-resonant thermal noise tails; however it is an appropriate model for most experiments, since typically the sensitivity is insufficient to resolve the off-resonant background. Exceptions are found in recent works from the LIGO collaboration, where the outstanding interferometric sensitivity allowed the resolution of low frequency thermal noise over many decades in frequency [54]. The structural damping scaling introduced interesting implications in quantum optomechanics experiments with extreme optical spring effect, including the observation of quantum radiation pressure shot noise and feedback cooling to small phonon occupations of macroscopic mirrors [5, 55, 56].

The divergence of the structurally-damped thermomechanical noise at low frequencies implies an infinite variance of displacement fluctuations (through 2.42), which is clearly non-physical. This discrepancy is also manifested by considering the impulse response  $\chi(t)$ , which can be real only if the loss angle is an odd function of frequency,  $\phi(\omega) = -\phi(-\omega)$  [43]. Both anomalies can be reconciled by assuming the loss angle not to be constant for all frequencies, but to vanish smoothly for  $\omega \rightarrow 0$  (as occurs for viscous damping). The condition is not stringent, as the low frequency displacement fluctuations become comparable to the contribution of the resonant peak only when considering  $\phi^{-1}$  octaves below the resonance [6], so that the deviation from a frequency-independent loss angle can in reality occur at immeasurably-low frequencies. A first-principles theory of structural damping in the solid state will hopefully emerge in the future.

The total variance of position fluctuations can be recovered from the integration of their power spectral density 2.75 over all frequencies [20],

$$\langle \chi^2 \rangle = \frac{1}{2\pi} \int_{-\infty}^{\infty} d\omega \bar{S}_{xx}(\omega) = \frac{k_{\text{B}}T}{m_{\text{eff}}\Omega^2}, \quad (2.78)$$

where the last equality holds both for viscous damping and for the Lorentzian approximation of the susceptibility: the fluctuation-dissipation theorem, formulated for thermal equilibrium, fulfills the equipartition theorem, and in particular the position

variance does not depend on the mechanical damping rate. The way this fact is manifested in the frequency domain is shown in Fig. 2.4b: as the quality factor of the oscillator increases, the thermomechanical peak becomes sharper and taller, in such a way that the total integral remains the same. Experimentally, resonances with higher quality factors will be more prominent in the spectral landscape, and their thermal noise will sooner decay below the sensitivity background of the measurement apparatus.

### 2.3.2 Dissipation dilution in a square drum

In order to acquire a sense of the magnitude and scaling of dissipation dilution, we consider a simple but illuminating example: a square, tensioned drum of side length  $L$  and surface  $L \times L$  [51]. This example is also experimentally relevant: thin film membranes made of transparent, strained  $\text{Si}_3\text{N}_4$  and used as sample holders for transmission electron microscopes were among the first mechanical resonators to be noticed for their long-lived resonances. Due to their low absorption at optical and near infrared wavelengths, they were soon employed for cavity optomechanics experiments [46], even before an explanation of their anomalously high quality factor was found in terms of dissipation dilution. These membranes are also commercially available from companies such as Norcada (<https://www.norcada.com>).

The static stress field in the thin film is assumed to be homogeneous, and lacking shear components:  $\bar{\sigma}_{xx} = \bar{\sigma}_{yy} = \sigma$  and  $\bar{\sigma}_{xy} = 0$ . The spatial parts of its out-of-plane flexural eigenmodes are described by the time-independent plate equation (see 2.25):

$$-\frac{D}{h}\nabla^4\phi + \sigma\nabla^2\phi = \hat{O}\phi = -\rho\Omega^2\phi, \quad (2.79)$$

It is useful to write the equation in dimensionless form, by using normalized variables  $p = x/L$ ,  $s = y/L$  ranging from 0 to 1, such that 2.79 becomes:

$$\frac{\lambda^2}{1-\nu^2}\nabla^4\phi - \nabla^2\phi = \frac{\rho\Omega^2L^2}{\sigma}\phi, \quad (2.80)$$

where differential operators are now expressed in terms of the derivatives with respect to  $p$  and  $s$ , and we introduced the *strain parameter* [24, 57]  $\lambda = \sqrt{\frac{E}{12\sigma}}\frac{h}{L}$ . Crucially, the strain parameter controls the shape of the flexural modes: in a high aspect-ratio plate with significant tension,  $\lambda \ll 1$ , and the first term of 2.80 can be neglected, except in regions where the bending is particularly strong and the fourth derivatives are large. In any case, for a tensioned, high aspect-ratio plate the first term can be considered as a small perturbation, carrying important consequences as we will see later. Solving the equation of Laplace operator without the first term of 2.80 amounts to finding the eigenfunctions of the Laplace operator. On a square domain, the method of the separation of variables can be applied, to find the eigenfunctions vanishing at the plate boundaries:

$$\phi_{n,m}^{(0)} \approx \sin\left(\frac{n\pi x}{L}\right) \sin\left(\frac{m\pi y}{L}\right) \quad (2.81)$$

With these mode shapes, the corresponding eigenfrequencies are easily obtained with the integral definitions of spring constant and effective mass in 2.32:



$$\Omega_{n,m} = \sqrt{\frac{k_{n,m}}{m_{\text{eff},n,m}}} = \sqrt{\frac{\int dS \phi_{n,m}^{(0)} \hat{O} \phi_{n,m}^{(0)}}{\rho h \int dS \phi_{n,m}^{(0)2}}} \approx \frac{\pi}{L} \sqrt{\frac{\sigma(n^2 + m^2)}{\rho}}, \quad (2.82)$$

We notice that the couples of modes with indices  $(n, m)$  and  $(m, n)$  are degenerate in frequency, as expected from the symmetry of the problem.

The mode shapes of 2.81 vanish on the plate boundaries, but they do not respect the clamped boundary conditions  $(\phi|_{\partial\Gamma} = \frac{\partial\phi}{\partial n}|_{\partial\Gamma} = 0)$ , which describe most nanomechanical resonators connected to a rigid support, since the normal derivatives are finite at  $x = 0, L$  and  $y = 0, L$ . A better approximation is obtained by applying a localized correction  $\phi^{(1)}$  in the vicinity of each of the four boundaries of the plate, which smoothly connects to the original mode shapes  $\phi^{(0)}$  and possesses a vanishing first derivative at the boundary. These corrections will be functions of a single variable, as only the normal derivatives need to be suppressed. Let us consider, for example, the edge defined by  $x = 0$ . In the vicinity of the boundaries, the amplitude of the mode shape is infinitesimally small, so that the adimensional plate equation 2.80 can be simplified to:

$$\frac{\lambda^2}{1 - \nu^2} \frac{d^4\phi}{dx^4} - \frac{d^2\phi}{dx^2} \approx 0 \quad (2.83)$$

The general integral of this differential equation is:

$$\phi(p) = A e^{\frac{\sqrt{1-\nu^2}p}{\lambda}} + B e^{-\frac{\sqrt{1-\nu^2}p}{\lambda}} + Cp + D \quad (2.84)$$

We can set  $A = 0$  since it controls a diverging term for  $x > 0$ . The remaining integration constants can be found by imposing that  $\phi$  and  $d\phi/dp$  vanish at  $p = 0$ , and that  $d\phi/dp \rightarrow \partial\phi^{(0)}/\partial p|_{p=0}$  as  $p \rightarrow \infty$ , providing a smooth connection to the unperturbed solutions. We find the following expression for the mode shape approximation in the vicinity of the edge  $x = 0$ :

$$\phi(x) \approx \frac{\partial\phi^{(0)}}{\partial x} \Big|_{x=0} \left( x + \frac{\lambda L}{1 - \nu^2} \left( e^{-\frac{\sqrt{1-\nu^2}x}{\lambda L}} - 1 \right) \right), \quad (2.85)$$

where the first term in the parentheses is the Taylor approximation of  $\phi^{(0)}$ , and we can identify the second term as the boundary correction. Adding the contribution of the remaining edges, we obtain the perturbation term <sup>9</sup>:

$$\begin{aligned} \phi_{n,m}^{(1)}(x, y) = \frac{n\pi\lambda}{1 - \nu^2} & \left( \left( e^{-\frac{\sqrt{1-\nu^2}x}{\lambda L}} - 1 \right) + (-1)^{n+1} \left( e^{-\frac{\sqrt{1-\nu^2}(L-x)}{\lambda L}} - 1 \right) \right) \sin\left(\frac{m\pi y}{L}\right) + \\ & \frac{m\pi\lambda}{1 - \nu^2} \left( \left( e^{-\frac{\sqrt{1-\nu^2}y}{\lambda L}} - 1 \right) + (-1)^{m+1} \left( e^{-\frac{\sqrt{1-\nu^2}(L-y)}{\lambda L}} - 1 \right) \right) \sin\left(\frac{n\pi x}{L}\right) \end{aligned} \quad (2.86)$$

<sup>9</sup> This expression of  $\phi^{(1)}$  satisfies the clamped boundary conditions only approximately, in the limit  $\lambda \ll 1$ .



We notice that the perturbation is truly local to the membrane edges, as the exponential corrections vanish for distances much larger than  $\lambda L$  from the membrane boundaries. This characteristic length can be well below a micrometer for thin nanomechanical membranes under tension; for example  $\lambda L \approx 5h$  for the typical mechanical parameters of stoichiometric LPCVD silicon nitride ( $\text{Si}_3\text{N}_4$ ) thin films.

With this approximated expression of the mode shapes, we can calculate the dilution factor with the prescription of 2.74, specifically, as a ratio of geometrically nonlinear and linear strain energies. To simplify calculations, we note that for a clamped plate, the second integral in the definition of linear elastic energy 2.20 (the one containing the Gaussian curvature) must be null, as can be seen by applying Green's theorem [51]<sup>10</sup>.

$$\begin{aligned} \Delta W^{(\text{lin})} &\approx \frac{D}{2} \int_{\Gamma} dx dy \left( \nabla^2 \phi_{n,m}^{(0)}(x, y) \right)^2 + \frac{D}{2} \int_{\Gamma} dx dy \left( \nabla^2 \phi_{n,m}^{(1)}(x, y) \right)^2 \\ &\approx \frac{D(n^2 + m^2)\pi^2}{8L^2} \left( \pi^2(n^2 + m^2) + \frac{2\sqrt{1-\nu^2}}{\lambda} \right), \end{aligned} \quad (2.87)$$

where the first summand in the parentheses comes from the square curvature integration over the standing wave ("antinode contribution") and the second from the integration over the four high curvature regions at the clamped boundaries ("clamping contribution"). The product term  $\propto \nabla^2 \phi^{(0)} \cdot \nabla^2 \phi^{(1)}$  can be neglected, as  $\nabla^2 \phi^{(0)} \approx 0$  in the vicinity of the boundaries, where  $\phi^{(1)}$  is appreciable. The geometrically nonlinear contribution is well-approximated by computing the integral of 2.23 over the unperturbed standing wave profile alone (the boundary correction is negligible, as it exhibits a vanishing normal derivative):

$$\Delta W^{(\text{nl})} \approx \frac{h\sigma}{2} \int_{\Gamma} dx dy \left( \left( \frac{\partial \phi^{(0)}}{\partial x} \right)^2 + \left( \frac{\partial \phi^{(0)}}{\partial y} \right)^2 \right) = \frac{h\sigma\pi^2}{8} (n^2 + m^2) \quad (2.88)$$

Note that the same result is obtained by calculating the kinetic energy,

$$K \approx \frac{\rho h \Omega^2}{2} \int_{\Gamma} dx dy \phi^{(0)2} = \frac{h\sigma\pi^2}{8} (n^2 + m^2), \quad (2.89)$$

by using the approximate resonance frequencies  $\Omega^2 \approx \sigma(n^2 + m^2)\pi^2/(\rho L^2)$ . This result, valid in the limit of small strain parameter  $\lambda \ll 1$ , is consistent with the virial theorem, that imposes the equality between the average kinetic energy and the average elastic energy (dominated by the geometrically-nonlinear component), and underlines that it is possible to obtain the dilution factor also as  $D_Q = K/\Delta W^{(\text{lin})}$ , a convenient expression for numerical estimations. The dilution factors are now given by the ratio of the two energy components:

$$D_Q = 1 + \frac{\Delta W^{(\text{nl})}}{\Delta W^{(\text{lin})}} \approx 1 + \frac{(1-\nu^2)}{(n^2 + m^2)\pi^2\lambda^2 + 2\lambda\sqrt{1-\nu^2}} \approx \frac{1}{2\lambda' + (n^2 + m^2)\pi^2\lambda'^2}, \quad (2.90)$$

<sup>10</sup> The following energy expressions have units of  $\text{Jm}^{-2}$ , since they are calculated using dimensionless modes shapes. To recover the actual energies of an oscillator's resonance, it is sufficient to multiply by the square of the displacement amplitude.

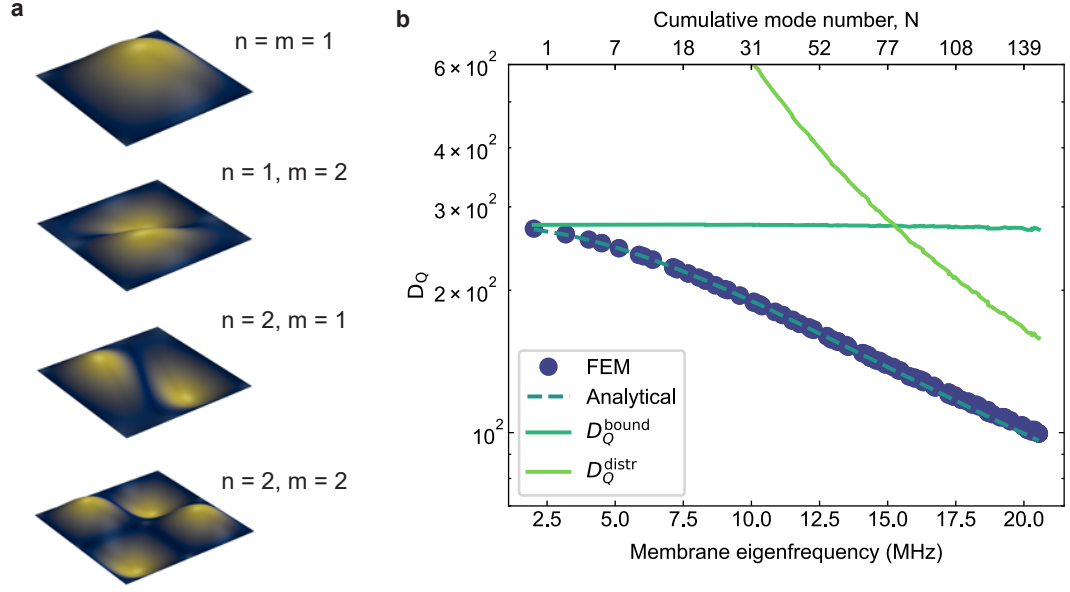


Figure 2.5: **a**, Mode shapes of the first four eigenmodes of a tensioned square membrane. The mechanical and geometrical parameters of the membrane (assumed to be patterned in thin film  $\text{Si}_3\text{N}_4$ ) are given in the main text. Note the small hybridization between the degenerate modes (1,2) and (2,1). **b**, Dilution factors of the first 150 eigenmodes of the membrane, inferred with a finite element simulation (purple dots). The dashed green line is the analytical approximation 2.90. The dark and light green full lines are dilution factor upper bounds computed using only the linear strain energy localized in  $3\lambda$ -wide strips adjacent to the membrane boundaries or the energy generated in the bulk of the membrane. With these definitions,  $D_Q = (1/D_Q^{\text{bound}} + 1/D_Q^{\text{distr}})^{-1}$ .

where we have redefined a more convenient strain parameter for the bidimensional bending case ( $\lambda' = \lambda/\sqrt{1-\nu^2}$ ) and, to write the last approximate equality, we have assumed  $D_Q \gg 1$ , which is satisfied for small strain parameters (high tension and high aspect ratio) and low order resonances. Several conclusions can be inferred from 2.90:

- For high tensile stress and high aspect ratio of the membrane, when  $\lambda' \ll 1$ , the quality factor can be diluted of many orders of magnitude.
- For low order modes of highly stressed resonators, the first term of the denominator, coming from the integration of the boundary correction to the mode shape, is dominant, and  $D_Q \propto 1/2\lambda'$ . This implies that the boundary curvature contribution, that is established in order to satisfy the clamped boundary conditions, is much stronger than the distributed curvature contribution.
- For higher order modes, as  $n$  or  $m$  approach  $1/\pi\sqrt{\lambda'}$ , the distributed curvature term starts to contribute significantly, and for very high order modes the quality factor will no longer be constant, but will roll off as  $D_Q \propto \Omega^{-2}$  (see Fig. 2.5b). The practical effectiveness of dissipation dilution is in fact limited to relatively low-order modes, of frequencies up to a few tens of MHz.

- The dilution factor also provides a small correction to the eigenfrequencies. The expression of 2.82 was calculated as  $\sqrt{k^{(nl)}/m_{\text{eff}}}$ , with the dominant geometrically-nonlinear component of the spring constant being evaluated using the unperturbed mode shape  $\phi^{(0)}$ . The first order correction is found by multiplying the eigenfrequencies with the factor  $(1 + k^{(lin)}/2k^{(nl)}) \approx (1 + (2D_Q)^{-1})$ , increasing as the mode index grows.

A visualization of the contributions to the dilution factor from the boundary regions and from the membrane bulk, for different flexural eigenmodes is presented in Fig. 2.5, where the dominant role of the boundary curvature for the low order modes is clear. The mechanical parameters used for the finite element simulation are  $E = 250$  GPa,  $\nu = 0.23$ ,  $\sigma = 1$  GPa (typical values for thin film  $\text{Si}_3\text{N}_4$  grown by low pressure chemical vapour deposition at temperatures around  $800^\circ\text{C}$ ) and the geometry of the membrane is described by  $L = 200\ \mu\text{m}$ ,  $h = 80$  nm, giving a strain parameter  $\lambda \approx 1.9 \times 10^{-3}$ . In order to distinguish the boundary and bulk contributions to the dilution factor, I defined partial dilution factors  $D_Q^{\text{bound}}$  and  $D_Q^{\text{distr}}$ , calculated with  $\Delta W^{(\text{lin})}$  evaluated close to the boundaries (strips of width  $3\lambda L$  around the clamped edges) or in the remainder of the membrane surface. In this way, the dilution factor  $D_Q = (1/D_Q^{\text{bound}} + 1/D_Q^{\text{distr}})^{-1}$  is smaller than the smallest of the two contributions, and it is clearly dominated by the boundary contribution for mode orders  $N \ll 70$ . Here, the cumulative mode number is defined as  $N(\omega) = \sum_{n,m:\omega \leq \Omega_{n,m}} 1$  [58].

This derivation carries another important insight: since the largest part of the lossy, linear elastic energy is associated to the boundary curvature, if the resonator supports flexural modes whose gradient decays smoothly towards the boundaries, no strong curvature will be produced, the dominant limit to the dilution factor will be suppressed and the quality factors will increase drastically compared to the simple standing waves supported by a uniform plate. The search of such resonator designs and mode shapes has led to several different classes of resonators exhibiting *soft clamping*, i.e. a scaling of dilution factors  $D_Q \propto \lambda^{-2}$ , dominated by the distributed mode shape curvature. The first example of soft clamping was obtained in membrane resonators via the patterning of a phononic crystal [25], as will be discussed in the next section.

Analogous expressions can be derived for a unidimensional string resonator with uniform cross section, under tensile stress, the main practical differences with the membrane case being in the relaxation of the static stress component transverse to the string profile and the corresponding reduction of tension due to Poisson's ratio, and the much smaller mode density, associated with the reduced dimensionality. The bending modes of a uniform string are described by the Euler-Bernoulli equation (given here in the time-independent form),

$$\frac{Eh^2}{12} \frac{d^4\phi}{dx^4} - \sigma \frac{d^2\phi}{dx^2} - \rho\Omega^2\phi = 0, \quad (2.91)$$

where  $\sigma$  is the static stress established after Poisson relaxation along the direction of the string (if the string was initially patterned from a uniformly tensioned thin film, it is given by  $\sigma = \sigma_{\text{film}}(1 - \nu)$ ). The same procedure described for the square plate gives the eigenfrequencies and dilution factors of the uniform nanostring:

$$\Omega_n \approx \frac{\pi n}{L} \sqrt{\frac{\sigma}{\rho}}, D_Q \approx \frac{1}{2\lambda + n^2\pi^2\lambda^2} \quad (2.92)$$

## 2.3.3 Soft clamping via dispersion engineering and phononic bandgaps

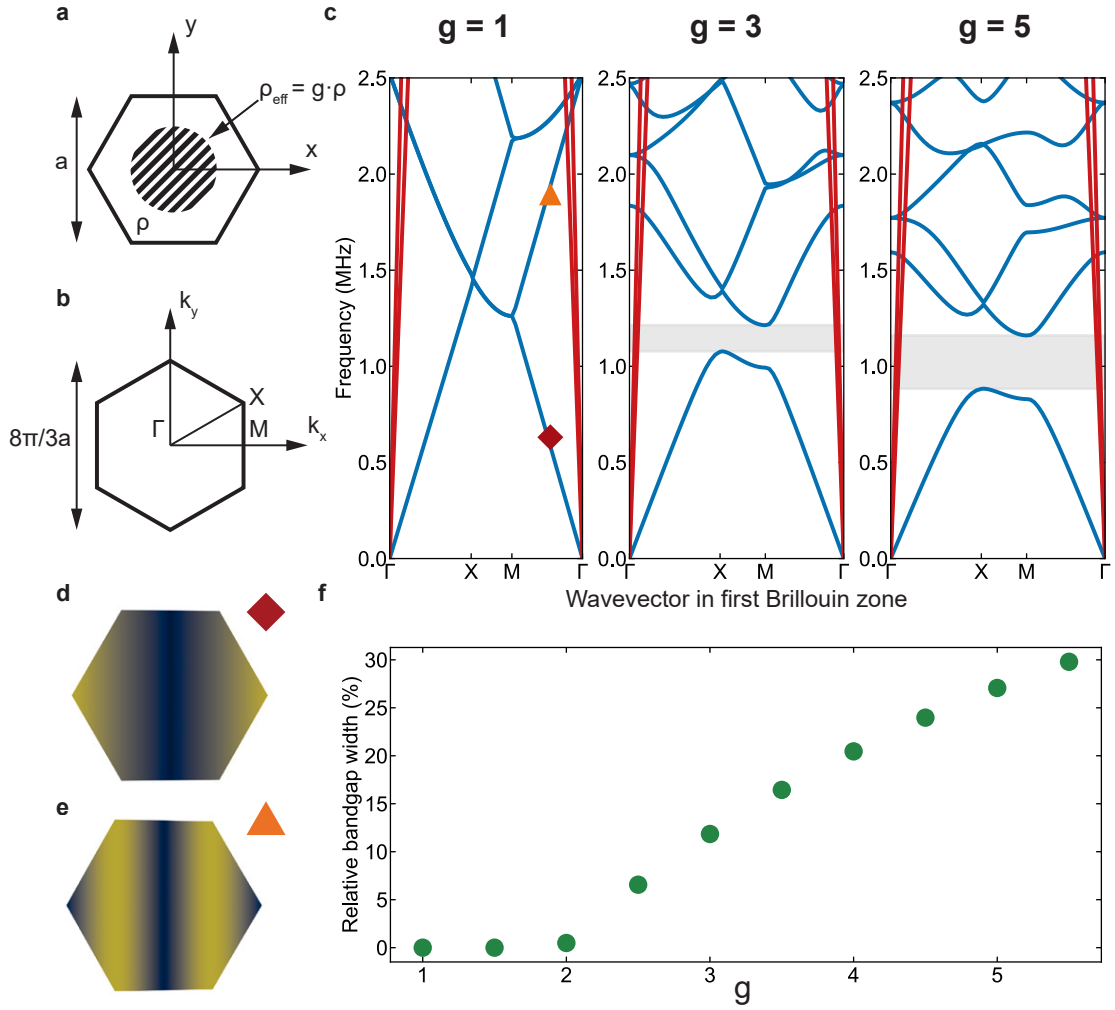


Figure 2.6: **a**, Unit cell of the triangular lattice of density modulation. Hatches represents a region of increased density. **b**, First Brillouin zone corresponding to the unit cell, with high symmetry points marked. **c**, Band diagrams of in-plane (red) and out-of-plane flexural modes (blue) for increasing periodic density modulation, as parameterised by  $g = \rho_{\text{eff}}/\rho$ . A bandgap for out-of-plane modes (shaded in grey) emerges for  $g \geq 2$ . Simulation parameters:  $a = 260 \mu\text{m}$ ,  $\sigma = 1 \text{ GPa}$ ,  $h = 20 \text{ nm}$ . The radius of the circular regions of increased density is  $r = 0.2a$ . **d-e**, Traveling waves with  $k_y = 0$  for the lowest two out-of-plane bands in the absence of density modulation, marked with the corresponding symbols on the band diagram in **c**. The color encodes displacement amplitude. **f**, Bandgap width normalized to center bandgap frequency versus density contrast.

A periodic modulation of material properties can drastically change the dispersion of elastic waves, and even introduce bandgaps, i.e. frequency ranges of forbidden elastic propagation. Such media are called *phononic crystals* (PnC), and were proposed and realized just few years after their electromagnetic counterparts, photonic crystals [59, 60]. In microscale devices, aided by developments in microfabrication techniques, phononic crystals have become an indispensable tool to implement low-mass, high-coherence,

localized vibrations that can couple strongly to electromagnetic fields, and to engineer spectral environments with low density of vibrational modes [61]. In the research group of Oskar Painter, the development of optomechanical crystals, i.e. nanoscale structures that can strongly co-localize optical and mechanical modes, led to a series of pioneering strides in quantum optomechanics, such as the first demonstration of ground state cooling of a mechanical mode of a macroscopic resonator [62] and the observation of quantum correlations created by the optomechanical interaction. Optomechanical crystals grew to be one of the most successful optomechanical platforms, currently employed for such endeavours as quantum-coherent transduction between radiofrequency and optical signals [63], implementation of quantum communication protocols [64] and of quantum memories [65]. Phononic crystals have one important advantage over their electromagnetic equivalents: since vacuum cannot support elastic waves, and air presents a massive impedance mismatch with elastic media, scattering to free-space is much less relevant in phononic crystals than in photonic crystals, where it is commonly mediated by imperfections that perturb their periodicity. This makes PnC devices much more robust to fabrication imperfections [26], and implies that the energy of a vibrational field confined in a PnC bandgap can only escape by tunneling through a finite-sized crystal or by coupling with a family of modes with no simultaneous bandgap, which is typically a weak mechanism.

In dissipation-diluted resonators, the aforementioned advantages are combined with another crucial aspect: the localization of a resonant mode with a mechanical frequency within an elastic bandgap, induced by the perturbation of the periodic translation symmetry of the PnC by the intentional introduction of a defect, leads to a displacement field envelope that decays exponentially in the PnC regions (as described by an imaginary wavevector). This type of displacement pattern approaches the boundaries with a vanishing gradient, suppressing the boundary contribution to  $\Delta W^{(\text{lin})}$  of orders of magnitude, which in turns enhances substantially the dissipation dilution factor. The application of phononic crystal to high aspect ratio, tensioned mechanical resonators is more recent [25, 66] and the understanding of their impact on dissipation engineering inaugurated research on soft clamping techniques [25, 26].

Let us clarify these concepts with a concrete example building on the case of a tensioned, thin film square membrane. Neglecting the flexural rigidity of the membrane in the limit  $\lambda \ll 1$ , the dispersion relation of out-of-plane flexural waves is described by a simple wave equation, and  $\Omega \propto \sqrt{k_x^2 + k_y^2}$ , with  $k_{x,y}$  being the wavevector. A periodic perturbation of the speed of sound can be introduced, e.g. via modulation of the material density, for example using compound materials or nanoscale patterns [67]. The local density can be described as  $\rho_{\text{eff}}(x, y) = g(x, y) \cdot \rho_{\text{material}}$ , where  $g(x, y)$  is repeating periodically in the plane according to a triangular lattice, whose unit cell is portrayed in Fig. 2.6a. Eigenfunctions take then the form of Bloch waves,  $\phi(x, y) = u(x, y)e^{i(k_x \cdot x + k_y \cdot y)}$ , where  $u$  is a function with the periodicity of the triangular lattice. The wave dispersion can be fully described within the first Brillouin zone in reciprocal space (the reciprocal lattice is also triangular), drawn in b. As shown in Fig. 2.6c, the dispersion relation of flexural modes is perturbed, especially on the boundaries of the Brillouin zone, with all flexural bands shifting to lower frequencies due to the increase in  $m_{\text{eff}}$  and a bandgap opening and gradually increasing in spectral

width (see Fig. 2.6f)<sup>11</sup>. The formation of a bandgap of forbidden elastic wave transmission can be explained by the constructive interference between waves scattered by the density modulation, for wavevectors lying on the boundaries of the Brillouin zone. The in-plane vibrational bands (drawn in red), on the other hand, are much less sensitive to the changes in  $\rho_{\text{eff}}$ , and no bandgap is observed at the same frequencies (the out-of-plane bandgap is more properly described as a quasi-bandgap). The coupling of in-plane and out-of-plane modes is however very weak, due to the large mismatch in phase velocities (the stiffness of the plate is much higher for in-plane bending than out-of-plane bending), and out-of-plane vibrations are effectively suppressed in the bandgap regions. Note that the band structure presented in Fig. 2.6c can be easily extended to different unit cell sizes, densities or stress due to the scaling properties of the wave equation: for examples an isotropic rescaling  $a \rightarrow a'$  will shift the out-of-plane bands to  $\Omega' = \Omega a/a'$ , and a change in stress will similarly shift the bands as  $\Omega' = \Omega \sqrt{\sigma'/\sigma}$ .

The discussed band structure is a property of an infinite, perfectly periodic medium. In real structures, vibrational modes with frequencies within the bandgap can exist at the membrane boundaries or localized to defects in the translation symmetry of the speed of sound modulation. Suppose one of the regions of high density is missing and the density there is locally uniform and equal to the lowest value in the unit cell. Finite element simulations reveal that one or two modes localized to the defect region emerge, decaying with an exponential envelope in the unperturbed PnC regions (see Fig. 2.7a). For those modes, the displacement field gradient is strongly suppressed towards the boundaries and the boundary curvature contribution  $\propto \lambda^{-1}$  that dominated in the  $D_Q$  expression of 2.90 for the case of a uniform membrane is strongly suppressed, in such a way that the distributed term  $\propto \lambda^{-2}$  prevails. This behaviour is characteristic of a soft clamped mode, where the clamped boundary conditions no longer strongly influence the dissipation dilution properties. The aspect ratio and frequency dependence become even stronger for soft clamped modes, as the  $\propto \lambda^{-2}$  term scales rapidly with the mode order. In order to enhance the quality factor, it is convenient to open a vibrational bandgap as close to the fundamental mode as possible, but this sets a constraint to the membrane extent and to the number of unit cells that surround the defect. In this case, the boundary curvature term could be incompletely suppressed and contribute to the localized mode  $D_Q$ , producing a trade-off between boundary and distributed curvature suppression. The trade-off is also manifested when varying  $\rho_{\text{eff}}$ , as shown in Fig. 2.7b, as an increase of the density contrast suppresses more strongly the boundary contribution to  $D_Q$  but enhances the decay rate of the defect mode exponential envelope and the distributed curvature associated to it. Note that the maximum  $D_Q = 3.46 \times 10^5$  for  $g \approx 3.9$  is about 18 times larger than the dilution factor of the  $n = m = 1$  mode of a square membrane of the same size. The size scaling is faster than for uniform membranes: enlarging uniformly the membrane extent increases monotonically the quality factor of the soft clamped mode and reduces its resonant frequency, since  $D_Q \propto L^2$  and  $\Omega \propto L^{-1}$ .

A general (approximate) upper bound can be found for the  $D_Q$  of dissipation-diluted modes of these density-modulated membranes with uniform stress, by consid-

<sup>11</sup> Note that the model of [68] cannot properly describe the bandgap width as a function of the speed of sound contrast in the unit cell, as the bandgap is generally indirect. In other words, the maximum of the lower band and the minimum of the upper band occur at different propagation directions of Bloch waves.



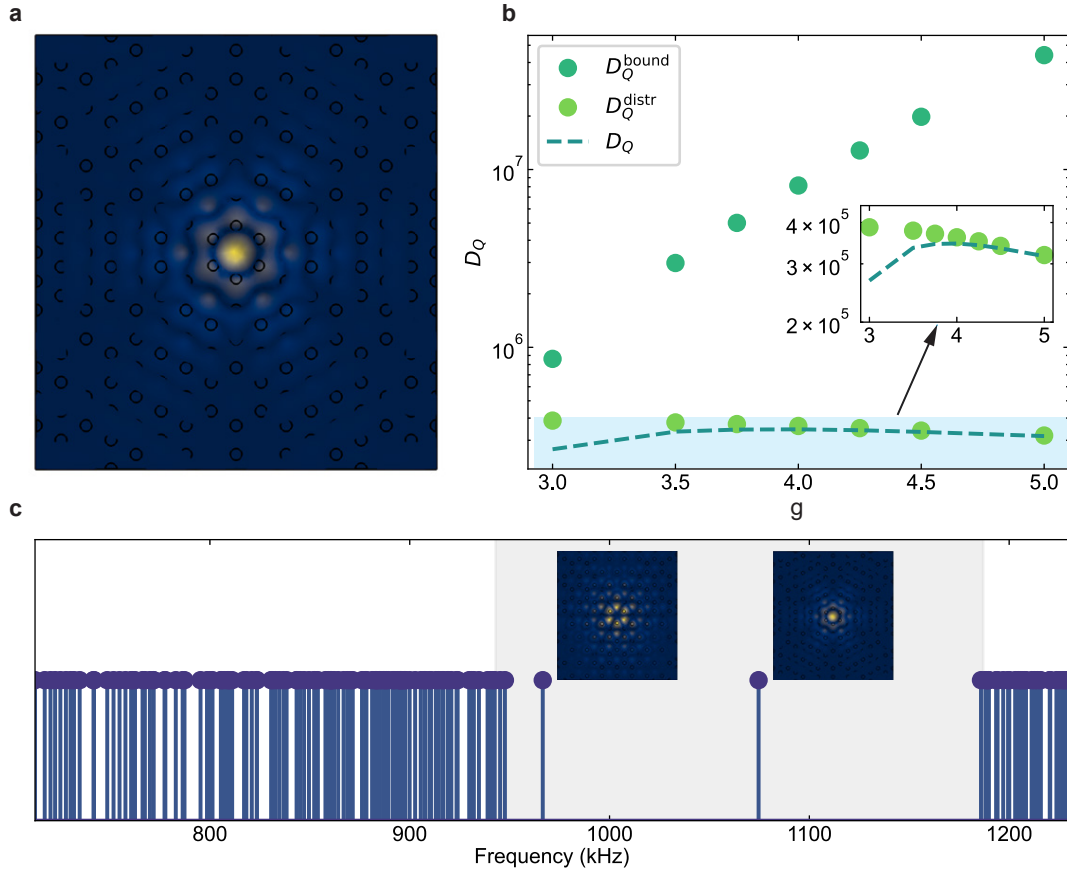


Figure 2.7: **a**, Displacement pattern of a mode localized to a defect in the triangular lattice of density modulation. **b**, Effect of varying  $g$  on the dilution factor of the localized mode. Dark green dots: boundary contribution to  $D_Q$ , light green dots: distributed contribution, dashed green line: overall  $D_Q$ . The inset zooms in on the lower region of the plot shaded in light blue. **c**, Spectral background in the vicinity of the bandgap region (shaded in grey) for the PnC membrane. Membrane resonances are marked with a vertical line, and the displacement patterns of the two localized modes are provided as insets.

ering the case of an insignificant contribution of the boundary curvature. By remembering that in plates where all the boundaries are subject to clamped conditions the Gaussian curvature integral is null [51], we can express the lossy linear strain energy as:

$$\begin{aligned}
 \Delta W^{(\text{lin})} &= \frac{Eh^3}{24(1-\nu^2)} \int_{\Gamma} dS (\nabla^2 \phi(x, y))^2 \geq -\frac{Eh^3 \Omega^2}{24\sigma(1-\nu^2)} \int_{\Gamma} dS \rho(x, y) \phi^{(0)} \nabla^2 \phi^{(0)} \\
 &\geq \frac{Eh^3 \Omega^2 \rho_{\min}}{24\sigma(1-\nu^2)} \int_{\Gamma} dS \left( \left( \frac{\partial \phi^{(0)}}{\partial x} \right)^2 + \left( \frac{\partial \phi^{(0)}}{\partial y} \right)^2 \right) \approx \frac{Eh^2 \Omega^2 \rho_{\min}}{12\sigma^2(1-\nu^2)} \Delta W^{(\text{nl})},
 \end{aligned} \tag{2.93}$$

where  $\rho_{\min}$  is the minimum volumetric density found on the membrane surface,  $\phi^{(0)}$  is the solution of the differential equation that approximates the displacement pattern far from the boundaries,  $\sigma \nabla^2 \phi^{(0)} + \rho \Omega^2 \phi^{(0)} = 0$ , and the second upper bound was

obtained using Green's identity and clamped boundary conditions. In writing the first inequality, we implicitly neglected the boundary curvature contribution. Using 2.74, the upper bound to the dilution factor is:

$$D_Q \leq \frac{12(1 - \nu^2)\sigma^2}{E\rho_{\min}h^2\Omega^2} \quad (2.94)$$

This bound closely corresponds to the one stated in [24] for soft clamped modes in nanostrings (where the case of nonuniform static stress through elastic strain engineering [26] is also considered). Note that this bound is not strictly applicable to the original soft clamped resonances demonstrated in [25] using periodically-pierced membranes with stress modulation in lieu of density modulation. The presence of hole boundaries free to displace implies that the Gaussian curvature integral is nonzero [69]<sup>12</sup> and the simplifications leading to 2.94 are not valid. Nevertheless, the performance of those devices is even further from the bound of 2.94 due to the effects of stress redistribution in a patterned resonator, which lower the diluting nonlinear elastic energy [24].

#### 2.3.4 Dissipation dilution of torsional modes

So far, all the examples of dissipation dilution in strained nanomechanical resonators we mentioned involved bending modes of high aspect ratio strings or membranes. It was recently demonstrated that *torsional* modes of tensioned beams can also exhibit significant geometric nonlinearity and dissipation dilution [71]. In this case the relevant aspect ratio governing  $D_Q$  is not the length of the beam over its thickness but rather the width over the thickness  $w/h$ , explaining why significant dilution of torsional modes was not observed earlier (nanobeams with  $w \gg 1 \mu\text{m}$  and  $h < 100 \text{nm}$  should be fabricated, and such dimensions imply significant fabrication challenges).

Consider a nanobeam undergoing torsional vibrations, parametrized by a rotation angle of its cross section  $\theta(x)$ . Let  $y$  be the coordinate running along the nanobeam width, and assume that the angular torsion rate is constant over the longitudinal coordinate  $x$ , reaching a maximum torsional angle of  $\bar{\theta}$  at one end of the beam. At the edges of the nanobeam, significant elongation of its longitudinal elements is witnessed, as the rotation of the cross section implies a displacement  $u_z \approx y\theta$ . The out-of-plane displacement imposes a longitudinal elongation  $\Delta L \approx u_z^2/(2L)$ , resulting in a geometrically-nonlinear dynamic strain  $\Delta L/L \approx \bar{\theta}^2 y^2/(2L^2)$ . Like flexural modes of long beams, a torsional mode of a sufficiently wide beam can store significant geometrically-nonlinear strain energy, that will dilute the linear dissipation. Furthermore, the torsional mode patterns can fulfill clamped boundary conditions without incurring in large boundary curvature, implying that the most significant limit to the  $D_Q$  of flexural modes is absent, and resulting in the soft clamping geometrical scaling.

It is shown in [71] that the following expressions for the torsional elastic energy components are valid for a uniform nanobeam (in the approximation  $\nu \approx 0$ ):

<sup>12</sup> In that case, the Gauss-Bonnet theorem implies that the linear strain energy component proportional to the Gaussian curvature is given by the geodesic curvature accumulated at the free membrane edges [70].



$$\begin{aligned}\Delta W^{(nl)} &\approx \frac{\sigma h w^3}{24} \int dx \left( \frac{d\theta}{dx} \right)^2 \\ \Delta W^{(lin)} &\approx \frac{E h^3 w}{24} \int dx \left( 2 \left( \frac{d\theta}{dx} \right)^2 + \frac{w^2}{12} \left( \frac{d^2\theta}{dx^2} \right)^2 \right),\end{aligned}\tag{2.95}$$

where  $w$  and  $h$  are the nanobeam width and thickness. In the linear strain energy term, the first integrand is due to shear strains  $\Delta \epsilon_{xy}^{(lin)}$  produced by torsion, and the second from normal linear strains  $\Delta \epsilon_{xx}^{(lin)}$ . Note that these expressions are special cases of the more general plate elastic energy 2.20, when a deformation field describing torsion is specified. In numerical simulations, therefore, the plate expressions are adequate also to compute torsional dissipation dilution.

Taking the energy ratio and assuming the torsional mode shapes  $\theta(x) = \sin(n\pi x/L)$  to follow normalized sinusoidal profiles vanishing at the clamping points (that, in contrast to flexural modes, do not violate the clamped boundary conditions), the following  $D_Q$  expression is found:

$$D_Q \approx \frac{\sigma}{2E} \left( \frac{w}{h} \right)^2 \frac{1}{1 + \frac{n^2 \pi^2}{24} \left( \frac{w}{L} \right)^2},\tag{2.96}$$

following the soft clamping scaling  $\propto (w/h)^2$  as long as the beam is sufficiently long and the mechanical frequency sufficiently low to fulfill  $L \gg nw$ .

For optomechanics experiments, torsional modes bring an advantage in that they are sensitively interrogated with optical lever detection methods, that are particularly simple to implement and do not require interferometric stability [71].

### 2.3.5 Finite element simulations of strained nanomechanical resonators

A digression is in order to discuss how to numerically compute the dilution factors from finite element simulations, in the cases where analytical solutions are not available. The method below was optimized and benchmarked mostly by Sergey A. Fedorov and me (and initiated by previous doctoral students in our research group).

We use the software package COMSOL Multiphysics and conduct solid mechanics simulations using the ‘Shell’ interface, which simplifies the differential equations of solid mechanics by assuming a small plate thickness compared to the lateral dimensions, and a simple form for the variation of the displacement field through the plate thickness. In this way, the solid mechanics problem becomes largely bidimensional, and much faster to formulate and solve. Moreover, the interface proved to be more accurate for extremely large aspect ratio structures ( $L/h$  up to  $10^5$ ), and does not require the creation of large aspect ratio elements along the plate thickness dimension, which can be tedious and problematic. In case the mechanical resonator contains free edges, a pre-stressed eigenfrequency study is carried out. This consist of two simulation steps: in the first stationary study, the initial stress field is relaxed to find an equilibrium configuration (see Fig. 2.8c). The thin film stress is usually chosen as homogeneous by setting an initial in-plane force of  $N_{xx} = N_{yy} = \sigma h$  within the node Linear Elastic material  $\rightarrow$  Initial Stress and Strain. If no free boundaries are

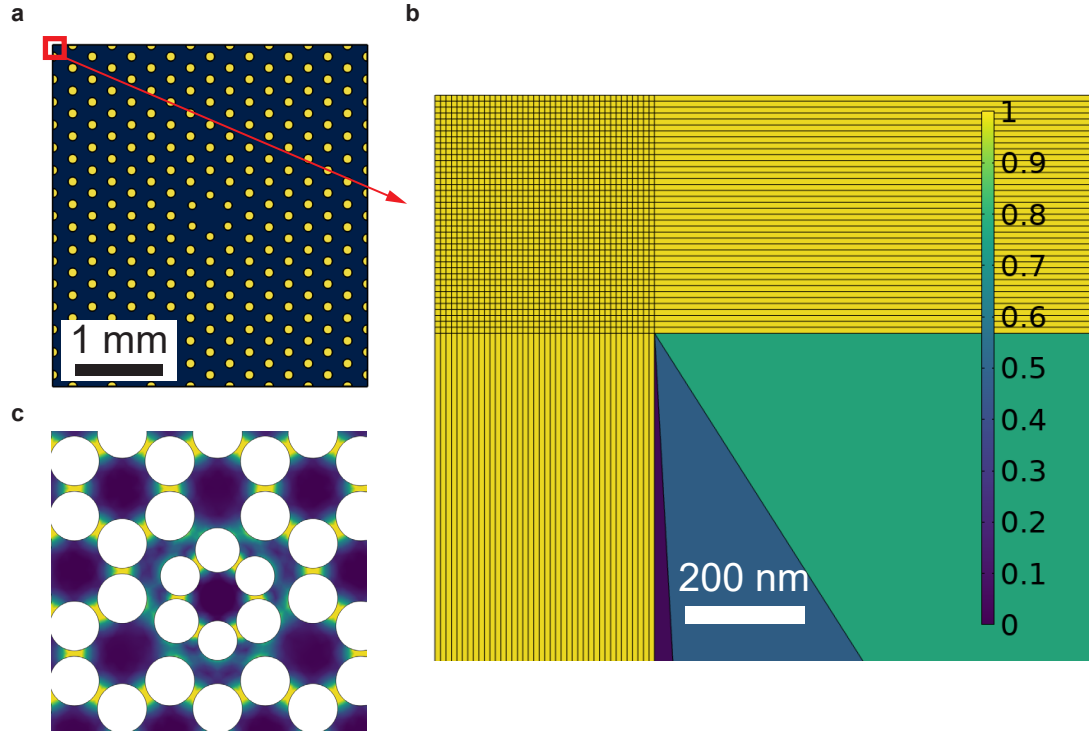


Figure 2.8: **a**, Finite element simulation domain for a density-modulated PnC membrane, with the color representing the local mass density. **b**, Enlarged view of the mapped mesh constructed in the vicinity of a boundary region (marked with the red square in panel **a**). The color bar represents the mesh elements quality as conveyed by a normalized skewness parameter. **c**, Example of output stress field calculated in the first stationary step of the pre-stressed simulation, for a stress-modulated, pierced PnC membrane. The color encodes Von Mises stress.

present (like in the case of density-modulated PnC membranes), this step is superfluous. The second simulation step is an eigenfrequency study which employs the results of the stationary step as an initial condition to find the eigenfrequencies and mode shapes. For this step we choose the option to ‘Include geometric nonlinearity’ (Study  $\rightarrow$  Step 2: Eigenfrequency) in order to properly compute the lossless elongation energy. Clamped boundary conditions  $\vec{u} = \partial\vec{u}/\partial\vec{n} = 0$  are applied to the appropriate resonator edges (Shell  $\rightarrow$  Fixed Constraint).

In order to find the correct mode shapes at the resonator boundaries, which can have a dramatic effect on the computed dilution factors of flexural modes, we make sure to mesh the boundary region with much smaller elements than the bulk surface of the mechanical resonator. In practice, we define strips of extent  $\sim 4\lambda L \approx \sqrt{4E/3\sigma} \cdot h$  ( $\lambda$  is the strain parameter) in the direction normal to the clamped boundaries, that we fragment into high aspect ratio rectangular elements using a Mapped meshing algorithm (Mesh 1  $\rightarrow$  Mapped, see Fig. 2.8b). We enforce at least several tens of elements in the direction orthogonal to the boundary; a good practice is to check all the simulation results (especially the dilution factors) while tuning the mesh density, ensuring that they are not very sensitive to changes in mesh element size.

While eigenfrequencies are given immediately by the finite element solver after the simulation is carried out, we need to compute explicitly the dilution factors. The safest

method is to make use of the displacement pattern produced by COMSOL and of the plate strain energy expression in 2.20, containing the second derivatives of the displacement which are easily extracted in COMSOL. In lieu of the nonlinear strain energy 2.23, that would require the tedious task of overlapping fields that are output from different simulation steps (in case of need, this can be carried out using the built-in function `withsol()`), we can appeal to the virial theorem and use the kinetic energy, whose cycle average is equal to the total elastic energy. Diluted quality factors are obtained as  $Q = Q_{\text{int}} \cdot \frac{\text{kin\_energy}}{\text{bend\_energy}}$ , and below we provide for convenience expressions that can easily be copy-pasted to COMSOL (Derived Values  $\rightarrow$  Global Evaluation). They make use of the user-defined parameter `h_mbr` for the plate thickness and the built-in parameters `shell.rho`, `shell.E`, `shell.nu`, `shell.omega` defined in the Shell interface. `intop1()` is an integration operator (Definitions  $\rightarrow$  Integration 1) over the whole plate surface.

$$\text{kin\_energy} = \text{intop1}((\text{h\_mbr} * \text{shell.rho} * \text{shell.omega}^2 * \text{shell.disp}^2) / 2)$$

$$\begin{aligned} \text{bend\_energy} = & \text{intop1}(\text{shell.E} * \text{h\_mbr}^3 * ((\text{dtang}(\text{dtang}(\text{w}, \text{x}), \text{x}) + \text{dtang}(\text{dtang}(\text{w}, \text{y}), \\ & \text{y}))^2 + 2 * (1 - \text{shell.nu}) * (\text{dtang}(\text{dtang}(\text{w}, \text{x}), \text{y})^2 - \text{dtang}(\text{dtang}(\text{w}, \text{x}), \text{x}) * \text{dtang}(\text{dtang}(\text{w}, \\ & \text{y}), \text{y}))) / (24 * (1 - \text{shell.nu}^2))) \end{aligned}$$

(note that the last two summands at the linear strain energy numerator define the Gaussian curvature integral, and can be omitted in case the resonator geometry only contains clamped edges). These expressions are valid also for the evaluation of dissipation dilution in modes with torsional character. The effective mass can similarly be computed from the calculated mode patterns, using the expression:

$$\text{m\_eff} = \text{intop1}(\text{shell.rho} * \text{h\_mbr} * (\text{shell.disp} / \text{maxop1}(\text{shell.disp}))^2)$$

There are at least two alternative methods for computing quality factors. The first one uses the built-in expressions of kinetic energy density and linear strain energy density, i.e.  $Q = Q_{\text{int}} * \text{shell.Wk\_tot} / \text{shell.Ws\_tot}$ . The second one relies on the definition of a complex Young's modulus  $E' = E(1 - i/Q_{\text{int}})$  (under Materials  $\rightarrow$  Material  $\rightarrow$  Young's modulus and Poisson's ratio). In this case, the eigenfrequencies returned by COMSOL will be complex, and the quality factor can be found using the identity  $Q = \text{Re}(\Omega) / 2\text{Im}(\Omega)$ . While in principle valid, the actual results returned using these methods are less reliable, and more sensitive to the resonator aspect ratio and to the version of COMSOL Multiphysics employed (i.e. to implementation details) than the perturbative calculation using the eigenmode displacement patterns.

In the rare case when the simulation geometry is genuinely three-dimensional and the plate energy and spring constant approximations are not valid, one should use the generic strain energy expressions in 2.11, as described in [24]. This requires a careful definition of overlap integrals between the static stress field output from Step 1 and the dynamic strain field output from Step 2.

### 2.3.6 Mechanical dissipation sources

In our derivation of dissipation dilution we assumed the existence of a loss angle  $\phi$  that *locally* connects the linear strain and the dissipative stresses generated during

mechanical oscillations. This is an extremely simple description of dissipation that is sometimes justified empirically. With this approximation, the mechanical quality factor of a strained resonator is given by 2.73. In order to understand the origin of  $\phi$  and the limits of applicability of the dissipation dilution picture we provided, it is useful to study some of the known elastic energy dissipation mechanisms in more detail. In broad terms, static stress will dilute the damping when it occurs through *intrinsic* mechanisms (for example thermoelastic coupling and interaction with two level systems), i.e. by coupling to degrees of freedom internal to the nanomechanical resonator. *Extrinsic* dissipation sources (for example gas damping and phonon leakage to the resonator environment) do not undergo dissipation dilution as simply, and can set a harsh limit on the observed quality factors. If one has many independent damping sources, the damping rates will sum, in such a way that the quality factor will be limited by the lowest of the single  $Q$ s, each of which will be diluted to a variable degree by stress:

$$Q^{-1} = \sum_k Q_k^{-1} \quad (2.97)$$

### 2.3.6.1 Anelastic relaxation

An *anelastic solid* is a material in which the stress-strain susceptibility can exhibit time-delayed effects. For example, upon application of a load, there can be an instantaneous deformation followed by a slower creep, occurring on a finite timescale  $\tau_\sigma$ . A generic linear time-independent relation of this type is given by the following differential equation (assuming for simplicity that stress and strain fields are described by scalars) [43]:

$$\sigma + \tau_\epsilon \frac{\partial \sigma}{\partial t} = E_0 \left( \epsilon + \tau_\sigma \frac{\partial \epsilon}{\partial t} \right), \quad (2.98)$$

where  $E_0$  is the steady-state Young's modulus measured after mechanical transients have elapsed. In the frequency domain, this equation corresponds to a complex Young's modulus:

$$E' = E_0 \frac{1 + \omega^2 \tau_\sigma \tau_\epsilon}{1 + \omega^2 \tau_\epsilon^2} \left( 1 - i \frac{\omega(\tau_\sigma - \tau_\epsilon)}{1 + \omega^2 \tau_\sigma \tau_\epsilon} \right) \quad (2.99)$$

Resulting in a frequency-dependent magnitude and loss angle (assuming  $\phi \ll 1$ ) of the viscous damping type:

$$\phi \approx \frac{\omega(\tau_\sigma - \tau_\epsilon)}{1 + \omega^2 \tau_\sigma \tau_\epsilon} = \Delta \frac{\omega \tau}{1 + \omega^2 \tau^2}, \quad (2.100)$$

with  $\tau = \sqrt{\tau_\sigma \tau_\epsilon}$  and  $\Delta = (\tau_\sigma - \tau_\epsilon)(\tau_\sigma \tau_\epsilon)^{-1/2}$ . This loss angle describes a broad dissipation peak centered around the mechanical frequency  $\omega = \tau^{-1}$ , the frequency at which the fields can excite effectively the relaxation mechanism<sup>13</sup>. A dissipation

<sup>13</sup> The frequency dependence in 2.100 is sometimes called a 'Debye peak', due to the analogy with the model formulated by Peter Debye for the response of dielectrics to AC electromagnetic fields.

peak of this type was found by Zener in his description of thermoelastic damping (see the next section) [72], and due to its very general character it is commonly found in experiments. For example, dissipation through coupling with a two level system can also manifest in a loss angle of the type in 2.100.

Often, the implicit temperature dependence of 2.100 allows the identification of a Debye peak. In the case that the relaxation process depends on the some microscopic mechanism acquiring a sufficient energy to surpass a barrier of height  $E_a$  in thermal equilibrium at temperature  $T$ , the relaxation time constant will be given by the Arrhenius equation,

$$\tau = \tau_0 e^{E_a/(k_B T)}, \quad (2.101)$$

where  $k_B$  is Boltzmann's constant. In this case, the Debye peak can be traced as the temperature of the resonator is varied, and the evaluation of  $E_a$  can provide information about the physical mechanism of relaxation, e.g. the movement of defects or dislocations in the crystalline structure of a solid, or slipping between grain boundaries in polycrystalline materials [43].

### 2.3.6.2 Thermoelastic damping

Consider a mechanical object undergoing vibrations that lead to volume expansion or shrinking of its constituent elements. Volumetric changes are coupled to temperature changes by the linear expansion coefficient  $\alpha$ , through the inverse process of thermal expansion. If  $\alpha > 0$  (as in the vast majority of cases), a volume expansion will lead to a decrease in temperature, and a contraction to a temperature increase. In the resonator, heat fluxes will start flowing from the contracting, hotter regions, to the expanding, colder regions, and the heat will flow at the cost of dissipating mechanical energy (see Fig. 2.9a). The temperature and displacement fields become coupled through the expansion coefficient  $\alpha$ , and one can write coupled differential equations for the displacement field and for heat diffusion. Note that thermal expansion can only occur for such vibrational patterns that induce volumetric changes (i.e., strain fields containing a volumetric component, in which  $\sum_j \epsilon_{jj} \neq 0$ ). These include flexural modes (in which the volumetric stress changes sign along the thickness dimension) and longitudinal modes, but torsional vibrations are purely deviatoric and unaffected by thermoelastic damping.

The problem of thermoelastic dissipation was first tackled in a series of papers by Zener [72], who introduced the standard model of the anelastic solid described in the previous section as a generalization of the thermoelastic damping results. More recently, in the context of high frequency nanomechanical resonators, the problem was revisited by Lifshitz and Roukes [73] who obtained a more general result that closely matches the Zener expression for low mechanical frequencies. These studies, however, did not consider the presence of static tension in the resonator and its dilution of thermoelastic damping. The most complete treatment of this case, to my knowledge, is contained in the doctoral thesis of Yeghishe Tsaturyan [74], who verified the validity of the simple dissipation dilution picture starting from the coupled solid mechanics and thermal diffusion equations in a square plate.

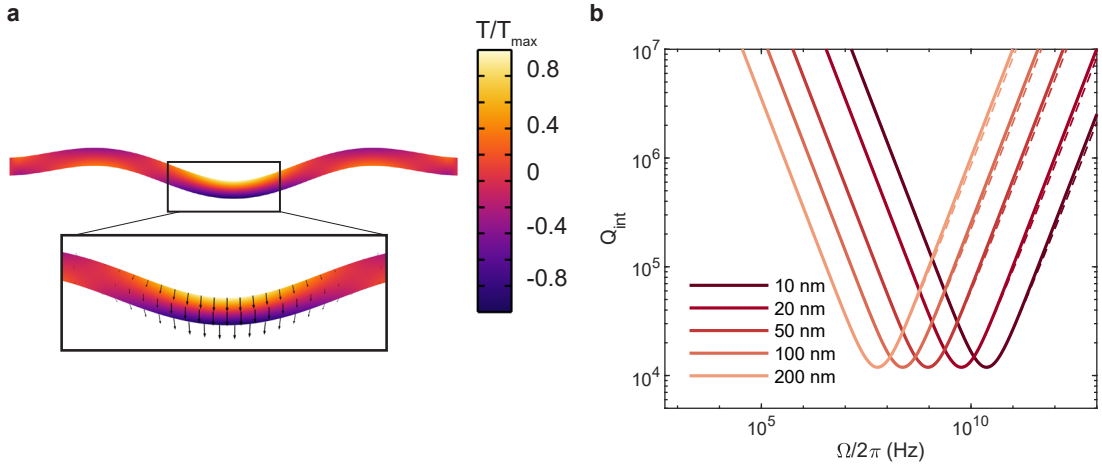


Figure 2.9: **a**, Temperature profile developed in the cross-section of a circular membrane undergoing bending oscillations (at 134 kHz), simulated with finite element methods. Notice how tension lowers the temperature, and compression increases it. Inset: zoomed-in view of the central antinode region, with black arrows indicating the heat flux field. **b**, Modelled  $Q_{\text{int}}$  (inverse loss angle) versus frequency of the flexural modes due to thermoelastic damping, for different values of resonator thickness. Full lines: Zener model 2.107, dashed lines, Lifshitz-Roukes expression 2.106, overlapping with the Zener model at low frequencies. The physical parameters used for the estimations are those of  $\text{Si}_3\text{N}_4$  at room temperature.

In a membrane resonator subject to in-plane (uniform) tension and undergoing bending vibrations, temperature gradients provide two additional terms in the plate equation of motion (compare with 2.25):

$$D\nabla^4\psi - \sigma h\nabla^2\psi + \nabla^2 M_T + N_T\nabla^2\psi = -\rho h \frac{\partial^2\psi}{\partial t^2}, \quad (2.102)$$

$N_T$  is an additional in-plane tension force (per unit length) due to thermal expansion,

$$N_T = \frac{E\alpha}{1-\nu} \int_{-h/2}^{h/2} dz \theta(x, y, z, t), \quad (2.103)$$

where  $\theta = T - T_0$  is the temperature increment from the temperature  $T_0$  established in static conditions ( $\alpha\theta$  being the thermal strain component), and  $M_T$  is a thermal bending moment (analogous to  $D\nabla^2\psi$ ), given by:

$$M_T = \frac{E\alpha}{1-\nu} \int_{-h/2}^{h/2} dz z\theta(x, y, z, t) \quad (2.104)$$

In the regime where the phonon mean free path is smaller than the resonator thickness (and of all its length scales), a local temperature field can be established, and heat transport is diffusive. With the contribution of the volumetric heating term due to material expansion, the heat equation can be written as follows:



$$k\nabla^2\theta = \rho c_p \frac{\partial\theta}{\partial t} - \frac{E\alpha T_0 z}{1-\nu} \frac{\partial(\nabla^2\psi)}{\partial t}, \quad (2.105)$$

where  $c_p$  is the specific heat capacity,  $k$  the thermal conductivity and  $-z\nabla^2\psi \sim \sum_j \epsilon_{jj}$ . These coupled equations can be solved in the Fourier domain to obtain the temperature and displacement field of their eigenmodes, depending on a complex thermal wavevector. Correspondingly, the eigenfrequencies will be complex, and the thermoelastic-damped quality factor can be evaluated from them as  $Q = \text{Re}(\Omega)/2\text{Im}(\Omega)$ . In the high-aspect-ratio limit, Tsaturyan finds a result in the form  $Q = D_Q \cdot Q_{\text{int}}$ , where  $D_Q$  is the uniform membrane dilution factor 2.90 and

$$Q_{\text{int}}^{-1} \approx \Delta_E \left( \frac{6}{\xi^2} - \frac{6}{\xi^3} \frac{\sin\xi + \sinh\xi}{\cos\xi + \cosh\xi} \right), \quad (2.106)$$

where  $\Delta_E = E \frac{\alpha^2 T_0}{\rho c_p} \frac{1+\nu}{1-\nu}$  and  $\xi = \sqrt{\frac{\pi^2 \Omega \tau}{2}}$ .  $\xi^2$  is a generalized frequency in terms of the timescale defined by  $\tau = \frac{h^2 \rho c_p}{\pi^2 k}$ , i.e. the characteristic time required for heat to diffuse between the top and bottom sides of the plate (where the heat gradient is established in bending vibrations). For silicon nitride,  $\tau \approx 6.4 \text{ ps} \cdot (h/10 \text{ nm})^2$  at room temperature, hence  $\xi \ll 1$  for frequencies in the megahertz range. In this limit, 2.106 can be approximated very well with the low-frequency tail of a Debye peak [73], where  $\tau$  sets the relaxation timescale, as originally found by Zener:

$$Q_{\text{int}}^{-1} \approx \Delta_E \frac{\Omega \tau}{1 + (\Omega \tau)^2}, \quad (2.107)$$

whereas in the high frequency limit  $\Omega \tau \gg 1$  the approximation is slightly worse. These estimates of thermoelastic damping are plotted in Fig. 2.9b for different values of membrane thickness. We can conclude that thermoelastic damping gets diluted by tension, despite dissipative stresses being given by a non-local thermal field. The effective loss angle is in this case averaged over the membrane thickness, and depends on the thermal wavevector.

Despite being an irrelevant loss mechanism for our large aspect-ratio tensioned mechanical resonators, the case of thermoelastic damping is instructive to shed light on the concept of loss angle and on the validity of a complex Young's modulus with a theoretically well-founded example. Moreover, thermoelastic damping is an important mechanical dissipation source in the suspension fibers of gravitational wave interferometer end-mirrors (with diameters of order  $\sim 1 \text{ mm}$ ), where great care is taken to minimize the effect [75].

### 2.3.6.3 Interaction with two level systems

In an amorphous solid, the quantum-mechanical ground state of the atomic lattice is accompanied by a vast number of low-energy excitations with very small energy separations. These excitations are secondary, local minima of the potential energy landscape, that correspond to tiny displacements of an atom or a small group of atoms, as evidenced by molecular dynamics simulations [76]. The secondary minima are present

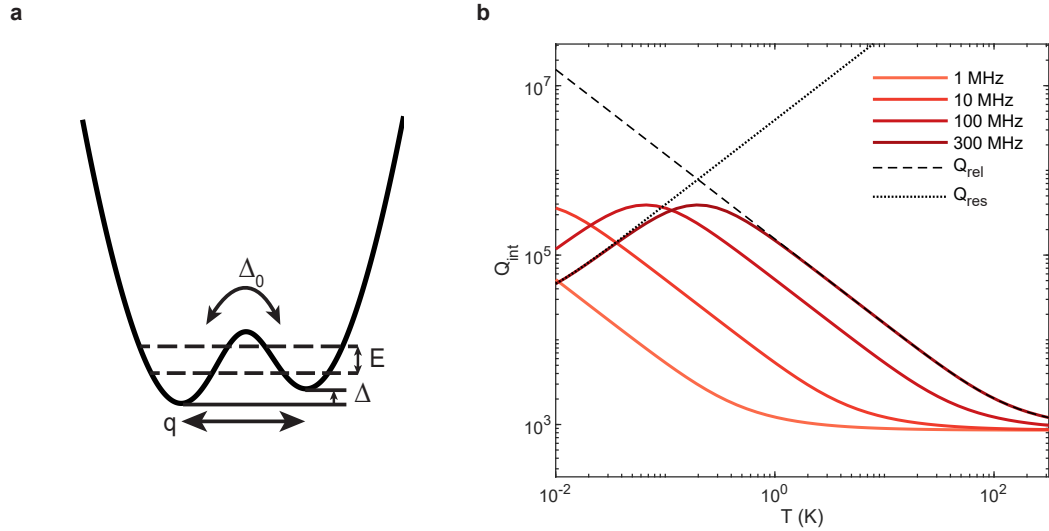


Figure 2.10: **a**, Schematic illustration of a double well potential and its two lowest energy levels (dashed lines), forming a TLS. The TLS parameters are labelled as in the text. **b**, Calculated quality factor contribution due to an ensemble of TLS at variable temperatures. Curves corresponding to different vibration frequencies are shown with different colors. The two contributions to the quality factor, resonant and relaxation damping, are displayed with a dotted and a dashed line, for the highest mechanical frequency. The physical constants employed for the calculation (density and speed of sound) correspond to those of  $\text{Si}_3\text{N}_4$ , while the TLS density and strain coupling parameters are assumed similar to those reported for fused silica.

in extremely large numbers due to the disordered nature of the atomic arrangement, in contrast to the existence of a well-defined ground state of a crystal, where such excitations require much larger energy exchanges due to the symmetries of the solid-state phase. Depending on the temperature and on the excitation frequency, these low-energy states can exchange energy and perturb an incoming elastic (or even electromagnetic) wave, and contribute to the medium dispersion and to the intrinsic friction, or attenuation that is observed. This interaction is truly local, as the extent of the structural defects is in the scale of  $10^{-10}$  m, and within the bulk of amorphous solids, isotropic and homogeneous, due to the random orientation of such defects. Therefore, this damping mechanism is prone to an effective description in terms of a material loss-angle, and can be diluted as usual by the co-existence of stress and geometric nonlinearity.

The description of the interaction of this multitude of structural defects with elastic and electromagnetic waves is provided by the *standard tunneling model* [77], in which pairs of minima in the configuration space of the atomic arrangement are conceptualized as two-level systems (TLS). The standard tunneling model proved very effective in describing the acoustic attenuation and the speed of sound dispersion in many glasses at low temperatures, and its predictions of universal scaling laws for the heat capacity and thermal conductivity at low temperatures, as well as the existence of a region of temperature-independent friction at  $T \sim 1$  K, were repeatedly confirmed by experiments with many amorphous solids [53]. In the standard tunneling model, a single structural defect in the amorphous state is treated as a double-well potential, i.e. two



identical harmonic potential wells split by a certain distance in the atomic configurational coordinate  $q$  and with an energy difference between the local minima given by  $\Delta$  (see Fig. 2.10a). At low enough temperatures ( $k_B T \ll E_0$ , with  $E_0/2$  the ground state energy of the single potential well) only the two most tightly bound states will be significantly populated, corresponding to the lowest energy levels of the isolated left and right wells. The other energy levels can then be neglected in order to construct a simple model involving only these two states, and the defect will be treated as a TLS. In the basis of the ground-state wavefunctions of the isolated wells, the Hamiltonian is written as:

$$\hat{H}_0 = \frac{\Delta}{2} \hat{\sigma}_z + \frac{\Delta_0}{2} \hat{\sigma}_x, \quad (2.108)$$

where  $\hat{\sigma}_i$  are the  $2 \times 2$  Pauli matrices and  $\Delta_0$  is a matrix element describing the transition amplitude between the two states, which depends exponentially on the distance  $q$  between the double-well minima. From the familiar spectrum of the Bloch Hamiltonian, the eigenvalues of  $\hat{H}_0$  are  $\pm E/2$ , with  $E = \sqrt{\Delta^2 + \Delta_0^2}$ , and the eigenfunctions are given by superposition of the isolated well wavefunctions with weights determined by  $\Delta/\Delta_0$ .

The defect embedded in the solid state is capable of exchanging energy with the medium excitations, in particular with phonons. Resonant coupling is negligible at low frequencies (at the temperatures above 10 mK which are relevant to most condensed matter experiments, the TLSs with  $2E/h \ll 200$  MHz will be thermally saturated, so that no net energy exchange will occur), but *relaxation* interactions can occur. An impinging strain wave will perturb the potential well parameters, in particular the asymmetry energy  $\Delta$ , and the population of the TLS states will redistribute to attain thermal equilibrium for the new energy level separation. This re-distribution draws energy from the strain field, resulting in an acoustic damping mechanism. Note that the extent of the TLS is much smaller than the typical acoustic wavelength, so that the dipole approximation can be employed. In the classical limit of an impinging strain wave with large amplitude  $\epsilon_{jk} = \epsilon_{jk}(\vec{r})$  (evaluated at the position of the TLS), the Hamiltonian describing the asymmetry-perturbing interaction between the TLS and the strain wave can be modelled as [77]:

$$\hat{H}_{\text{int}} = \left( \frac{\Delta}{E} \hat{\sigma}_z + \frac{\Delta_0}{E} \hat{\sigma}_x \right) \gamma_{jk} \epsilon_{jk}, \quad (2.109)$$

expressed in the basis of the eigenstates of 2.108. Here  $\gamma_{jk} = \partial\Delta/2\partial\epsilon_{jk}$  is the strain-TLS coupling tensor. Through 2.109, the TLS will interact with all the phonons of the solid state medium, driving transition between the eigenstates of  $\hat{H}_0$ . The relaxation time  $\tau$  is defined as the time required for the TLS population difference  $\langle \hat{\sigma}_z \rangle$  to relax to the equilibrium distribution after having been perturbed by a strain wave, and it corresponds to the inverse of the sum of the transition rates  $E_+ \rightarrow E_-$  and  $E_- \rightarrow E_+$ . The relaxation rates can be calculated using time-dependent perturbation theory and Fermi's golden rule, to obtain [78]:

$$\tau^{-1} \propto \gamma^2 E^{D-2} \Delta_0^2 \coth \left( \frac{E}{2k_B T} \right), \quad (2.110)$$

where  $D$  is the mechanical resonator dimensionality<sup>14</sup>, which influences the observed relaxation damping rates [78–80] and  $\gamma$  is an effective strain-TLS coupling energy, after averaging over the random TLS orientation and all possible strain wave polarizations. The dependence on  $D$  arises when accounting for the phonon density of states in the resonator, and the temperature dependence from the bosonic occupation of those phonon families.

The relaxation process is governed by the dynamics of the TLS population difference,  $s = \langle \hat{\sigma}_z \rangle$ . In thermal equilibrium, the static population difference  $s_0$  is given by Bose-Einstein statistics:

$$s_0 = -\tanh\left(\frac{E}{2k_B T}\right) \quad (2.111)$$

But as the energy level splitting  $E$  is perturbed by the strain field, the population difference will evolve towards a new equilibrium value  $\bar{s}$ :

$$\bar{s} \approx s_0 + \frac{\partial s_0}{\partial E} \delta E = s_0 - \text{sech}^2\left(\frac{E}{2k_B T}\right) \frac{\delta E}{2k_B T} \quad (2.112)$$

the extent to which  $s$  will be able to relax to  $\bar{s}$  depends on the relaxation time and on the perturbation frequency. The evolution of the population difference can be modelled with a first-order differential equation

$$\frac{d\delta s}{dt} = -\frac{\delta s + s_0 - \bar{s}}{\tau}, \quad (2.113)$$

where  $\delta s = s - s_0$ . We can apply a Fourier transform to express the response of the population inversion to the perturbation in the frequency domain:

$$\delta s(\omega) \approx -\frac{\delta E}{2k_B T} \text{sech}^2\left(\frac{E}{2k_B T}\right) \frac{1}{1 - i\omega\tau} \quad (2.114)$$

This result, combined with 2.110, lets us directly calculate the damping rate induced on an elastic wave by the relaxation process of the TLS ensemble. The interaction energy 2.109, in fact, contains a dissipative part proportional to  $\text{Im}(\delta s(\omega))$  that induces damping on an interacting elastic field at frequency  $\Omega$ . After integrating over the distribution of TLS (with variable  $\Delta$  and  $\Delta_0$ ) interacting with the strain wave, the inverse quality factor is found as [78]:

$$Q_{\text{int,rel}}^{-1} \approx \frac{\gamma^2}{\rho v^2 k_B T} \int_0^\infty d\Delta \int_0^\infty d\Delta_0 h(\Delta, \Delta_0) \left(\frac{\Delta}{E}\right)^2 \text{sech}^2\left(\frac{E}{2k_B T}\right) \frac{\Omega\tau(E, \Delta)}{1 + (\Omega\tau(E, \Delta))^2}, \quad (2.115)$$

<sup>14</sup> The dimensionality of a mechanical resonator is reduced along a particular direction when its characteristic length  $L$  across that direction is too small to support thermally excited phonons, i.e.  $L \ll \hbar v_{\text{min}} / (2k_B T)$ , where  $v_{\text{min}}$  is the minimum speed of sound among different phonon polarizations (assuming a linear dispersion). When  $L$  is comparable to the wavelength of thermal phonons, non-integer dimensions can be observed in the experiment [79].

where  $v$  is an effective speed of sound of the damped elastic wave,  $\rho$  is the mass density and  $h(\Delta, \Delta_0)d\Delta d\Delta_0$  is the distribution counting the TLSs per unit volume with asymmetry within  $(\Delta, \Delta + d\Delta)$  and tunneling energy within  $(\Delta_0, \Delta_0 + d\Delta_0)$ . In the standard tunneling model a form  $h = P/\Delta_0$  is postulated, in order to model a broad distribution of TLS parameters [77].  $P$  is a constant that is usually kept as a free parameter of the model, to be found by fitting to damping rate data. Note that in 2.115, each TLS contributes to the damping with a Debye peak at its particular relaxation rate, and due to the  $\text{sech}^2$  term, only the TLSs with  $E \lesssim 2k_B T$  are significant for the relaxation process (since in the others the population inversion will not be significantly perturbed by small change in well asymmetry). Although 2.115 cannot be expressed analytically in a closed form, asymptotic values can be found in the low temperature case ( $\Omega\tau_{\min} \gg 1$ ) and in the high temperature case ( $\Omega\tau_{\min} \ll 1$ ). In both cases, the integration in 2.115 can be carried out explicitly in polar coordinates, giving  $Q \propto \Omega/T^D$  in the low temperature limit, and a constant  $Q \approx \frac{2\rho v^2}{\pi\gamma^2 P}$ , independent of the system dimensionality, in the high temperature limit (see Fig. 2.10b). Both limits of the relaxation damping have been confirmed experimentally in many bulk amorphous solids (case  $D = 3$ ), hence being some of the most successful predictions of the standard tunneling model [53, 81].

The interaction Hamiltonian 2.109 implies that the TLSs can also induce *resonant damping* to the strain field when the their frequencies are matching and the temperature is such that only the ground state of the TLS is populated, so that phonon absorption is the dominant process. This implies that resonant damping is relevant only for high acoustic frequencies and extremely low temperatures [82], i.e.  $k_B T \lesssim \hbar\Omega$  (see the highest frequencies curves in Fig. 2.10b), and that it is a more relevant loss mechanism for microwave fields such as those in a superconducting cavity or qubit [83, 84]. In the acoustic case, the inverse quality factor for resonant damping is given by:

$$Q_{\text{int, res}}^{-1} \approx \frac{\pi\gamma^2 P}{\rho v^2} \tanh\left(\frac{\hbar\Omega}{2k_B T}\right), \quad (2.116)$$

in the weak field limit. Strong fields can saturate the resonant TLSs, resulting in non-linear damping that decreases at higher powers [82].

As silicon nitride is an amorphous solid, the dissipation behaviour is expected to be governed by two level systems at low temperatures. Faust et al. [85] conducted damping measurements on  $\text{Si}_3\text{N}_4$  strings with resonant frequencies  $\Omega/2\pi \sim 10\text{MHz}$  as a function of the temperature at  $T > 4\text{K}$ , and found a behaviour consistent with a single Debye peak around  $\sim 180\text{K}$  and with an ensemble of two level systems for  $T < 100\text{K}$  (using the distribution function proposed by Vacher et al. [86]). More recent experiments [87, 88] were carried out in dilution refrigerators (reaching temperatures down to  $\approx 20\text{mK}$ ), and a qualitative behaviour suggesting TLS relaxation damping was observed, with a high temperature plateau and a power law scaling for low temperatures, but without a precise quantitative explanation. As an historical note, it is interesting to recall that a model, alternative to the dissipation dilution picture, was proposed to explain the low dissipation in high-stress silicon nitride by assuming that stress can increase the asymmetry energy  $\Delta$  or decrease the strain coupling  $\gamma_{jk}$  [49]. This model would however imply a strong dependence of the low-temperature specific heat and of the thermal conductivity on the stress, which was not observed in subsequent inves-

tigations [89]. Interestingly, this finding proves that the TLS bath is not perturbed by the presence of stress in a solid state structure.

Despite the fact that the TLS ensemble picture finds a clear physical justification in the case of amorphous solids, dispersion and damping similar to the ones predicted by the standard tunneling model have been witnessed also in crystalline materials [79, 90, 91], albeit usually characterized by much smaller densities. This can usually be explained by the formation of native oxides at the interfaces of the crystals, or by the presence of thin amorphous-like damage layers near the interfaces, created during the resonator fabrication process. Usually, TLS ensembles in crystals have narrower parameters distributions, and  $h(\Delta, \Delta_0)$  can be modified to provide a more accurate modelling [92]. The low TLS densities in single-crystals explains the extremely high acoustic quality factors often witnessed at low temperatures [18, 93, 94]. The high mechanical Qs of single-crystals motivated the development of strained crystalline materials for nanomechanics and optomechanics in this thesis work, combining the low loss angle of crystalline material with dissipation dilution. Our investigation will be discussed in Chapter 3.

#### 2.3.6.4 Surface losses

A common empirical observation in mechanical resonators is that, as the surface-to-volume ratio increases the acoustic quality factor decreases. This is explained in terms of an increased friction at the resonator interfaces, which can be induced by formation of native oxides, contamination, adsorbed gaseous species and damage induced by the fabrication process [95]. Even in the absence of a microscopic explanation, this surface contribution manifests as an thickness-dependent intrinsic dissipation, as will be shown below. Such a thickness scaling was observed for unstrained nanomechanical elements [96] as well as in tensioned  $\text{Si}_3\text{N}_4$  resonators [25, 26, 57] where it can partially compensate the  $D_Q$  thickness dependence. In particular, for resonances where the elastic energy is dominated by the clamping curvature,  $D_Q \propto h^{-1}$  cancels out with  $Q_{\text{int}} \propto h$  and results in quality factors approximately independent on thin film thickness.

Once again, we model the local dissipative response with a complex Young's modulus, and assume a sharp loss angle increase at the upper and lower interfaces of our plate resonator:

$$\phi(z) = \phi_{\text{vol}} + b_{\text{surf}} (\delta(z - h/2) + \delta(z + h/2)) \quad (2.117)$$

(where  $b_{\text{surf}}$  has units of length). We insert this inhomogeneous loss angle in the expression for the dissipated power 2.67 and carry out the integration over  $z$ :

$$\begin{aligned} P &= 2\omega \int_{-h/2}^{h/2} dz z^2 \phi(z) \frac{E}{2(1-\nu^2)} \int_{\Gamma} dx dy (\text{Sqr. avg. curv.}) + 2(1-\nu)(\text{Sqr. Gauss. curv.}) \\ &= 2\omega \left( \phi_{\text{vol}} + 6 \frac{b_{\text{surf}}}{h} \right) \Delta W^{(\text{lin})} \end{aligned} \quad (2.118)$$

by repeating the same steps that led to the expression of the diluted quality factor, we obtain again  $Q = D_Q \cdot Q_{\text{int}}$ , but the intrinsic quality factor is now expressed as

$Q_{\text{int}} = (Q_{\text{vol}}^{-1} + Q_{\text{surf}}^{-1})^{-1}$ , with  $Q_{\text{surf}} = \beta h$ . Note that for a string resonator, where lateral interfaces also present increased mechanical friction, we would get an additional loss angle contribution, inversely proportional to the beam width but with a different numerical pre-factor, dictated by the strain distribution in out-of-plane flexural modes. In general, the calculation above indicates that, in the case of inhomogeneous friction in the resonator (e.g. multiple materials or bilayer plates), an effective loss angle is obtained by performing an average over the resonator volume, weighted by the geometrically linear elastic energy density.

For tensile-stressed silicon nitride thin films deposited with PECVD and LPCVD methods, a study by Villanueva and Schmid [57] showed that a model including a combination of volume and surface loss correctly explains the observed dependence of the dissipation on nanomechanical resonator thickness. From fitting damping data reported in the literature, they obtain  $Q_{\text{vol}} = 28000 \pm 2000$  and  $\beta = (6 \pm 4) \cdot 10^{10} \text{m}^{-1}$ , where the error bars represent confidence intervals due to uncertainties in the estimation of  $D_Q$ . These parameters imply that for  $h \leq 100 \text{ nm}$  (practically, for any thin film resonator with large dissipation dilution) the intrinsic quality factor will be dominated by surface losses and  $Q_{\text{int}} \approx \beta h$ . The dominance of surface losses is also shown by the large degradation of intrinsic  $Q$  observed when a nanometer-thickness layer of oxide is grown on the interfaces by purposeful exposure of a  $\text{Si}_3\text{N}_4$  membrane to oxygen plasma [97].

#### 2.3.6.5 Gas damping

Low-loss nanomechanical resonators need to be operated in a high vacuum environment in order not to compromise their quality factors and, subsequently, their force sensitivity and frequency stability performance [98]. One of the most easily observed loss channels in mechanical resonators is, in fact, gas damping due to collision with the molecules of the surrounding fluid, impinging on the surface of the vibrating element. Due to the vibrational motion, the rate of collisions on the leading face will be higher than that on the trailing face, leading to viscous dissipation through kinetic energy transfer to the gas molecules. Gas damping is an example of an extrinsic dissipation mechanism, as the friction is generated by degrees of freedom external to the mechanical resonator, and as such it is not modelled by a material loss angle and cannot be diluted by tension.

The correct damping model depends on the density of the medium surrounding the resonator. A discriminant parameter is the *Knudsen number*:

$$\text{Kn} = \lambda_f / L, \quad (2.119)$$

where  $\lambda_f$  is the mean free path of molecules in the surrounding medium, and  $L$  a characteristic length scale of the system (e.g. the resonator size, or the gap between the resonator and an adjacent body). In our high vacuum experiments,  $\text{Kn} \gg 1$  places the system in the *free molecular flow* regime, where the collisions between molecules can be neglected and the gas can be treated with the tools of statistical physics. This is the situation we focus on for the calculation below (at atmospheric pressure or in liquids, where  $\text{Kn} \ll 1$  the fluid surrounding the mechanical resonator must be modelled as a continuum using the Navier-Stokes equations [99]).

Consider a surface element  $dx dy$  of a plate undergoing bending motion, which moves through the medium at speed  $V$  along the direction  $z$  [100]. As the plate hits a gas molecule, the latter will undergo an almost perfectly elastic collision (due to the great mass mismatch between the resonator and the molecule), and the magnitude of its velocity component  $v_z$  will change depending whether the collision was head-on (on the leading face of the plate) or rear-end (on the trailing face), as depicted in Fig. 2.123b. In the approximation of elastic collisions, the magnitude of the molecule velocity component will be  $v'_z = v_z + 2V$  after hitting the plate leading face, and  $v'_z = v_z - 2V$  after hitting the trailing face (here we neglect the small fraction of molecules that hit the leading face while moving in the same direction of the plate but slower than it, since for typical gas molecules statistics and MEMS motional amplitudes and oscillation frequencies,  $V \ll v_z$ ). Due to the change of the molecule velocity magnitude, a small amount of kinetic energy per collision is transferred from the plate to the molecule and vice-versa. For leading and trailing face collisions, respectively:

$$\begin{aligned}\Delta E_{\text{lead}} &\approx 2mv_z V + 2mV^2 \\ \Delta E_{\text{trail}} &\approx -2mv_z V + 2mV^2,\end{aligned}\tag{2.120}$$

where  $m$  is the (average) mass of a gas molecule, and the energy increments were expressed in the approximation  $v_z \gg V$ . The number of collisions in a time interval  $dt$  is also different between the leading and trailing faces of the plate, due to the plate motion in the medium. They are given by the following expressions:

$$\begin{aligned}dN_{\text{lead}} &= dx dy dv_z n f(v_z)(v_z + V) dt \\ dN_{\text{trail}} &= dx dy dv_z n f(v_z)(v_z - V) dt,\end{aligned}\tag{2.121}$$

where  $f(v_z)dv_z$  is the Maxwell distribution of gas velocities and  $n = P/(k_B T)$  the number density of gas molecules ( $P$  is the gas pressure). We can then sum and integrate these contributions to obtain the total kinetic energy lost by collisions with the gas molecules during an oscillation cycle:

$$\begin{aligned}\Delta E &\approx \frac{P}{k_B T} \int_{\Gamma} dx dy \int_0^{2\pi/\Omega} dt \int_0^{\infty} dv_z 8mv_z V(x, y, t)^2 \\ &= \frac{\pi P}{\rho h \Omega} \sqrt{\frac{2m}{\pi k_B T}} \langle K \rangle,\end{aligned}\tag{2.122}$$

where we have used  $\int_0^{\infty} dv_z v_z = \sqrt{k_B T/(2\pi m)}$  for the Maxwell distribution and, in the last equality, we have introduced the kinetic energy of a uniform plate averaged on an oscillation cycle,  $\langle K \rangle = \rho h \Omega \int_{\Gamma} dx dy \int_0^{2\pi/\Omega} dt V(x, y, t)^2$ . Finally, using the definition of quality factor and the virial theorem, we obtain the free molecular flow gas damping expression:

$$Q_{\text{gas}} = \frac{4\pi \langle K \rangle}{\Delta E} \approx \sqrt{\frac{\pi}{2}} \sqrt{\frac{RT}{M_m}} \frac{\rho h \Omega}{4P},\tag{2.123}$$

where  $R$  is the gas constant and  $M_m$  the molar mass of the gas medium.



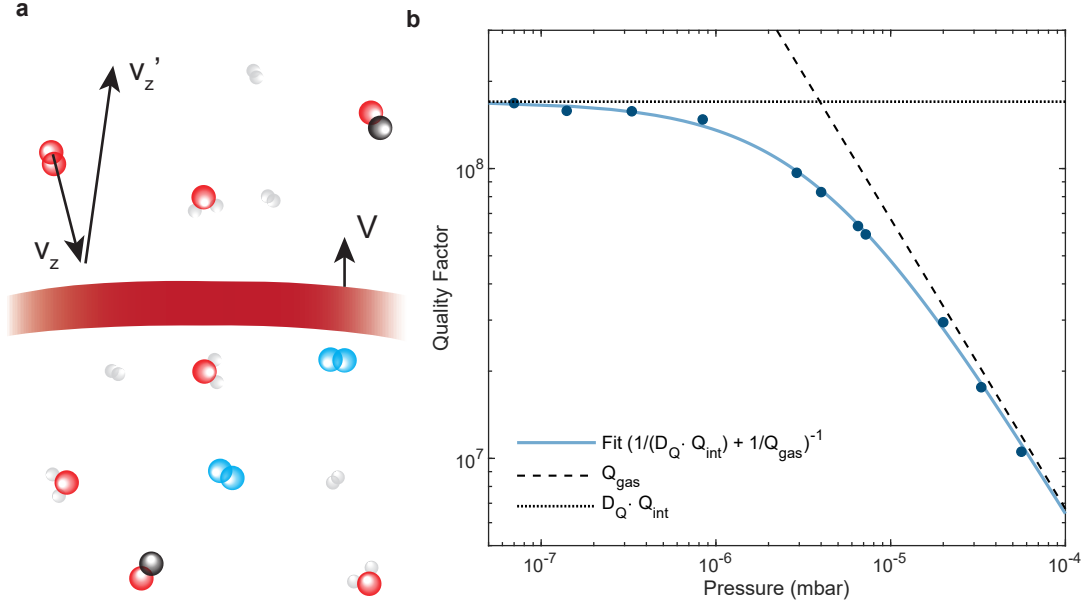


Figure 2.11: **a**, Elastic collisions between gas molecules in a rarefied phase and an oscillating mechanical resonator. **b**, Experimental verification of gas damping in the free molecular flow regime. Blue dots are data points at varying vacuum chamber pressure, the light blue line is a fit to a gas damping model saturating to intrinsic damping at pressures  $P \lesssim 10^{-6}$  mbar, and the dashed and dotted black lines are the components of the fit model, i.e. intrinsic damping independent of pressure and gas damping  $Q_{\text{gas}} \propto P^{-1}$ .

In case the resonator is suspended in the vicinity of another solid body (as happens often in microfabricated devices, where the micromechanical element is separated from its support chip by a thin gap of height  $g$ , defined by the thickness of a sacrificial thin film), the expression 2.123 must be adjusted to take into account an additional damping term from the molecules that remain ‘trapped’ underneath the bottom surface and undergo multiple collisions with the resonator before leaving the plate area. This mechanism is often called *squeeze-film damping*, and it provides the following correction to 2.123 (in the free molecular flow regime) [100, 101]:

$$Q_{\text{sqz}} \approx \frac{Q_{\text{gas}}}{1 + \beta \frac{L}{g}}, \quad (2.124)$$

where  $L$  is a characteristic dimension of the resonator and  $\beta$  is a numerical factor depending on the geometry of the resonator surface ( $\beta \approx 0.02$  for a rectangular plate).

A numerical evaluation of 2.123 gives  $Q_{\text{gas}} \approx 3.7 \times 10^8 \cdot \frac{\Omega}{2\pi \cdot 1 \text{ MHz}} \cdot \frac{h}{20 \text{ nm}} \cdot \frac{10^{-6} \text{ mbar}}{P} \cdot \left(\frac{T}{300 \text{ K}}\right)^{1/2}$ , assuming the resonator material to be  $\text{Si}_3\text{N}_4$  and the residual gas composition in the vacuum chamber to be similar to air (leading probably to an underestimation of  $Q_{\text{gas}}$ , as heavier molecules are pumped out more efficiently than the lighter ones in vacuum systems). It is clear that state-of-the-art dissipation diluted nanomechanical resonators are then quite sensitive to the residual pressure in the vacuum environment, and a pressure-dependent quality factor is frequently observed as the chamber is first pumped down after breaking the vacuum to insert a sample. Figure 2.11b shows the

effect of gas damping on a  $\text{Si}_3\text{N}_4$  soft clamped membrane resonator (with the stress-modulated design described in [25]), where the quality factor is dominated by intrinsic loss only for  $P \lesssim 10^{-6}$  mbar. Squeeze film damping is likely completely negligible for the data in Fig. 2.11b, as the substrate material was completely removed below the membrane resonator (to enable optical transmission). Note that the high pressure part of the fit model gives a  $Q_{\text{gas}}$  that is just 6% smaller than the estimation from 2.123 (the thickness of this membrane sample was  $h \approx 40$  nm and the resonant frequency  $\Omega/2\pi = 853$  kHz). Since regulating the pressure level in a vacuum chamber is relatively easy, gas damping becomes a useful tool to reversibly tune the mechanical resonator  $Q$  in case the experimentalist wants to suppress measurement backaction effects, as will be described in Chapter 4.

#### 2.3.6.6 Phonon radiation

Elastic waves in solid-state microresonators cannot radiate in vacuum, but they can easily leak out of the device by exciting propagating waves in the support structure (for microfabricated devices, a chip made of semiconducting or insulating materials). Since radiation involves the interaction of the resonator with its environment, this is another extrinsic loss mechanism that cannot be diluted by tension, although tension plays a fundamental role in determining the dispersion of sound waves and their impedance matching with the support material. This source of energy dissipation is named alternatively radiation loss, phonon tunneling loss, anchoring loss or (confusingly) clamping loss, as the forces imposed at the resonator clamped boundaries play a dominant role.

Phonon radiation is particularly difficult to model accurately. Many theoretical models with semi-analytical solutions have been proposed. A class of these models computes damping by the forces and torques imposed at the resonator boundaries during oscillations, that launch waves in the support medium, leaking away part of the resonant mode energy [102]. Dissipation is then calculated as the elastic power radiating in the far field due to the support response. Other models compute the radiation rate with a perturbative approach based on Fermi's golden rule, leveraging overlap integrals between the resonator and support eigenmodes [103, 104]. This approach gives rise to a complex menagerie of damping rates, as the strain field polarization determines how strongly the resonator will be coupled to the support, and symmetries in the mode pattern and resonator boundaries can lead to interference effects in the far field that reduce or enhance phonon radiation. An interesting experimental demonstration of radiative damping was reported by Singh and Purdy, who used highly directional radiation patterns of nanomechanical membranes to sense the temperature of blackbody absorbers placed at different locations on the chip frame, exploiting their preferential coupling to different mechanical modes [105].

A significant limitation of these models is that, in order to obtain analytical results, they assume a support with infinite extent (modelling the support either as a Kirchhoff-Love plate with unlimited lateral dimensions or as an elastic half-space). At frequencies around 1 MHz, typical of our dissipation-diluted oscillators, the wavelength of antisymmetric Lamb waves in silicon is  $\approx 2.5$  mm [106], comparable to the lateral chip size and much larger than the chip thickness (typically varying between 200 – 800  $\mu\text{m}$ ). This implies that the assumption of an infinite, homogeneous support postulated for the analytical models is inaccurate, and that phonon radiation will be influenced significantly by reflection from the chip interfaces and by the experimental assembly below the



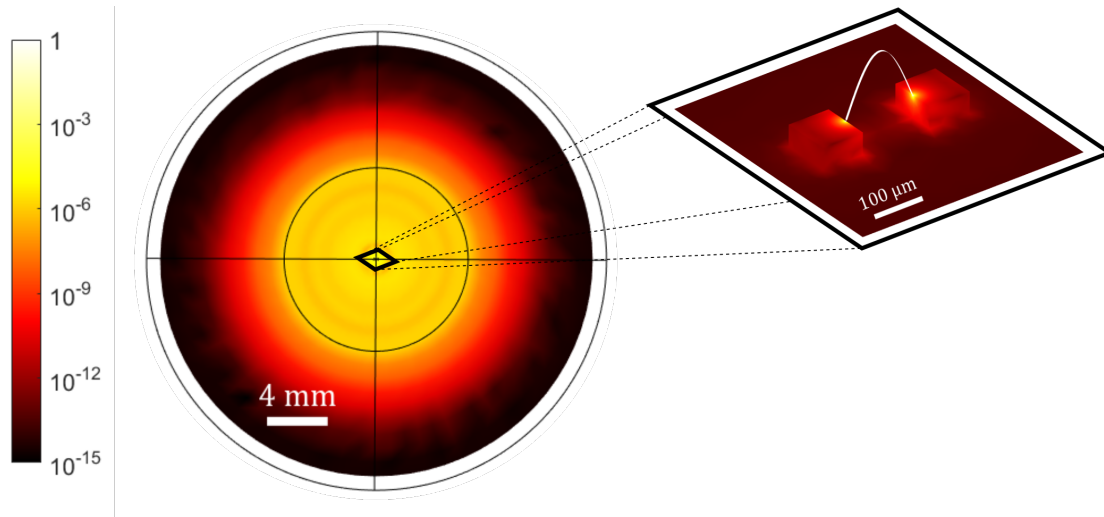


Figure 2.12: Finite element simulation of the elastic radiation pattern launched by an oscillating nanostring (enlarged view to the right) in the supporting silicon chip. The colour encodes the displacement field magnitude. Notice that the elastic wavelength is much larger in the chip bulk than in the nanostring resonator. The black contour indicates the boundary to a perfectly-matched domain, that is used to calculate the rate of radiative damping in the simulation. The figure is reproduced from [108].

chip (sample holder, clamps, vacuum grease, piezoelectric elements, etc.), with inhomogeneous dispersion and friction. Finite elements simulations provide more precise estimates, but many of the relevant system parameters are usually unknown. In Fig. 2.12 we show an example of such a simulation, where the damping is introduced with an acoustically-absorbing domain in the far field of the oscillating nanostring. This is implemented as a *perfectly-matched layer* (PML), a fictitious anisotropic material whose elastic absorption coefficient varies radially, and provides a perfect acoustic impedance matching with the lossless propagation domain [107].

As a consequence of this long-range coupling, it is common to observe, especially in dissipation-diluted nanomechanical membranes with low intrinsic losses, bending mode quality factors that are highly sensitive to the clamping conditions of the support, e.g. the application of pressure to the chip frame to hold it in place, or the use of glues or epoxies [109]. This also presents a practical constraint for assembling membrane-in-the-middle (MiM) optomechanical systems, where a membrane resonator is placed inside a Fabry-Pérot cavity and interacts with the light field confined therein.

Mechanical hybridization is frequently witnessed when a resonator eigenfrequency matches approximately with a plate resonance of the support chip. In this case, radiative coupling is enhanced and the damping rate becomes even more sensitive to the loss angle of the support chip material and its surface losses [6]. This was shown experimentally in [110], where laser heating allowed for a large tuning of membrane eigenfrequencies through several support resonances, each manifesting as a sharp dissipation peak. The mode density for typical dimensions of chip supports can be very large at MHz frequencies, thus contributing to a stochastic spread of the quality factors of different eigenmodes, and a poor experimental reproducibility for different samples with nominally identical designs. Phonon radiation and the sensitivity to clamping conditions can be overcome with the use of a low frequency mechanical filter struc-

ture, which reduces the susceptibility to forces applied to the outer part of the support [111, 112]. Alternatively, leakage of acoustic energy can be suppressed in a finite frequency band by patterning a phononic crystal shield in the support [61], but this type of isolating structure is cumbersome to fabricate for low frequency ( $\Omega/2\pi \lesssim 500$  kHz) mechanical resonators, as multiple unit cells with a pitch satisfying the Bragg condition need to surround the resonator on each side, with a total extent easily surpassing several centimeters. In addition, these isolating structures introduce unwanted thermo-mechanical noise in optomechanics experiments, associated with their low frequency resonances [112]. A serendipitous solution was the integration of the phononic crystal directly in the nanomechanical resonator design, simultaneously shielding a localized mode from radiation losses and implementing soft clamping in tensioned, high aspect-ratio devices, as previously described.

### 2.3.7 Anharmonicity from geometric nonlinearity

Finally, we give a schematic outline of the effect of tension in the mechanical resonator on the anharmonicity occurring when a mechanical mode is driven to high amplitudes. When the oscillation amplitude is high, energy terms associated with the geometric nonlinearity in 2.11 become stronger. In particular, the nonlinear strain components give rise to a (previously neglected) energy term that is fourth-order in the displacement amplitude. For an isotropic thin plate undergoing bending motion, this term can be expressed as [69]:

$$\Delta W^{(\text{el})} = \frac{Eh}{8(1-\nu^2)} \int_{\Gamma} dx dy \left( \left( \frac{\partial \psi}{\partial x} \right)^2 + \left( \frac{\partial \psi}{\partial y} \right)^2 \right)^2 \quad (2.125)$$

This quartic potential energy induces an additional restoring force of geometrical origin, that is due to the elongation of the plate elements as the deflections grow beyond the linear regime. A rigorous treatment of large oscillations [33] would require modifying the equations for the flexural vibrations of the plate, but in the case of weak nonlinearity, it is sufficient to evaluate 2.125 on unperturbed eigenmodes obtained by solving 2.25 to obtain an evaluation of the anharmonicity induced by the geometric nonlinearity.

By performing the mode expansion of section 2.1.3, we obtain a Duffing equation for the amplitude  $x$  of a single mechanical mode (considering for simplicity the case of viscous damping),

$$m_{\text{eff}} (\ddot{x} + \Omega^2 x + \Gamma \dot{x} + \gamma x^3) = 0, \quad (2.126)$$

where  $\gamma = 4\Delta W^{(\text{el})}(\phi)/m_{\text{eff}}$  is the Duffing parameter that describes the deviation from the harmonic regime due to geometric nonlinearities, and  $\Delta W^{(\text{el})}(\phi)$  is now evaluated using the normalized mode shape  $\phi(x, y)$ . The study of a weakly-anharmonic Duffing oscillator shows that the resonance frequency undergoes a shift proportional to the square of the oscillation amplitude,  $x_0$  [113]:

$$\Delta\Omega = \Omega - \Omega_0 \approx \frac{3\gamma x_0^2}{8\Omega_0}, \quad (2.127)$$

where  $\Omega_0$  is the unperturbed resonance frequency in angular units. To get an idea of the magnitude of the geometric anharmonicity in tensioned resonators, we can evaluate these expressions for the, now familiar, case of a square membrane. By using the normalized mode shapes of order  $(n, m)$  from 2.81 (high stress regime,  $\lambda' \ll 1$ ), we obtain, for the Duffing parameter:

$$\gamma_{n,m} \approx \frac{\pi^4 E}{32\rho(1-\nu^2)L^4} ((n^2 + m^2)^2 + 8(n^4 + m^4)), \quad (2.128)$$

and for the relative frequency shift during oscillations of amplitude  $x_0$ , by using 2.127:

$$\frac{\Delta\Omega_{n,m}}{\Omega_{0,n,m}} \approx \frac{9\pi^4}{64} \lambda'^2 \left( (n^2 + m^2) + 8 \frac{n^4 + m^4}{n^2 + m^2} \right) \left( \frac{x_0}{h} \right)^2 \quad (2.129)$$

From the last relation, we notice that, as expected, the effect of geometric nonlinearities is appreciable only when the amplitude of oscillations approaches the plate thickness,  $x_0 \sim h$ . Moreover, the Duffing spring hardening is diluted by tension in the resonator (due to the squared strain parameter at the numerator); i.e. tension increases the linearity range of the oscillator. The dynamic range of linear vibrations of a mechanical oscillator is usually defined by the onset of bistability at high driven amplitudes [114], that for a Duffing oscillator is witnessed at the critical amplitude  $x_c$ , depending on the oscillator parameters as follows [115]:

$$x_c^2 = \frac{2\sqrt{3}\Omega_0^2}{9\gamma Q} \approx \frac{8h^2}{45\sqrt{3}\pi^2\lambda'^2 Q}, \quad (2.130)$$

where the last equality is evaluated in the case of the fundamental bending mode ( $n = m = 1$ ). We notice that tension also increases the amplitude dynamic range of the resonator, as a direct consequence of 2.129, when disregarding the dependence of the quality factor on  $\lambda'$ .

This observation has important consequences for applications of mechanical resonators as sensors. The sensed variable often induces resonant frequency shifts, that can be monitored in time (for example, a change of temperature can perturb the resonant frequencies by affecting the elastic constants and inducing differential thermal expansion that modulates the tension). The fundamental limit for detecting small frequency shifts is dictated by thermodynamic fluctuations of the resonant frequency, as imposed by the fluctuation-dissipation theorem 2.59. The phase noise decreases as the amplitude of driven motion grows, as thermal fluctuations of a given amplitude in the motional quadratures will correspond to smaller angular excursion in the quadrature space. Frequency noise can be written as  $S_{\Omega\Omega}(\omega) = \omega^2 S_{\phi\phi}(\omega) = \omega^2 S_{xx}(\omega) / \langle x_0^2 \rangle$  [117]. Larger oscillation amplitudes allow the resolution of smaller frequency shifts, until the nonlinear character of the oscillator starts to correlate amplitude and phase noise, leading to excess frequency noise from the driving mechanism. A higher value of  $x_c$ , as allowed by tension, leads potentially to higher frequency sensitivity. We note that the effect of the quality factor on frequency sensitivity is less straightforward and depends on the precise experimental conditions, as was recently pointed out [118]. In mechanical resonators, however, the observed frequency fluctuations are usually much

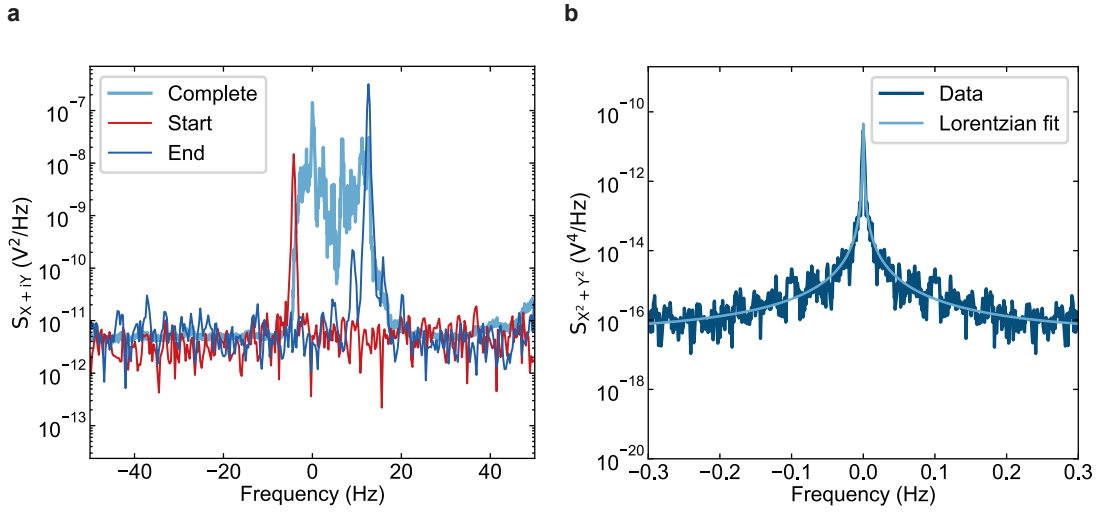


Figure 2.13: Thermomechanical motion recorded at room temperature for a perimeter mode of a polygon resonator, such as those introduced in [27]. A quality factor  $Q \approx 6 \cdot 10^8$  was measured for this sample with the ringdown method, corresponding to a damping rate  $\Gamma \approx 2\pi \cdot 0.5 \text{ mHz}$ . The spectra are centered around an offset frequency  $\Omega/2\pi = 306.3 \text{ kHz}$ . **a**, The light blue curve presents the thermomechanical motion spectrum (in voltage units, as given from a photocurrent record) computed over one hour of observation. The spectrum shows a clear upward frequency drift in time, as is also evident from spectra computed from 7.2 s-long chunks of the thermomechanical record at the beginning (red) and at the end (dark blue) of the acquisition time. Consequently, the thermomechanical spectral feature is much broader than the amplitude damping rate. **b**, By taking the square magnitude of the demodulated quadratures and displaying its spectrum, one obtains a much narrower peak, with a linewidth corresponding to the amplitude damping rate:  $X^2 + Y^2$  is insensitive to slow frequency drifts [116]. A Lorentzian fit (light blue) gives the estimate  $\Gamma \approx 2\pi \cdot 0.6 \text{ mHz}$ , in good agreement with the ringdown decay rate.

higher than the thermodynamic limit, and have been attributed both to intrinsic mechanisms as well as to drifts in external parameters [79, 119, 120]. Experimental evidence of frequency noise and slow temporal drifts is shown in Fig. 2.13, for a polygon resonator with the design we introduced in [27]. Some of the studied causes of frequency noise are processes of absorption and desorption of gas molecules, transition between states of the TLS population in the resonator, and the variation of tension due to temperature fluctuations.

The described geometric anharmonicity is certainly the most common and easily-understood source of nonlinearity observed in mechanical resonators. Other deviations from the harmonic regime can arise by motion in force fields that vary non-linearly in space, or by coupling between vibrational motion and electron transport [121, 122].

*God made the bulk; surfaces were invented by the devil.*

— Wolfgang Pauli

Part of this thesis work was devoted to the development of high aspect-ratio strained nanomechanical resonators in a crystalline material, namely *strained silicon* (sSi). Most of the content of this chapter has been published in [28]; my contributions to this work consisted in designing and fabricating all the employed resonators, developing a new fabrication process used for suspending high aspect-ratio string resonators, building the interferometric setup and using it to characterize the resonators (with support from the co-authors, in particular Diego A. Visani, Sergey A. Fedorov and Nils J. Engelsen), performing data analysis with support from Diego A. Visani and Nils J. Engelsen, and writing the manuscript with Nils J. Engelsen (with the supervision of T. J. Kippenberg). Victor Boureau, an expert electron microscopy scientist at the CIME facility in EPFL, deserves recognition for acquiring and analyzing all the TEM images and DFEH maps.

As previously discussed, most of the pioneering and state-of-the-art demonstrations of highly dissipation-diluted resonators, and the associated optomechanics experiments, were conducted with the amorphous  $\text{Si}_3\text{N}_4$ . This is a thin film material common in microfabrication technologies, that can be grown with high quality and high tension ( $\sim 1$  GPa) using low pressure chemical vapour deposition (LPCVD), and presents negligible optical absorption. On the other hand, there has been significant interest in extending the methods of dissipation dilution to single-crystal materials, ever since early works with  $\text{Si}_3\text{N}_4$ . Amorphous or glassy materials, irrespective of their precise composition, exhibit universal properties due to the presence of two-level systems (TLSs), such as high dissipation at low temperatures [53, 77]. TLSs can couple to the strain field of acoustic vibrations [84], giving rise to acoustic absorption (see the section 2.3.6.3). In crystalline materials, TLSs only form due to defects and energy exchanges with TLS ensembles are drastically reduced. Through control of spurious damping channels, exceptionally low vibrational damping has been demonstrated in single-crystal resonators [93, 123, 124], where even without dissipation dilution quality factors  $Q \sim 10^9 - 10^{10}$  were observed.

In nanomechanical resonators,  $Q_{\text{int}}$  is known to be lower than in macroscopic devices, primarily due to pronounced surface effects such as friction in surface oxides, adventitious adsorbed layers or reconstructed surfaces [18, 57, 95]. Despite this, the use of crystalline materials can be highly advantageous: the temperature dependence of intrinsic mechanical dissipation processes often makes the coupling of phonons to TLSs the dominant loss mechanism at cryogenic temperatures. Several demonstrations of dissipation dilution in single crystal materials, such as GaAs [125], SiC [126, 127] and InGaP [128, 129], have been reported but could not attain lower dissipation than  $\text{Si}_3\text{N}_4$  devices.

In this chapter, I report on our implementation of strained silicon mechanical resonators with ultralow dissipation. Strained silicon was developed as material for micro-

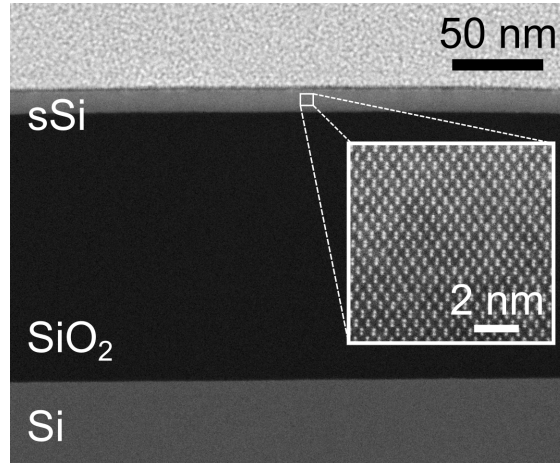


Figure 3.1: Scanning transmission electron micrograph of the cross-section of a processed sSOI sample. The inset shows the strained silicon crystalline lattice, imaged with a higher magnification.

electronic devices, and has been used to improve the carrier mobility in MOSFETs [130] and to induce a Pockels coefficient for optical modulation in silicon photonics [131], but nanomechanical applications of sSi were unexplored. In soft clamped strained silicon nanostrings, we demonstrated quality factors up to  $(1.3 \pm 0.2) \cdot 10^{10}$  around 1.4 MHz at temperatures of approximately 7 K. This represents the highest  $Q$  reported for a mechanical oscillator at liquid He temperatures, exceeded only at mK temperatures in single-crystal silicon optomechanical cavities ( $Q = 5 \cdot 10^{10}$ ) [79]. As shown in the latter work, the  $Q_{\text{int}}$  of crystalline silicon increases monotonically with decreasing temperatures between 1 K – 10 mK, and we expect a qualitatively similar improvement of mechanical friction in strained silicon characterized at millikelvin temperatures.

The chapter will be structured as follows. I will present the results on the investigation of strained silicon as a material for nanomechanics, starting from the description of the microfabrication methods we developed, successively detailing the techniques that can be used to characterize the elastic strain in the nanoscale devices, then presenting the main results on the cryogenic characterization of the phononic crystal nanostring samples. I will then discuss the optical interferometer setup we assembled and employed for acquiring all the data presented in this section. This type of apparatus is extremely useful for preliminary mechanical characterization before conducting optomechanics experiments, and we routinely employ a few variants of the described interferometer for the measurement of all the samples fabricated in the Optomechanics team. Finally, I will expose some accessory measurements of the bolometric effect observed in the sSi strings (optical heating).

### 3.1 MICROFABRICATION OF STRAINED SILICON NANOSTRINGS

We use strained silicon on insulator substrates<sup>1</sup>, where the strained silicon layer is grown epitaxially and bonded to a carrier wafer [132]. As in SOI technology, the sSi layer is conveniently separated from the silicon substrate by a buried oxide layer, fa-

<sup>1</sup> sSOI, Soitec SA. To the best of our knowledge, Soitec has interrupted the production of sSOI wafers, and only some stock wafers remain in their inventory.



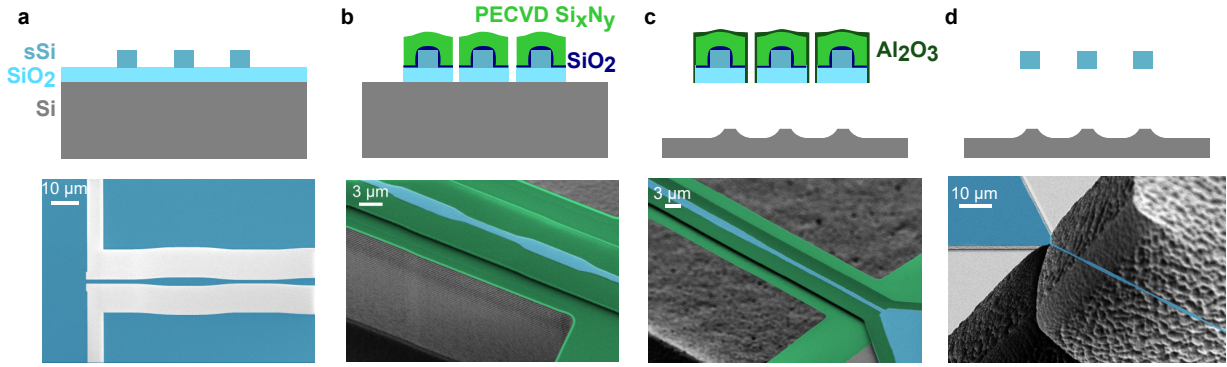


Figure 3.2: Simplified fabrication process, divided into: **a** device layer patterning, **b** encapsulation of the nanostrings, **c** undercut and **d** release and removal of the encapsulation layer. False-colour SEM micrographs are shown for each step of the process.

cilitating the fabrication of suspended nanomechanical resonators. The average initial thicknesses of the sSi and buried oxide films in our samples are, respectively, about 14 nm and 145 nm. A transmission electron microscope (TEM) cross-sectional image of the film stack is shown in [Figure 3.1](#).

We developed a fabrication method to suspend high aspect ratio phononic crystal (PnC) nanostrings [26], outlined in [Figure 3.2](#). Millimeter-scale nanostrings require a large clearance ( $> 10 \mu\text{m}$ ) from the substrate to be reliably suspended without stiction and collapse. An added complication is the chemical identity of the substrate and the device layer, offering no chemical selectivity for undercut steps. To circumvent these issues, our process includes the deposition of several encapsulation layers and a sequence of dry and wet etch steps for suspending the nanostrings (see [Figure 3.2](#)). The process was developed and all the samples were fabricated at the Center of MicroNanoTechnology (CMi) at EPFL.

Nanofabrication of the sSi mechanical resonators starts from 300 mm-diameter sSOI wafers. Strained silicon is obtained by heteroepitaxial growth on  $\text{Si}_{1-x}\text{Ge}_x$ ; the crystal lattice constant mismatch can be tuned by changing the Ge concentration ( $x$ ), leading to typical biaxial stress levels in excess of 1 GPa. The epitaxially-strained silicon film is bonded to a silicon carrier wafer capped by an oxide layer, and separated from its original substrate by a sequence of ion implantation, thermal treatment and selective etch of the  $\text{Si}_{1-x}\text{Ge}_x$  buffer layer [132]. Our wafers consist of a  $\approx 800 \mu\text{m}$ -thick Si substrate, with 145 nm  $\text{SiO}_2$  and 14 nm (nominal thickness) strained silicon thin films on the front side.

Wafers are resized through laser cutting to a 100 mm diameter, suitable for handling and processing in our clean room. After thoroughly stripping the wafer of the protective layer of photoresist (with a combination of room temperature acetone and  $\text{O}_2$  plasma), we proceed to pattern the sSi layer.

#### 3.1.1 Device layer patterning

The electron beam resist ZEP520A at 50% dilution is employed, spun at a thickness of roughly 150 nm (spin coater rotation frequency of 3000 RPM). Since ZEP is a positive electron beam resist, the patterns are divided into a sleeve region, surrounding the

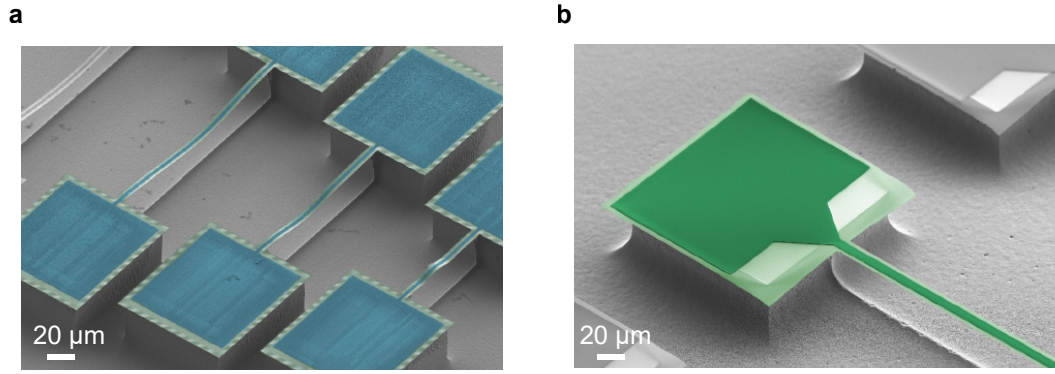


Figure 3.3: **a**, Suspended nanostrings without a stress-compensation layer are subject to a compressive load well beyond the critical value for out-of-plane buckling. Green -  $\text{SiO}_2$ , blue - patterned sSi + FOX16 mask. **b**, The encapsulation layers (dark and light green) compensate compressive stress; the suspended beam is tensioned and flat.

nanosttring edges and discretized with a fine grid, and a bulk region, including larger patches of the patterns with no common borders with the mechanical resonators. Proximity effect correction is performed to adjust the local exposure dose point by point. With this procedure, we can achieve line roughness  $\lesssim 10$  nm, while maintaining a reasonable duration for the exposure job (line edge roughness is measured in a Scanning Electron Microscope, over a  $\sim 5 \times 5 \mu\text{m}^2$  field of view, after dry etching the sSi layer, and we quote here a  $3\sigma$  confidence interval). The nanobeams are patterned along  $\langle 110 \rangle$  directions (with a tolerance of approximately  $\pm 1^\circ$ , dominated by the precision of the reference wafer cut), because this direction makes the stress relaxation upon release negligible due to a minimal Poisson's ratio of  $\nu \approx 0.06$  (Young's modulus  $E \approx 169$  GPa) [133].

Using ZEP520A as a mask, we pattern the sSi layer with ICP-RIE, using  $\text{SF}_6 + \text{C}_4\text{F}_8$  gases. Only a few seconds of exposure to plasma are needed to etch the film, landing on the  $\text{SiO}_2$  underneath. In order to increase reproducibility, we therefore pre-condition the ICP chamber by exposing a test Si wafer to the same chemistry prior to etching the actual devices. We then strip the ZEP resist residues before proceeding with the following microfabrication steps. In order to avoid the formation of heavily cross-linked and burnt resist residues, that are almost impossible to remove, we routinely employ the following sequence:

- Exposure to  $\text{O}_2$  plasma (600 W RF power, 400 sccm flow rate) for 30 s to clear the hardened resist crust formed during dry etching,
- Immersion in hot N-Methyl-2-pyrrolidone (NMP) at  $70^\circ\text{C}$  for 10 minutes to remove the bulk of the resist,
- Exposure to  $\text{O}_2$  plasma (600 W RF power, 400 sccm flow rate) for 3-5 minute to remove the remaining, loose residues of resist.

This procedure is carefully repeated after each etch step, to strip photo- or e-beam lithography resist masks.



### 3.1.2 Dielectric film encapsulation

The goal of the process at this stage is to create sufficient clearance between the sSi layer and the substrate to suspend mm-scale devices. To achieve this, we encapsulate the sSi strings in a protective oxide layer, then use deep reactive ion etching (DRIE) and an isotropic undercut (in a sequence similar to the method described in [26]) with high oxide chemical selectivity. However, an additional constraint arises: when such a multi-layer beam is suspended, it will buckle and very commonly collapse or break, due to the high compressive stress intrinsic to thermal and deposition oxides (see Figure 3.3a). The solution is to ensure the encapsulating layer has tensile stress and is sufficiently thick to compensate the compressive stress in the buried oxide underneath (around  $-400$  MPa to  $-300$  MPa)<sup>2</sup>, as in Figure 3.3b.

In practice, multiple dielectric films are deposited. First, roughly 10 nm of SiO<sub>2</sub> is deposited through atomic layer deposition (ALD), covering the patterned surface. Then, hydrogen-rich Si<sub>x</sub>N<sub>y</sub> is grown through plasma-enhanced chemical vapour deposition (Oxford PlasmalabSystem100 PECVD with 2% SiH<sub>4</sub>:N<sub>2</sub> and NH<sub>3</sub> as the precursors. The flow rates were respectively 975 and 30 sccm. The chamber pressure was 800 mtorr and the reactor temperature was set to 300 °C during the deposition). With 40 W of RF power generating the plasma, the film exhibits strong tensile stress, stable in time, of approximately +330 MPa (characterized through the Stoney wafer bending method [134]; see Figure 3.4). Its thickness must be sufficient to keep the thickness-averaged stress positive, i.e.

$$t_{\text{SiN}} > \frac{\sigma_{\text{SiO}_2} (1 - \nu_{\text{SiO}_2})}{\sigma_{\text{SiN}} (1 - \nu_{\text{SiN}})} t_{\text{SiO}_2}, \quad (3.1)$$

where  $t$  is the film thickness and  $\sigma, \nu$  are the initial stress ( $\sigma_{\text{SiO}_2} \approx -360$  MPa) and Poisson's ratio. We usually deposit an approximately 400 nm-thick nitride layer, verifying the thickness by reflectance spectroscopy.

This stack of dielectric films is patterned through conventional photolithography and RIE (He + H<sub>2</sub> + C<sub>4</sub>F<sub>8</sub> plasma precursors), with a rescaled mask which completely envelopes the nanobeam sidewalls, exposing the Si substrate. To improve the resilience of the encapsulation layer to the Si undercut process, an additional 30 nm film of Al<sub>2</sub>O<sub>3</sub> is deposited by ALD. Another photolithography mask defines the pattern of Al<sub>2</sub>O<sub>3</sub> and protects the encapsulation structure during a DRIE step (Bosch process, pulsed SF<sub>6</sub> and C<sub>4</sub>F<sub>8</sub>), which creates a (roughly) 30  $\mu\text{m}$ -thick recess into the Si substrate.

A thick, protective layer of photoresist is then spun over the patterned frontside, and the wafer is diced into chips; the process then continues chip-wise. Samples are cleaned carefully with a procedure similar to each post-RIE cleaning (taking care not to use Piranha solution for stripping organic residue: it quickly dissolves Al<sub>2</sub>O<sub>3</sub>).

### 3.1.3 Plasma undercut

Selective undercut (Figure 3.2c) is carried out with isotropic etching in SF<sub>6</sub> plasma; for this step the single chips are bonded to a Si carrier wafer in order to homogenize the etch rate and increase process reproducibility. Importantly, the separate patterning

<sup>2</sup> The presence of the sSi layer can be ignored, due to its negligible thickness.

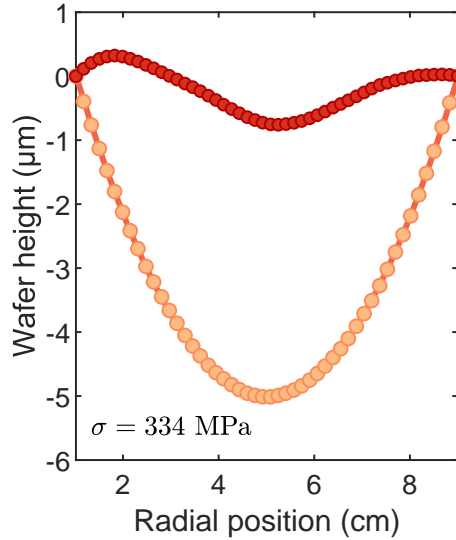


Figure 3.4: Determination of the intrinsic stress in PECVD  $\text{Si}_x\text{N}_y$  through wafer bow. The wafer height profile is measured by scanning a laser beam and recording the angular deflection of the beam reflected off the surface. The magnitude and sign of the profile curvature permit to reconstruct the biaxial stress. Red circles—wafer profile before nitride deposition, orange circles—wafer bow after nitride deposition, with the initial profile subtracted.

of the  $\text{Al}_2\text{O}_3$  allows fine control of the geometry of the isotropic undercut process, preventing the formation of overhang at the string anchoring pads. Overhang at the clamping points can be detrimental to the purpose of suspending structures with high dissipation dilution, and the released film can relax its tensile stress by buckling.

#### 3.1.4 Wet release

The strings are now suspended and encapsulated in a rescaled, thicker dielectric beam. To conclude the process and expose sSi one must remove the encapsulation layers selectively to Si. For this purpose we employ concentrated HF (10% volume fraction in water solution). We previously employed buffered HF (BHF, HF 50% :  $\text{NH}_4\text{F}$  40% 1:7 volume fraction), but observed a non-negligible attack of the sSi layer, possibly due to its higher pH [135]. No significant modification of the sSi layer could be noticed when performing the etch in concentrated HF (see Figure 3.5). To ensure the survival of the fragile suspended samples during wet etch, it was crucial to design and construct appropriate PTFE<sup>3</sup> chip holders that minimize the flow of liquids in the vicinity of the devices and allow gradual dilution of etchants and solvents, inspired by the “turbulence-shielding” methods detailed in [136]. One of the “puddle holders” we designed (Sergey Fedorov, myself and Mohammad Bereyhi, over several generations with incremental improvements) is shown in Figure 3.6. The design satisfies the compromise of maintaining gentle liquid flows during the transfers between liquid etchants, deionized water for neutralization and solvents, while ensuring that acids

<sup>3</sup> PTFE has excellent resistance to chemicals, but is somewhat tricky to machine with adequate tolerances. We are indebted with the staff of the Microtechnology mechanical workshop of EPFL for patiently advising us and fabricating all our prototypes.

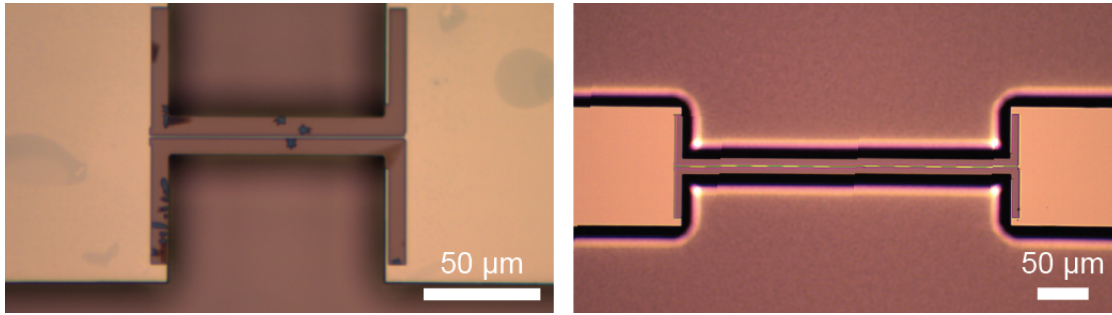


Figure 3.5: In the left microscope image, the strained silicon layer (yellow) exposed to buffered HF (HF 50% :  $\text{NH}_4\text{F}$  40% 1:7 volume fraction) for 7 minutes presents significant consumption and damage, manifesting as an inhomogeneous darkening of the thin film. In the right image, a nanostring exposed to HF (10% volume fraction diluted in water) for 5 minutes does not present signs of damage.

will not stagnate in closed volumes and can be fully rinsed. In case acids are not properly rinsed from the holder and the devices, they could damage the CPD tool employed for sample drying, and macroscopic residues will compromise the devices. Moreover, the holder ensures that the devices remain submerged in a puddle of stagnant fluid during movements and transfers, avoiding their exposure to catastrophic surface tension or hydrodynamic forces, that would cause their collapse or stiction. Employing such holders increased the survival yield of the strained silicon nanostring samples by orders of magnitude, and is similarly crucial for the release step of high aspect ratio near-field optomechanical systems. [137].

In the holder shown in Figure 3.6, the chips sit within cavities on the bottom plate and are constrained by the thin fingers protruding from the top holder, in such a way that they are free to move over hundreds of micrometers, and no narrow cavities, difficult to rinse, are formed. The holder can be displaced by inserting a rod in the central hole. Transfers between different baths are carried out by repeatedly inserting and retracting the holder through the liquid meniscus with extremely gentle movements. In this way, the liquids gradually fill the chip cavities by flowing from the gaps between the top and bottom plate, and slowly replace the previous chemicals. The movement should be repeated until full neutralization is achieved, which can be verified with a pH indicator paper.

After the wet etch step, we transfer the samples to an ethanol bath and start the process of critical point drying (CPD) which removes the liquids while minimizing stiction forces. The suspended strings can be (optionally) exposed to  $\text{O}_2$  plasma for further cleaning of organic residues. Before the chips are loaded in the vacuum chamber for characterization, they are briefly exposed to vapor HF for a few seconds to strip the spontaneously-formed native oxide layer and to improve the chemical stability of surfaces through hydrogen termination [138]. After vapor HF exposure, the samples are brought to the cryostat vacuum chamber within 20 minutes. An image of a suspended PnC nanostring sample, obtained by stitching together many scanning electron micrographs, is shown in Figure 3.7.

We remark that the complex fabrication process, including encapsulation, creation of a recess and release with wet etching and CPD, was rendered necessary by our sacrificial oxide layer thickness being fixed to 145 nm, too small to provide an adequate

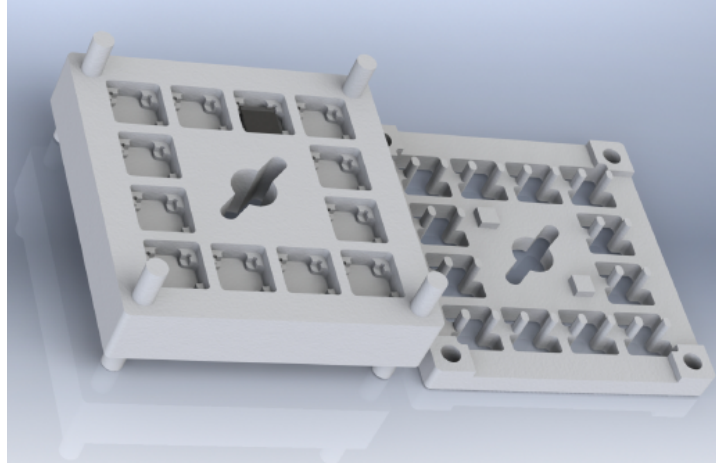
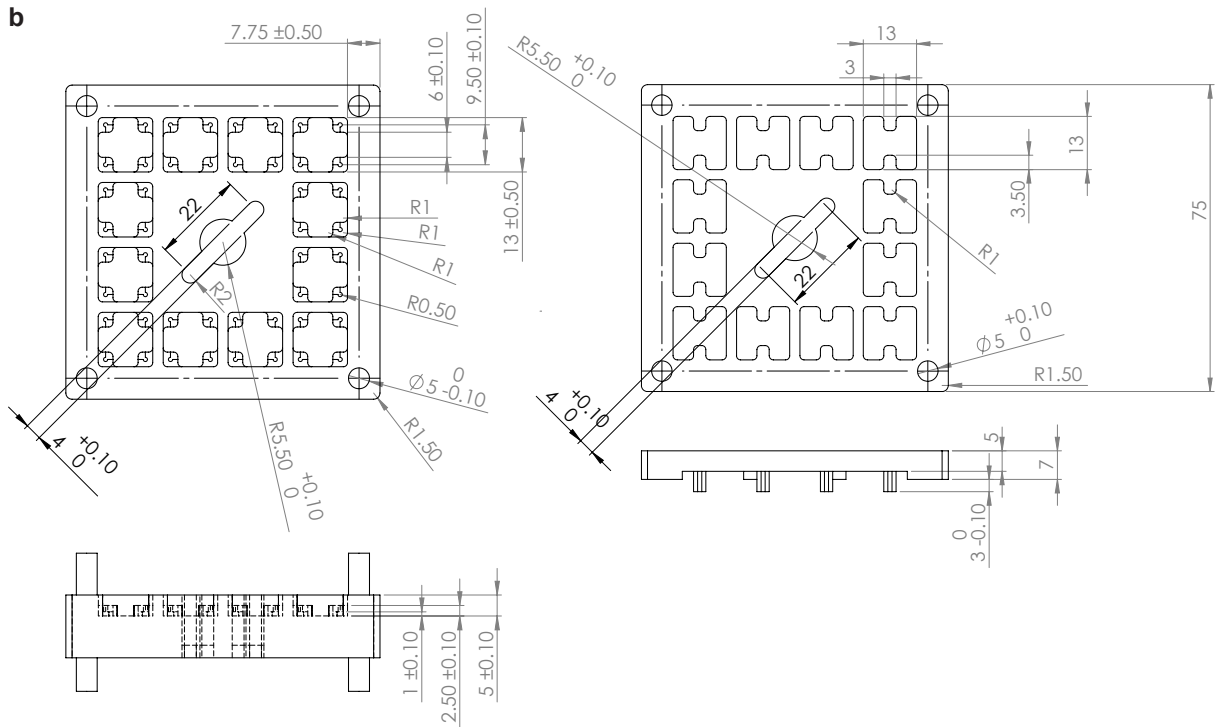
**a****b**

Figure 3.6: **a**, Rendering of the disassembled PTFE chip holder. A chip lies horizontally in the bottom plate. As the top plate is mated using the cylindrical alignment pins, the chips are secured (without contact) by thin fingers that align with the chip edges. **b**, Drawings of the bottom and top plates (top and side views), with dimensions and fabrication tolerances quoted in millimeters.

clearance for the undercut of our high aspect ratio devices. In principle, after epitaxial growth, the sSi layer could be bonded to glass wafers, or wafers with arbitrarily thick oxide films, as much as several micrometers. In that case, the devices could be simply undercut via exposure to highly selective, stictionless vapor HF, with minimal risk of collapse onto the substrate. We were previously able to release strings of lengths up to 100  $\mu\text{m}$  with a simple protocol consisting of electron-beam lithography, pattern transfer via dry etching and vapor HF release, exploiting the thin sacrificial layer of our



Figure 3.7: False-color SEM micrograph of a high aspect ratio PnC nanostring. Different scale factors have been applied in the horizontal and vertical directions.

substrates. Longer strings would always get stuck to the substrate during the vapor-phase undercut.

## 3.2 STRAIN IMAGING

### 3.2.1 Dark field electron holography

We assess the strain in the sSi film after fabrication by imaging a thin cross section of the chip, cleaved from the PnC nanostring pad, in a transmission electron microscope (TEM)<sup>4</sup>. A thin cross-sectional slice ( $\sim 100$  nm thickness) is carved from the support pads of the nanobeams, using a focused ion beam (FIB) specimen preparation technique. The slice can then be observed in the TEM (see Figure 3.1). An electronic interference method, dark-field electron holography [140], is employed to quantitatively map the strain in the crystalline films (Si substrate and bonded sSOI layer), with nanometer-scale resolution, as displayed in Figure 3.8. From the signal-to-noise ratio of the strain distribution in the sSi film, we calculate a 95% confidence interval on the average biaxial strain ( $0.85 \pm 0.06$ ) % (stress ( $1.53 \pm 0.11$ ) GPa; 95% confidence interval on the mean), close to the supplier specification of 1.3 GPa. The strain is significantly higher than the  $\sim 0.4\%$  value of stoichiometric  $\text{Si}_3\text{N}_4$  on silicon [57], due to a lower (direction-averaged) Young's modulus.

In order to acquire the dark-field electron holography strain map, the impinging electron wave is diffracted by the crystal of the specimen, set in two-beam condition to enhance the intensity of the (220)-diffracted beam which is selected with an objective aperture placed in the back-focal-plane of the objective lens of the TEM. Then, an electron biprism is used to interfere the reference wave emerging from the unstrained Si substrate (the dark-field image of the substrate) with the wave emerging from the measurement area (the dark-field image of the sSOI), to generate a hologram. Fourier processing is used to retrieve the geometric phase encoded in the interference fringes of the hologram, and the in-plane strain map is calculated from the gradient of the geometric phase, being proportional to the displacement field of the (220) crystal lattice planes [139]

Electron holography experiments were performed with a double aberration-corrected FEI Titan Themis operated at 300 kV. Stacks of 50 holograms of 5 s exposure time were recorded with a FEI Ceta camera to improve the signal-to-noise ratio of the strain maps [139]. The biprism bias was 200 V, giving a hologram carrier frequency of  $0.69 \text{ nm}^{-1}$ . The numerical aperture used for the Fourier processing limits the spatial resolution of the strain map to 2.75 nm.

<sup>4</sup> All TEM observations and DFEH experiments were conducted in the CIME Interdisciplinary Center for Electron Microscopy at EPFL, with the support of Dr. Victor Boureau.



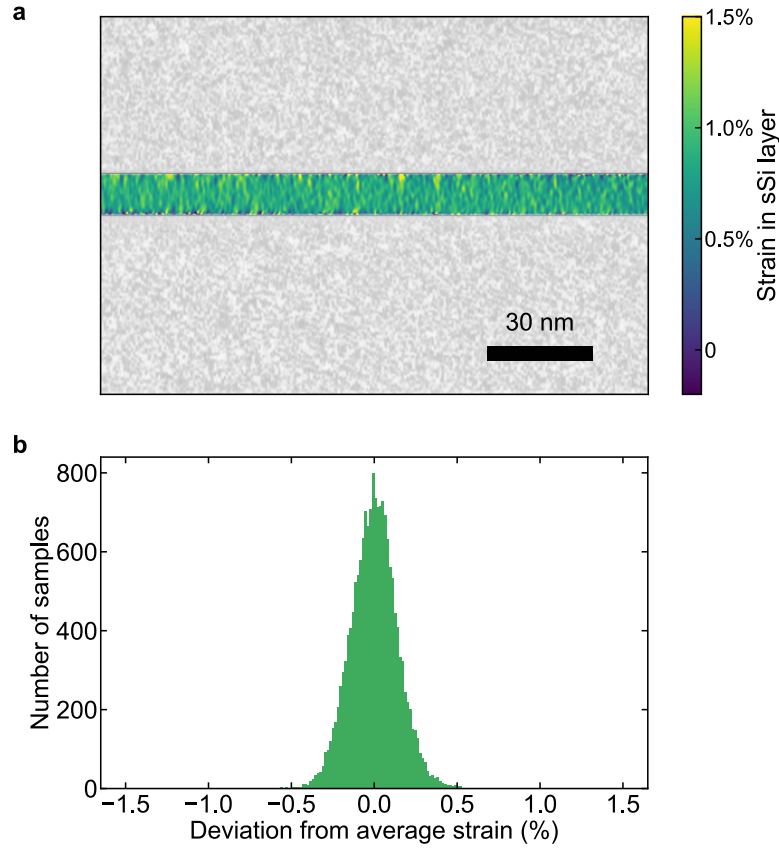


Figure 3.8: ]

**a**, Color-coded strain map of crystalline silicon, measured with dark-field electron holography [139]. The noisy maps from the amorphous layers of SiO<sub>2</sub> (bottom region) and evaporated Pt layer (top region) are desaturated for clarity. **b**, Distribution of reconstructed strain values in the sSi layer, centered on the average strain  $\langle \epsilon \rangle = 0.85\%$ .

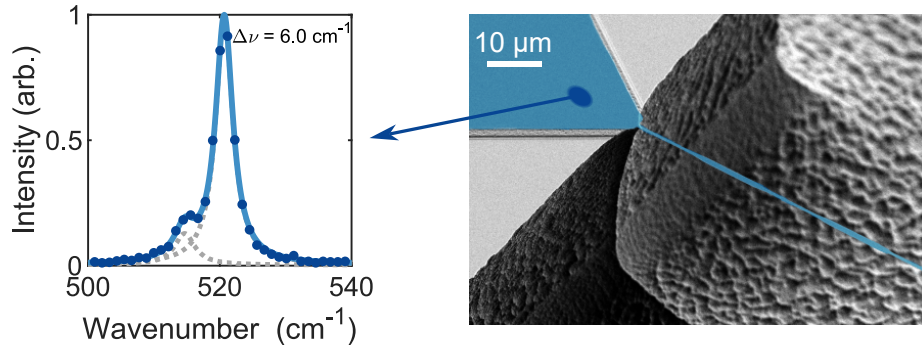


Figure 3.9: Raman Stokes spectrum acquired on a string anchoring pad (left). The approximate location where the Raman spectrum was measured is indicated on the right image with a dark blue spot.

### 3.2.2 Raman spectroscopy

Local strain can also be measured in suspended resonators by Raman spectroscopy [141]. Micro-Raman has been long recognized as a powerful technique to characterize

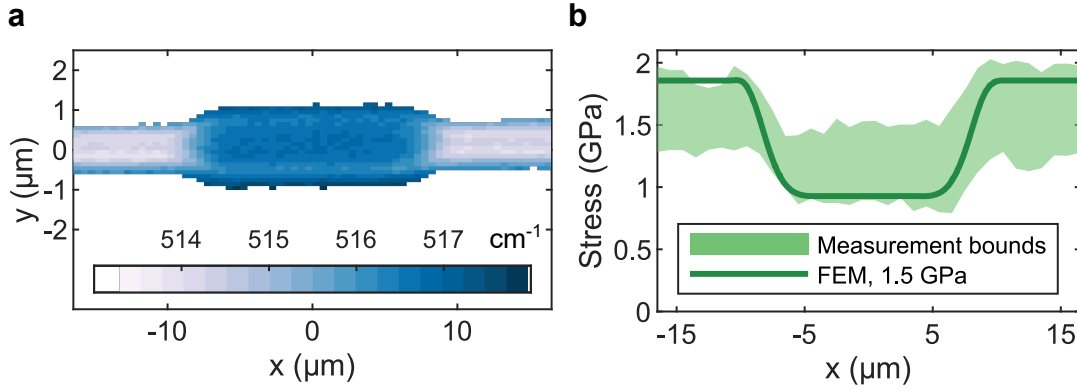


Figure 3.10: **a**, Micro Raman map over the unit cell of a corrugated nanostring. The colour scale represents the central frequency of Raman emission. **b**, Light green band: stress profile along a  $y = 0$  cut in the unit cell, reconstructed from **h**. The width of the band depicts experimental uncertainties. Dark green line: output of a finite-element simulation with 1.5 GPa initial stress.

the local stress state of crystalline samples, owing to the high spatial resolution achievable with confocal microscopy, and the high resolving power of diffraction gratings, compared to typical stress-induced Raman shifts [141].

For silicon, tensile (compressive) strain is known to decrease (increase) the Stokes scattering frequency. When collecting the Stokes signal from the sSOI stack, we observed spectra similar to the one depicted in Figure 3.9, where a red-shifted contribution from the sSi film can be resolved from the more intense peak at  $521\text{ cm}^{-1}$ , scattered by the unstrained substrate. We then collect Raman-scattered light from a suspended nanostring with nonuniform width and display the spatial variation of the Stokes frequency in Figure 3.10a: the frequency changes along the longitudinal axis  $x$ , being lower in the thin parts of the unit cell. This occurs due to re-distribution of stress in a string with nonuniform width [24]. From the Stokes frequency we can estimate the uniaxial stress along the unit cell (Figure 3.10b), taking laser heating into consideration [141, 142], as explained in the following paragraphs. We display a band of finite width for the reconstructed stress, accounting for uncertainties in the elements of the stiffness-strain tensor and in the Stokes peak from unstrained silicon. The reconstructed stress profile agrees fairly well with an initial stress of approximately 1.5 GPa, as displayed in Figure 3.10b.

Reconstruction of the local strain state from the Stokes frequency is aided by the numerous studies of silicon under different states of stress in the literature of micro-Raman spectroscopy. The frequencies of long-wavelength optical phonons in Si are perturbed by strain. In the absence of strain  $\epsilon$ , the normal modes are degenerate at a wavenumber of  $\nu_0 \approx 520\text{ cm}^{-1}$  ( $\omega_0 = 2\pi \cdot 15.6\text{ THz}$ ); the introduction of strain modifies the crystal stiffness tensor and perturbs the mode frequencies, breaking their degeneracy [141]. This influence is generally approximated as a linear dependence; by symmetries of the silicon lattice, only three independent elements appear in the stiffness-strain tensor:  $p, q$  and  $r$ . These are usually determined experimentally, and different values have been reported in the literature [142]. We report here the numerical values from [143]:

$$\begin{aligned}
p &= -1.3 \cdot \nu_0^2 \\
q &= -1.9 \cdot \nu_0^2 \\
r &= -0.66 \cdot \nu_0^2
\end{aligned} \tag{3.2}$$

The perturbed normal modes frequencies are obtained by finding the eigenvalues  $\lambda$  of the matrix:

$$\begin{pmatrix}
p\epsilon_{11} + q(\epsilon_{22} + \epsilon_{33}) & 2r\epsilon_{12} & 2r\epsilon_{13} \\
2r\epsilon_{12} & p\epsilon_{22} + q(\epsilon_{11} + \epsilon_{33}) & 2r\epsilon_{23} \\
2r\epsilon_{13} & 2r\epsilon_{23} & p\epsilon_{33} + q(\epsilon_{11} + \epsilon_{22})
\end{pmatrix}, \tag{3.3}$$

from which the phonon wavenumbers can be computed as  $\nu \approx \nu_0 + \lambda/2\nu_0$ . Phonon polarizations are found as the corresponding eigenvectors. Raman scattering selection rules impose that only scattering by longitudinal phonons (polarized along  $z$ ) can be measured, upon reflection on a (100) surface [144].

A particular strain state is assumed to simplify the eigenvalue equation and extract a single strain or stress component from the measurement of  $\Delta\nu$ . Importantly, matrix 3.3 is expressed in the reference system [100], [010], [001], so that the strain tensor must be rotated to the same axes.

We report here the resulting linear relations between stress and Raman shift in the relevant cases.

- Uniaxial stress directed along [110] or [100]:  $\Delta\nu/\sigma \approx -2.0 \text{ cm}^{-1}/\text{GPa}$
- Biaxial stress,  $\sigma_{xx} = \sigma_{yy} = \sigma$ :  $\Delta\nu/\sigma \approx -4.1 \text{ cm}^{-1}/\text{GPa}$ ,

confirming the general observation that tensile (compressive) stress leads to a red (blue) shift in the Raman scattering peak.

In our confocal microscope setup, we excite Raman scattering by focusing a 488 nm laser with typical output power of 10 – 50 mW on the sample (located at room temperature and atmospheric pressure), we detect the Stokes peak in reflection and separate it from the laser line with a diffraction grating with high resolving power. The intensity and wavenumber of the Stokes peak are recorded by a CCD sensor. When the laser beam is focused on the suspended string, the spectrum consists of a single Lorentzian, since the recessed substrate is beyond the depth of focus of the microscope. On the other hand, when the laser is focused on a region where sSi is not undercut, two contributions can be distinguished: an intense Lorentzian line at  $\nu_0$  collected from the unstrained substrate and a redshifted Lorentzian peak from the biaxially-stressed sSi layer (see Figure 3.9). By extracting  $\Delta\nu = \nu - \nu_0$  from the fit, the stress magnitude can be inferred as described above. We measure a Stokes shift from the unstrained substrate of  $\nu_0 = 521 \text{ cm}^{-1}$ , at small impinging optical power.

Heating in the sSi layer influences the reconstructed stress magnitude. Silicon absorbs strongly at the pump laser wavelength, and heating is exacerbated by the poor thermal conductance of the nanostrings. A temperature increase leads to a redshift of the phonon frequency, due to anharmonic terms in the potential energy of atomic



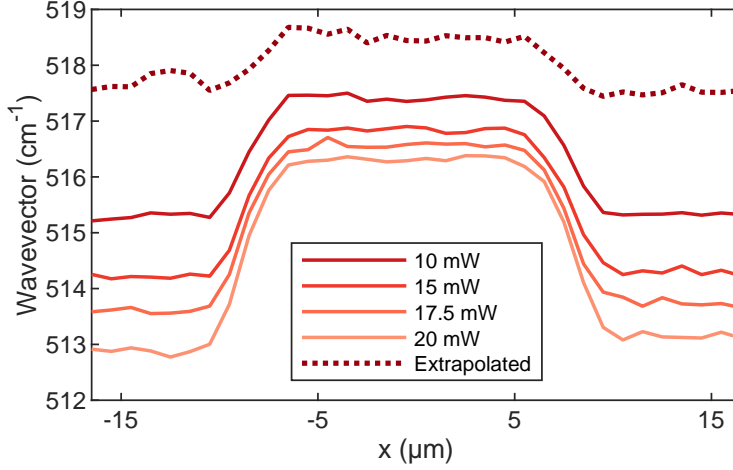


Figure 3.11: Micro-Raman scans along a corrugated beam section are conducted, with variable laser power. A linear dependence of the Raman scattering wavevector on the power is observed; the dotted line indicates the extrapolation to zero optical power.

bonds [145], and changes the local strain. We account for this temperature dependence experimentally, by varying the pump power and extracting, point by point, the Stokes shift at vanishingly small power via linear extrapolation (see Figure 3.11).

In Figure 3.10b, we account for experimental uncertainties by displaying a plausible region for the reconstructed stress as a function of position. The light green band is obtained by varying  $\nu_0$  between 520.5 and 521.5 cm<sup>-1</sup> and  $\Delta\nu/\sigma$  between -2.0 and -2.3 cm<sup>-1</sup>/GPa [143, 146].

### 3.3 SOFT CLAMPED PNC NANOSTRINGS

The  $D_Q$  expression for uniform nanostrings of 2.92 can be generalized to strings with an arbitrary width corrugation, as is derived in [24]:

$$D_Q = \frac{1}{2\alpha_n\lambda + \beta_n\zeta_n^2\lambda^2}, \quad (3.4)$$

where  $n$  is the mode order,  $\alpha_n$  and  $\beta_n$  are factors which depend on the width profile of the string and on the mode shape and  $\zeta_n$  is the dimensionless mechanical frequency,  $\zeta_n^2 = \frac{\rho L^2 \Omega_n^2}{eE}$ . As seen in section 2.3.2, we recall that the dominant  $\lambda$  term in the denominator of equation 3.4 stems from the displacement field curvature close to the clamping points of the string, while the  $\lambda^2$  term originates from the curvature maxima associated with each antinode in the vibrational modeshape.

We apply soft clamping to sSi nanostrings using width corrugations, implementing a phononic crystal and opening a bandgap around an acoustic wavelength twice as long as the width modulation period [26] (as portrayed in Figure 3.12b). The width corrugation profile is illustrated schematically in Figure 3.12a and is implemented with width modulation  $w_{\max}/w_{\min} = 2$  and unit cell length  $l_{UC} = 108 \mu\text{m}$ . The transition between wide and narrow parts of the unit cell is defined by a polynomial curve extending over  $0.1 l_{UC}$ , with vanishing derivatives up to the third order at both ends.

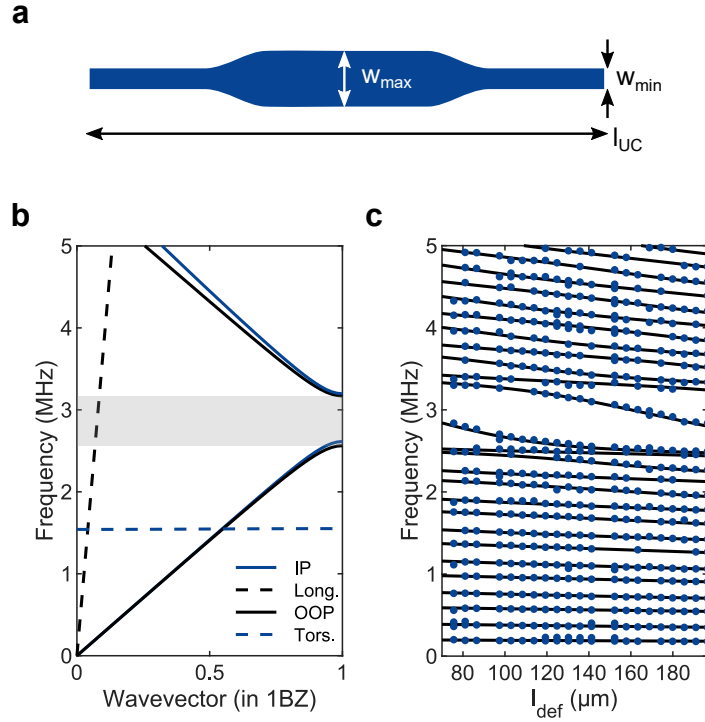


Figure 3.12: **a**, Unit cell of the width corrugation profile. **b**, Vibrational bandstructure arising from the beam width corrugation. Branches: IP—in-plane flexural, Long.—longitudinal, OOP—out-of-plane, Tors.—torsional. The OOP bandgap is highlighted in gray. **c**, OOP mode frequencies for strings with varying length of the center defect region. The length of the strings is about 1.6 mm.

The maximum acceptable width corrugation is constrained by buckling of the unit cells (described in section 3.3.1), that dramatically reduces the  $D_Q$ . A defect which perturbs the translational symmetry is introduced by stretching the length of the narrow region in the string center to  $l_{def}$ . The defect is surrounded on each side by 7 unit cells (see Figure 3.7).

We characterize the devices in an interferometric setup (described in section 3.7), and acquire thermomechanical noise spectra to find the out-of-plane (OOP) frequencies of the resonators. The resulting vibrational spectra are compiled in Figure 3.12c, displaying the OOP flexural modes of soft-clamped nanostrings with  $L \approx 1.6$  mm. To match the frequencies and the numerical predictions, we assume an initial stress in the sSi layer around 1.0 – 1.2 GPa, varying for different chips and fabrication runs. We speculate that this value, significantly lower than the stress reconstructed via TEM and Raman methods, might be attributed to the presence of a thin layer of native oxide on the exposed silicon surfaces, which lowers the effective stress in the string cross-section [95].

A bandgap manifests around 2.8 – 3.2 MHz. One or two resonances appear in the bandgap, corresponding to localized modes; their frequency responds much more sensitively to variations in  $l_{def}$  than those of distributed modes. Such a localized mode, implemented in a 6.0 mm-long nanostring, with 12 unit cells on each side of the defect ( $l_{def} \approx 2.3l_{UC} \approx 0.5$  mm), is displayed in Figure 3.13 and exhibits soft clamping, i.e. the clamping point curvature is suppressed with respect to a uniform string (see Fig-

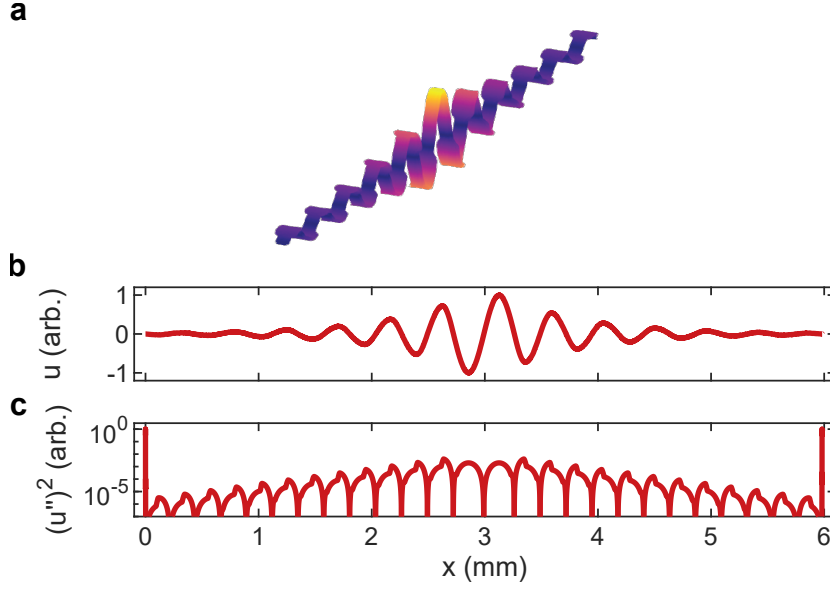


Figure 3.13: **a**, Three-dimensional vibrational pattern of a soft clamped mode localized with a PnC. The mode shape was obtained with finite element methods. **b**, Displacement field and **c**, squared curvature of the localized mode of a 6.0 mm-long nanostring, with 12 unit cells on each side of the defect.

Figure 3.13c). For the localized mode,  $\alpha_n \approx 0$  in equation 3.4, and one is left with a more favorable  $D_Q$  scaling:

$$D_Q \approx \frac{1}{\pi^2 (\Omega_m/\Omega_1)^2 \lambda^2} \propto \frac{\epsilon L^2}{h^2}, \quad (3.5)$$

where  $\Omega_m$  is the localized mode frequency and  $\Omega_1$  the fundamental mode frequency. Soft-clamped modes of high aspect ratio strings exhibit an enhanced  $D_Q$  compared to distributed modes, far from resonance with the PnC, and their  $Q$  scales inversely with the thickness  $h$ , in the common case of surface loss-limited  $Q_{\text{int}}$  [25, 26].

We experimentally characterize the  $D_Q$  enhancement resulting from soft clamping in the 6.0 mm nanostring. The measurements are performed at the base temperature of our cryostat,  $T \approx 7$  K. The PnC localizes a mechanical mode at  $\Omega_m/2\pi = 1.46$  MHz, shown in Figure 3.13. We evaluated the damping of OOP modes by resonantly exciting them and recording ringdown traces upon interruption of the drive (see Figure 3.15; more details in section 3.7). Since the laser beam increases the sample temperature and influences the reconstructed damping rates (as will be discussed in the following), we perform gated detection by periodically blocking the probe laser with a mechanical shutter. The repetition rate of the gates is much slower than thermal relaxation, which occurs at timescales below one second<sup>5</sup>.

The measured  $Q$ s are shown in Figure 3.14: modes out of the vibrational bandgap display a weak dependence on frequency, due to the  $\lambda^{-1}$  dependence seen in equation 3.4 for hard clamped modes. The mode  $n = 26$  (blue circle), localized to the defect

<sup>5</sup> The thermal relaxation time constant could be measured experimentally by observing how fast the nanostring resonant frequencies responded to rapid changes in the 1550 nm probe beam power.

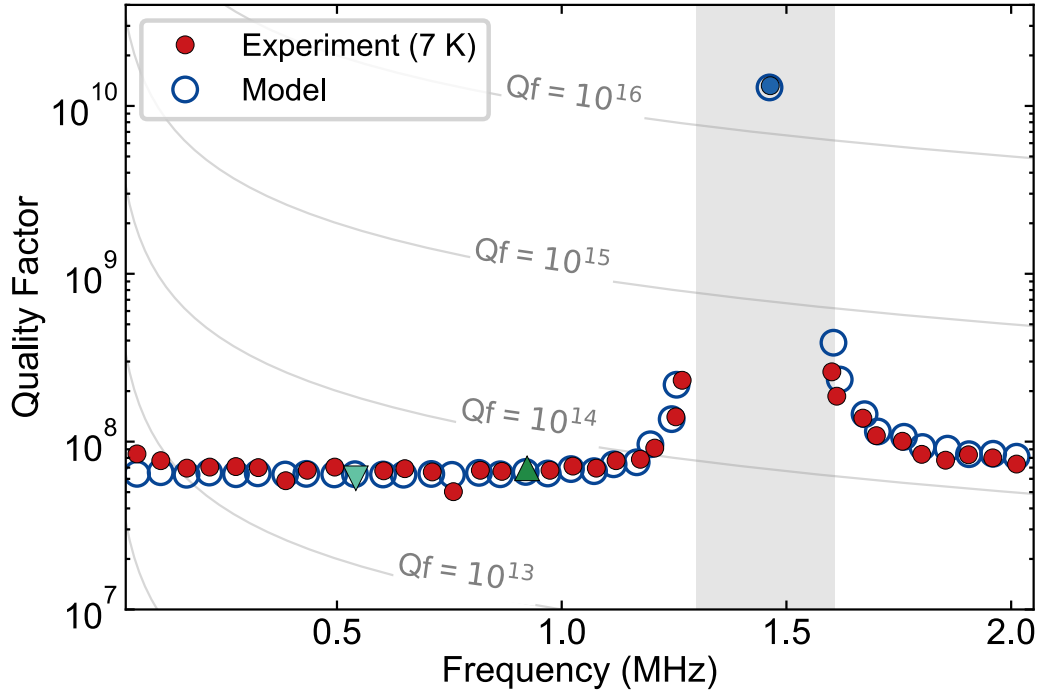


Figure 3.14: Quality factors and frequencies of the flexural modes of the 6.0 mm-long nanos-tring, characterized at 7 K. Measurement data are displayed with filled symbols, while predictions from a model supported by FEM simulations are displayed with blue empty circles. The mechanical bandgap region is shaded. The triangular and filled blue circle symbols mark modes analyzed in Figure 3.17.

region, exhibits a  $Q = (1.3 \pm 0.2) \cdot 10^{10}$ , more than two orders of magnitude beyond the  $Q$  of distributed modes. The uncertainty corresponds to a 95% confidence interval, estimated from 7 separate gated ringdowns. The observed  $Q$  enhancement from soft clamping is too large to be explained only by the suppression of the intrinsic loss produced by the bending curvature around the clamping points. In order to reliably model the experimental data, we have to assume additional dissipation in the clamping regions, which can be due to phonon radiation or mechanical losses in the  $\text{SiO}_2$  layer underneath the clamping points. We fit a model with two free parameters (open circles in Figure 3.14), the first related to the intrinsic dissipation of Si ( $Q_{\text{int}}$ ), and the second representing dissipation in the boundary regions of the string (affecting mostly the out-of-bandgap modes). In the presence of an inhomogeneous mechanical loss,  $Q$  can be written as:

$$Q = \frac{1}{1/D_Q^{\text{bound}} \cdot (1/Q_{\text{int,distr}} + 1/Q_{\text{bound}}) + 1/(D_Q^{\text{distr}} \cdot Q_{\text{int,distr}})}, \quad (3.6)$$

where  $D_Q^{\text{bound}}$  and  $D_Q^{\text{distr}}$  (the same quantities that are displayed in Figure 2.7b) are evaluated with the method summarized in section 2.3.5, with the kinetic energy integral in the numerator extending over the whole string, and the linear elastic energy integral in the denominator extending in the first case to thin regions close to the

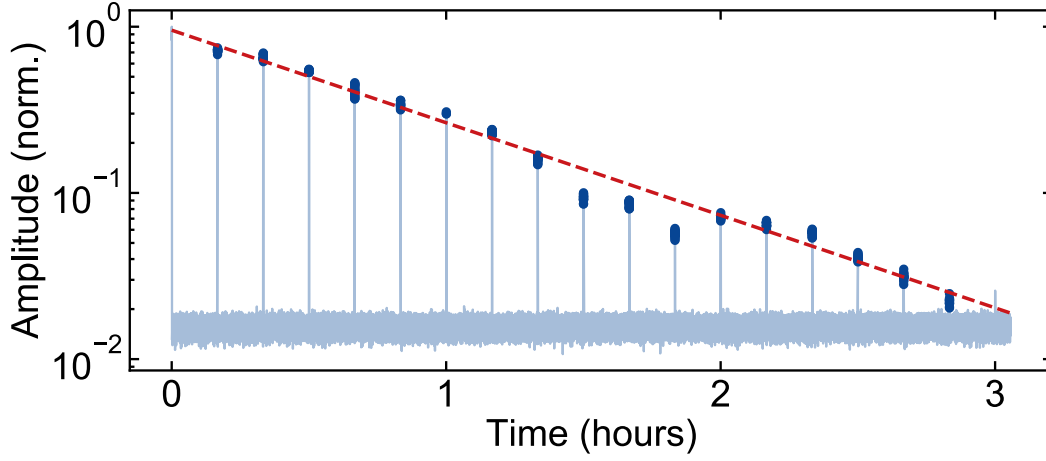


Figure 3.15: Gated ringdown of the localized mode in Figure 3.14 (filled blue circle). An exponential fit is shown with a dashed red line. The small deviation from exponential decay around 1.5 hours may be due to alignment drifts in the characterization interferometer.

boundaries, of length a few multiples of  $\lambda L$ , and in the second case to the remainder of the string. With these definitions,  $D_Q = 1 / (1/D_Q^{\text{bound}} + 1/D_Q^{\text{distr}})$ . The precise extent of the domains is unimportant, as long as  $D_Q^{\text{bound}}$  is evaluated over the whole region of large clamping curvature. We remark that phonon radiation loss would not be diluted in the same manner as intrinsic dissipation, but the fit model of 3.6 would still be valid with the identification  $D_Q^{\text{bound}} \cdot Q_{\text{bound}} \rightarrow Q_{\text{rad}}$ . In general, one would expect radiative losses to depend on eigenmode index and frequency [104], a feature that is not encountered in the data of Figure 3.14.

From the fit procedure, we obtain  $Q_{\text{int,distr}} = (8 \pm 3) \cdot 10^3$  and  $Q_{\text{bound}} = 3 \cdot 10^3$ . We take  $Q_{\text{int,distr}}$  as our estimate for the strained silicon  $Q_{\text{int}}$  at 7 K, consistent with previous observations and surface-dominated mechanical losses [95]. Its confidence interval is primarily determined by the statistical scatter in  $Q$  inferred by ringdown measurements and by the uncertainty of the string thickness.

### 3.3.1 Buckling in large corrugations

An important design constraint for PnC nanostrings is the insurgence of buckling when the width modulation is increased beyond a limit value. In practice, the occurrence of buckling provides an upper bound on the mechanical frequency of modes that can be localized with high  $Q$ , especially when the stress and, correspondingly, the speed of sound, are enhanced by width tailoring [26].

PnC nanostrings are prone to localized buckling around the transition region of the width corrugation. This effect is due to the development of compressive stress in the direction transverse to the string axis, when the string is suspended and the biaxial stress is relaxed [108]. This phenomenon is particularly relevant for very thin films, and occurs when the aspect ratio of the unit cell is decreased, i.e. for short and wide unit cells.

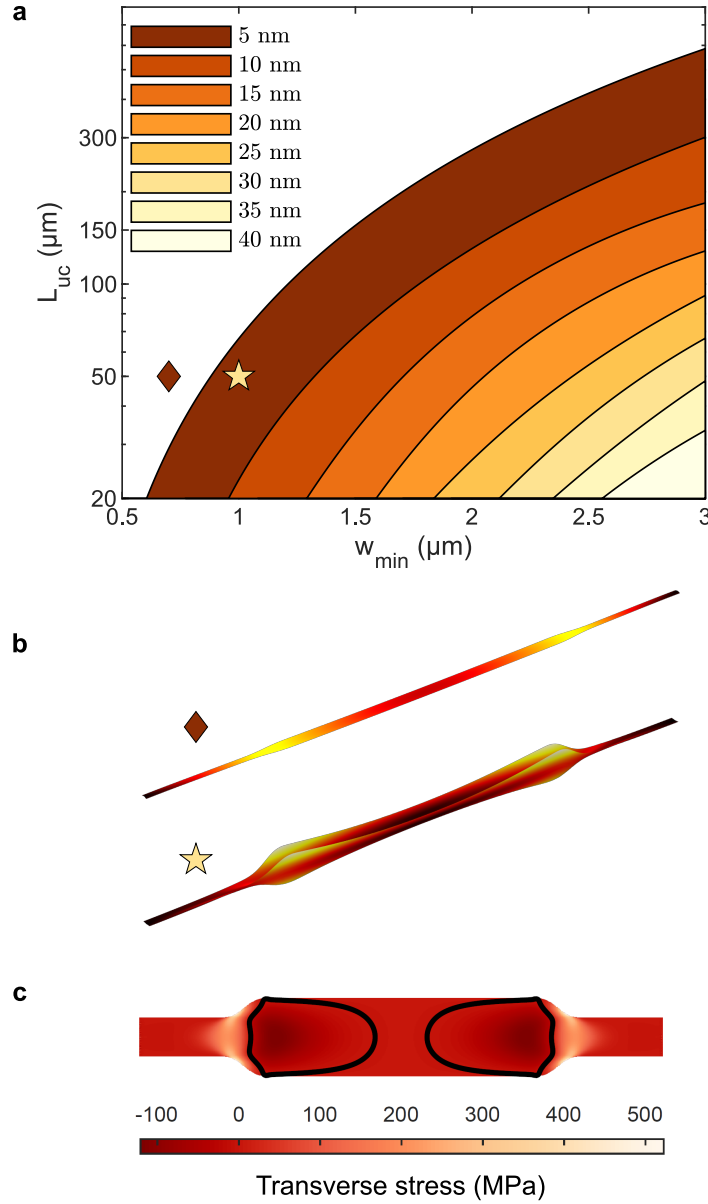


Figure 3.16: **a**, Buckling instability contours for unit cells of varying thickness and in-plane dimensions. Coloured areas mark instability regions for fixed film thickness. **b**, Post-buckling deformation for a unit cell thickness of 5 nm and in-plane dimensions marked with the corresponding symbol in **a**. **c**, Stress distribution in the transverse direction in a 20  $\mu\text{m}$ -long, 1  $\mu\text{m}$ -wide unit cell. The black lines depict the contours of zero transverse stress.

In order to design PnC strings that do not exhibit buckling, we performed a finite element simulation of a single unit cell, with periodic boundary conditions. An eigenmode analysis is carried out, and the presence of eigenfrequencies with nonzero imaginary parts is interpreted as a manifestation of static instabilities leading to buckling. The simulation is repeated for different string aspect ratios, and the results are displayed in [Figure 3.16a](#): coloured regions represent geometrical domains of instability for variable film thickness  $h$ . The area of instability regions increases as the thickness

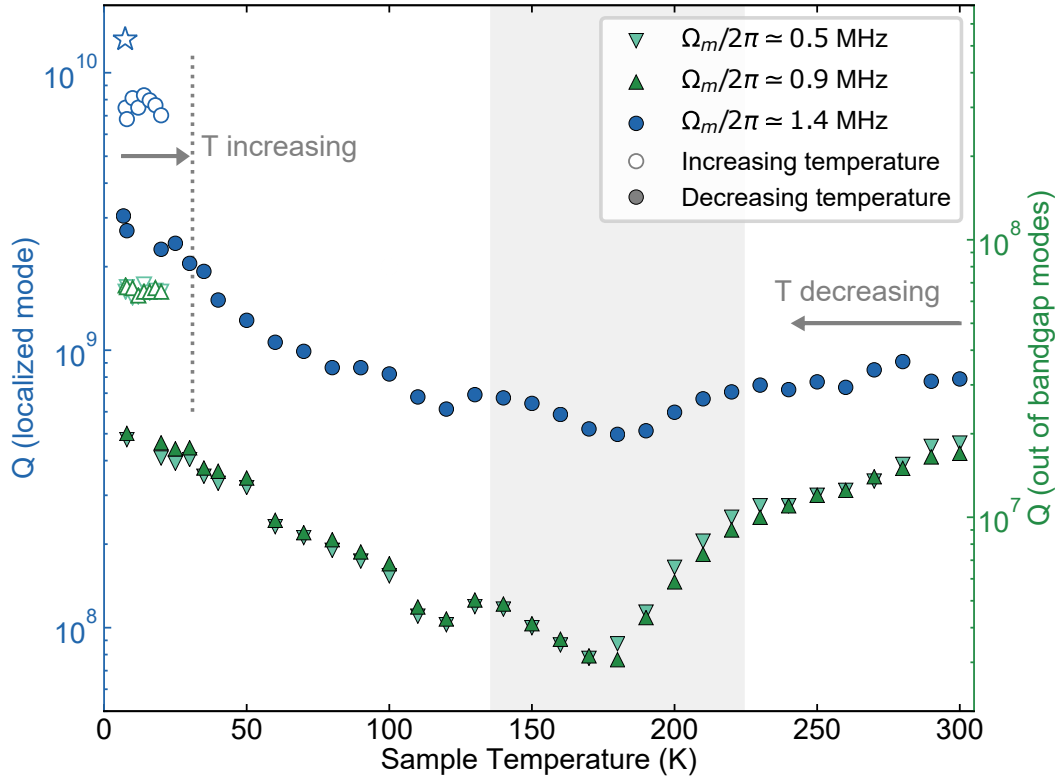


Figure 3.17: Variation of  $Q$  with temperature for different modes of a soft-clamped nanostring. Blue circles: localized mode, triangles: modes with frequencies below the mechanical bandgap. Empty symbols show measurements performed while increasing the temperature, closed symbols are measured later, as the temperature was decreased. Different axes are used for the quality factors of out-of-bandgap modes (green) and the localized mode (blue).

is decreased. The unit cells aspect ratios of all devices presented in the main text are chosen outside of the buckling region for  $h = 10$  nm. The simulation method can be validated by performing a stationary-state stress relaxation analysis with a small out-of-plane load applied to the unit cell surface, breaking the symmetry of the model: when the cell aspect ratio lies inside the coloured regions, the perturbation reveals the unstable character of the non-buckled solution and produces a visualization of the buckling mode of the unit cell (see [Figure 3.16b](#)).

### 3.4 QUALITY FACTOR TEMPERATURE DEPENDENCE

We characterize the quality factors of several modes of the 6.0 mm nanostring as the sample holder temperature is tuned with a resistive heater. We probe two modes well below the lower bandgap edge ( $\Omega_m/2\pi \sim 500, 900$  kHz) and the localized mode at  $\Omega_m/2\pi \sim 1.4$  MHz, highlighted in [Figure 3.14](#). The results are shown in [Figure 3.17](#). We initially increase the sample temperature (measured with a thin film resistive thermometer connected to the sample plate) from 7 K to 20 K (open symbols in [Figure 3.17](#)),



without significant variations of all the  $Q$ s. We then heat the sample to 300 K and step down the temperature gradually (closed symbols in Figure 3.17). While the  $Q$  of the localized mode around room temperature is partially limited by gas damping (as shown in section 3.4.1), we believe this to be negligible at low temperatures, due to lower pressures attained in cryogenic conditions ( $< 10^{-8}$  mbar).

Importantly, as the cryostat base temperature is reached again, we do not recover the initially observed  $Q$ s: the mechanical dissipation is increased by a factor of about 3. This observation corresponds to a gradual sample degradation over several days (the time required to complete the temperature-dependent measurements) while the sample was kept cold, which also explains the difference in dissipation of the measurements displayed with star and open circle symbols in Figure 3.17, where the latter points were acquired approximately four days later. This degradation was reversible: we could reproduce  $Q > 10^{10}$  multiple times after heating the chip to room temperature and cooling it back to 7 K. On the other hand, the mechanical frequencies drifted irreversibly to lower values, hinting to stress relaxation or to the growth of native oxide. This reversible increase in mechanical dissipation could be due to slow processes of condensation on the sample of the residual gases in the cold cryostat, or to gas damping induced by the rapid variation of hydrogen partial pressure around 10 K [147]. This slow degradation reversible upon thermal cycling was not observed with different samples in our research group, even though no other sample approached such high quality factors yet. It is rather common, instead, to witness a degraded mechanical dissipation just after cooling down the cryostat, which can sometimes be reverted by thermal cycling to room temperature.

The  $Q$  of all modes has a minimum (the dissipation is peaked) around 175 K to 180 K, and increases rapidly (but not monotonically) for lower temperatures. A closer examination of the relevant temperature range (Figure 3.18a) shows that the temperature of the dissipation peak varies with the mode frequency, suggesting the presence of thermally-activated defects [43, 148], with activation energy around 0.2 eV, extracted with a fit to an Arrhenius thermal relaxation model (see equations 2.100 and 2.101), shown in solid lines in Figure 3.18a. The  $Q$  degradation is smaller for the localized mode, which could indicate a weaker coupling to the defect ensemble. A secondary dissipation peak is visible for all modes, around 120 K. The absence of  $Q$  peaks around 125 K and 20 K, where the linear expansion coefficient of silicon approaches zero excludes thermoelastic damping as a relevant dissipation source, as expected from the string dimensions [149] (see also Figure 2.9).

While the  $Q$ s of the two out-of-bandgap modes differ less than 15% at any temperature, the ratio of  $Q$ s for localized and distributed modes exhibits a complex temperature dependence, shown in Figure 3.18b. Were all modes affected by the same intrinsic damping mechanisms, the ratio would depend very weakly on the temperature and approximately correspond to the dilution factor ratio,  $D_Q^{\text{loc}}/D_Q^{\text{oob}}$ , displayed by the green band in Figure 3.18b, where *loc* identifies the localized mode and *oob* the out-of-bandgap modes. The dependence of strain and string dimensions on temperature cannot explain the observed variation. As previously discussed, the PnC must therefore partially shield the localized mode from additional external loss channels, especially at cryogenic temperatures. At high temperatures, the  $D_Q$  ratio approaches the numerical prediction; the small discrepancy can be explained by the contribution of gas damping to the dissipation of the localized mode at room temperature.



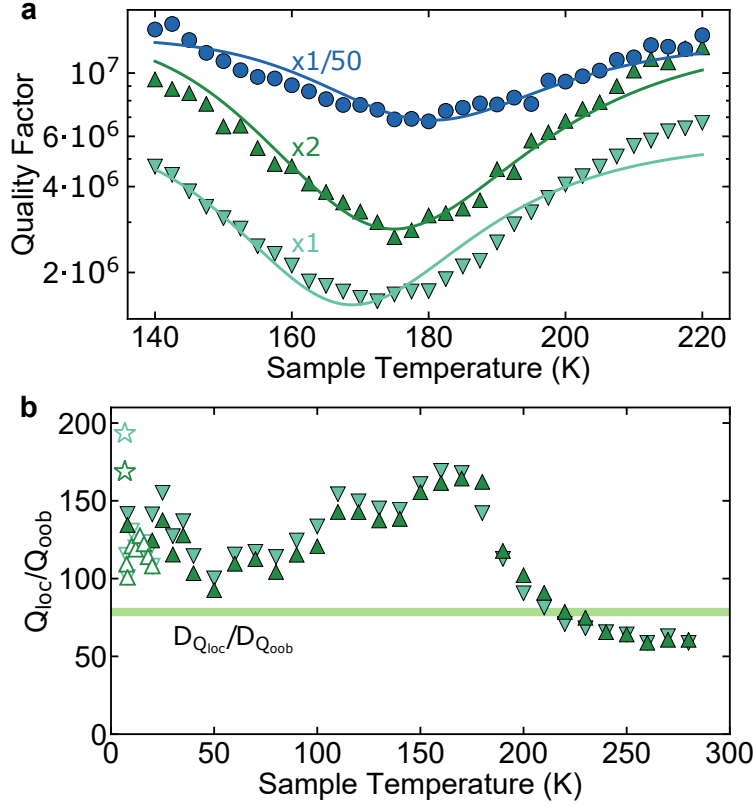


Figure 3.18: **a**, Finer temperature sweep around the region shaded in gray in Fig. 3.17, where all modes present a dissipation peak. Continuous lines portray the results of simultaneous fits to a model of a thermally-activated defect (equations 2.100 and 2.101). Scaling factors are applied to different series in order to display them on the same axis. **b**, Ratio of Qs between the localized mode and the two out-of-bandgap modes, displayed with the same symbols as in Fig. 3.17. The horizontal band displays an interval for the ratio of  $D_{Qs}$  obtained with a finite element simulation. **b**

#### 3.4.1 Gas damping of the localized mode at room temperature

As mentioned in the previous section, at temperatures  $T \sim 300$  K, we observed a relevant contribution of gas damping in limiting the quality factor of the localized mode. As discussed in section 2.3.6.5, the nanostring dissipates its kinetic energy through random collisions with residual gas molecules in the vacuum chamber. At room temperature, the lowest attainable pressure in the vacuum chamber was around  $p = 2.2 \times 10^{-7}$  mbar, where we can estimate  $Q_{\text{gas}} \approx 1.0 \cdot 10^9$  from equation 2.123. At this pressure, we measured  $Q = 0.67 \cdot 10^9$  and therefore concluded our  $Q$  was partially influenced by gas damping. We proceeded to measure the quality factor as a function of pressure in the chamber and then used a fit of form

$$Q = \frac{1}{1/Q_{\text{beam}} + 1/Q_{\text{gas}}} \quad (3.7)$$

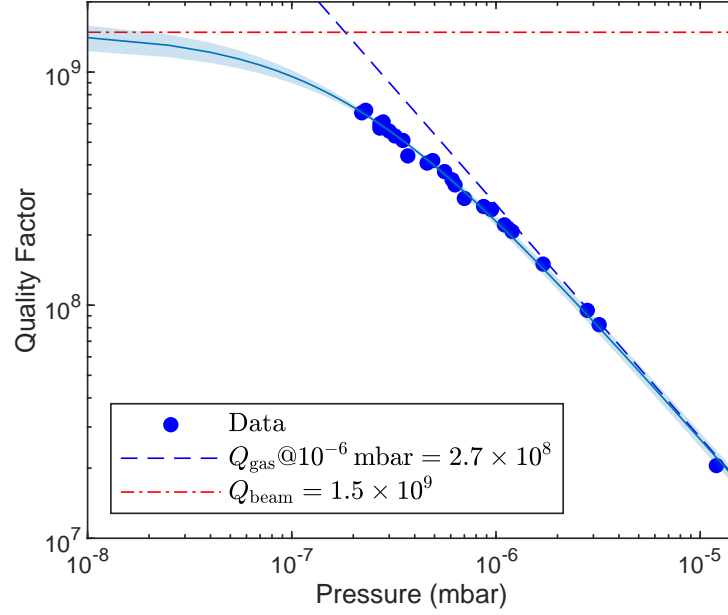


Figure 3.19: Quality factor of the localized mode at room temperature, as a function of pressure. Solid line shows fit as described in the text, with 95% confidence intervals shown by the shaded area.

to extract the quality factor of the beam in the absence of gas damping,  $Q_{\text{beam}}$  (see Figure 3.19).

At lower temperatures, the contribution of the gas damping rate was found to be negligible, due to significant cryopumping in the vacuum chamber (see section 3.7.1).

### 3.5 QUALITY FACTORS OF ADDITIONAL SAMPLES

In addition to the PnC device that we described in the previous sections, we fabricated multiple chips with 6.0 mm-long strings, each containing 25 samples with a variable number of unit cells. A large variance of quality factors was observed, indicating probable contamination issues arising from the fabrication process. For example, on the same chip containing the string analyzed in Figure 3.14, we characterized about 10 released nanostrings supporting soft-clamped modes (a 40% yield of devices that survived the last release step). The quality factors at room temperature ranged from  $> 10^8$  for 3 devices, to low enough that the linewidth could be resolved on our spectrum analyzer ( $Q < 10^6$ ). On a similar chip, we observed a second string with the same design as the one presented in the main text and comparable mechanical parameters:  $\Omega_m/2\pi = 1.45$  MHz and  $Q \approx 6.4 \cdot 10^8$  at room temperature (limited by gas damping, as discussed in the previous section), and  $\approx 6.3 \cdot 10^9$  at 6.7 K.

We additionally fabricated 6.0 mm-long strain engineered samples [26], with a width tapering ratio of 3/1 between anchoring points and central defect, supporting a mode at 1.0 MHz localized by 9 unit cells on each side of the defect. This particular set of nanostrings appeared, however, to be affected by contamination-induced mechanical dissipation, much larger than the intrinsic loss in strained silicon, and we could not identify any sample with a quality factor on par with the simpler PnC strings. Due

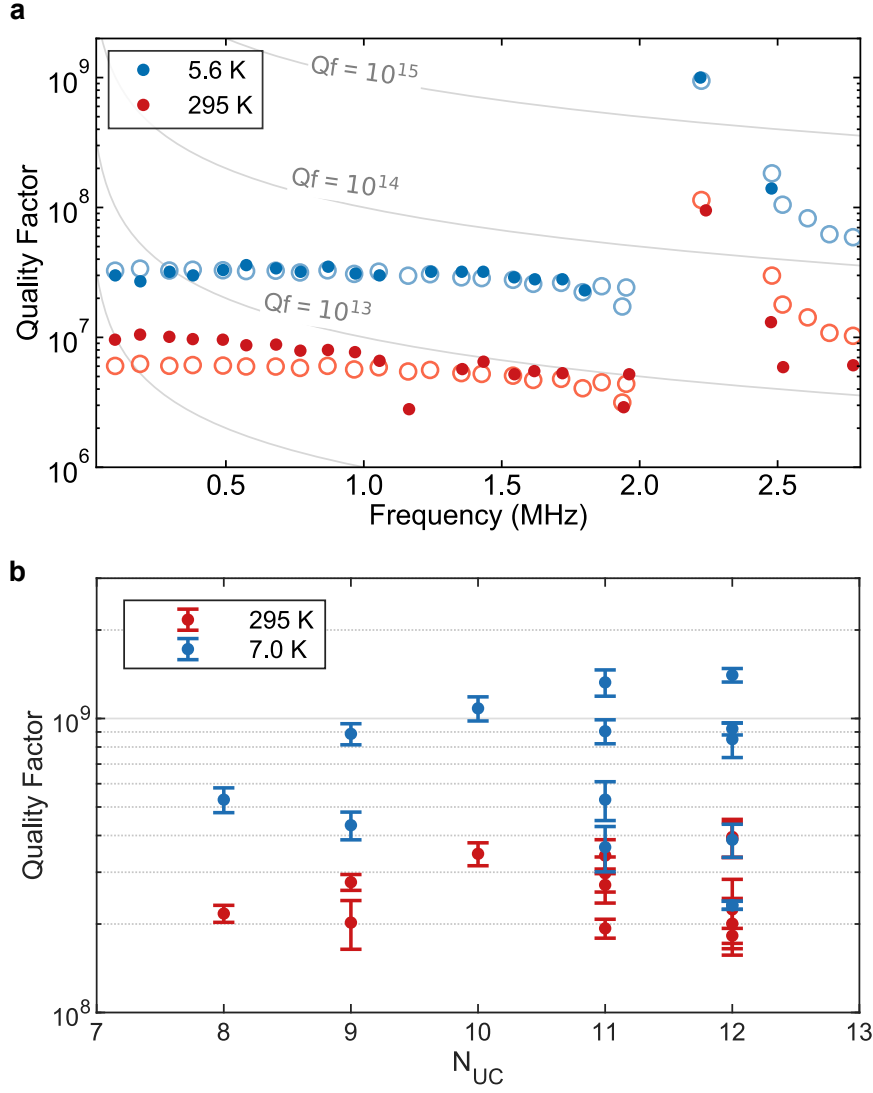


Figure 3.20: **a**, Quality factors of flexural mechanical resonances of a 3.2 mm-long PnC string with 10 unit cells per side. Open circles represent a numerical model accounting for dissipation dilution via FEM. **b**, Quality factor versus number of unit cells per side of the defect, for a set of 4.2 mm-long strings. The devices were characterized at room temperature and at the cryostat base temperature; different temperatures are distinguished by the colors of the dots. Error bars represent 95% confidence intervals on  $Q$ , estimated from 5 repeated measurements.

to the large scatter of mechanical  $Q$ , on this chip, we do not believe this reduced performance to be due to design flaws.

Shorter devices exhibited generally a higher dissipation, as expected from the soft clamping scaling. In Figure 3.20a, we present a measurement of the quality factors for multiple mechanical modes of a 3.2 mm-long PnC string, analogous to Figure 3.14, with 10 unit cells on each side of the defect. The characterization was repeated at room temperature and at 5.6 K, and the data was fitted with the  $D_Q$  computed by finite elements simulation. For the cryogenic measurement, as in Figure 3.14, an additional boundary loss contribution was included to improve the agreement of model and data,

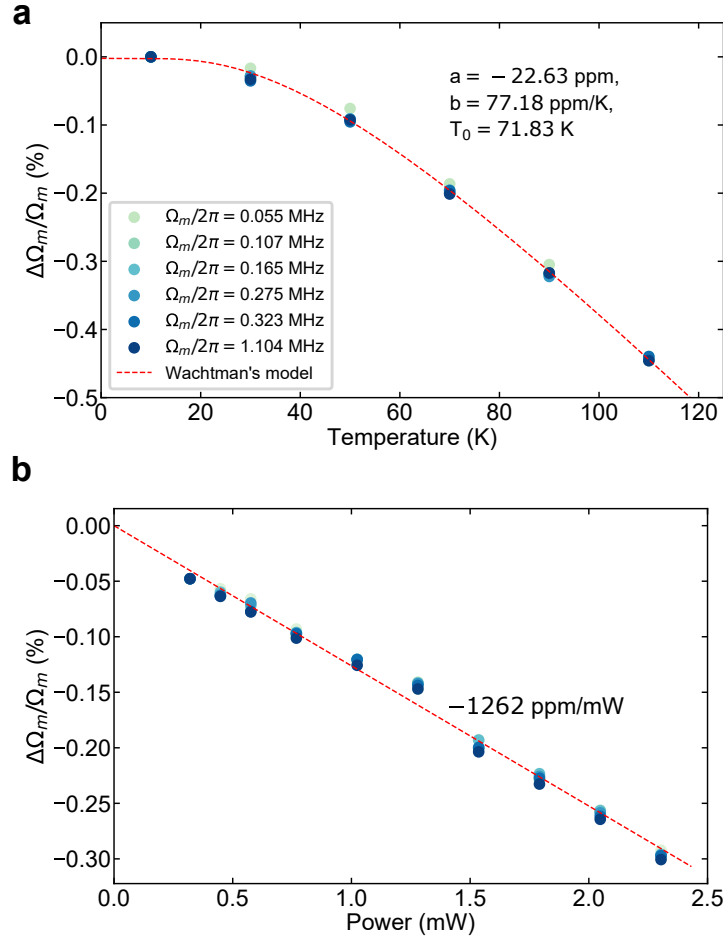


Figure 3.21: **a**, Relative variation of resonance frequencies of multiple modes with the heater temperature, referred to the maximum measured frequency. The red dashed line is a fit to the curve  $a - b\text{Temp}(-T_0/T)$  [150]. **b**, Relative variation as a function of the impinging optical power, at  $T = 10$  K. The red dashed line is a linear fit.

allowing the inference of  $Q_{\text{int}} \approx 1.4 \cdot 10^3$ , significantly lower than for the 6 mm device ( $Q_{\text{int}} = (8 \pm 3) \cdot 10^3$ ).

A batch of 4.2 mm-long PnC strings showed a good yield of devices with high- $Q$  localized modes, with quality factors between  $10^8$  and  $4 \cdot 10^8$  at room temperature (11 strings out of the 25 originally patterned on the chip). However, the improvement at liquid Helium temperatures was lower than for previously-discussed devices, suggesting a different dominant dissipation mechanism. The number of unit cells was varied for these samples as well; by keeping the overall string length constant, we could localize mechanical modes between 1.3 MHz to 2.1 MHz. No strong correlation between the number of unit cells and the  $Q$  of the localized mode was observed, as displayed in Figure 3.20b: likely acoustic radiation is an irrelevant loss mechanism for these strings.

## 3.6 OPTICAL HEATING

With all the characterized strained silicon nanostrings, we noticed significant heating effects, which manifested in marked resonant frequency shifts when the power of the 1550 nm optical probe used for characterization was varied. This is not surprising: despite the lack of direct optical absorption from silicon at 1550 nm, a small heating from defect states and surface adsorbates, or two-photon absorption, can result in a significant temperature increase due to the poor thermal conductance of the high-aspect-ratio nanostrings. We attempted to elucidate the origin of optical heating by acquiring spectra at variable powers and temperatures, using the same sample of Figure 3.14 and Figure 3.17.

The eigenfrequencies of the nanostrings can be computed with a perturbative approach [151], starting from the solutions  $u$  of the Euler-Bernoulli equation (generalizing equation 2.91 for a variable string cross section):

$$\frac{d^2}{dx^2} \left( EI(x) \frac{d^2 u}{dx^2} \right) - \mathcal{T} \frac{d^2 u}{dx^2} + \rho_l(x) \frac{d^2 u}{dt^2} = 0, \quad (3.8)$$

where  $u$  is the displacement pattern of flexural modes,  $I(x) = w(x)h^3/12$  is the bending stiffness,  $w(x)$  is the nanobeam width,  $\mathcal{T}$  is the static tension force (constant along the nanobeam profile),  $\rho_l = \rho w(x)h$  is the linear mass density,  $\rho$  is the volume density of silicon, and  $x$  is the string longitudinal coordinate, running from 0 to  $L$ .

The equation can be rewritten in terms of a normalized coordinate  $s = x/L$ , running from 0 to 1:

$$\lambda^2 \sigma_{\text{avg}} \frac{d^2}{ds^2} \left( \epsilon(s) v(s) \frac{d^2 u}{ds^2} \right) - \sigma_{\text{avg}} \frac{d^2 u}{ds^2} + \rho(s) v(s) L^2 \frac{d^2 u}{dt^2} = 0, \quad (3.9)$$

where  $\sigma_{\text{avg}} = \mathcal{T}/(w_0 h)$  is the stress along  $x$  averaged over the nanostring,  $w_0 = \frac{1}{L} \int_0^L w(x) dx$  is the average string width,  $v(s) = w(s)/w_0$  is a normalized width profile, and a potential position dependence was made explicit in the density and Young's modulus,  $\rho = \rho(s)$  and  $E = E_0 \cdot \epsilon(s)$ .  $\lambda = \sqrt{\frac{E_0}{12 \sigma_{\text{avg}}}} \frac{h}{L}$  is the usual strain parameter.

Following a procedure analogous to the mode expansion of section 2.1.3, we can separate  $u$  in a product of space- and time- dependent parts,  $u(s, t) = U(s) \cdot q(t)$ , and write a harmonic oscillator equation for  $q$  by multiplying the previous equation by  $U(s)$  and integrating over  $s$ , using the clamped boundary conditions  $U(0) = U(1) = 0$  and  $U'(0) = U'(1) = 0$ . The spring constant  $k$  of the oscillator is subdivided in two series components,  $k^{(\text{lin})}$ , associated with the bending stiffness, and  $k^{(\text{nl})}$ , related to the tension in the string. The spring constant and effective mass  $m_{\text{eff}}$  of the oscillator are:

$$k^{(\text{lin})} = \frac{\lambda^2 \sigma_{\text{avg}} w_0 h}{L} \int_0^1 \epsilon(s) v(s) (U''(s))^2 ds \quad (3.10)$$

$$k^{(\text{nl})} = \frac{\sigma_{\text{avg}} w_0 h}{L} \int_0^1 (U'(s))^2 ds \quad (3.11)$$

$$m_{\text{eff}} = h w_0 L \int_0^1 \rho(s) v(s) U^2(s) ds \quad (3.12)$$

$$(3.13)$$

Since  $\lambda \ll 1$  for high aspect ratio strings under tension, we can neglect  $k^{(\text{lin})}$  in the following steps. Eigenfrequencies are obtained as  $\Omega_m \approx \sqrt{k^{(\text{nl})}/m_{\text{eff}}}$ .

We consider now the effect of a small variation in the physical properties of the string due to a non-uniform temperature profile  $\theta(s)$  [152]. Small relative variations in  $\Omega_m$  are given by:

$$\frac{\Delta\Omega_m}{\Omega_m} \approx \frac{\Delta k^{(\text{nl})}}{2k^{(\text{nl})}} - \frac{\Delta m_{\text{eff}}}{2m_{\text{eff}}} = \frac{\Delta\sigma_{\text{avg}}}{2\sigma_{\text{avg}}} - \frac{\Delta L}{L} - \frac{\int_0^1 \Delta\rho(\theta(s))v(s)U^2(s)ds}{2 \cdot \int_0^1 \rho(s)v(s)U^2(s)ds} \quad (3.14)$$

Note that an explicit dependence on the mode profile  $U(s)$  is retained only through the variation of mass density (generally due to thermal expansion).

Using equation 3.14, we interpret now the variation of resonant frequencies of a 6 mm-long PnC nanostring with temperature, obtained by resolving thermomechanical peaks with a spectrum analyzer. We monitor the 5 lowest-order flexural resonances of the nanostring and a higher order mode with  $\Omega_m/2\pi \approx 1.1$  MHz. The temperature was tuned from 10 K to 110 K with a resistive heater fixed on the cryogenic mount. We notice in Figure 3.21a that the relative frequencies decrease at a rate around  $-77$  ppm/K beyond  $\sim 40$  K, and saturate at lower temperatures. The trend is similar to the predicted variation of Young's modulus at low temperatures [149, 150], but it could also indicate a poor thermalization of the string to the sample plate at the lowest temperatures. Moreover, the magnitude of  $\Delta\Omega_m/\Omega_m$  is more than one order of magnitude larger than the thermal expansion coefficient and has the opposite sign; hence we conclude that the stress variation (due to the change of Young's modulus or thermal strain) is the dominant effect in equation 3.14 in our temperature range. The presence of native oxide on the exposed surfaces of the string, however, may also influence the observed variation.

Absorption of 1550 nm light has a similar effect on the string resonances, that drift towards lower frequencies as the optical power is increased. This effect is displayed in Figure 3.21b, where the sample mount temperature is kept at 10 K and power is measured at the microscope objective output. Note that in Figure 3.21a, we accounted for the power dependence by recording at each temperature the value of the resonant frequencies as the optical power was varied, and extrapolating to vanishing power. As before, we do not observe any modeshape dependence of the relative frequency variation, suggesting that the last term in equation 3.14 does not relevantly contribute. The temperature profile in the nanostring is now expected to be strongly peaked at the laser position, due to strong variation of the conductivity with temperature.

We conclude therefore that absorption of 1550 nm light, through two-photon processes or defect states, significantly heats up the Si nanostring. However,  $\Delta\Omega_m/\Omega_m$  in Figure 3.21a and b cannot be directly compared to infer the absorption-induced heating. When optical power is absorbed locally, a large temperature difference is established between the string and the substrate chip, probably leading to stronger variations of  $\sigma_{\text{avg}}$  compared to the case of a uniform string and substrate temperature. In fact, stress is often observed to depend on temperature through thermal expansion mismatch between the device and substrate materials [134].

When the laser power is stepped or the shutter is opened, resonant frequencies are observed to relax at characteristic times below 1 s. This justifies the use of the gated

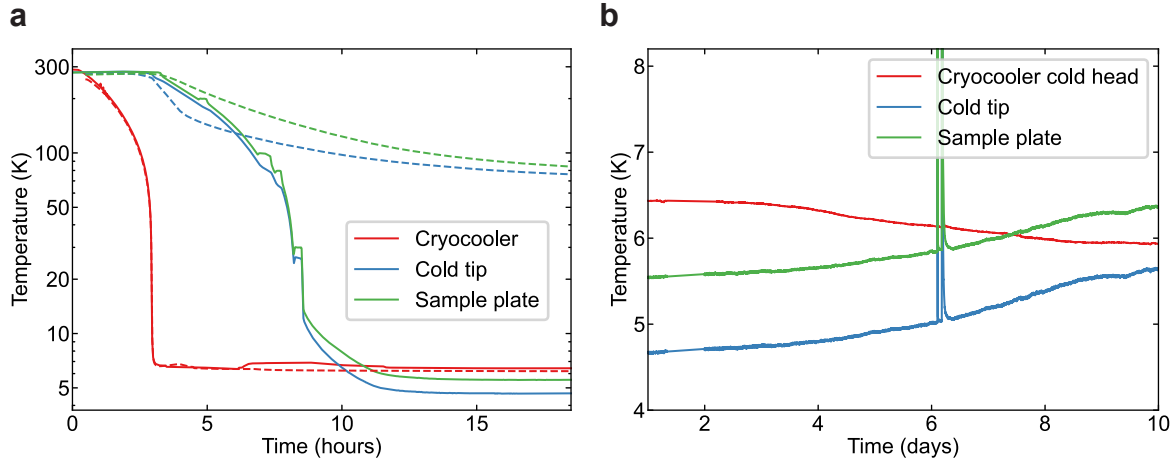


Figure 3.22: **a**, Temperature probe records at various locations in the cryostat during a cooldown. The full lines correspond to a successful cooldown, while dashed lines display temperature records acquired during a run when the He capillary clogged and the chamber could not reach base temperature. **b**, Long-term drift of the base temperature during the 10 days following the successful cooldown in **a**.

ringdown technique to characterize mechanical damping, and the assumption that the string temperature is close to the temperature of the cryostat.

### 3.7 CHARACTERIZATION METHODS

In this part of the chapter, I take a brief digression to delve into details about the experimental methods used to characterize the sSi devices. Specifically, I will describe the Helium cryostat where the measurements are carried out, the optical interferometer that allows a sensitive displacement detection of the mechanical resonators, how to calibrate trajectories in displacement units and how to acquire ringdown measurements in order to extract the devices dissipation properties.

#### 3.7.1 Low-vibration cryostat

In order to observe ultralow dissipation in strained silicon resonators, operation at cryogenic temperatures around the liquefaction point of Helium was essential ( $T \approx 5 - 10$  K). Many physics experiments, from superfluidity to quantum optomechanics, can only be conducted at such temperatures, where thermal excitations are drastically reduced. In optomechanics, it is frequently required to reduce the enormous thermal occupation and thermal decoherence rates affecting mechanical resonators at room temperature, in order to observe minute radiation pressure effects leading to quantum correlations. When working with high-Q mechanical resonators, moreover, gas damping represents often a major source of dissipation, as described in section 2.3.6.5. Cryogenic cooling offers the possibility of reducing this damping source, since residual gas species will freeze on the walls of the cryostat chamber (with the exception of He



and  $H_2$  in trace amounts) and the pressure will be significantly reduced. This effect is sometimes called ‘cryopumping’.

In our laboratory, a closed-cycle He cryostat by ColdEdge ([coldedge.tech.com](http://coldedge.tech.com)) was designed and commissioned by Sergey Fedorov and Nils Engelsen. It allows continuous operation around 5–7 K at vacuum pressures  $P < 5 \times 10^{-9}$  mbar (the upper bound is provided by a pressure gauge mounted tens of centimeters away from the cold head). The first stage of cooling is provided by a Grifford-McMahon cryocooler (manufactured by Sumitomo) extracting heat by cycling compression and expansion of Helium, by means of a compressor. Closed-cycle cryocoolers are experimentally convenient, as they recuperate their working fluid and do not require periodic refilling. On the other hand, their pulsed operation notoriously generates substantial vibrations (with a repetition rate  $\sim 1$  Hz). These perturbations can disrupt the operation of optical interferometers located in the vicinity, and excite mechanical resonators in optomechanics experiments [153, 154]. In our cryostat, this limitation is overcome with two layers of mechanical isolation. The second stage of cooling is in fact implemented by circulating He gas in a separate circuit, where it is initially cooled by exchanging heat with the cryocooler. Mechanical isolation is obtained by avoiding direct contact: heat is transmitted through a gap filled with buffer He gas. The Helium gas line is embedded in a flexible connector that routes it to the vacuum chamber, thus providing another stage of mechanical isolation. The flexible connector is commercialized as ‘Stinger’ by ColdEdge. Moreover, the cryocooler is located in an acoustic enclosure, whose walls are padded with acoustic foam.

Finally, He gas passes through a thin capillary and undergoes Joule-Thomson expansion<sup>6</sup> at the cold tip, in contact with the experimental assembly, further dropping the temperature from  $\approx 7$  to 5 K. The cooldown requires overall slightly more than 12 hours from the moment the cryocooler is started, as is shown by the temperature logs in Figure 3.22a. The base temperature can be maintained for several weeks, during which it slowly raises of a few Kelvins (see Fig. 3.22b). This behaviour is attributed to gradual ‘clogging’ of the capillary where Helium is circulated, and can be reverted by cycling all the cryostat stages to room temperature.

### 3.7.2 Optical interferometer

Mechanical motion can be measured very sensitively in an optical interferometer, with spectral imprecision levels typically on the order of  $\sim 10 \text{ fm Hz}^{-1/2}$  for a few milliwatts of optical power impinging on the resonator. The measurement apparatus is typically a heterodyne or homodyne interferometer, where a signal beam reflected from the microresonator is combined on a beam splitter with a local oscillator with or without a frequency offset. When the measurement background is dominated by shot noise of the light field and the contribution of less fundamental noise channels, such as electronic noise of the photodetector or further in the measurement chain, is negligible, the imprecision level in displacement units (i.e., the displacement sensitivity) can be estimated by:

<sup>6</sup> The cooling or heating of a non-ideal gas (finite thermal expansion coefficient) as it expands irreversibly by flowing through a small orifice.



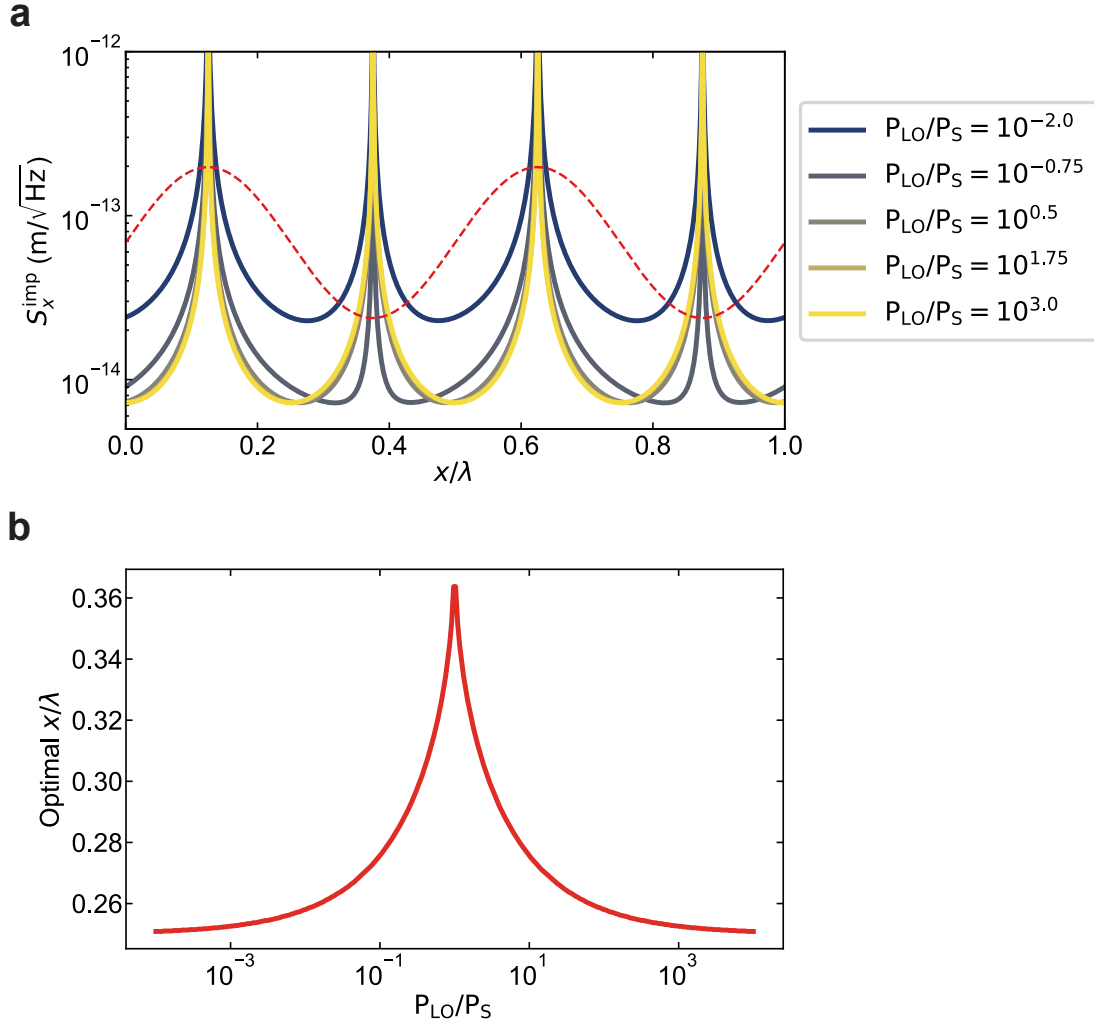


Figure 3.23: **a**, Displacement sensitivity of a Mach-Zehnder interferometer as a function of the position of the mechanical resonator. Full lines with different colors indicate different power ratios between the signal and local oscillator fields. The dashed red curve shows the interference fringes corresponding to the mechanical resonator position. For the calculation, the signal beam power is kept fixed to  $100\text{ }\mu\text{W}$  and the LO power is varied between  $1\text{ }\mu\text{W}$  and  $100\text{ mW}$ . A detection efficiency  $\eta = 0.1$  is assumed. **b**, Optimal position of the resonator to minimize the displacement imprecision, as a function of the ratio of powers between the two fields.

$$S_x^{\text{imp}} = \frac{2\Phi}{(d\Phi/dx)^2}, \quad (3.15)$$

where  $\Phi$  represents the photon flux impinging on the photodetector. Consider a homodyne Michelson or Mach-Zehnder interferometer, that is path-stabilized so that the phase relation between the two interfering fields is fixed. The electromagnetic field that interacts with (reflects on) the mechanical resonator and carries displacement information is usually called ‘signal’ field, and the other field, typically much more intense, is called ‘local oscillator’. Suppose they respectively carry optical powers  $P_s$  and  $P_{\text{LO}} = P_s/p$ . I assume that the phase difference between the two branches is simply

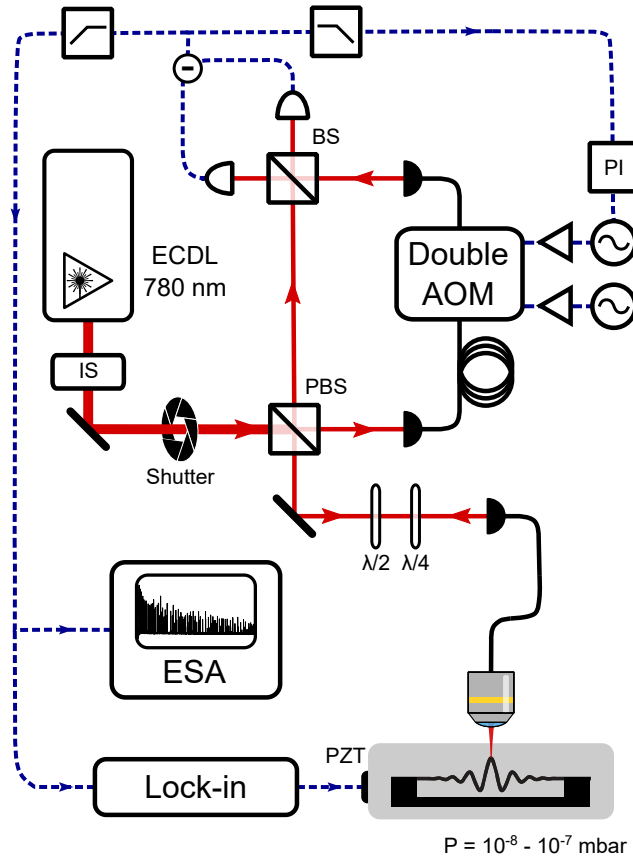


Figure 3.24: Simplified scheme of the mechanical characterization setup. ECDL: external cavity diode laser. IS: intensity stabilizer. PBS: polarizing beam splitter. BS: 50 – 50 beam splitter. AOM: acousto-optic modulator.  $\lambda/2$  and  $\lambda/4$ : half-wave and quarter-wave plate. PI: proportional-integral feedback controller. PZT: piezoelectric actuator. ESA: electrical spectrum analyzer.

$2kx$  (with  $k$  the wavevector of the light in vacuum), that is the one accumulated by reflection upon a moving mirror.

It is easy to compute the interference fringes, as a function of the displacement  $x$ , after the combiner beam splitter:

$$P_d = \frac{P_s + P_{LO}}{2} + \sqrt{P_s P_{LO}} \cdot \sin(2kx), \quad (3.16)$$

which let us express the shot-noise dominated imprecision level in homodyne detection, by using equation 3.15 [155]:

$$S_x^{\text{imp}} = \frac{\hbar c \lambda}{4\pi\eta P} \frac{1 + p + 2\sqrt{p} \cdot \sin(2kx)}{2p \cdot \cos^2(2kx)}, \quad (3.17)$$

where  $c$  is the speed of light,  $\lambda$  is the optical wavelength of the interferometer, and I have identified  $P = P_{LO}$  for brevity. A factor  $\eta < 1$  takes into account the imperfect detection efficiency (optical losses, quantum efficiency of the detector). As expected, the imprecision scales inversely with optical power [156], and it can reach extremely low

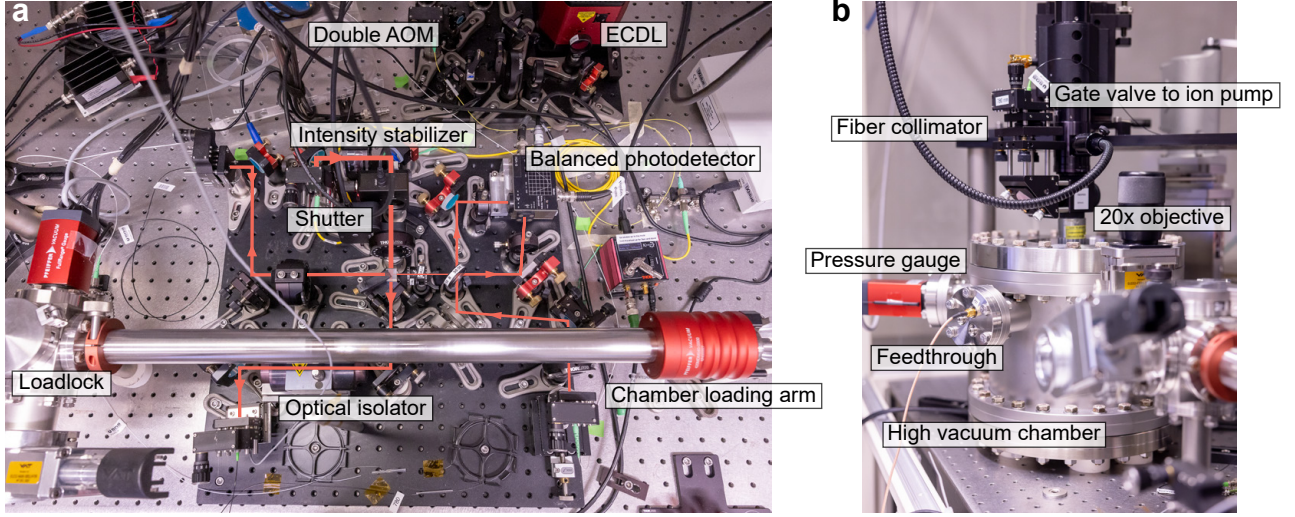


Figure 3.25: **a**, Photograph of the interferometric setup sketched in Figure 3.24, with the main elements labeled. **b**, Photograph of the vacuum chamber and of the optics that focus the signal beam on the device under test in the chamber.

values with intense optical fields injected in the interferometer, even without an optical cavity [157]. Moreover, equation 3.17 reveals that the displacement sensitivity varies according to the phase difference between the two interfering fields, as expected (see Figure 3.23a): when the average displacement is such that the interference is perfectly destructive or constructive, the interferometer does not provide any displacement sensitivity to first order in the displacement amplitude. The optimal quadrature angle for the lowest displacement imprecision depends on the ratio between the two field powers, as shown in Fig. 3.23b. When the LO power is much smaller or much larger than the signal power, the optimum sensitivity occurs at  $\chi = \lambda/4$  (fields in quadrature), but when the two powers are comparable, the optimum moves towards destructive interference, reaching  $\chi = 3\lambda/8$  for  $P_{LO} \approx P_s$ .

The sensitivity achieved in an optical interferometer is more than sufficient to resolve the thermomechanical motion of nanomechanical oscillators around resonance. From the shot noise-limited imprecision in equation 3.17 and the fluctuation-dissipation relation equation 2.75, we can compute the maximum signal-to-noise ratio (SNR) of the thermomechanical peak over the detection background:

$$\text{SNR} = \frac{S_x^{\text{th}}(\Omega_m)}{S_x^{\text{imp,min}}} \approx \frac{16\pi k_B T \eta P_s}{m_{\text{eff}}} \frac{Q}{\hbar c \lambda \Omega_m^3} \quad (3.18)$$

For example, a mechanical mode characterized by  $m_{\text{eff}} = 10 \text{ ng}$ ,  $\Omega_m = 2\pi \cdot 1 \text{ MHz}$  and  $Q = 10^5$ , analyzed with a signal beam power of  $P_s = 1 \text{ mW}$  and a detection efficiency of  $\eta = 0.1$  is resolved with  $\text{SNR} \approx 45 \text{ dB}$  at the resonant frequency. Equation 3.18 also reflects a strong frequency dependence, that makes it challenging to resolve thermomechanical noise beyond  $\sim 10 \text{ MHz}$  with a simple interferometer. In practice, it is feasible to achieve the SNR limit of 3.18 within a range of optical powers, but the observed SNR can be degraded by the photodetector electronic noise, laser noises or electromagnetic interference around the apparatus.

In our laboratory, we built several homodyne interferometers for basic mechanical characterization, with minor technical differences. The one used for the measurement of sSi devices employs a wavelength of 1550 nm, where the linear absorption of silicon is negligible. Here, however, I will describe the 780 nm apparatus that we use most frequently for rapidly characterizing mechanical resonators, as it is the most practical one among the various implementations we constructed over the years. sSi nanostrings could only be characterized with very low incident power in that interferometer, as the combination of optical absorption and low thermal conductance usually leads to a rapid temperature increase and sample destruction. The apparatus implements a balanced Mach-Zehnder homodyne interferometer (see Fig. 3.24), where 10 mW to 20 mW of light at  $\sim 780$  nm from an external cavity diode laser (New Focus) are injected. Low-frequency amplitude fluctuations are suppressed with an liquid crystal intensity stabilizer (Thorlabs LCC3112H/M) at the interferometer input, before the light is split into a signal and a local oscillator path with a polarizing beam splitter. In the signal arm of the interferometer, the light beam is focused through a microscope objective with  $20\times$  magnification on the sample under examination, and a small fraction (0.1 – 10%) of the impinging optical power is collected in reflection and steered on a beam splitter where it interferes with a stronger local oscillator beam ( $P_{LO} \approx 1$  mW to 5 mW). In order to observe any displacement signal, the spatial and angular overlap, as well as the light polarization, of the local oscillator and the signal beam need to be closely matched. It is useful to monitor the fringe visibility during alignment, by adding a small frequency offset between the signal and local oscillator beams with the pair of acousto-optic modulators, and compare it with the theoretical visibility  $\mathcal{V}_{\max}$  from equation 3.16:

$$\mathcal{V} = \frac{P_{\max} - P_{\min}}{P_{LO} + P_s}$$

$$\mathcal{V}_{\max} = \frac{2\sqrt{P_{LO}P_s}}{P_{LO} + P_s} \quad (3.19)$$

Any mismatch in the polarization, alignment and optical mode shape (in amplitude and spatial phase profile) will degrade the observed visibility from  $\mathcal{V}_{\max}$ <sup>7</sup>. For this purpose, before overlapping the beams on the beam splitter, it is useful to inject them in single-mode fibers that provide spatial filtering (as can be seen in the photograph in Figure 3.25a). The optical paths from the free-space collimators at the fiber outputs and the beam splitter should be roughly equidistant, in order to match the Gaussian beams divergence. A good target for the measured visibility is  $> 90\%$  of the one predicted from the beam powers.

After the beams are overlapped, they are directed to the two detectors in a balanced photodiode pair, where photocurrents proportional to the impinging powers are generated, and their difference is converted to a voltage with an integrated transimpedance amplifier. Balanced detection has several advantages:

- The dynamic range is increased with respect to a single detector, as the subtraction of the DC signal avoids amplifier saturation.

<sup>7</sup> For our laser sources, usually the coherence length is much larger than the difference in propagation lengths. In case this condition is violated by using a large-linewidth laser source,  $\mathcal{V}$  could be further degraded.

- Laser amplitude fluctuations are common-mode: they subtract at the photodetector, and are strongly suppressed.
- Laser phase fluctuations can only get completely suppressed if the optical path lengths of the two beams between the splitting and recombination points are perfectly matched. Different frequency components of the fluctuations, in fact, accumulate different phases for a given delay in the arrival time, giving an incomplete cancellation when the photocurrents are subtracted. If we indicate the laser phase noise spectrum with  $S_{\Theta}(\omega)$ , it can be shown that the resulting noise in the voltage photodetection spectrum will be approximately proportional to [158]:

$$S_V \propto S_{\Theta}(\omega) \cdot \sin^2\left(\frac{\omega\tau}{2}\right), \quad (3.20)$$

(in the limit of a length imbalance much shorter than the laser coherence length), where  $\tau$  is the time delay accumulated between the two beams before the recombination. In order to effectively suppress laser phase noise at high frequencies, the experimenter must carefully length-balance the interferometer: for example, to suppress noise at 1 MHz by 60 dB, the length imbalance should be  $\lesssim 10$  cm.

Since we use diode lasers, whose phase noise can be significantly higher than the shot noise, we always length-balance the interferometer arms. A convenient way to balance the lengths is to splice or cut appropriately a length of optical fiber, as done in the setup of Fig. 3.25a for the local oscillator beam. In free-space, we implemented an analogous method using a retroreflector installed on a cage mount, that can be translated without changing significantly the angular alignment of the reflected beam. It is possible to monitor the length imbalance by modulating the laser frequency: if the angular frequency is swept linearly in time at a rate  $d\omega_l/dt$ , we will observe time-varying interference fringes imprinted on the photodetector signal:

$$V \propto \sqrt{P_s P_{LO}} \cdot \sin\left(\frac{\langle n \rangle \Delta L}{c} \frac{d\omega_l}{dt} \cdot t + \frac{\langle n \rangle \omega_l \Delta L}{c}\right), \quad (3.21)$$

whose frequency depends on the length imbalance  $\Delta L$  ( $\langle n \rangle$  is the length-averaged refractive index of the interferometer optical paths). The fringe frequency can be monitored on an oscilloscope or a spectrum analyzer, and gradually minimized by cutting appropriate lengths of fiber.

The low frequency fluctuations of the interferometer path length difference are stabilized by means of two cascaded acousto-optic modulators (Brimrose; see Fig. 3.24) the first shifts the frequency of the local oscillator beam by +100 MHz, while the second shifts it back by −100 MHz, with a small frequency offset controlled using the low-frequency signal from the balanced photodetector couple as an error signal, and a proportional feedback controller. With this arrangement, the phase difference can be tuned finely with practically unlimited actuation range. The phase difference is stabilized close to phase quadrature (the inflection point of the fringes). This quadrature corresponds usually (but not always, as discussed in section 3.7.4) to the largest transduction of mechanical displacement.



The samples are housed in a high vacuum chamber (see Fig. 3.25b) pumped with an ion pump, capable of reaching pressures below  $10^{-8}$  mbar, sufficient to suppress gas damping for high-Q resonant frequencies  $\Omega_m/2\pi \gtrsim 100$  kHz. The chip sample holder is mounted on 3-axis Attocube nanopositioners, that allow fine alignment between the device under test and the laser probe. A piezoelectric plate, used to resonantly actuate the devices, is connected to the sample mount. The vacuum chamber is equipped with a loadlock, separated by a valve from the main chamber, and a loading arm (visible in Fig. 3.25a). In order to insert or swap samples, it is sufficient to vent and pump the loadlock; this is much more rapid than breaking the vacuum in the vacuum chamber and allows to reach lower base pressures. This feature makes the vacuum chamber particularly useful for quick characterization of many nanomechanics chips. More information on the design of the vacuum chamber is provided in the doctoral thesis of Amir H. Ghadimi [159], who assembled it with the help of Mohammad Bereyhi.

### 3.7.3 Ringdown characterization

Despite the simplicity of resolving thermomechanical noise, for high-Q dissipation-diluted samples ( $Q \gtrsim 10^6$ ) the damping rate cannot simply be inferred from the linewidth of the noise peak. Typically their linewidths are below the resolution limit of a real-time spectrum analyzer, and, even tracking the displacement for longer times, often produces spectra dominated by frequency fluctuations and drift (see Figure 2.13a). The preferable methods are to fit the  $X^2 + Y^2$  Brownian spectrum, as in Figure 2.13b, or observing the free-decay amplitude ringdown. The latter is the most practical and widely used technique.

Ringdown measurements in the interferometer setup are initiated by exciting a mechanical resonance with the piezoelectric plate or with an intensity-modulated auxiliary laser<sup>8</sup>. After the mode frequency is identified from the thermomechanical spectrum, a driving tone is generated with an MFLI lock-in amplifier (Zürich Instruments), and either swept manually around resonance, or locked to it by means of a digital phase-locked-loop (PLL, implemented in the MFLI software). When the driven amplitude has surpassed the thermomechanical noise of one or two decades, we abruptly switch off the mechanical excitation and we record the slowly-decaying amplitude of the displacement signal, obtained by demodulating the photocurrent signal at the excitation frequency with the MFLI. A demodulation bandwidth exceeding 100 Hz is employed, to mitigate the effect of mechanical frequency drifts, induced e.g. by temperature or optical power fluctuations. Some examples of ringdown traces can be seen in Figure 3.15 and 3.28. As detailed in section 3.7.5, gated measurements are often performed in order to minimize the influence of optical backaction of the probing beam; to this end, a mechanical shutter inserted at the output of the laser, is actuated periodically.

<sup>8</sup> The latter method was the preferred one for the characterization of sSi nanostrings. The high absorption of silicon at 800 nm was exploited in order to generate a bolometric resonant force.

### 3.7.4 Displacement calibration with interferometric nonlinearity

Measurement records from the optical interferometer are produced in electrical units (typically voltage readings from the photodiode transimpedance amplifier). A calibration procedure of time- or frequency-domain interferometric displacement traces from voltage to displacement units is often necessary to make these measurements easier to compare, and compute derived quantities. In order to obtain such a calibration, the experimenter can sweep the interferometer phase by scanning, for example, the position of a mirror or the laser frequency and measure the voltage excursion corresponding to the peak-to-peak amplitude of an interferometric fringe,  $V_{pp}$ . Knowing that such a voltage corresponds to a path-length change of  $\lambda/2$ , it is readily possible to convert a measured spectrum to displacement units by applying the following conversion rule [160]:

$$S_x(\omega) = \left( \frac{\lambda}{2\pi V_{pp}} \right)^2 \times S_V(\omega), \quad (3.22)$$

obtained by assuming that the interferometer is operating at the maximum displacement sensitivity point. However, this technique is only valid when all the photons in the signal beam have interacted with the mechanical resonator, and fails when it is mixed with spurious reflections. In the reality of the experiment, this condition is not trivial to satisfy, because reflections of a similar magnitude as the sample reflection are easily generated, for example from the recessed chip substrate, several tens of micrometers below the microresonator, from glass-air interfaces in the optical setup or from imperfect fiber connectors.

As our micromechanical devices typically exhibit such spurious reflections (with the exception of membrane samples, which are suspended over an optically-transmitting window that perforates the chip substrate), we devised an alternative method that exploits *interferometric nonlinearity* to calibrate mechanical motion [27]. Such a method was mentioned before in the literature [161], but without reporting the implementation details. Since interference fringes are sinusoidal, an interferometer linearly transduces mechanical motion only when displacement amplitudes are low. When the amplitude becomes comparable with the optical wavelength, however, the optical intensity transduction is distorted, and sidebands are generated at higher harmonics of the vibrational frequency. If the wavelength is known, the amplitude of these sidebands can be fitted to reconstruct the displacement amplitude corresponding to the observed level of harmonic distortion; effectively, the optical wavelength is used as a ruler against which the mechanical displacement is compared. This method is robust against the presence of spurious reflections, requiring only that the local oscillator beam is much more intense than them.

In order to observe interferometric nonlinearity, one mode of the mechanical resonator under test is driven harmonically to large amplitudes ( $x_0 \gg 10 \text{ nm}$ ); the lower the resonant frequency and the higher its quality factor, the stronger it can be excited for a fixed driving power. In principle, the resonator could also be driven off-resonance to achieve displacement calibration, but it would be challenging to obtain the required motional amplitudes. Piezoelectric or radiation pressure actuation are both suitable in order to achieve large oscillation amplitudes. First, the resonant frequency is identified with good accuracy ( $< 100 \text{ Hz}$ ) from the thermomechanical noise spectrum. Then,



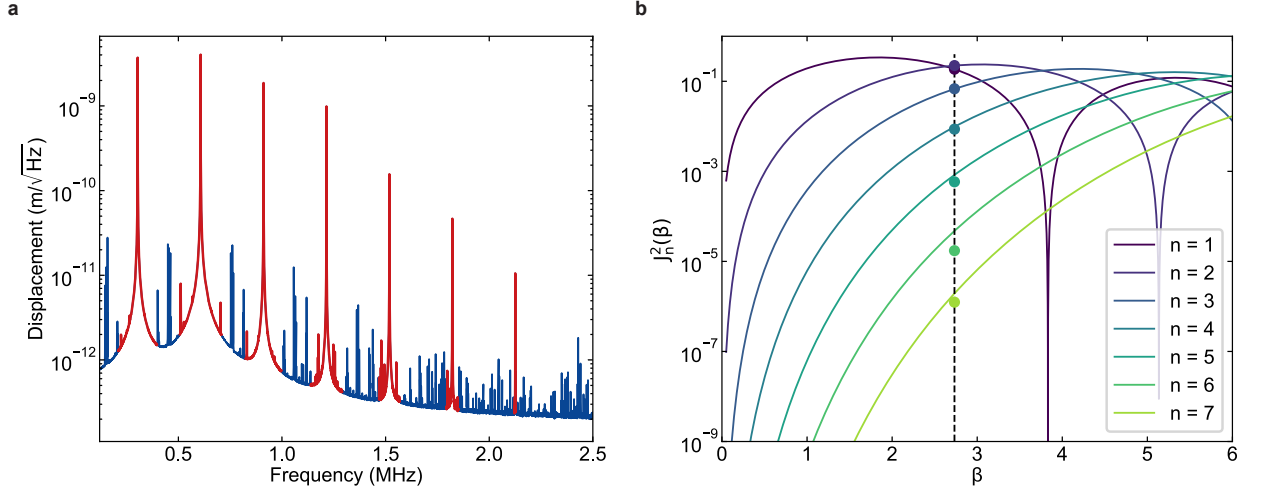


Figure 3.26: **a**, Driven motional spectrum of a polygon mechanical resonator, exhibiting interferometric nonlinearity. The oscillation amplitude is around 170 nm. Harmonics of the driven mode at 304 kHz are highlighted in red. **b**, Sideband powers (dots) normalized by  $P_n(\varphi_0)$  and fit to Bessel functions of the first kind as a function of the modulation index  $\beta$  (colored lines).

the mode is excited to an intermediate amplitude level by manually tuning the frequency of the driving tone (typically generated with a Zürich Instruments UHFLI or MFLI lock-in amplifier) to bring it into resonance. When the oscillation amplitude is high enough, the displacement signal-to-noise ratio (SNR) of mechanical motion is sufficient to switch the UHFLI oscillator to phase-locked-loop (PLL) tuning, using the mechanical record to provide an error signal for the regulation of the driving tone frequency and phase. At this stage, the PLL phase setpoint must generally be chosen empirically, in order to provide mechanical excitation rather than damping. With the PLL on, the driving tone can track resonance drifts and fluctuations, and bring the oscillation amplitude to large, stable values (with a response time determined by the mechanical damping rate).

At this point, multiple harmonics of the resonant mode should be visible in the spectrum of mechanical motion (acquired either with the FFT feature of the UHFLI or with a Spectrum Analyzer), as displayed in Fig. 3.26a. Their relative powers can be related to the oscillation amplitude by expressing the output voltage of the balanced photodiode as:  $V = V_0 \sin(\phi(t) + \varphi_0) + V_{\text{ext}}$ , where  $\phi(t) = \beta \cdot \cos(\Omega_m t)$  is the phase accumulated due to harmonic displacement of the resonator,  $\Omega_m$  is the mechanical frequency,  $\beta = 4\pi x_0/\lambda$  is the phase modulation index,  $\varphi_0$  is the interferometer quadrature angle and  $V_{\text{ext}}$  encompasses additional interference terms which are not associated with reflection from the mechanical resonator. Exploiting the Jacobi-Anger identity, we can write the phase modulation spectrum of that signal:

$$S_V(\omega) = 2V_0^2 \sum_{n=1}^{\infty} P_n(\varphi_0) J_n^2(\beta) \mathcal{L}(\omega - n\Omega_m) + S_{V, \text{ext}}(\omega), \quad (3.23)$$

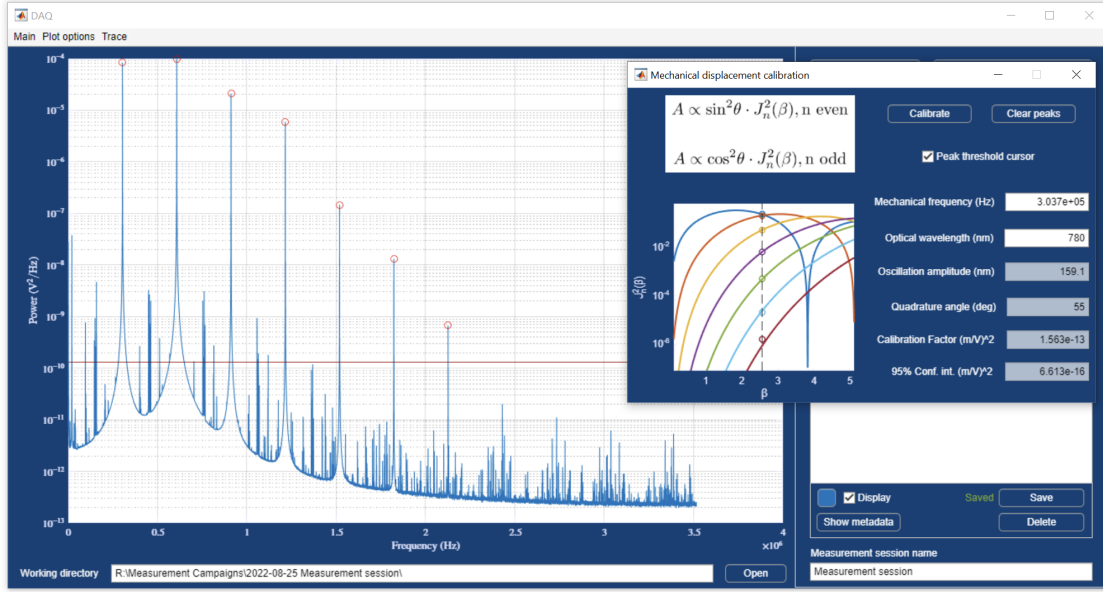


Figure 3.27: MATLAB app for fitting interferometric nonlinearity and obtaining displacement calibration.

$$P_n(\varphi_0) = \begin{cases} \cos^2(\varphi_0), & \text{if } n \text{ is odd} \\ \sin^2(\varphi_0), & \text{if } n \text{ is even} \end{cases} \quad (3.24)$$

where  $\mathcal{L}$  is a unit-normalized sharply-peaked function, whose lineshape depends on the mechanical damping, on the noise of the driving oscillator and on the spectrum analyzer bandwidth, and  $J_n$  is the Bessel function of the first kind of order  $n$ . Using this relation, one can integrate the spectral density below each visible harmonic of the driven motion and fit the sideband powers using  $A_n = 2V_0^2 P_n(\varphi_0) J_n^2(\beta)$ , in order to extract  $V_0$ ,  $x_0$  and  $\varphi_0$ . An example of a successful fit is shown in Fig. 3.26b, where powers are divided by  $P_n(\varphi_0)$  in order to show odd and even Bessel functions with a shared vertical axis. The spectrum (in the linear transduction regime) can then be converted to displacement units with the calibration factor (analogous to equation 3.22):

$$S_x = \left( \frac{\lambda}{4\pi V_0 \cdot \cos(\varphi_0)} \right)^2 \times S_V \quad (3.25)$$

I wrote MATLAB code for such a fitting routine for driven motion spectra, which can be found in a repository for the Instrument Control MATLAB suite developed in our Optomechanics team (<https://github.com/engelsen/Instrument-control>) (see Fig. 3.27). The routine takes as inputs the optical wavelength and motional frequency (if no frequency is provided, it tries to infer it from the spectral harmonics) and returns the fit parameters, a spectral calibration factor and a confidence interval associated with the fit uncertainty (if at least five sidebands are detected). Note that at least three sidebands should be visible in the driven motion spectrum for a well-defined fit procedure; if fewer than three sidebands are recognised, the fit routine will return an error.

A common cause of failure for this fitting procedure is photodiode saturation at very large AC voltage swings, which induces harmonic distortion of its own. This is usually recognized by an inaccurate fit result, and is easily fixed, for example by lowering the local oscillator intensity.

Once the calibration factor is obtained, a simple method to check whether the result is accurate is to acquire a Brownian motion spectrum of the mechanical resonance (after letting it thermalize for a time larger than the mechanical damping timescale). The area under a well-calibrated thermomechanical peak should correspond to that given by the equipartition relation 2.78, reproduced here for convenience:

$$\langle x^2 \rangle = \frac{k_B T}{m_{\text{eff}} \Omega_m^2}, \quad (3.26)$$

where  $T$  is the bath temperature and  $m_{\text{eff}}$  the mode effective mass. An estimate of the effective mass is typically available from a finite element simulation of the mechanical resonator, and it can be compared against that obtained from equation 3.26. For very high- $Q$  modes ( $Q > 10^8$ ), the integration time required to average over the Brownian motion is prohibitively large, and  $T$  can be affected by laser backaction effects. In that case, the mode can be mildly cold-damped with an actuator and a feedback loop using the displacement record to generate a delayed, dissipative force. The effective linewidth can easily be broadened by cold damping to values around  $\Gamma_{\text{eff}}/2\pi \sim 1$  Hz. When the oscillator is still in the classical regime and no squashing effect from the finite displacement imprecision is noticeable, the effective temperature can be determined:  $T_{\text{eff}} = T \frac{\Gamma_m}{\Gamma_m + \Gamma_{\text{eff}}}$  [20]. The intrinsic linewidth  $\Gamma_m$  can be determined by a separate ringdown measurement. The effective mass can then be similarly reconstructed from the equipartition relation, this time using the effective temperature 3.26.

### 3.7.5 Light-induced damping and antidamping

The laser probe that is used for the mechanical quality factor characterization in the setup can exert backaction on vibrational modes and affect the observed energy decay rates. This effect has to be avoided in order to extract intrinsic mechanical properties. The magnitude and the sign of the optically induced damping depend sensitively on the sample type and the position of the laser spot. In many cases, the optical damping is negligible, while sometimes it is strong enough to self-excite resonator modes under continuous illumination. sSi nanostrings exhibited relatively strong optical damping and antidamping rates, whose magnitude could easily become comparable to the minuscule intrinsic linewidth, as can be observed in Fig. 3.28.

To eliminate the effects of optical damping, we gate the ringdown measurements, by keeping the sample illuminated by the probe light only during short intervals of time. The total duration of time over which the probe light is on relative to the entire measurement time is typically between 0.1% and 1% in our measurements. We refer to this ratio as duty cycle. While characterizing a resonant mode, the absence of optical backaction can be confirmed by measuring with different duty cycles and/or laser beam positions on the sample, and checking whether the inferred linewidth is consistent within experimental errors.

An example of particularly strong optical backaction is illustrated in Figure 3.29. Panel a shows two ringdown measurements of the fundamental mode of a trampo-

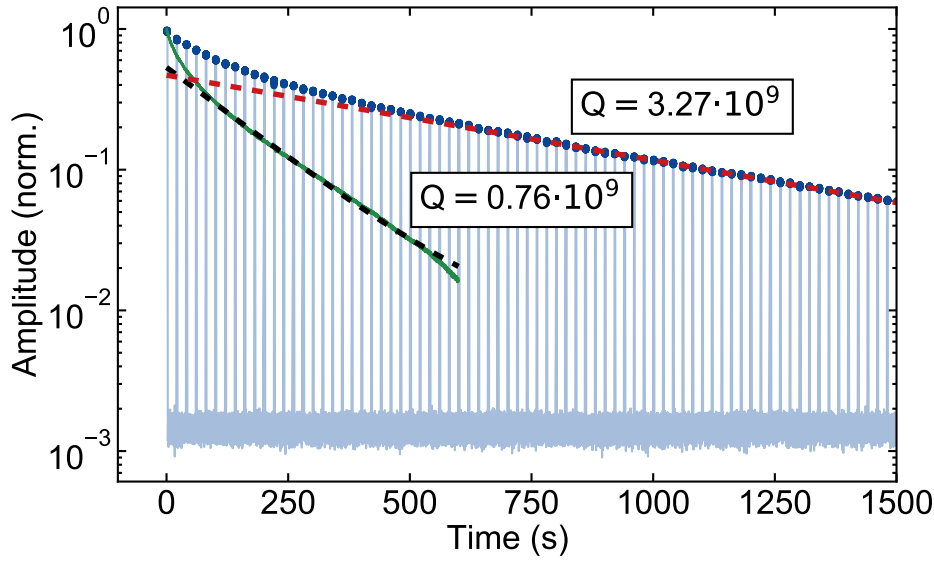


Figure 3.28: Comparison of ringdowns with continuous and gated acquisition. The probe laser, with an impinging power  $\gtrsim 1$  mW, induces, in the continuous ringdown (green line), additional optical damping, leading to a faster amplitude decay rate than the one set by the intrinsic dissipation of the nanostring. For the gated ringdown (blue dots), the measurement duty cycle (ratio of gate duration over the time interval between successive gates) is 10%, and the gate repetition rate is 1/20 s. In both ringdowns, nonlinear damping is observed at the highest amplitudes [69], and exponential fits (dashed lines) are performed only within the linear decay regions. The data were acquired at  $T \approx 10$  K for the 6.0 mm sSi nanostring of Figure 3.17.

line resonator with branching tethers (a membrane design described in Chapter 4), performed with the 780 nm probe beam directed at the resonator central pad. The displayed measurements made at two different gate duty cycles had decay rates differing of a factor of 2.5. A deviation from exponential decay manifests at high amplitudes, close to the trace beginning. This is due to the strong phase modulation imparted on the probe upon reflection from the trampoline, whose oscillation amplitude approaches the wavelength, as described in section 3.7.4. In these traces, therefore, only the linear amplitude decay regime was fit, with a simple exponential model.

When the duty cycle grows beyond  $\approx 2\%$ , the mode becomes self-excited, as shown by a close-up plot of one of the measurement intervals in Figure 3.29b. The optical damping rate inferred from these data is  $\Gamma_{\text{opt}} = -2\pi \times 48.4$  mHz at the continuous optical power of around  $100 \mu\text{W}$ , more than an order of magnitude larger than the intrinsic damping rate of the sample (see Figure 3.29c). In gated measurements, the optical antidamping was reduced proportionally to the duty cycle, which is shown by the data in Figure 3.29c. While Figure 3.29 presents an extreme example of optical backaction, usually such effects can be reduced or eliminated entirely by directing the laser beam to a position of the device where the mode amplitude is lower.

Our main observations on optical (anti)damping in interferometric detection can be summarized as follows:

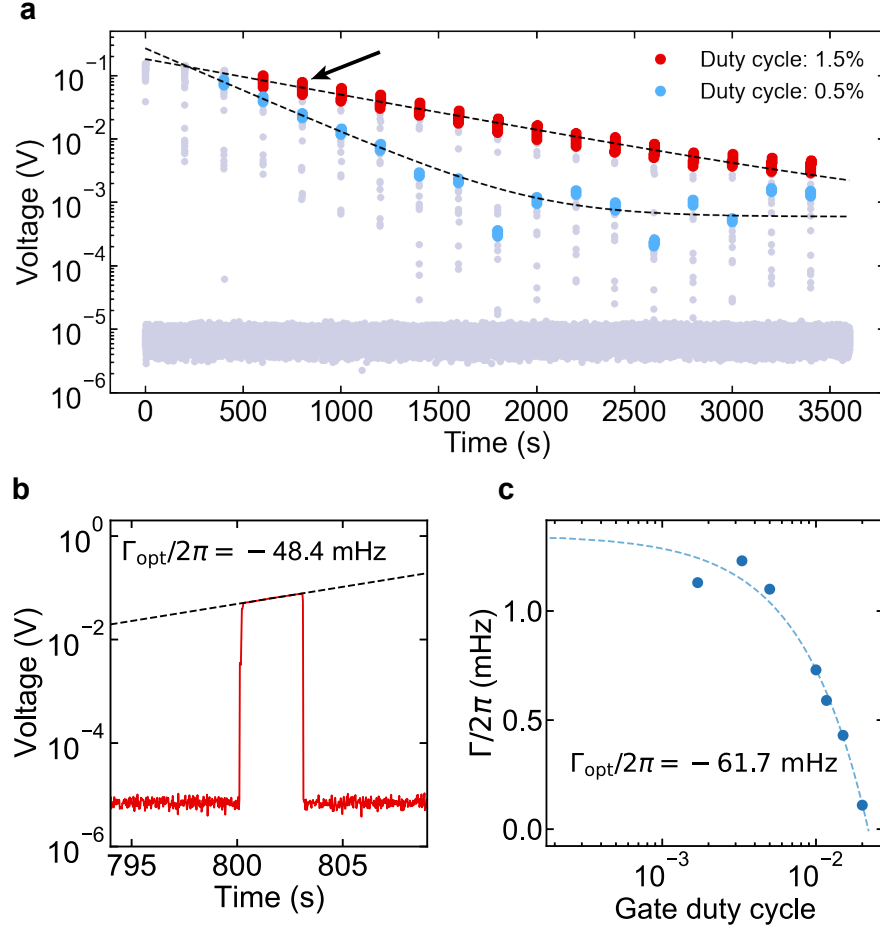


Figure 3.29: Optical antidamping of a trampoline resonator. **a**, Ringdown traces with different gate duration, exhibiting different optical antidamping rates. Gray points correspond to the noise background and the rising/falling edges of the gates, and are excluded from the fits. **b**, Homodyne signal within the gate indicated with a black arrow in panel a. The positive slope of the voltage within the gate implies anti-damping. **c**, Extracted net damping rate as a function of gate duty cycle. A linear fit used to extract the optical antidamping rate yields  $\Gamma_{\text{opt}} \approx 2\pi \times (-61.7 \text{ mHz})$  (in fair agreement with the growth of the displacement signal within a single gate, shown in panel b) and an intrinsic dissipation rate of  $\Gamma_{\text{m}} \approx 2\pi \times 1.3 \text{ mHz}$ .

- Optical (anti)damping manifests as a correction to the intrinsic linewidth, therefore, for a fixed  $Q$ , it is stronger at lower frequencies.
- The magnitude of optical (anti)damping is much higher when the resonator is suspended in the vicinity of a substrate, compared to the case when the substrate is completely removed in microfabrication.
- The magnitude of optical (anti)damping depends linearly on the impinging power, as shown in Fig. 3.29c.
- The sign and magnitude of the optical damping are wavelength-dependent.

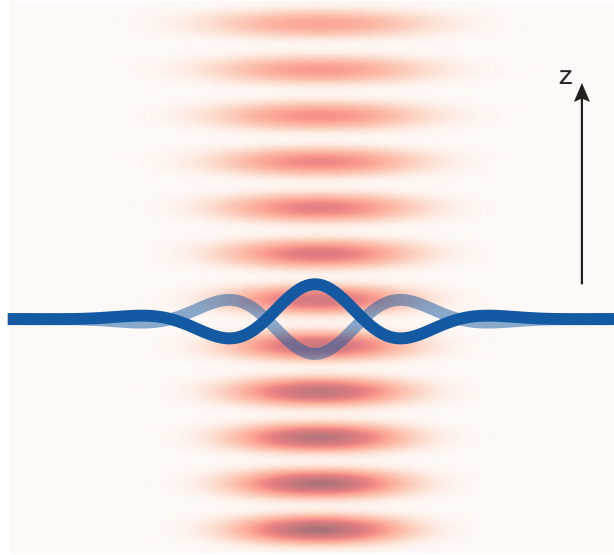


Figure 3.30: Schematic illustration of a mechanical resonator oscillating in an optical standing wave, generated by a reflection of the laser probe.

- The magnitude of optical (anti)damping can also depend on the distance between the sample and the laser beam focusing element, as shown in [26].

A model that could explain these observations is the photothermal backaction picture of [162] (see also a recent work with  $\text{Si}_3\text{N}_4$  trampoline membranes, [163]). Suppose an optical standing wave is formed by reflection from the substrate below the resonator (see Figure 3.30), such that the optical power can be written as:

$$P(z) = P_0(1 + R) + 2\sqrt{R}P_0 \cdot \cos(2kz - \varphi), \quad (3.27)$$

(neglecting the beam's finite extent and diffraction), with  $R$  the substrate reflectance and  $\varphi$  the phase shift acquired upon reflection. The resonator oscillates in the standing wave, sampling different optical intensities as it moves. The optical field can act on the mechanical motion through different effects, of which likely the most relevant is the bolometric backaction [164]. A small optical absorption in the nanomechanical device will increase the temperature, affect the film stress and modulate the mechanical frequencies through thermal expansion. If  $\theta = T - T_0$  is the increase of temperature averaged over the resonator volume, the mechanical frequencies will shift as (see section 2.3.6.2):

$$\Delta\Omega \approx \frac{-E\alpha\Omega}{2\sigma(1-\nu)}\theta, \quad (3.28)$$

where  $\alpha$  is the thermal expansion coefficient and  $\sigma$  the static stress in the thin film. The average temperature change over time can be modelled with a simple first order differential equation that takes into account optical absorption through the absorption coefficient  $\mu_a$  and linear heat dissipation through Newton's law with a heat transfer coefficient  $\kappa$ :

$$\dot{\theta} = -\frac{\kappa}{\rho c h} \theta + \frac{\mu_a}{\rho c} \cdot P(z), \quad (3.29)$$

where  $\rho$  is the material density and  $c$  the specific heat capacity. The mechanical displacement follows harmonic oscillator evolution, but with a resonant frequency varying in time through the temperature dynamics:

$$\ddot{z} + \Gamma \dot{z} + \Omega \left( 1 + 2 \frac{\Delta\Omega [\theta(t)]}{\Omega} \right) (z - z_{\text{eq}}) = \delta F_{\text{th}} / m_{\text{eff}}, \quad (3.30)$$

where  $\delta F_{\text{th}}$  is the stochastic thermomechanical force. Equations 3.29 and 3.30 form a system of coupled nonlinear differential equations, that can produce damping, antidamping and limit cycle oscillations of  $z$ . For example, if the beam oscillates around a node or antinode of the optical standing wave,  $z_{\text{eq}} = (n\pi/2 + \varphi/4\pi) \cdot \lambda$  a resonance frequency modulation at  $2\Omega$  (with amplitude  $\Delta\Omega_0$ ) will be generated, producing parametric driving or damping [165]. If the modulation is weak, the induced optical (anti)damping will be  $\Gamma_{\text{opt}} \approx \pm \Delta\Omega_0$ .

This model is not straightforward to validate quantitatively, because of the additional optical interactions that may complicate the picture (radiation pressure, dielectrophoretic force) and the unknown values of the absorption coefficient and of thermal transport parameters in low-dimensional devices.

### 3.8 OUTLOOK FOR SSI NANOMECHANICS

In conclusion, in this chapter I have reported the development of strained silicon crystalline nanomechanical resonators with  $Q > 10^{10}$ , one order of magnitude beyond previous implementations in  $\text{Si}_3\text{N}_4$  at liquid Helium temperatures [29, 58]. The built-in mechanical isolation of the soft clamped modes in this work eliminates many spurious loss mechanisms and provides access to the intrinsic material damping of silicon. The highest observed  $Q$  is due to a combination of ultrahigh dilution factor,  $D_Q^{\text{loc}} \approx 2 \cdot 10^6$ , and a suppressed intrinsic loss of single-crystal silicon in a cryogenic environment.

When considering future investigations and applications of strained silicon, the high yield stress of crystalline materials seems particularly attractive for implementing strain engineered resonators [26, 166], and the low intrinsic loss of silicon may be combined with other mode-shape engineering techniques [27, 58, 108] to decrease damping even further. In addition, surface passivation techniques could be employed to diminish the effect of native oxide formation on dissipation [95]. At millikelvin temperatures, thermal transport in strings with low dimensionality might be particularly unconventional, and laser heating could be probed by examining the mechanical properties of the strings. The exceptionally high  $Q$  may also lend itself to force sensing, including recently-proposed searches for dark matter particles [167].

Although we constrained ourselves to the sSOI wafer stack, with fixed layer thicknesses, for this initial exploration of sSi nanomechanics, in future implementations we envision a simpler fabrication process by using a thicker oxide sacrificial layer. Carrying out high temperature oxidation of silicon in the presence of water vapour,  $\text{SiO}_2$  sacrificial layers thicker than  $5 \mu\text{m}$  can be grown, which provide a large enough clearance to avoid stiction to the substrate in microfabrication, especially using vapour HF



for gas-phase undercut. Since Soitec SA stopped commercialization of sSOI substrates, the silicon-on-insulator process should be reproduced, including the wafer bonding of sSi to the oxidized silicon substrate. The epitaxial growth of sSi on SiGe substrates is offered by commercial foundries.

The temperature scaling of dissipation in strained silicon at millikelvin temperatures could be very appealing, owing to low densities of TLSs. For example, Fig. 2.10 indicates that a 1 MHz resonance, dominated by TLS relaxation damping, would see a rapid increase in its quality factor at temperatures below 100 mK. In light of recent demonstrations in unstrained optomechanical crystals of  $Q_{\text{int}} = 5 \cdot 10^{10}$  [79], soft-clamped strained silicon devices might achieve  $Q > 10^{12}$ , and even probe the existence of novel mechanical dissipation mechanisms. These temperatures can be reached in a different type of cryostat, a *dilution refrigerator*. Optical measurements would be hindered by the lower cooling power available at base temperature in a dilution refrigerator; nevertheless gated ringdowns would allow the complete thermalization of the samples between intervals of optical observation. High-aspect-ratio mechanical resonators were observed to reach thermal equilibrium at temperatures down to  $\sim 30$  mK in dilution refrigerators, with a sufficiently low laser probe power [168, 169]. The acoustic isolation provided by PnC structures would aid cryogenic operation, as the samples are protected from the strong, repetitive vibrations generated at the 4 K pre-cooling stage.



## MEMBRANE-IN-THE-MIDDLE OPTOMECHANICS

*[...] theories don't prove nothing, they only give you a place to rest on, a spell, when you are tuckered out butting around and around and trying to find out something there ain't no way to find out [...] There's another trouble about theories: there's always a hole in them somewheres, sure, if you look close enough.*

— Mark Twain (Tom Sawyer Abroad)

The major part of this thesis work was dedicated to realizing a cavity optomechanical system that could operate in the quantum regime at room temperature. In the quantum regime, the product between imprecision noise and force fluctuations (as described in the next section) approaches the Heisenberg inequality lower bound. As the quantitative description of decoherence implies [17], this regime becomes more and more difficult to access as the oscillators grow larger in mass, and their environment gets hotter and noisier. In spite of these difficulties, the last five years have seen a number of experiments operating close to, or within, the quantum regime for larger and larger resonators [5, 29, 170], or at ever higher temperatures [5, 171–173]. The challenge of preparing quantum mechanical states of macroscopic resonators is of sheer scientific interest by itself, as they probe the limits of applicability of quantum mechanics and the existence of fundamental mechanisms of ‘loss of coherence’ as quantum superpositions grow larger [174]. Another motivation for preparing macroscopic objects in quantum states is to test experimentally some theoretical predictions of interplay between gravity and quantum mechanics [175, 176].

We strive to enter the quantum regime of cavity optomechanics at room temperature with a membrane-in-the-middle (MiM) system, one of the best-studied and advanced optomechanical platforms [29, 46, 109, 177]. The protagonist of these experiments is a dissipation-diluted nanomechanical membrane of the type described in chapter 2. Over the years of development of the MiM platform by the optomechanics community, such resonators have evolved hand-in-hand with the evolution of dissipation dilution techniques. The mechanical modes of interest have changed from a distributed standing waves extended to the whole membrane surface, to the soft clamped modes confined by a defect within a phononic crystal. The effective mass of the latter resonances is of the order of several nanograms, comparable to the mass of a glass bead with a radius of  $\sim 8\,\mu\text{m}$ , and many orders of magnitude beyond the scales of atoms, molecules, and even levitated nanoparticles. The mass of an object is, in fact, not the most appropriate predictor of the occurrence of quantum mechanical behaviour. The energy dissipation rate gives a better indication of the decoherence of a quantum mechanical object, and provides an approximate quantification of the vague notion of ‘isolation from the environment’. Dissipation dilution has proven to be an invaluable tool in engineering extremely well-isolated nanomechanical oscillators, allowing the interaction with an optical probe to surpass the strength of the fluctuations imposed by the thermal environment.

In this chapter, after a brief introduction to cavity optomechanics, I will present our experimental efforts with the room-temperature MiM system. I will detail the fabrication process of soft clamped  $\text{Si}_3\text{N}_4$  membranes, and describe the first experimental challenge we faced in the operation of the room-temperature experiment. Quantum optomechanics requires quantum-limited displacement detection, and in the first MiM experiments we noticed an amplitude noise orders of magnitude higher than the quantum limit (shot noise) imprinted on the laser field output from the optical cavity. We termed this noise *thermal intermodulation noise* and described quantitatively how it originates from the cavity nonlinear transduction. We also developed and implemented methods for circumventing it experimentally. These findings have been published in [178]. In this work, the experiments and the theoretical explanation have been carried out by Sergey Fedorov, while I contributed with the development and fabrication of the membrane samples, the design of the optical cavity, and aided the numerical modelling, together with Amirali Arabmoheghi. Nils Engelsen supervised every stage of the work.

Thermal intermodulation noise arises from the multimode nature of the optomechanical cavity. Engineering resonators with sparser mechanical spectra dramatically impacts intermodulation noise, potentially relegating it to a negligible magnitude. Aware of this fact, we designed a different class of trampoline nanomechanical resonators for the MiM experiment, where soft clamping was implemented for the lowest order modes. Our experimental investigation of these dissipation-diluted devices, that appear as a hierarchical network of nanostrings, is published in [58]. This work was a collaborative effort of many researchers, as it involves trampoline devices with a large pad for placement in a MiM cavity, as well as fractal-like nanostrings. Sergey Fedorov conceived the idea of dissipation-dilution in fractal-like nanostrings, and the trampoline devices were designed by him and me. The samples were fabricated by Robin Groth, Mohammad Bereyhi (fractal-like strings) and I (trampoline membranes), and characterized by all of us, with the help of Amirali Arabmoheghi and Nils Engelsen. Tobias Kippenberg supervised the work at every stage and provided the funding sources for the fabrication and experiments. I will briefly summarize this class of resonators in this chapter, for what concerns the MiM experiment.

In the last part of the chapter I will expose our latest experimental advances, including the development of a fabrication process for density-modulated PnC membranes (inspired by the work of Høj et al. [67]) with lower dissipation rates, the reduction of the thermomechanical noise of the cavity mirrors, and the operation in the quantum regime  $C_Q \sim 1$  at room temperature. In the latter developments, the contributions of Guanhao Huang and Nils Engelsen have been indispensable.

#### 4.1 RUDIMENTS OF CAVITY OPTOMECHANICS

The most common and easily-implemented cavity optomechanical interaction is the *dispersive coupling* condition, i.e. the regime in which the motion of a mechanical oscillator perturbs the resonant frequency  $\omega_c$  of an optical cavity [20]. We focus here on the case of a single mechanical resonator interacting with a single optical cavity mode. The dispersive interaction is described by the frequency pull parameter (also called optomechanical coupling strength)  $G$ , that gives the cavity frequency shift per unit displacement of the mechanical oscillator:

$$G = -\frac{d\omega_c}{dx} \quad (4.1)$$

The simplest case of dispersive coupling is that of a Fabry-Pérot cavity with one movable mirror. Suppose the length of this cavity is  $L$ . Since the resonant frequencies of the longitudinal modes supported by the cavity are  $\omega_{c,n} = n\pi c/L$ , the frequency pull factor corresponding to the longitudinal motion of the end-mirror is simply  $G = \omega_c/L$ .

The Hamiltonian describing the dynamics of an optical and a mechanical mode and their dispersive coupling is then (neglecting the zero-point energy):

$$\hat{H} = \hbar\omega_c \hat{a}^\dagger \hat{a} + \hbar\Omega \hat{b}^\dagger \hat{b} - \hbar g_0 \hat{a}^\dagger \hat{a} (\hat{b} + \hat{b}^\dagger) + \hat{H}_{c,ext} + \hat{H}_{c,o} + \hat{H}_{m,ext}, \quad (4.2)$$

where  $\hat{a}, \hat{b}$  are the annihilation operators for the optical cavity and the mechanical mode,  $\Omega$  is the mechanical resonant frequency,  $\hat{H}_c$  and  $\hat{H}_m$  are coupling terms with the environment and the input ports of the cavity, and  $g_0 = Gx_{zpf}$  is the *vacuum optomechanical coupling rate*. The equations of motion for the optical and mechanical oscillators in the Heisenberg picture are obtained by evaluating the commutation of the relevant operators with the Hamiltonian,  $\dot{\hat{O}} = i[\hat{H}, \hat{O}]/\hbar$ . Let us express the evolution of  $\hat{a}$  and  $\hat{x} = x_{zpf}(\hat{b} + \hat{b}^\dagger)$ :

$$\begin{aligned} \dot{\hat{a}} &= -\left(i\left(\omega_c - g_0 \frac{\hat{x}}{x_{zpf}}\right) + \frac{\kappa}{2}\right) \hat{a} + \sqrt{\kappa_0} \hat{a}_0 + \sqrt{\kappa_1} \hat{a}_{in,1} + \sqrt{\kappa_2} \hat{a}_{in,2} \\ m_{eff}(\ddot{\hat{x}} + \Gamma \dot{\hat{x}} + \Omega^2 \hat{x}) &= \hat{F}_{th}(t) + \hbar G \hat{a}^\dagger \hat{a} \end{aligned} \quad (4.3)$$

These are called *quantum Langevin equations* of single-mode cavity optomechanics. Here,  $\kappa$  is the cavity linewidth (energy dissipation rate),  $\kappa = \kappa_0 + \kappa_1 + \kappa_2$ .  $\kappa$  is decomposed in an intrinsic decay rate, associated with the fraction of the cavity field that is lost and becomes inaccessible to the observer,  $\hat{a}_0$ , and external decay rates  $\kappa_{1,2}$ , that connect the intracavity field to the output ports of the cavity.  $\hat{a}_{in,(1,2)}$  represent the input fields at ports 1 and 2<sup>1</sup>, and the output fields leaking from 1 and 2 can be collected by the experimenter and carry information on the intracavity field and on the mechanical oscillator. The relationship between the input and output fields at any cavity port is given by the input-output theory:  $\hat{a}_{out,i} = \hat{a}_{in,i} - \sqrt{\kappa_i} \hat{a}$  [179]. The fluctuation and dissipation terms are derived by considering a linear coupling with a bath (the same as in chapter 2), embedded in the Hamiltonians  $H_{c,m}$ . Due to the immensely different excitation numbers at the mechanical and optical cavity frequencies, these manifest as thermal fluctuations  $\hat{F}_{th}$  or vacuum fluctuations  $\hat{a}_0^2$ .

The quantum Langevin equations 4.3 are nonlinear. In order to describe many basic predictions of cavity optomechanics, it is sufficient to consider a linearized regime, where we are interested in small fluctuations of the optical and mechanical variables around the steady state values (the latter being approximated by complex numbers in lieu of operator quantities). The description of fluctuations can be obtained through

<sup>1</sup> Here I consider a double-sided cavity in order to maintain a picture consistent with a Fabry-Pérot resonator.

<sup>2</sup> For the input field, excess fluctuations can arise from laser technical noise beyond shot noise.

the substitutions<sup>3</sup>  $\hat{a} \rightarrow \bar{a} + \hat{a}$ ,  $\hat{x} \rightarrow \bar{x} + \hat{x}$  (with  $\bar{a} \gg 1$ ), such that we can write the linearized equations of motion:

$$\begin{aligned} \dot{\hat{a}} &\approx -\left(i\omega'_c + \frac{\kappa}{2}\right) \hat{a} + ig \frac{\hat{x}}{\chi_{\text{zpf}}} + \sqrt{\kappa_0} \hat{a}_0 + \sqrt{\kappa_1} \hat{a}_{\text{in},1} + \sqrt{\kappa_2} \hat{a}_{\text{in},2} \\ m_{\text{eff}}(\ddot{\hat{x}} + \Gamma \dot{\hat{x}} + \Omega^2 \hat{x}) &\approx \hat{F}_{\text{th}}(t) + \hbar \frac{g}{\chi_{\text{zpf}}} (\hat{a} + \hat{a}^\dagger), \end{aligned} \quad (4.4)$$

Here,  $g = g_0 \bar{a} = g_0 \sqrt{n_c}$  is the field-enhanced optomechanical coupling rate, amplified by the presence of an average number of photons  $n_c = \langle \hat{a}^\dagger \hat{a} \rangle$  within the cavity, and  $\omega'_c$  is the cavity resonant frequency including a small optomechanical dispersive shift. Moreover, to write 4.4, I have defined the phase of the intracavity field as the reference,  $\arg(\bar{a}) = 0$ . This definition is innocuous in the case of a single cavity mode.

Finally, we can write frequency-domain relations by moving to a frame rotating at the frequency of the intracavity field  $\omega_l$ , with the transformation  $\hat{a} \rightarrow \hat{a} e^{-i\omega_l t}$ , and performing a Fourier transform of 4.4. We obtain:

$$\begin{aligned} \chi_o^{-1}(\omega) \cdot \hat{a}(\omega) &= ig \frac{\hat{x}(\omega)}{\chi_{\text{zpf}}} + \sqrt{\kappa_0} \hat{a}_0(\omega) + \sqrt{\kappa_1} \hat{a}_{\text{in},1}(\omega) + \sqrt{\kappa_2} \hat{a}_{\text{in},2}(\omega) \\ \chi_m^{-1}(\omega) \cdot \hat{x}(\omega) &= \hat{F}_{\text{th}}(\omega) + \frac{\sqrt{2}\hbar g}{\chi_{\text{zpf}}} \hat{X}(\omega), \end{aligned} \quad (4.5)$$

The optical and mechanical susceptibilities have appeared in 4.5:

$$\begin{aligned} \chi_o(\omega) &= \frac{1}{-i(\Delta + \omega) + \frac{\kappa}{2}} \\ \chi_m(\omega) &= \frac{1}{m_{\text{eff}}((\Omega^2 - \omega^2) - i\Gamma\omega)} \end{aligned} \quad (4.6)$$

Furthermore, we have introduced the detuning  $\Delta = \omega_l - \omega_c$  between the intracavity field and the cavity resonance, and the optical field amplitude and phase quadratures,  $\hat{X} = (\hat{a} + \hat{a}^\dagger)/\sqrt{2}$  and  $\hat{Y} = -i(\hat{a} - \hat{a}^\dagger)/\sqrt{2}$ , analogous to the position and momentum of the mechanical oscillator.

#### 4.1.1 Dynamic backaction

In the equations of motion 4.5, the mechanical motion imparts a phase modulation on the intracavity field, and the field couples back to mechanical motion by exerting a force proportional to its amplitude quadrature. We can substitute  $\hat{a}(\omega)$  in the equation of motion for  $\hat{x}(\omega)$  (remembering that  $\hat{X}(\omega) = (\hat{a}(\omega) + \hat{a}^\dagger(-\omega))/\sqrt{2}$ ) to obtain a closed form expression for the displacement fluctuations in the frequency domain. The fluctuations then take the form:

$$\chi_{\text{eff}}^{-1}(\omega) \cdot \hat{x}(\omega) = \hat{F}_{\text{th}}(\omega) + \hat{F}_{\text{ba}}(\omega), \quad (4.7)$$

<sup>3</sup> I keep the same symbols for the fields in 4.3 and their fluctuations in the following, for lightness of notation.

where  $\chi_{\text{eff}}^{-1}$  is the mechanical susceptibility modified by the optomechanical interaction, satisfying:

$$\chi_{\text{eff}}^{-1}(\omega) = \chi_{\text{m}}^{-1}(\omega) + 2m_{\text{eff}}\Omega g^2 \left[ \frac{1}{(\Delta + \omega) + i\frac{\kappa}{2}} + \frac{1}{(\Delta - \omega) - i\frac{\kappa}{2}} \right] \quad (4.8)$$

This perturbation of the oscillator linear response from radiation pressure is called dynamic backaction (DBA), as it is induced by an autonomous feedback mechanism involving the optical cavity. In general, the oscillator lineshape will be modified by DBA, but if the interaction strength is moderate ( $g \ll \kappa$ ), the effect of DBA can be described by a shift in resonant frequency (optical spring) and a broadening or sharpening of the linewidth (optical damping), proportional to the intracavity photon number. In our cavity optomechanics experiments, the situation of interest is that of a cavity response faster than the mechanical frequency, also known as the *unresolved sidebands* regime or Doppler regime:  $\kappa \gg \Omega$ . In this limit, the resonant frequency and damping rate modified by the optomechanical interaction are approximated as follows:

$$\begin{aligned} \Omega_{\text{eff}} &\approx \Omega \sqrt{1 + \frac{4g^2}{\Omega} \frac{\Delta}{\Delta^2 + \kappa^2/4}} \approx \Omega + 2g^2 \frac{\Delta}{\Delta^2 + \kappa^2/4} \\ \Gamma_{\text{eff}} &\approx \Gamma - 4g^2 \Omega \frac{\Delta \kappa}{(\Delta^2 + \kappa^2/4)^2} \end{aligned} \quad (4.9)$$

Equation 4.9 shows how the mechanical susceptibility is only modified for off-resonant pumping,  $\Delta \neq 0$ . In particular, a red-detuned field ( $\Delta < 0$ ) will soften the spring constant and broaden the linewidth, and vice versa for a blue-detuned field. It can be shown that blue-detuned pumping leads to a parametric instability of the mechanical oscillator [180, 181] as  $\Gamma_{\text{eff}} \approx 0$ , and that red-detuned pumping has the additional effect of cooling the mechanical oscillator, effectively coupling it to the zero-temperature bath of the laser field vacuum fluctuations [20]. In the resolved sideband regime ( $\kappa \lesssim \Omega$ ) red-detuned pumping with a sufficiently low-noise field can prepare the mechanical oscillator in the ground state, as has been shown using optical and microwave superconducting cavities [62, 182–184].

#### 4.1.2 Displacement measurement in cavity optomechanics

We now focus on the case of resonant probing,  $\Delta = 0$ , where the oscillator parameters are not modified by DBA and the mechanical displacement can be tracked faithfully. The second effect of the optomechanical interaction on the oscillator's motion in 4.7 is the appearance of a radiation pressure force term, governed by the intracavity amplitude fluctuations. For the case of probing on the cavity resonance, this *stochastic backaction* force can be written, in the frequency domain, as:

$$\hat{F}_{\text{ba}}(\omega) = \frac{2\sqrt{2}\hbar g}{x_{\text{zpf}}\sqrt{\kappa} \left(1 - i\frac{2\omega}{\kappa}\right)} \left( \sqrt{\eta_0}\hat{X}_0(\omega) + \sqrt{\eta_1}\hat{X}_{\text{in},1}(\omega) + \sqrt{\eta_2}\hat{X}_{\text{in},2}(\omega) \right), \quad (4.10)$$

where  $\eta_i = \kappa_i/\kappa \leq 1$ . The complex factor at the denominator accounts for the low-pass filter behaviour of the cavity, that does not efficiently transduce fluctuations at



frequencies  $\omega \gtrsim \kappa/2$ . Using equation 2.41, we can calculate the spectral density of the radiation pressure backaction force heating the oscillator at  $\Delta = 0$ . We assume that all the input fluctuations are in the vacuum state, such that  $S_{XX} = 1/2$ ; this descends from the autocorrelation properties of vacuum fields:

$$\begin{aligned}\langle \hat{a}_0^\dagger(t) \hat{a}_0(0) \rangle &= 0 \\ \langle \hat{a}_0(t) \hat{a}_0^\dagger(0) \rangle &= \delta(t) \\ \langle \hat{a}_0(t) \hat{a}_0(0) \rangle &= \langle \hat{a}_0^\dagger(t) \hat{a}_0^\dagger(0) \rangle = 0\end{aligned}\tag{4.11}$$

Any excess amplitude noise on the input field will increase the backaction force driving the oscillator. Since the input fields are uncorrelated, the backaction force spectral density is:

$$S_{FF}^{\text{ba}}(\omega) = \frac{\hbar^2 C \Gamma}{x_{\text{zpf}}^2} \cdot \frac{1}{\left(1 + \frac{4\omega^2}{\kappa^2}\right)},\tag{4.12}$$

where I have defined the (field-enhanced) *cooperativity*:

$$C = \frac{4g^2}{\kappa\Gamma} = \frac{4g_0^2 n_c}{\kappa\Gamma}\tag{4.13}$$

At  $\Delta = 0$ , the oscillator displacement is imprinted on the phase quadrature of the field leaking out of the cavity<sup>4</sup>. We assume that only the output field from port 2 is collected, and its phase quadrature is measured with a phase-sensitive photodetection scheme (for example, homodyne detection). The input-output relation implies that:

$$\hat{a}_{\text{out}} = \hat{a}_{\text{in},2} - \sqrt{\kappa_2} \hat{a}\tag{4.14}$$

Combining equations 4.14 and 4.5 we obtain an expression for the output field's phase quadrature:

$$\begin{aligned}\hat{Y}_{\text{out}}(\omega) &= \frac{1}{1 - i\frac{2\omega}{\kappa}} \left[ \left(1 - 2\eta_2 - i\frac{2\omega}{\kappa}\right) \hat{Y}_{\text{in},2} - 2\sqrt{\eta_0\eta_2} \hat{Y}_{\text{in},0} - 2\sqrt{\eta_1\eta_2} \hat{Y}_{\text{in},1} - \frac{2\sqrt{2\eta_2}g}{\sqrt{\kappa}x_{\text{zpf}}} \hat{x} \right] = \\ &= -\frac{1}{1 - i\frac{2\omega}{\kappa}} \frac{2\sqrt{2\eta_2}g}{\sqrt{\kappa}x_{\text{zpf}}} (\hat{x} + \hat{x}_{\text{imp}}),\end{aligned}\tag{4.15}$$

where the phase quadrature is not simply proportional to  $\hat{x}$ , but presents an additional background noise  $\hat{x}_{\text{imp}}$  transduced by the vacuum fluctuations in the phase quadratures of the cavity input fields. The spectral density of this position-referred *imprecision noise* is:

<sup>4</sup> At finite detuning, the displacement is maximally coupled to a different quadrature of the output field, rotated by  $\approx \text{atan}(2\Delta/\kappa)$  from the phase quadrature.

$$S_{xx}^{\text{imp}}(\omega) = \frac{x_{\text{zpf}}^2}{C\Gamma} \cdot \frac{1}{4\eta_2} \cdot \left(1 + \frac{4\omega^2}{\kappa^2}\right), \quad (4.16)$$

where the growth for large  $\omega$  is due to the lack of sensitivity to fluctuations outside of the cavity bandwidth. The product of the displacement imprecision and radiation pressure backaction spectral density then satisfies:

$$S_{xx}^{\text{imp}} \cdot S_{FF}^{\text{ba}} = \frac{\hbar^2}{4\eta_2} \geq \frac{\hbar^2}{4}, \quad (4.17)$$

which is one formulation of Heisenberg's uncertainty principle [20]: by increasing the cooperativity we are tracking more precisely the mechanical motion, at the cost of increasing the perturbation imparted by radiation pressure quantum noise. How closely the lower bound in 4.17 is met depends on the detection efficiency of the displacement measurement, on the presence of excess noises in the optical fields and on the existence of excess mechanical oscillator heating beyond radiation pressure backaction, for example from optical absorption [29, 185].

Imprecision and backaction fluctuations impose excess noise contributions, the first apparent and the second concrete, in the reconstruction of mechanical displacement. The overall spectrum of mechanical motion reconstructed at the cavity output (associated with a measurement variable  $\hat{y} = \hat{x} + \hat{x}_{\text{imp}}$ ) can be written as:

$$S_{yy}(\omega) = S_{xx}^{\text{th}}(\omega) + S_{xx}^{\text{imp}}(\omega) + |\chi_m(\omega)|^2 S_{FF}^{\text{ba}}(\omega) = S_{xx}^{\text{th}}(\omega) + S_{xx}^{\text{add}}(\omega) \quad (4.18)$$

we can choose the optimal input power to the cavity by minimizing  $S_{xx}^{\text{add}}(\omega)$  with respect to the cooperativity; at the optimum, the contributions of backaction and imprecision are perfectly balanced (see Figure 4.1). The minimum added noise at optimal C is given by:

$$S_{xx}^{\text{add}}(\omega) \geq \frac{\hbar}{\sqrt{\eta_2}} |\chi_m(\omega)| \geq \hbar |\chi_m(\omega)| := S_{xx}^{\text{SQL}}(\omega) \quad (4.19)$$

This lower bound is called the *standard quantum limit* of optomechanical displacement detection, and is depicted in yellow in Figure 4.1b. Evaluating  $S_{xx}^{\text{SQL}}$  at the mechanical resonance gives  $S_{xx}^{\text{SQL}}(\Omega) = 2x_{\text{zpf}}^2/\Gamma$ . By comparison with the fluctuation-dissipation relation of equation 2.58,

$$S_{xx}^{\text{th}}(\Omega) = \frac{4x_{\text{zpf}}^2}{\Gamma} \left( \bar{n} + \frac{1}{2} \right), \quad (4.20)$$

we can see that the effects of optomechanical displacement measurement add a noise equivalent to at least half a phonon on mechanical resonance.

In many optomechanics experiments, displacement sensing at the SQL is not directly accessible, because the added noise is overwhelmed by thermomechanical noise at any feasible intracavity power. This limitation is particularly stringent for room temperature experiments, where the oscillator's thermal occupation is usually very high

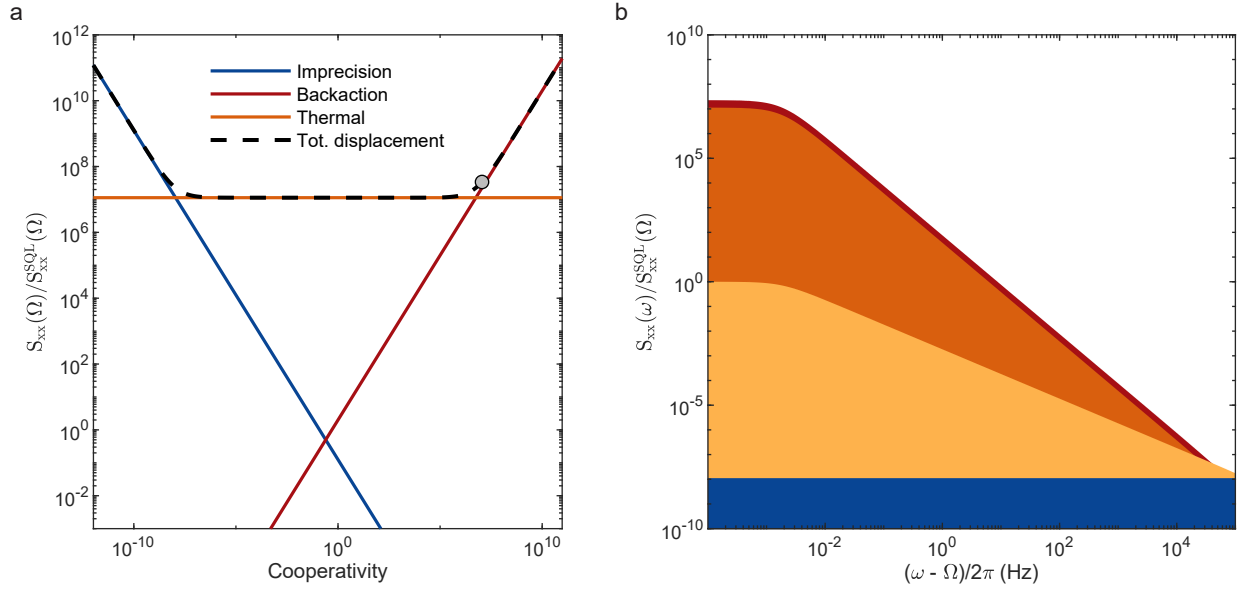


Figure 4.1: **a**, Displacement sensitivity on mechanical resonance as a function of the cooperativity, decomposed in the noise contributions from imprecision, backaction and thermomechanical motion. The thermal occupation of the oscillator is  $\approx 6 \cdot 10^6$ . **b**, Frequency-resolved displacement noise, corresponding to the cooperativity marked with a gray circle in the left panel ( $C_q = 2$ ). Spectra are normalized to the peak of the SQL spectrum, that is shown in yellow. The oscillator is assumed to have  $Q = 3 \cdot 10^8$ . As in the left panel, the imprecision spectrum is shown in blue, the thermal noise in deep orange and the radiation pressure backaction in red.

( $\approx 6 \cdot 10^6$  for a harmonic oscillator at 1 MHz). In order to perform quantum-limited position measurements of an oscillator undergoing thermal fluctuations, it is necessary that a major part of the oscillator's motion is excited by the backaction force vacuum noise:

$$\frac{S_{FF}^{ba}}{S_{FF}^{th}} \approx \frac{C}{\bar{n}} \cdot \frac{1}{1 + \frac{4\omega^2}{\kappa^2}} := \frac{C_q}{1 + \frac{4\omega^2}{\kappa^2}} \geq 1, \quad (4.21)$$

where the ratio was calculated in the high temperature limit  $\bar{n} \gg 1$ , and I have introduced the *quantum cooperativity*  $C_q = 4g_0^2 n_c / (\kappa \Gamma \bar{n})$ . The condition 4.21 is a prerequisite for many quantum optomechanics experiments. Due to the dominance of thermal fluctuations, radiation pressure shot noise at large intracavity powers was observed only quite recently [186, 187], and to the best of my knowledge, only in a single experiment employing a nanomechanical object at room temperature [54]. State-of-the-art experiments have now closely approached the SQL sensitivity limit [29], and employed quantum correlations to surpass it [188, 189].

#### 4.1.3 Ponderomotive squeezing

The optomechanical interaction creates correlations between the quadratures of the cavity field. As we have seen above, the amplitude quadrature of the cavity field generates radiation pressure shot noise, that induces (delayed) fluctuating motion in the

mechanical oscillator. In turn, the mechanical displacement is imprinted on the phase quadrature of the optical field, establishing a coupling between amplitude and phase. This is equivalent to what occurs in an optical medium with the Kerr effect, where four-wave mixing generates correlations that can lead to squeezing below the vacuum fluctuations of the optical field [190, 191]. In cavity optomechanics, *ponderomotive squeezing* is mediated by the mechanical susceptibility, and produced at frequencies close to resonance. Once again, ponderomotive squeezing is challenging to observe in the presence of large thermal noise, typically requiring  $C_q \gtrsim 1$  in order to be detected [177, 192–194].

In the case of pure phase quadrature detection described in the previous section (see equation 4.15), correlations do not manifest in the photodetection record. In order to observe quantum correlations and squeezing, mixed quadratures lying between the amplitude and phase of the output field should be detected. This can be done by either using a pump field detuned from resonance,  $\Delta \neq 0$  with direct photodetection at the cavity output port, or a resonant field,  $\Delta = 0$ , probed by homodyne detection. We will now focus on the latter case for analytical simplicity. For the same reason, we will restrict the calculations to the fast cavity limit,  $\kappa \gg \omega$ .

The detected quadrature is rotated of an angle  $\theta$  from the amplitude quadrature, by means of interference with a local oscillator:

$$\hat{X}_{\text{out}}^\theta = \hat{X}_{\text{out}} \cdot \cos\theta + \hat{Y}_{\text{out}} \cdot \sin\theta \quad (4.22)$$

The spectral density of this quadrature contains a cross-correlation term between the amplitude and phase of the output field:

$$S_{XX}^{\theta, \text{out}} = S_{XX}^{\text{out}} \cdot \cos^2\theta + S_{YY}^{\text{out}} \cdot \sin^2\theta + \bar{S}_{XY}^{\text{out}} \cdot \sin 2\theta, \quad (4.23)$$

that can be computed from the expression of the output field phase 4.15 and amplitude quadratures. Since  $\hat{X}_{\text{out}}$  is in the vacuum state, the field quadrature fluctuations spectrum can be expressed as:

$$S_{XX}^{\theta, \text{out}} \approx \frac{1}{2} + \frac{2\eta_2 C \Gamma}{\chi_{\text{zpf}}^2} \left( S_{xx}(\omega) \cdot \sin^2\theta + \frac{\hbar\eta_2}{2} \text{Re}(\chi_m(\omega)) \cdot \sin 2\theta \right), \quad (4.24)$$

where  $S_{xx}(\omega)$  is the oscillator's displacement noise, comprising thermal and back-action contributions, and the first term represents the shot noise (imprecision) background. For  $\theta \neq 0, \pi/2$  and in a limited frequency band close to resonance, the term in parentheses can be negative, and the fluctuations dip below the shot noise level, implying that the output field is squeezed. Note that the same ponderomotive radiation pressure correlations producing squeezing also reduce the displacement noise below the standard quantum limit in so-called variational measurements [188, 189, 195].

#### 4.1.4 Feedback cooling

As mentioned in section 4.1.1, the cavity dynamics can be exploited in the resolved sideband regime in order to efficiently cool the mechanical oscillator. In the case when

the cavity response is much faster than the oscillator's frequency,  $\kappa \gg \Omega$ , which is the regime of our MiM experiment, red-detuned cooling is less effective and does not permit cooling of the oscillator to the ground state. On the other hand, another technique is available in this regime, where the oscillator's motion is tracked faithfully: measurement-based *feedback cooling* (also known as *cold damping*) [29, 185, 196, 197]. Feedback cooling consists of synthesizing a feedback force from the measurement record of thermal and backaction-induced motion,  $90^\circ$  out of phase with the oscillator's displacement, in order to provide viscous damping. The feedback force is then applied to the oscillator through an external actuator, which can be for example a piezoelectric element or the radiation pressure of an auxiliary laser beam. By increasing the feedback cooling strength, the oscillator is gradually damped and cooled, eventually reaching the ground state if the thermal motion can be resolved with sufficient precision. This technique typically requires tracking the oscillator displacement with a cooperativity well-beyond the standard quantum limit, but radiation pressure heating does not impose any limit: the optomechanical backaction can be cancelled by the feedback force, as long as the intracavity power does not increase the thermal bath temperature through direct optical absorption.

A feedback force leading to oscillator cooling can be obtained with different control laws, but the simplest one to treat analytically is the case of a pure derivative controller. In this idealized scenario, the actuator imposes an additional force term on the oscillator, given, in the frequency domain, by [185]:

$$\hat{F}_{fb}(\omega) = i m_{\text{eff}} \omega g \Gamma \cdot (\hat{x} + \hat{x}_{\text{imp}}), \quad (4.25)$$

where  $g$  is a dimensionless gain parameter, proportional to the control effort of the feedback loop. At steady state, the effects of this force are a modification of the oscillator susceptibility to  $\chi_{\text{eff}}(\omega)$ , where the linewidth is increased by damping:

$$\chi_{\text{eff}}(\omega) = \frac{1}{m_{\text{eff}} (\Omega^2 - \omega^2 - i \Gamma (1 + g) \omega)} \quad (4.26)$$

and the introduction of additional force noise, given by the finite imprecision in the displacement record. The vacuum noise in photodetection results in force fluctuations that can heat up the oscillator at sufficiently large gains ( $g$ ). Their spectral density is given by:

$$S_{\text{FF}}^{\text{fb,imp}}(\omega) = m_{\text{eff}}^2 g^2 \Gamma^2 \omega^2 \cdot S_{\text{xx}}^{\text{imp}}(\omega) \quad (4.27)$$

The average phonon occupation of the oscillator can be obtained with the equipartition relation 2.78 applied to the oscillator's position fluctuations<sup>5</sup>:

$$\begin{aligned}\bar{n} &= \frac{1}{2} \left( \int_{-\infty}^{\infty} \frac{d\omega S_{xx}(\omega)}{2\pi\chi_{zpf}^2} - 1 \right) \\ &= \frac{1}{4\pi\chi_{zpf}^2} \left( \int_{-\infty}^{\infty} d\omega |\chi_{\text{eff}}(\omega)|^2 \left( S_{FF}^{\text{th}}(\omega) + S_{FF}^{\text{ba}}(\omega) + m_{\text{eff}}^2 g^2 \Gamma^2 \omega^2 S_{xx}^{\text{imp}}(\omega) \right) \right) - \frac{1}{2}\end{aligned}\quad (4.28)$$

The three terms within the integral on the right hand side of 4.28 establish a trade-off between cold damping of thermal and backaction fluctuations and heating by displacement imprecision. An optimal gain can be found that minimizes the occupation for a given displacement sensitivity. The minimum occupation corresponds to [185]:

$$\bar{n}_{\min} \approx \frac{1}{2} \left( \sqrt{\frac{1}{\eta} \left( 1 + \frac{1}{C_q} \right)} - 1 \right), \quad (4.29)$$

where  $\eta$  is an overall measurement efficiency that includes not only the coupling efficiency as in 4.16, but also the efficiency of the subsequent detection apparatus, e.g. finite homodyne visibility, finite quantum efficiency of the photodetector, thermal noise in the photodetector and signal amplifiers, etc. The phonon occupation of 4.29 corresponds to the occupation of the quantum state conditioned by the measurement record [29, 199], showing that the derivative filter is nearly an ideal control law for feedback cooling. Optimal filter responses can also be constructed with the theory of optimal control [200, 201], but so far have not shown a significant advantage over the derivative control law in improving the phonon occupation realized in experiments.

#### 4.2 MIM DISPERSIVE OPTOMECHANICS

The hamiltonian model of 4.2 is rather abstract and suitable to describe most cavity optomechanical systems, if one is not interested in the *a priori* calculation of the system interaction rates. For the case of a dielectric membrane with low optical losses inserted inside a Fabry-Pérot cavity, the dispersive optomechanics hamiltonian has been derived as a particular case of the radiation pressure interaction between a dielectric slab and a cavity field [202]. With this analysis, the frequency pull factor can be calculated numerically, and analytically under some approximations.  $G$  can be expressed as a product of a longitudinal and a transverse profile, with respect to the membrane position:

$$G = \frac{\omega_c}{L} \cdot \Lambda(z) \cdot \Theta(x, y), \quad (4.30)$$

where  $z$  is a coordinate running along the cavity axis,  $L$  is the cavity length, and  $x, y$  are coordinates in the transverse plane (parallel to the mirror surface). Note that, as

<sup>5</sup> Strictly speaking, the derivative control law 4.25 stabilizes the oscillator to a state in which the variance of the position is not equal to the variance of momentum fluctuations [198]. However, in experimental reality, the control law cannot have an infinite bandwidth as for an idealized derivative filter. In this limit the use of the equipartition law is appropriate.

seen before,  $\omega_c/L$  is the frequency pull factor for longitudinal motion of an end-mirror of the Fabry-Pérot cavity. The longitudinal profile is quasi-periodic in the membrane equilibrium position  $z$  (for a small excursion compared to the cavity length), and, when the membrane is placed in the vicinity of the cavity beam waist, is given by [203]:

$$\Lambda(z) \approx \frac{2|r|\sin(2kz)}{\sqrt{1-|r|^2\cos^2(2kz)}}, \quad (4.31)$$

where  $r$  is the membrane reflection coefficient and the wavevector  $k$  takes discrete values determined by the optical resonances. The transverse profile is the overlap integral between the mechanical mode shape and the intracavity optical intensity:

$$\Theta(x, y) = \int_{\Gamma} dp ds \phi(p, s) I(p - x, s - y), \quad (4.32)$$

where both the mechanical displacement  $\psi$  and the optical intensity  $I$  are normalized, such that  $\Theta \leq 1$ . In the case of a TEM<sub>00</sub> cavity mode and the simple tensioned square membrane of chapter 2, the overlap integrals for flexural modes indexed by  $(n, m)$  are given by [193]:

$$\Theta_{(n,m)}(x, y) = \exp\left(-\frac{w^2}{8} \left(\frac{n^2\pi^2}{B^2} + \frac{m^2\pi^2}{B^2}\right)\right) \sin\left(\frac{n\pi x}{B}\right) \sin\left(\frac{n\pi y}{B}\right), \quad (4.33)$$

where  $B$  is the membrane side length and  $w$  is the cavity beam waist at the membrane location. The Gaussian term induces a sharp cutoff of the optomechanical coupling rate for higher frequency mechanical modes, as the acoustic wavelength becomes smaller than the beam waist, and the sinusoidal terms reflect the vanishing of the “scattering amplitude” for membrane modes antisymmetric with respect to the probe field location. The longitudinal modulation expressed by 4.31 implies that, for a chosen mechanical mode, the optomechanical coupling rate varies strongly for different cavity resonances, being maximized when the membrane is located halfway between a node and an antinode of the cavity field. At these positions,  $|G| = \frac{2|r|\omega_c}{L} \cdot |\Theta|$ . Note that the frequency pull factor can be substantially larger when the membrane is placed close to one of the cavity mirrors [204], but this regime was not explored in our experiments.

The presence of the membrane also modifies the optical cavity damping rate  $\kappa$ , as discussed in [70, 203]. The modulation can be understood with the formation of two “sub-cavities” with different free spectral ranges, coupled by transmission through the membrane; the intracavity field experiences different mirror losses for different resonances. In experiments, the presence of additional damping sources complicates the picture, e.g. angular tilts of the membrane with respect to the cavity field, photon scattering from the edges of patterned membranes, and optical absorption by the membrane. The latter contribution is usually very small in the case of stoichiometric Si<sub>3</sub>N<sub>4</sub> [203].

#### 4.3 DESIGN AND ASSEMBLY OF THE FABRY-PÉROT CAVITY

We now proceed to the description of our experimental apparatus in practice. The foremost task for the realization of a MiM experiment is the design of the Fabry-Pérot



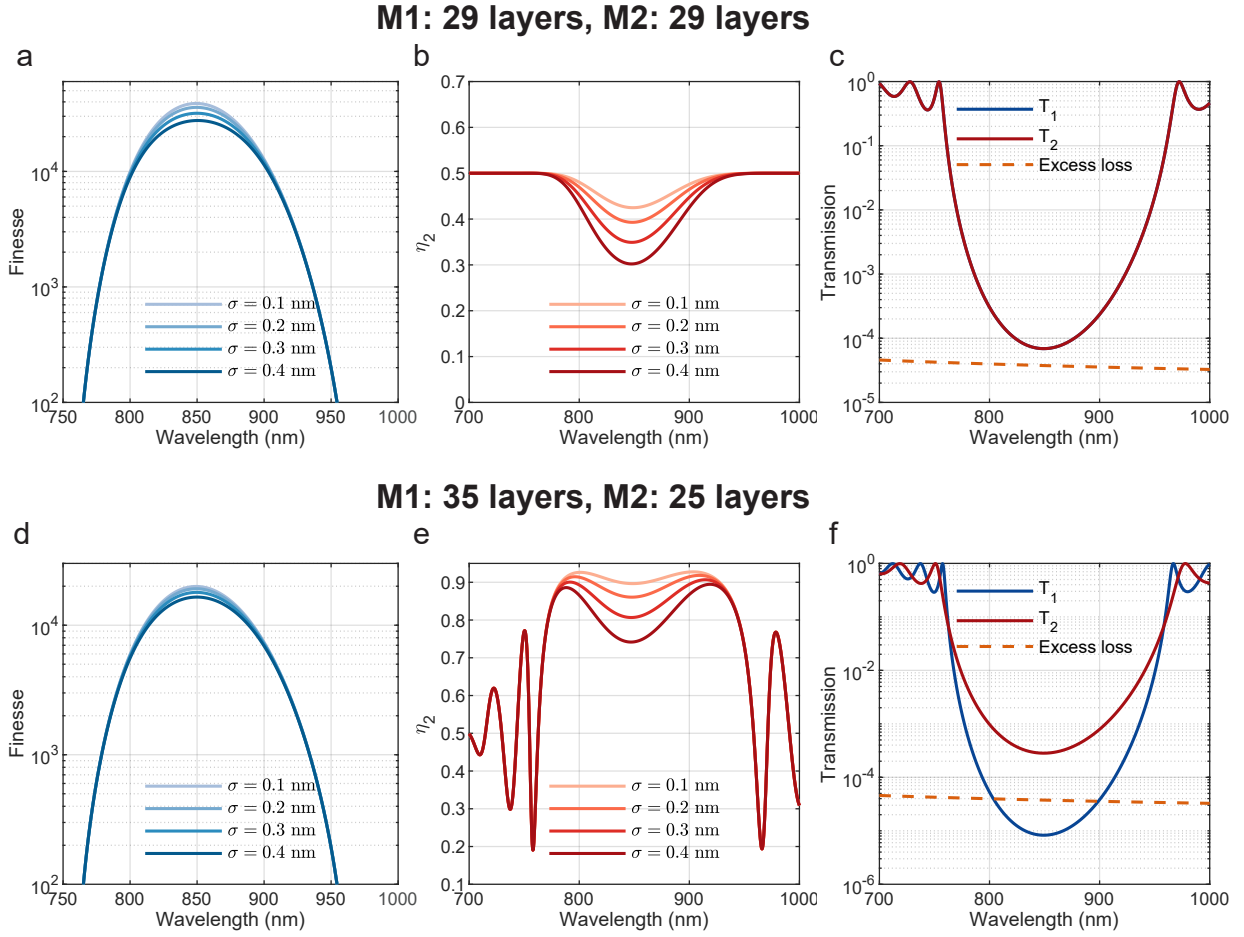


Figure 4.2: **a**, Cavity finesse, **b**, Coupling rate from curved mirror  $\eta_2 = \kappa_2/\kappa$  and **c**, Power transmission versus wavelength for a symmetric cavity with 29 dielectric film layers on both the flat and the curved mirror. The different curves in **a**, **b** are plotted assuming added optical losses from mirror surfaces roughness with RMS amplitude between 0.1 – 0.4 nm. The orange dashed curve in **c** corresponds to the scattering loss from a surface with RMS roughness of 0.2 nm. **d-f**, Similar calculations for an asymmetric cavity with 35 and 25 layers.

cavity. The reflectivity of the end mirrors must be appropriately selected in order to achieve as high as possible a finesse  $\mathcal{F} = 2\pi/(\text{total loss per round trip})$ , which increases the cooperativity of the system. At the same time, the cavity loss rate due to mirror transmission should be higher than the loss rate induced by the membrane, in order to retain an acceptable detection efficiency. The mirror reflectivities should preferably be asymmetric, since then one of the fields leaking out of the cavity will contain most of the mechanical information and the detection of this single field will provide high-efficiency displacement records. The mirror peak reflectivity and its reflection bandwidth can be tuned over a large range by employing dielectric Bragg mirrors, whose fabrication has reached levels of perfection sufficient to routinely achieve  $\mathcal{F} > 10^5$ . In collaboration with the coating supplier **FiveNine Optics**, we have realized different types of coating on planar and curved substrates. The planar substrates implement the input mirror in our cavity, and were fabricated by ion beam sputtering alternating  $\text{Ta}_2\text{O}_5$  and  $\text{SiO}_2$  dielectric layers on a borosilicate glass, superpolished wafer (Ohara

GmbH) with a thickness of 1 mm. The roughness after the polishing process was specified below 0.2 nm by the manufacturer (in terms of an average of the absolute value of the profile deviations from the mean). After the coating run, we diced the wafers into squares of  $9.9 \times 9.9$  mm for convenience of cavity assembly. For maximizing the reflectance, the coating film thicknesses are fixed to  $\lambda_0/4n_{L,H}$ , with  $\lambda_0 = 850$  nm being the center wavelength of the coating and  $n_{L,H}$  the refractive index of the dielectric films at 850 nm, corresponding to  $n_L \approx 1.45$  for  $\text{SiO}_2$  and  $n_H \approx 2.06$  for  $\text{Ta}_2\text{O}_5$ . The output mirror was realized with the sputtering of the same type of coatings on top of fused silica cylindrical substrates with a concave surface (radius of curvature 5 cm, mirror thickness 4 mm and diameter 7.75 mm), provided by FiveNine Optics. Finally, a simple anti-reflection coating (single layer) was sputtered on the opposite surface of either mirror.

The optical properties of the dielectric mirrors and of the empty cavity can be calculated with a simple transfer matrix model, by associating to each dielectric layer a matrix that connects the electric field and magnetic field amplitudes at the outer and inner interface [205]:

$$\begin{pmatrix} E_j \\ H_j \end{pmatrix} = \mathcal{M}_j \cdot \begin{pmatrix} E_{j-1} \\ H_{j-1} \end{pmatrix} \quad (4.34)$$

For orthogonal incidence<sup>6</sup>, the polarization is irrelevant. If the film thickness is chosen as  $\lambda_0/4n_j$ , the transfer matrix is then given by:

$$\mathcal{M}_j(\lambda) = \begin{pmatrix} \cos\left(\frac{\pi \lambda_0}{2 \lambda}\right) & iZ_0 \sin\left(\frac{\pi \lambda_0}{2 \lambda}\right) / n_j \\ in_j \sin\left(\frac{\pi \lambda_0}{2 \lambda}\right) / Z_0 & \cos\left(\frac{\pi \lambda_0}{2 \lambda}\right) \end{pmatrix}, \quad (4.35)$$

with  $Z_0 = \sqrt{\mu_0/\epsilon_0}$  being the vacuum impedance. The overall transfer matrix of the coating is simply the matrix product of the individual layer matrices. If the coating is realized with an odd number  $N$  of sputtered films:

$$\mathcal{M} = (\mathcal{M}_H \cdot \mathcal{M}_L)^{\frac{N-1}{2}} \cdot \mathcal{M}_H \quad (4.36)$$

and the mirror reflection coefficient can be calculated using the formula:

$$r_m = \frac{m_{11}/Z_0 + n_s m_{12}/Z_0^2 - m_{21} - n_s m_{22}/Z_0}{m_{11}/Z_0 + n_s m_{12}/Z_0^2 + m_{21} + n_s m_{22}/Z_0}, \quad (4.37)$$

where the  $m_{ij}$  are matrix elements of  $\mathcal{M}$ , and  $n_s$  is the substrate refractive index ( $n_s \approx n_L$  for fused silica). The results of this numerical modelling approach is shown in Fig. 4.2, where the finesse, the coupling efficiency from of the output coupler  $\eta_2 = \kappa_2/\kappa$  and the mirrors' power transmission are displayed. The calculation is repeated for the

<sup>6</sup> This condition is well satisfied in our Fabry-Pérot cavity, where the  $\text{TEM}_{00}$  modes do not contain components with large transverse wavevectors. This is due to the fact that the cavity length is much shorter than the top mirror's radius of curvature,  $L \ll R_M$ .

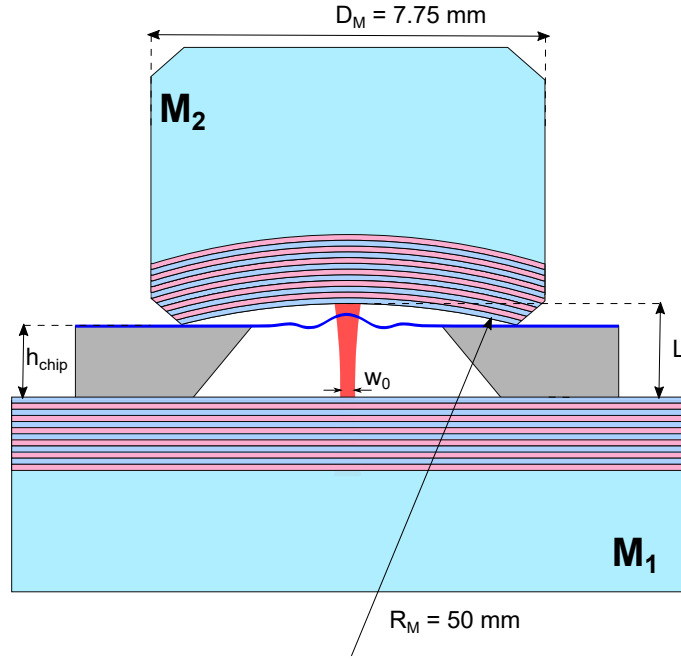


Figure 4.3: Schematic illustration of the compact MiM assembly.

two generations of MiM cavities we realized in the lab: the first, used for the experiments in [178], a symmetric cavity with a 29-layer coating on each mirror, and the current one an overcoupled cavity with 35 layers on the input and 25 layers on the output mirror. The modelled finesse agrees well with experimental characterization. In Fig. 4.2, I also added an intrinsic loss term of  $\sim (4\pi\sigma/\lambda)^2$ , modelling the scattering from mirror interfaces with an RMS roughness of  $\sigma$ , for reasonable roughness values quoted by the substrate suppliers. The intrinsic losses introduced by membrane clipping and tilt are more difficult to estimate and keep under control, so we always preferred to choose conservative mirror transmission values in order to realize reasonably-overcoupled cavities. The trends of Figure 4.2 hint at one practical advantage of the dielectric mirrors: for experiments in which a lower finesse is required, it is sufficient to seek cavity resonances detuned from the coating center wavelength. Around  $\sim 810$  nm, the finesse is reduced by a factor of about 2, but the coupling rate through the output mirror is retained. This can be useful for multimode optomechanics experiments, as will be discussed in the following.

The MiM cavity assembly is quite simple, and inspired by previous experiments in the research group of Albert Schliesser [29, 193]. After carefully cleaning the mirror surfaces and the backside of the membrane chip with lint-free swabs and an adhesive gel-pack (for collecting dust particles), the cavity is assembled by stacking vertically the flat mirror, the membrane chip and the curved mirror on top of the membrane chip. The top mirror diameter  $D_M = 7.75$  mm is smaller than the chip side length (8.75 mm), but larger than the membrane window frame size. Alignment of the cavity mode to the membrane PnC defect is achieved by gently translating the curved mirror on top of the membrane chip with tweezers, while monitoring the cavity reflection and imaging the mode waist in a dedicated setup. After good alignment has been achieved, the assembly is gradually clamped with a steel spring pushing on the top mirror, and

transferred to the experiment vacuum chamber. More details can be found in the thesis of Sergey Fedorov [70], and a schematic illustration of the cavity geometry is shown in Figure 4.3. The length of our MiM cavity is determined both by the membrane chip thickness  $h_{\text{chip}}$  and by the radius of curvature of the top mirror,  $R_M$  (see Fig. 4.3 for a definition of the geometric parameters):

$$L = h_{\text{chip}} + R_M - \sqrt{R_M^2 - D_M^2/4} \approx h_{\text{chip}} + \frac{D_M^2}{8R_M} \quad (4.38)$$

The total cavity length was  $L \approx 0.35$  mm for the experiments reported in [178] and  $L \approx 0.68$  mm in its more recent incarnation. The reason for the increased length was the switch to thicker silicon substrates in order to facilitate the membrane fabrication, from  $h_{\text{chip}} = 200$   $\mu\text{m}$  to  $h_{\text{chip}} = 525$   $\mu\text{m}$ . The average free spectral range<sup>7</sup> correspondingly changed from about 1.0 nm to 0.53 nm. We found both values suitable for the experiment, in which we need to select the optomechanical coupling rate by pumping different  $\text{TEM}_{00}$  resonances with a widely-tunable Ti:Sapph laser (Matisse, Sirah), emitting between 780 nm to 900 nm. In a planar-concave Fabry-Pérot cavity the beam waist is located on the flat mirror surface. Neglecting the presence of the membrane, we estimate the cavity waist ( $e^{-2}$  intensity radius) to be  $w_0 \approx 29$   $\mu\text{m}$  for the shorter and  $w_0 \approx 37$   $\mu\text{m}$  for the longer cavities, at 850 nm. The beam waist does not change significantly along the cavity, that is much shorter than the Rayleigh distance. The membrane designs are carefully checked so that, at the PnC defect location, the beam intercepts an unpatterned membrane area much larger than  $w_0$ , in order not to introduce significant optical scattering losses with the thin film edges.

#### 4.4 STRESS-MODULATED PNC MEMBRANES

The earliest membrane samples we fabricated for our room temperature MiM experiment were inspired by the soft clamped PnC devices first presented in [25]. By etching a periodic array of circular holes, arranged in a honeycomb lattice, in a high aspect ratio  $\text{Si}_3\text{N}_4$  membrane, the film stress acquires a spatial modulation, and a quasi-bandgap for flexural modes is opened close to the acoustic resonant frequency, in an analogous way to the density-modulated membranes introduced in Chapter 2. A defect in the PnC pattern is created by removing one of the holes, and by translating and/or deforming the neighbouring ones. For an appropriate defect geometry, one or more soft clamped modes with high quality factors will be hosted within the bandgap.

In contrast with the devices presented in [25], we maintained the same PnC honeycomb hole pattern but tweaked the defect design. Our main goals were hosting a single mode in the quasi-bandgap, and lowering the effective mass in order to improve the optomechanical coupling rate,  $g_0$ . The designs we conceived and fabricated are shown in Figure 4.4: we call them respectively *trampoline defect* (4.4a) and *triangular defect* (4.4b) membranes. They both feature a single flexural mode confined in the bandgap, a lower effective mass compared to the earliest PnC soft clamped membranes [25] (but similar to the device of [29, 188]), and a comparable quality factor (the dissipation-diluted  $Q$  is

<sup>7</sup> The presence of the membrane inside the cavity modulates the FSR, but on average the FSR corresponds to that of the empty cavity.

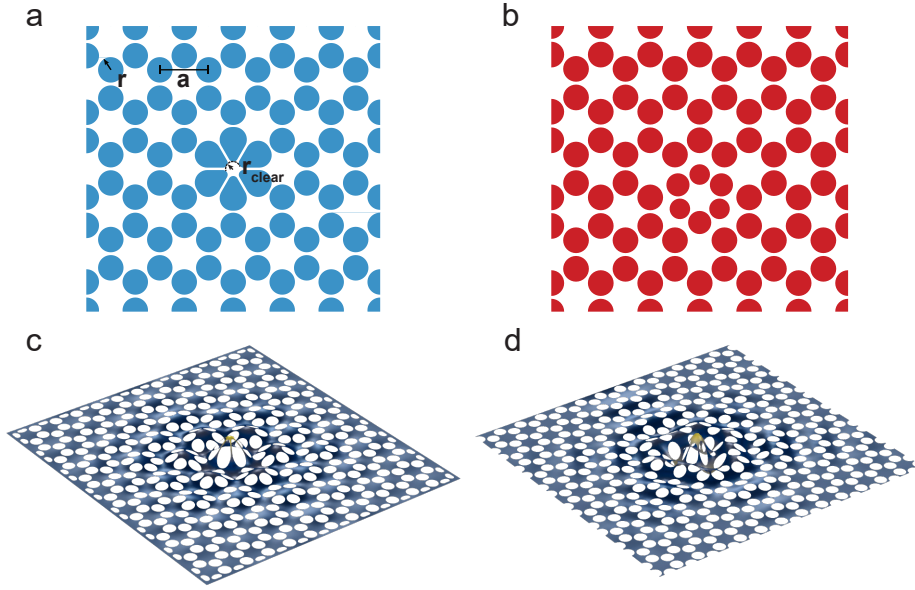


Figure 4.4: **a**, Trampoline defect membrane, PnC hole arrangement close to the defect. The hole radius  $r$  and unit cell pitch  $a$  are marked. **c**, FEM simulation of a soft clamped mode hosted by a PnC membrane with a trampoline defect. **b** and **d**, similar illustrations for a PnC triangular defect membrane. The simulated geometry has a lower number of unit cells compared to that of **c**.

quite robust to the defect geometry). The simulated parameters of our designs are summarized in Table 1, for a unit cell pitch  $a = 230 \mu\text{m}$  that corresponds to the formation of an acoustic bandgap around  $\sim 1 \text{ MHz}$ . Different mechanical frequencies were achieved by fabricating a membrane resonator with a uniformly-scaled pattern, as explained in section 2.3.3. The mechanical parameters of the trampoline defect membrane's soft clamped mode are slightly more favourable, but the triangular defect membrane offers a larger unpatterned area for interaction with the cavity mode ( $r_{\text{clear}}$  is the radius of the largest circle that can be inscribed in the membrane defect), and its soft clamped mode is almost perfectly located at the bandgap center. This can be appreciated from the thermomechanical spectra of the membrane devices, shown in Figure 4.5. The triangular defect PnC membrane thus produces a better approximation of single-mode optomechanics, and the thermal motion of neighbouring out-of-bandgap modes pollutes the frequency environment of the soft clamped mode less. The "spectral isolation" parameter in Table 1 refers to the frequency separation between the soft clamped mode and the closest flexural mode.

An important consideration for the design of PnC membrane resonators is the potential presence of flexural *edge modes*, localized by the phononic crystal close to the membrane edges (see Figure 4.6a). These edge modes are not soft clamped, typically exhibit a particularly low  $Q$  and have resonant frequencies close to or within the acoustic bandgap. They can occasionally be observed in cavity-enhanced displacement records (even if the optical mode is intercepting the defect, at the membrane center), and are deemed capable of hybridizing with the soft clamped mode and substantially degrade its mechanical  $Q$  [206]. They can be rendered innocuous, being shifted to very high frequencies, by an appropriate PnC patterning which extends all the way to the device's edges. In microfabrication, this requirement translates to achieving a good front-to-

Design	a ( $\mu\text{m}$ )	h (nm)	Dimensions	$r_{\text{clear}}$ ( $\mu\text{m}$ )	$\Omega/2\pi$ (MHz)
Trampoline	230	20	$2.8 \times 3.1\text{mm}$	33	0.962
Triangular	230	20	$3.0 \times 2.9\text{mm}$	56	1.048
Design	Q	$m_{\text{eff}}$ (ng)	$\sqrt{S_{F,\text{th}}}(\text{aN Hz}^{-1/2})$	Spectral isol. (kHz)	
Trampoline	$2.2 \cdot 10^8$	1.4	25	29	
Triangular	$1.9 \cdot 10^8$	1.9	33	84	

Table 1: Simulated geometric and mechanical parameters for the membranes in Figure 4.4. The thermomechanical force noise density  $S_{F,\text{th}}$  is computed for a temperature of 300 K. Finite elements simulation methods are discussed in section 2.3.5.

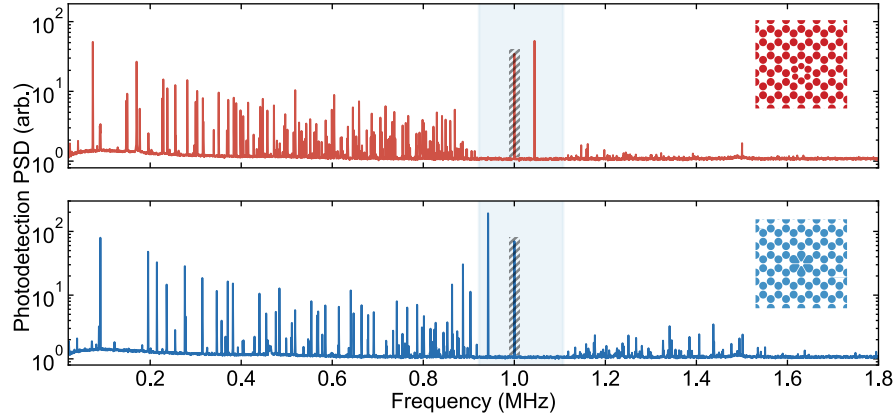


Figure 4.5: Thermomechanical spectra of our PnC membrane designs ( $a = 230\text{ }\mu\text{m}$  for both devices): top figure, triangular defect membrane; bottom figure, trampoline defect membrane. The data is acquired in the setup described in section 3.7.2 with the laser probe focused on the membrane defect. The peak at 1 MHz in both spectra (inside the hatched box) does not correspond to mechanical motion, but is phase noise associated with electromagnetic pickup. The acoustic bandgap is shaded in light blue.

back lithography alignment precision ( $\lesssim 10\text{ }\mu\text{m}$ ). I found the edge hole pattern illustrated in Fig. 4.6b to be suitable for the suppression of edge modes. The sharp corners of the semicircular holes have been smoothed, because they have been observed to produce local tears and defects in the suspended membrane devices, probably due to high stress concentration in the corners.

#### 4.4.1 Microfabrication walk-through

The fabrication process has been described in the original work that introduced soft clamping in  $\text{Si}_3\text{N}_4$  membranes [25]. We initially reproduced it, and later adapted it to facilitate the step of separation into individual chips by the use of a dicing saw, yielding cleaner microresonators ready for insertion in the optical cavity. Here I will shortly review the key points of microfabrication. This information was previously published as a short technical article on the [nanofab-net.org](http://nanofab-net.org) open access repository [207].



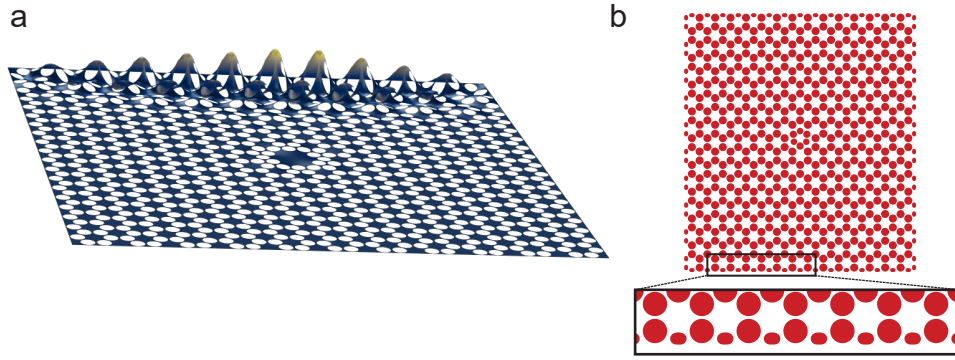


Figure 4.6: **a**, Simulated displacement profile of an edge mode at the lower bandgap edge. **b** Hole pattern that prevents edge mode localization (magnified in the lower box).

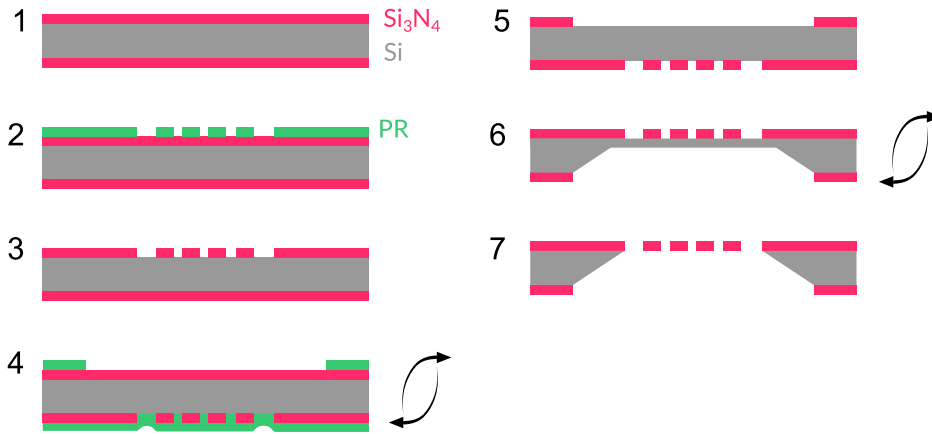


Figure 4.7: Simplified fabrication process of  $\text{Si}_3\text{N}_4$  membrane resonators. 1 –  $\text{Si}_3\text{N}_4$  LPCVD, 2 – Frontside layer lithography, 3 – Frontside layer dry etching, 4 – backside layer lithography, 5 – Backside layer dry etching, 6 – Partial KOH undercut and chip separation 7 – Membrane release with KOH etching. The curved arrows indicate that the wafer is flipped for processing on the opposite face.

Membrane samples are fabricated on 100 mm silicon wafers. Stoichiometric, high stress  $\text{Si}_3\text{N}_4$  is grown by low pressure chemical vapor deposition (LPCVD) on both sides of a 200  $\mu\text{m}$  or 525  $\mu\text{m}$ -thick silicon wafer, with (100) surface orientation<sup>8</sup>. The initial deposition stress is estimated a posteriori from the observation of membrane resonant frequencies, and varies in the range 900-1100 MPa, changing slightly with deposition run. The fabrication process relies on bulk wet etching of silicon in KOH through the whole wafer thickness, to create openings for optical access to the membranes samples [25, 208–210]. The extremely high selectivity of  $\text{Si}_3\text{N}_4$  to Si during KOH etching allows the use of the backside nitride layer as a mask, to define the outline of the membranes on the frontside.



#### 4.4.1.1 *Device layer and membrane windows patterning*

Initially, the frontside nitride ( $\text{Si}_3\text{N}_4$ ) layer is patterned with h-line UV photolithography (our photoresist of choice is MicroChemicals AZ ECI3007,  $\sim 600\text{ nm}$ -thick) and  $\text{CHF}_3/\text{SF}_6$ -based reactive ion etching (RIE) (steps 2-3 of figure 4.7). For devices with particularly thin features and where the dimensional control is crucial, such as the membranes presented in [58], we use ebeam lithography instead, with positive-tone,  $\sim 150\text{ nm}$ -thick ZEP520A as the mask. In the frontside mask, alignment markers should be included in regions optically accessible to the exposure tool used for backside alignment. I use 8 alignment crosses in the wafer peripheral regions to ensure a precise translation and rotation compensation over the majority of the wafer surface.

A careful removal of the spent photoresist is important, in order to avoid the formation of very hard-to-clean organic residues. We found a good procedure to be a short exposure to  $\text{O}_2$  plasma (600 W RF power, 30 seconds duration), followed by immersion in  $70^\circ\text{C}$  N-Methyl-2-Pyrrolidone (NMP) for at least 10 minutes, and then a final exposure to  $\text{O}_2$  plasma, for 3-5 minutes, to incinerate loose residues of the resist mask. This procedure is carefully repeated for each resist strip step, and after each we characterize the surface cleanliness with a scanning electron microscope.

The frontside nitride layer is then protected by spinning a  $\sim 3\text{ }\mu\text{m}$  layer of positive-tone photoresist (MicroChemicals AZ ECI3027), prior to flipping the wafer and beginning the patterning of membrane windows on the backside nitride layer (steps 4-5). We noticed a reduction in the occurrence of local defects and increased overall membrane yield when the unreleased membranes on the frontside were protected from contact with hot plates, spin-coaters and plasma etchers chucks, and this observation justifies the use of a protection layer. Alternatively, a couple micrometers of amorphous silicon (aSi) could be deposited by PECVD for the frontside protection. The advantages of such a protection layer are that it would get removed without effort by KOH exposure in step 7, and that it does not present the risk of contamination of the wafer chucks in the clean room tools, unlike a photoresist film. However, in our PECVD tool the deposition of a thick aSi film is problematic, so I have not investigated this alternative in depth.

The backside layer is then patterned with membrane windows, in a completely analogous way. The exposure step is done with an MLA150 laser writer, that features a set of optics dedicated to alignment with reference markers on the wafer backside. The critical dimension of this step is extremely large, so that practically any exposure tool with backside alignment capabilities should be suitable. It is crucial to remember to flip the backside mask design, to ensure a correct front-to-back alignment, and to obtain a precise alignment with the frontside markers, in order to avoid the generation of undesired, unpatterned membrane strips that can support the edge modes described in the previous section. Moreover, the membrane windows should be resized of an amount depending on the wafer thickness, to account for the slope of slow-etching planes in KOH. In fact, KOH etches silicon anisotropically, with the  $\langle 111 \rangle$  planes being attacked particularly slowly (likely due to a high atomic packing density). As a consequence, rectangular windows in the  $\text{Si}_3\text{N}_4$  mask result in cavities in the shape of truncated pyramids forming during wet etching, with a base angle of  $\arccos(1/\sqrt{3}) = 54.74^\circ$  (see

<sup>8</sup> We purchase LPCVD coating services from Hahn-Schickard-Gesellschaft für angewandte Forschung e.V. We observed particularly low mechanical intrinsic losses in their  $\text{Si}_3\text{N}_4$  thin films [58].

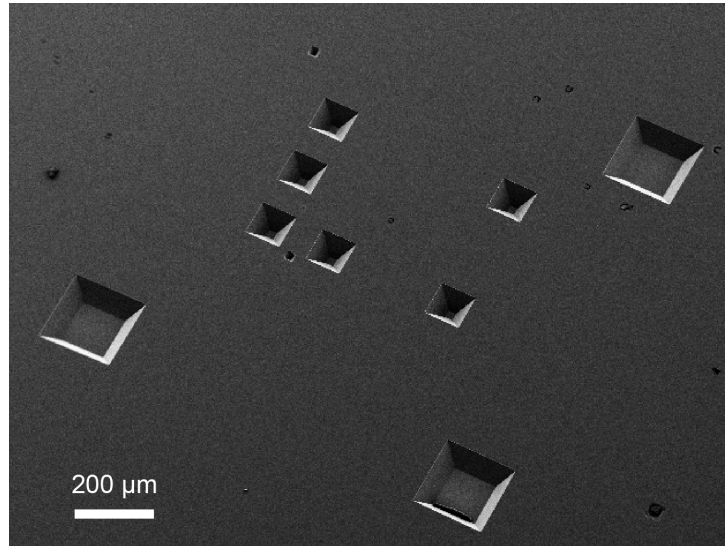


Figure 4.8: Truncated pyramid holes formed by KOH wet etching under square apertures. This hole arrangement represents an identifier pattern, resistant to exposure to KOH, for a membrane chip.

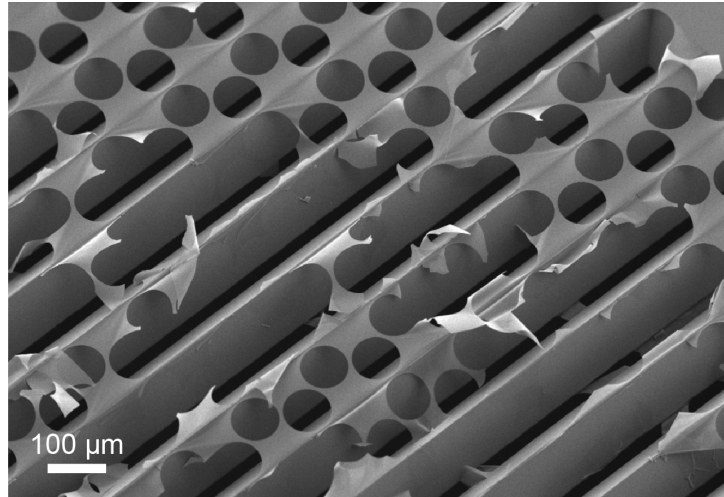


Figure 4.9: SEM micrograph of a PnC sample after partial double-sided undercut. Triangular prisms of silicon following [111] crystallographic directions are obtained as a result of anisotropic KOH etch below the PnC holes.

**Figure 4.8).** To compensate for the anisotropic etching, the backside rectangular mask should simply be larger of an amount  $\sqrt{2}h_{\text{chip}}$  in both dimensions, compared to the desired window size on the frontside.

#### 4.4.1.2 KOH deep etching

After stripping the photoresist and checking the surface quality on the device layer, the wafer is installed in a chemically-resistant PEEK holder<sup>9</sup> for the first wet etching step in KOH 40% at  $\approx 70^\circ\text{C}$  (step 6 in **Figure 4.7**). The holder clamps the wafer along its rim, sealing off the wafer frontside with a rubber O-ring, while exposing the backside to

<sup>9</sup> Single IL wafer holder by AMMT GmbH.

chemical etching by KOH. This procedure is necessary to ensure that PnC membranes are suspended correctly: we noticed that releasing PnC samples by etching from both sides of the wafer produced a large number of defects in the phononic crystal, probably due to the particular dynamics of undercut and stress relaxation in the film (see the SEM micrograph of a broken membrane in [Figure 4.9](#)). Instead, splitting the process in two steps works very well: the first etch from the backside should end 30–40  $\mu\text{m}$  short of suspending the  $\text{Si}_3\text{N}_4$  film (etched depth can be measured with an optical microscope with a high magnification objective and using a large aperture; the displacement of the stage between the positions where the surface and the bottom of the pit are in focus provides a good estimate of the etched depth), and the membrane release is performed as the last step, after the wafer has been separated into chips with a dicing saw.

The best practice for wet etching is to clean beakers and holders with IPA and fiberless cloths prior to the process. The concentration of KOH is regulated with the help of a buoyant density meter at room temperature, then the solution is heated to the desired temperature and we wait for the hotplate to stabilize; the temperature will overshoot significantly then drop down when the holder is inserted. We start a timer for the etch process when we see tiny  $\text{H}_2$  bubbles being produced at the exposed Si surfaces, which indicate that the Si native oxide has been stripped and the chemical reaction with silicon has started. A magnetic bar is used to stir the KOH bath and homogenize the temperature profile in the beaker, during the whole deep etch process.

The wafer is etched until 30–40  $\mu\text{m}$  of silicon remains (the etch rate along  $\langle 100 \rangle$  directions is about  $28 \mu\text{m h}^{-1}$  at this temperature), leaving the membrane samples robust enough to endure the subsequent fabrication steps. The PEEK holder mounts a lightbulb in a waterproof space behind the wafer, that can be used to check for light transmission from the remaining silicon membrane, occurring when  $\lesssim 20 \mu\text{m}$  of silicon are remaining. In my experience, it is best to stop the etching shortly before or just as soon as light starts to be transmitted from the silicon membranes, to maintain a better structural integrity. The wafer is then removed from the KOH bath and the PTFE holder, rinsed and cleaned in HCl 20% at  $55^\circ\text{C}$  for about 1 hour. This cleaning step removes some scattered contamination generally observed after KOH etching, probably due to iron oxide particles suspended in the KOH solution [\[211\]](#).

#### 4.4.1.3 Chip-scale undercut

After the partial silicon etching, the wafer frontside is coated with thick, protective photoresist (AZ ECI3027, thickness  $\sim 3 \mu\text{m}$ , with HMDS adhesion promoter and soft bake at  $90^\circ\text{C}$ ) and the wafer is separated into  $8.75 \text{ mm} \times 8.75 \text{ mm}$  chips using a dicing saw (the blades we use cut lines with a width of 30  $\mu\text{m}$  or 200  $\mu\text{m}$ ). The remainder of the process is carried on chip-wise. The photoresist is cleaned off the chips by means of hot solvents and  $\text{O}_2$  plasma, and the membrane release is completed by exposing chips to KOH from both sides (step 7; see [Figure 4.10](#))<sup>10</sup>. The temperature of the solution is lowered ( $\approx 55^\circ\text{C}$ , etch rate  $\sim 13 \mu\text{m h}^{-1}$ ), to mitigate the perturbation of fragile samples by buoyant  $\text{H}_2$  bubbles, a byproduct of the etching reaction. The reaction rate and  $\text{H}_2$  production rate scale, in fact, exponentially with the solution temperature. After the

<sup>10</sup> The survival yield of the delicate tensioned structures depends on their design and on the remaining Si thickness before this step. Both stress-modulated PnC membranes and the polygon resonators of [\[27\]](#) can be suspended successfully only if the silicon thickness is reduced to  $\lesssim 40 \mu\text{m}$  during the first backside etch step.

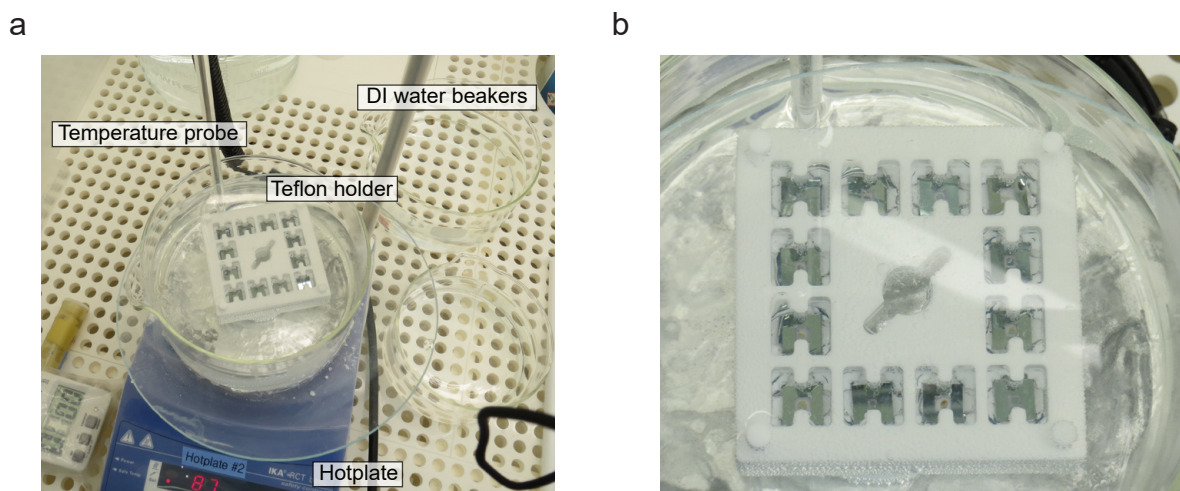


Figure 4.10: **a**, Membrane release step in hot KOH. The puddle holder shown in [Figure 3.6](#) is employed. **b**, Close-up of the membrane chips immersed in KOH. The bubbles lining the PTFE surfaces are byproducts of the silicon chemical etch.

undercut is completed, the samples are carefully rinsed, cleaned again in HCl and transferred to an ethanol bath. Rinsing should be thorough, especially when using a chip holder which constrains the flow in the orthogonal direction, but movements and transfers should be extremely gentle while the samples are immersed in liquids. The more delicate the samples, the gentler the displacements should be, in terms of mounting conditions, steadiness of movements, control of bath perturbations and all factors that can influence sample survival. Trampolines and strings are much more fragile than PnC and unpatterned membranes, for a fixed aspect ratio. A good rinsing procedure is slowly moving the chip holder up and down, crossing the interface of the DI water bath a couple of times. This should be repeated 3-4 times, each time using a fresh de-ionized water bath. To ensure that no traces of acids or bases are left after the rinsing step, the pH of the bath can be measured with an indicator strip. Since the puddle holder of [Fig. 3.6](#) presents narrow volumes that can be tricky to purge from acid/bases residues, for samples that are relatively robust to surface tension forces (like the PnC membranes), it is much more practical to utilize a holder where the chips are sitting vertically into slits with thickness of a couple millimeters, and where the liquids are completely flushed during the holder transfers. As the last step, the sample holder is moved to the chamber of a critical point dryer (CPD) filled with ethanol, in order to delicately dry the suspended devices. CPD is not strictly required, since stiction does not affect membrane samples where the substrate is completely undercut, but it is still useful: if done properly, it can be gentler and cleaner than manual drying. Before running the CPD cycle, we make sure that the samples are immersed sufficiently long in ethanol to let the liquid diffuse in the proximity of the chips. The membrane samples can then be examined with an optical microscope to check for visual defects (see [Fig. 4.11](#)), and brought to the setup shown in [section 3.7.2](#) for mechanical characterization.

Further insight on the wet release of high aspect ratio membranes can be gained by reading [\[212\]](#), where the authors reported on the fabrication methods of extremely large  $\text{Si}_3\text{N}_4$  membranes for applications as mask pellicles in EUV lithography.



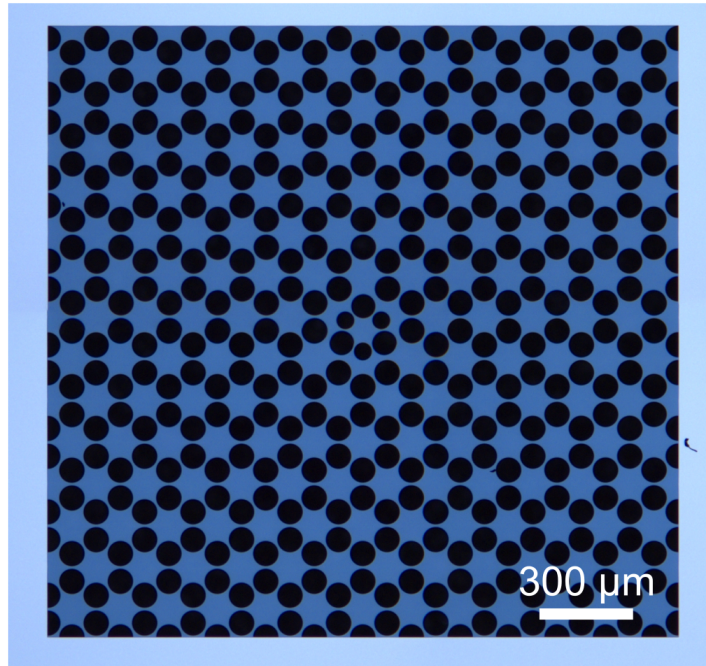


Figure 4.11: Optical microscope image of a suspended triangular-defect PnC membrane, at the end of the fabrication process.

#### 4.5 OBSERVATION OF THERMAL INTERMODULATION NOISE

The first experiments with our MiM cavity at room temperature led to the unexpected observation of substantial amplitude noise in the transmission spectra of the optomechanical cavity, that was clearly related to mechanical displacement. In particular, for the PnC soft clamped membranes described in the previous section, the amplitude noise was characterized by a flat and almost featureless background at the bandgap frequencies, several orders of magnitude beyond the vacuum fluctuations of the laser field. This was not explained by the naïve, linearized theory of cavity optomechanics (see section 4.1), where thermomechanical motion is presumed to be imprinted only on the phase fluctuations of the cavity field. We understood this noise process as being related to the optical cavity nonlinearity, and provided a quantitative analysis of its magnitude, finding an excellent agreement with our model. Although quadratic transduction was observed in different optomechanical cavities [213, 214], it was never reported in MiM systems, where the large density of highly-coupled modes unexpectedly results in a massive amplitude noise, that imposes significant constraints to quantum optomechanics. I will present here a summary of our findings [178].

The conventional framework in which optical measurements are described assumes linear transduction of cavity frequency fluctuations into the optical field, justified by the frequency excursions being small compared to the cavity linewidth. However, the nonlinearity of transduction is inherently present in any cavity. It gives rise to qualitatively new effects and results in the conversion of Gaussian fluctuations of cavity frequency into non-Gaussian fluctuations of the optical field. When a cavity is coupled to a quantum system, this phenomenon has been proposed for performing nonlinear

quantum measurements [213–215], which cannot be described within the leading order perturbation theory [38]. At the same time the nonlinear conversion of thermal frequency fluctuations can impose qualitatively new constraints on a broad range of precision experiments, which to date have not been analyzed.

We will show that nonlinear modulation of the optical field by thermal frequency fluctuations can manifest as a broadband added noise in detection, whose bandwidth is limited by the cavity decay rate. We refer to this noise as *thermal intermodulation noise* (TIN), since it mixes different Fourier components of cavity frequency fluctuations. This noise dominates when the linearly transduced thermal fluctuations are small, such as when detecting the intensity of near-resonant optical probe. As it is the leading-order contribution, TIN it is not necessarily negligible even when the nonlinearity of cavity transduction is small.

Using a  $\text{Si}_3\text{N}_4$  membrane resonator hosting a high-Q and low mass soft clamped mode, we operate at a nominal  $C_q \approx 1$ , i.e. in the regime where the linear measurement quantum backaction (arising from radiation pressure quantum fluctuations) is expected to overwhelm the thermal motion. This regime is required for a range of quantum enhanced measurement protocols [189, 216] and for generation of optical squeezed states [177, 192]. Yet, the nonlinearity of our cavity prevents the observation of quantum correlations between the field quadratures, and manifests itself in TIN significantly above the shot noise level. Surprisingly, we find that TIN dominates the fluctuations of the intensity of the optical field even when the thermally induced frequency fluctuations are substantially smaller than the cavity linewidth. Since TIN is a coherent effect, it only requires the knowledge of spectrum of cavity frequency fluctuations to be modeled, and our experimental data is well matched by a model with no free parameters.

We show that for a particular “magic” detuning from the cavity TIN is fully cancelled in direct detection. Our observations, while made for an optomechanical system, are broadly applicable, irrespective of the underlying thermal noise source. Thermal intermodulation noise can be of relevance to any cavity-based measurement scheme at finite temperature.

#### 4.5.1 Theory of TIN

We begin by presenting the theory of thermal intermodulation noise in the classical regime with the assumption that the cavity frequency fluctuations are slow compared to the optical decay rate. We concentrate on the lowest-order, i.e. quadratic, nonlinearity of the cavity detuning transduction. We consider (as in our experimental setup) an optical cavity with two ports, which is driven by a laser coupled to port one. The output from port two is directly detected on a photodiode. In the classical regime, i.e. neglecting vacuum fluctuations and treating the fields as complex numbers, the amplitude of the intracavity optical field,  $a$ , and the output field  $s_{\text{out},2}$  can be found from the input-output relations:

$$\dot{a}(t) = \left( i\Delta(t) - \frac{\kappa}{2} \right) a(t) + \sqrt{\kappa_1} s_{\text{in},1}, \quad (4.39)$$

$$s_{\text{out},2}(t) = -\sqrt{\kappa_2} a(t), \quad (4.40)$$

where  $s_{\text{in},1}$  is the constant coherent drive amplitude,  $\Delta(t) = \omega_l - \omega_c(t)$  is the laser detuning from the cavity resonance, modulated by the cavity frequency noise, and  $\kappa_{1,2}$  are the external coupling rates of ports one and two ( $\kappa_1 = \kappa_2$  in our case) and  $\kappa = \kappa_1 + \kappa_2$ . In the fast cavity limit, when the optical field adiabatically follows  $\Delta(t)$ , the intracavity field is found as:

$$a(t) = 2\sqrt{\frac{\eta_1}{\kappa}} L(\nu(t)) s_{\text{in},1}, \quad (4.41)$$

where we introduced for brevity the normalized detuning  $\nu = 2\Delta/\kappa$ , the cavity decay ratios  $\eta_{1,2} = \kappa_{1,2}/\kappa$  and Lorentzian susceptibility

$$L(\nu) = \frac{1}{1 - i\nu}. \quad (4.42)$$

Expanding  $L$  in equation 4.41 over small detuning fluctuations  $\delta\nu$  around the mean value  $\nu_0$  up to second order we find the intracavity field as:

$$a = 2\sqrt{\frac{\eta_1}{\kappa}} L(\nu_0) (1 + iL(\nu_0)\delta\nu - L(\nu_0)^2\delta\nu^2) s_{\text{in},1}. \quad (4.43)$$

According to equation 4.43, the intracavity field is modulated by the cavity frequency excursion,  $\delta\nu$ , and the frequency excursions squared,  $\delta\nu^2$ . By contrast, in the linearized optomechanical equation of motion 4.4, only the first two terms in the right hand side parentheses in equation 4.43 are retained. If  $\delta\nu(t)$  is a stationary Gaussian noise process, like typical thermal noises, the linear and quadratic contributions are uncorrelated (despite clearly not being independent). This is due to the fact that odd-order correlations vanish for Gaussian noise,

$$\langle \delta\nu(t)^2 \delta\nu(t + \tau) \rangle = 0, \quad (4.44)$$

where  $\langle \dots \rangle$  is the time average, for an arbitrary time delay  $\tau$ . Next, we consider the photodetected signal, which, up to a conversion factor, equals the intensity of the output light and is found to be

$$I(t) = |s_{\text{out},2}(t)|^2 \propto |L(\nu_0)|^2 \left( 1 - \frac{2\nu_0}{1 + \nu_0^2} \delta\nu(t) + \frac{3\nu_0^2 - 1}{(1 + \nu_0^2)^2} \delta\nu(t)^2 \right). \quad (4.45)$$

Notice that  $\delta\nu(t)$  and  $\delta\nu(t)^2$  can be distinguished by their detuning dependence [217]. The linearly transduced fluctuations vanish on resonance ( $\nu_0 = 0$ ), where  $\partial|L|^2/\partial\nu = 0$ . Similarly, when  $\partial^2|L|^2/\partial\nu^2 = 0$ , the quadratic frequency fluctuations vanish, and thus also the thermal intermodulation noise. We refer to the corresponding detuning values,

$$\nu_0 = \pm 1/\sqrt{3}, \Delta_0 \approx \pm 0.29 \cdot \kappa \quad (4.46)$$

as “magic”. In the following experiments, we perform measurements at  $\nu_0 = -1/\sqrt{3}$  and  $\nu_0 = 0$  to independently characterize the spectra of  $\delta\nu(t)$  and  $\delta\nu(t)^2$ , respectively.



The total spectrum of the detected signal,  $I(t)$ , is an incoherent sum of the linear term given by,

$$S_{vv}[\omega] = \int_{-\infty}^{\infty} \langle \delta v(t) \delta v(t + \tau) \rangle e^{i\omega\tau} d\tau, \quad (4.47)$$

and the quadratic term, which for Gaussian noise can be found using Wick's theorem [218]

$$\langle \delta v(t)^2 \delta v(t + \tau)^2 \rangle = \langle \delta v(t)^2 \rangle^2 + 2 \langle \delta v(t) \delta v(t + \tau) \rangle^2, \quad (4.48)$$

as

$$\begin{aligned} S_{vv}^{(2)}[\omega] &= \int_{-\infty}^{\infty} \langle \delta v(t)^2 \delta v(t + \tau)^2 \rangle e^{i\omega\tau} d\tau = \\ &= 2\pi \langle \delta v^2 \rangle^2 \delta[\omega] + 2 \cdot \frac{1}{2\pi} \int_{-\infty}^{\infty} S_{vv}[\omega'] S_{vv}[\omega - \omega'] d\omega', \end{aligned} \quad (4.49)$$

where  $\delta[\omega]$  is the Dirac delta function.

#### 4.5.2 Brownian intermodulation noise

In an optomechanical cavity, the dominant source of cavity frequency fluctuations is the Brownian motion of mechanical modes coupled to the cavity,

$$\delta v(t) = 2 \frac{G}{\kappa} x(t), \quad (4.50)$$

where  $G = -\partial\omega_c/\partial x$  is the linear optomechanical coupling constant, and  $x$  is the total resonator displacement, i.e. the sum of independent contributions  $x_n$  of different mechanical modes. The spectrum of the Brownian frequency noise is then found to be:

$$S_{vv}[\omega] = \frac{4G^2}{\kappa^2} \sum_n S_{xx,n}[\omega], \quad (4.51)$$

where  $S_{xx,n}[\omega]$  are the displacement spectra of individual mechanical modes. The thermomechanical frequency noise given by equation 4.51 produces TIN which contains peaks at sums and differences of mechanical resonance frequencies and a broadband background due to the off-resonant components of thermal noise. The magnitude of the intermodulation noise is related to the quadratic spectrum of the total mechanical displacement,  $S_{xx}^{(2)}$ , as:

$$S_{vv}^{(2)} = \frac{16G^4}{\kappa^4} \sum_n S_{xx,n}^{(2)}[\omega] \quad (4.52)$$

as will be discussed in the next section.

A reservation needs to be made: the theory presented in section 4.5.1 is only strictly applicable to an optomechanical cavity when the input power is sufficiently low, such

that the driving of mechanical motion by radiation pressure fluctuations created by the intermodulation noise is negligible; otherwise the fluctuations of  $x(t)$  and  $\delta v(t)$  may deviate from purely Gaussian and correlations exist between  $\delta v(t)$  and  $\delta v(t)^2$ . On a practical level, this reservation has minor significance for our experiment. On the other hand, the presence of linear dynamical backaction does not change the results of section 4.5.1 but does modify  $S_{xx}$ .

Thermal intermodulation noise can preclude the observation of linear quantum correlations, which are induced by the vacuum fluctuations of radiation pressure between the quadratures of light and manifest as ponderomotive squeezing [177, 192], Raman sideband asymmetry [219] and the cancellation of shot noise in force measurements [188, 189, 216]. The observation of quantum correlations typically requires selecting a mechanical mode with high quality factor,  $Q$ , a spectral neighbourhood free from other modes, and a high optomechanical coupling rate. If TIN is taken into account, simply increasing the quantum cooperativity is not sufficient, and the following condition also needs to be satisfied:

$$C_q \left( \frac{g_0}{\kappa} \right)^2 \Gamma \bar{n} \frac{S_{xx}^{(2)}[\omega]}{x_{zpf}^4} \ll 1. \quad (4.53)$$

From the condition given by equation 4.53, one can immediately observe that by reducing the mechanical dissipation and  $g_0/\kappa$ , one can keep the quantum cooperativity constant while lowering the intermodulation noise. The engineering of the mode spectrum to reduce  $S_{xx}^{(2)}$  at the desired frequency might also be a fruitful approach. One way to accomplish this would be selectively coupling the cavity to only one high- $Q$  mechanical mode so that  $S_{xx}^{(2)}$  is peaked at twice the mechanical resonance frequency and has most of its power outside a detection band centered on the mechanical resonance frequency. Selectively coupling to modes of solid-state mechanical resonators, however, is experimentally challenging, especially at low frequencies (MHz-range and below). The selectivity can be improved by working with the fundamental resonator mode, which has the largest RMS thermal displacement fluctuations and therefore dominates  $S_{xx}^{(2)}$ .

#### 4.5.3 Experimental observation with uniform membranes

We first characterize the TIN in cavities with 20 nm-thick  $\text{Si}_3\text{N}_4$  uniform square membranes of different sizes. In this experiment, the MiM cavity consists of two dielectric mirrors with 100 ppm transmission and a 200  $\mu\text{m}$ -thick silicon membrane chip, which is sandwiched directly between the mirrors. The total length of the cavity is around 350  $\mu\text{m}$ , the cavity beam waist for the  $\text{TEM}_{00}$  mode is about 35  $\mu\text{m}$ . The MIM cavity is placed in a vacuum chamber at room temperature and probed using a Ti:Sapph laser or a tunable external cavity diode laser at a wavelength around 840 nm, close to the maximum reflectivity wavelength of the mirrors (see Figure 4.2). The Ti:Sapph laser was used in all the thermal noise measurements, whereas the diode laser, whose emission frequency can be tuned more rapidly, was used for characterization of optical linewidths. The optomechanical cooperativity was kept low in order to eliminate dynamical backaction of the light; this is achieved by increasing the pressure in the vacuum chamber and keeping the mechanical modes gas damped to  $Q \sim 10^3$ . The

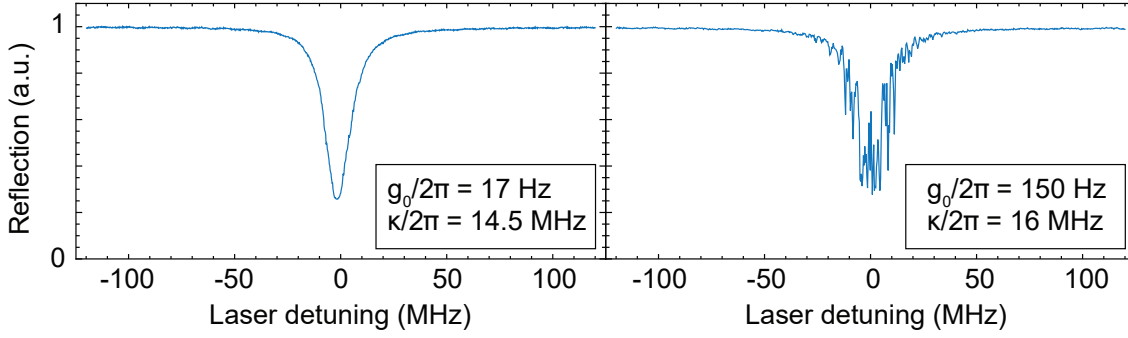


Figure 4.12: MiM cavity reflection signal as the laser is scanned over two resonances, with low (left) and high (right) optomechanical coupling. TIN is proportional to  $(g_0/\kappa)^4$  (see Figure 4.14), and induces large noise in the transmission signal from the highly-coupled resonance. The cavity is built around a 2 mm square  $\text{Si}_3\text{N}_4$  membrane.

reflection signals of two resonances of a MiM cavity, obtained by sweeping the laser wavelength over the resonance, containing a membrane with a side length of 2 mm are presented in Figure 4.12. The resonances have similar optical linewidths (about 15 MHz), but their optomechanical coupling is different by a factor of ten. The resonance with high coupling ( $g_0/2\pi = 150$  Hz) shows clear signatures of thermal noise. For this resonance the total RMS thermal frequency fluctuations are expected to be around 2 MHz, which is still well below the cavity linewidth,  $\kappa/2\pi = 16$  MHz. The detuning scan rates are approximately 1 THz/s for both plots in Figure 4.12.

Thermal fluctuations of the reflection signal are clearly observed in the right panel of Figure 4.12 even when the laser is resonant with the cavity. This is not expected in linear optomechanics, where the mechanical motion only modulates the phase of a resonant laser probe. Typical spectra of the detected noise are shown in Figure 4.13 for a cavity with a different, 1 mm, square membrane. With the laser detuned from the cavity resonance (close to the “magic” detuning,  $\nu_0 \approx -1/\sqrt{3}$ ), the transmission signal is dominated by the Brownian motion of membrane modes transduced by the cavity (shown in Figure 4.13a) and by the extraneous thermal noise from the mirrors (i.e. Brownian motion of the mirrors’ flexural modes [173, 203]), in agreement with the prediction of linear optomechanics. The magnitude of thermomechanical noise is gradually reduced at high frequencies due to the averaging of membrane mode profiles [193, 203] over the cavity waist, until it meets shot noise at around 15 MHz. With the laser on resonance, from linear optomechanics it is expected that the output signal is shot noise limited. However, the experimental signal (shown in Figure 4.13b) contains a large amount of thermal noise—at an input power of 5  $\mu\text{W}$  the classical relative intensity noise (RIN) exceeds the shot noise level by about 25 dB at MHz frequencies. The spectrum of the resonant RIN is different from the spectrum of detuning fluctuations, owing to the nonlinear origin of the noise. At high frequency, the RIN level approaches shot noise.

An unambiguous proof of the intermodulation origin of the resonant intensity noise is obtained by examining the scaling of the noise level with  $G/\kappa$ . In thermal equilibrium, the spectral density of frequency fluctuations,  $\delta\nu(t)$ , created by a particular membrane is proportional to  $(G/\kappa)^2$ , and therefore the spectral density of intermodulation

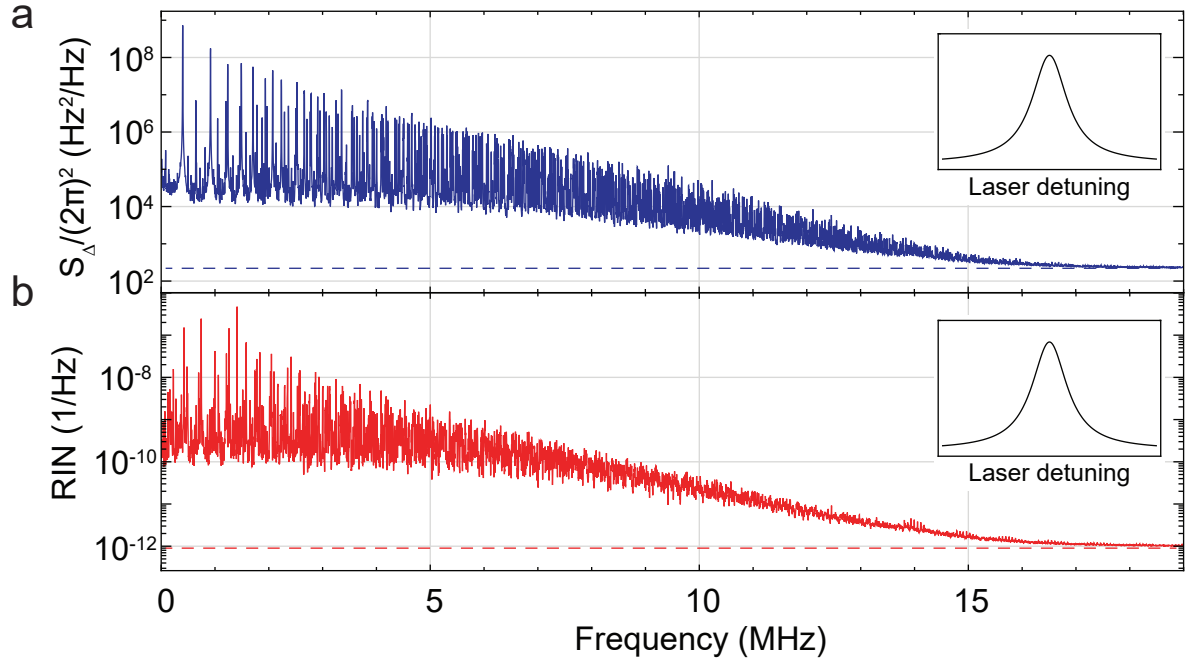


Figure 4.13: **a**, Detuning noise of a MiM cavity with a 1 mm square membrane,  $\kappa/2\pi = 26.6$  MHz and  $g_0/2\pi = 330$  Hz for the fundamental mode, measured at the laser detuning  $2\Delta/\kappa \approx -1/\sqrt{3}$ . **b**, Resonant RIN measured under the same conditions as in **a** but at  $\Delta = 0$ . The dashed line indicates for both plots the level of vacuum fluctuations, in terms of cavity frequency noise or RIN, respectively.

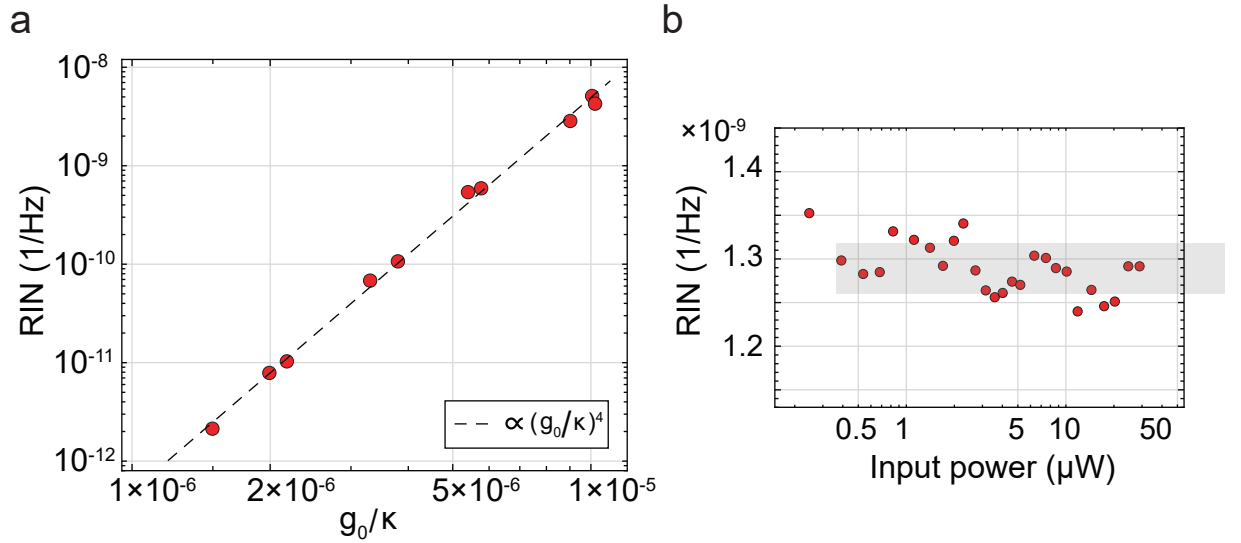


Figure 4.14: **a**, Dependence of the average RIN in a 0.6 – 1.6 MHz band on  $g_0/\kappa$ . **b**, Dependence of resonant relative intensity noise (RIN), averaged over 0.6 – 1.6 MHz, on the input power. Parameters:  $\kappa/2\pi = 9.9$  MHz,  $g_0/2\pi = 84$  Hz for the fundamental mode. The interval of  $\pm$  one standard deviation around the mean is shaded gray.

noise is expected to be proportional to  $(G/\kappa)^4$ . We confirm this scaling by measuring the resonant intensity noise for different optical resonances of a cavity with a 2 mm

membrane and present in [Figure 4.14a](#) the average noise magnitude as a function of  $g_0/\kappa$ , where  $g_0$  is the optomechanical coupling of the fundamental mode. By performing a sweep of the input laser power on one of the resonances of the same cavity we show (see [Figure 4.14b](#)) that the resonant intensity noise level is power-independent and therefore the noise is not related to radiation pressure effects.

The TIN observed in our experiments agrees well with our theoretical model. By first calculating the spectrum of linear detuning fluctuations according to equation [4.51](#) and then applying the convolution formula from equation [4.49](#) as follows, we can accurately reproduce the observed noise. The spectrum of the linear fluctuations,  $S_{vv}[\omega]$ , is a linear combination of thermomechanical motion of each mode, due to the fact that the Brownian motions of different modes are statistically independent. For an accurate modelling, we must take into account the position dependence of the frequency pull factor  $G$  (see section [4.2](#)). The transverse factor  $\Theta_{(n,m)}$  determines a different weight of different mechanical modes for both the linear and quadratic detuning fluctuations [[193](#)]. In the experiment, we calibrate the fundamental mode optomechanical coupling rate, and we can use  $G_{(1,1)}$  to simply express the contribution of higher order modes:

$$S_{vv}[\omega] = \frac{4G_{(1,1)}^2}{\kappa^2} \sum_{n,m} \left( \frac{\Theta_{(n,m)}}{\Theta_{(1,1)}} \right)^2 S_{xx,(n,m)}[\omega]. \quad (4.54)$$

The frequency dependence of  $\Theta_{(n,m)}$ , explicitly written down in equation [4.33](#), induces a cutoff in the detuning fluctuation spectra, when the acoustic wavelength becomes smaller than the cavity waist.  $S_{xx,n}[\omega]$  is given by the fluctuation-dissipation theorem, in the high temperature limit (see equation [2.59](#)):

$$S_{xx,(n,m)}[\omega] = \frac{2kT}{\omega} \text{Im}\{\chi_{(n,m)}[\omega]\} \quad (4.55)$$

where  $\chi_{(n,m)}[\omega]$  is the susceptibility of mode  $(n, m)$ . Recalling the results of section [2.3.2](#) a thin, high stress square membrane of side length  $L$ , supports flexural modes whose displacement is approximately given by products of sine waves (see section [2.3.2](#))<sup>11</sup>:

$$\phi_{(n,m)} = \sin\left(\frac{n\pi x}{L}\right) \sin\left(\frac{m\pi y}{L}\right), \quad (4.56)$$

with the mode frequencies  $\Omega_{(n,m)} = \frac{\pi}{L} \sqrt{\frac{\sigma(n^2+m^2)}{\rho}}$ . The effective mass for all modes is given by  $m_{\text{eff}} = \rho L^2 h/4$ , a quarter of the total mass of the membrane. For these experiments, the membrane is surrounded by a low vacuum environment: damping is predominantly viscous, with a constant damping rate given by  $\Gamma_{(n,m)} = \Omega_{(n,m)}/Q_{(n,m)}$ . Piecing it all together, the susceptibility of the mode  $(n, m)$  is given by

$$\chi_{(n,m)}[\omega] = \frac{1}{m_{\text{eff}} \left( \Omega_{(n,m)}^2 - \omega^2 - i\Gamma_{(n,m)}\omega \right)}. \quad (4.57)$$

<sup>11</sup> Non-flexural membrane modes present negligible optomechanical coupling and can be ignored for the modeling of linear and quadratic fluctuations.

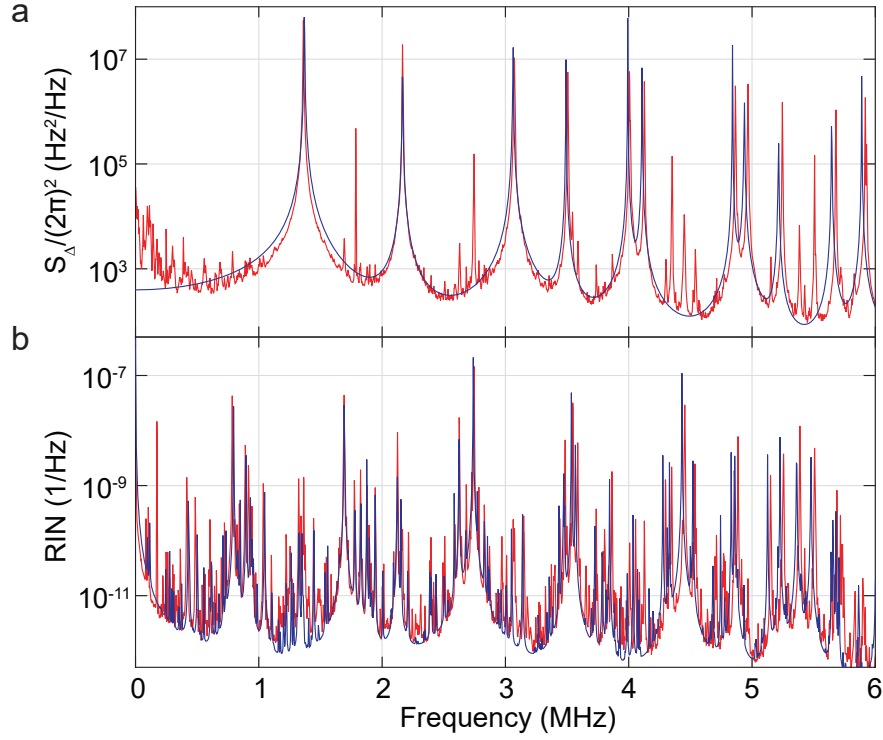


Figure 4.15: Comparison of theoretical and experimental frequency and resonant intensity noises. a) Detuning fluctuation and b) relative intensity noise spectra produced by the Brownian motion of a 20 nm-thick, 0.3 mm,  $\text{Si}_3\text{N}_4$  membrane. Red shows experimental data and blue is the theoretical prediction.

Once computed the linear fluctuation spectrum, the quadratic fluctuations of  $v$  can be calculated using the convolution integral of equation 4.49:

$$S_{vv}^{(2)}[\omega] = \frac{1}{\pi} \int_{-\infty}^{\infty} S_{vv}[\omega'] S_{vv}[\omega - \omega'] d\omega', \quad (4.58)$$

where we have dropped the DC term which is irrelevant to the numerical model. Finally the total photocurrent spectrum is obtained from equation 4.45.

In Figure 4.15, we compare the measured detuning and intensity noise spectra with the theoretical model. While this model is not detailed enough to reproduce all the noise features, it accurately reproduces the overall magnitude and the broadband envelope of the intermodulation noise observed in the experiment.

#### 4.5.4 TIN with a soft clamped PnC membrane

Next, we describe our observation of thermal intermodulation noise with a PnC membrane hosting a ultracoherent, soft clamped mode. Owing to their high  $Q$  and low effective mass, which result in low thermal force noise,  $S_{F,\text{th}} = 4k_B T m_{\text{eff}} \Gamma$ , these modes are promising for quantum optomechanics experiments [29], especially at room temperature [173], where the thermal fluctuations are preponderant. On the other hand, the high number of membrane modes probed by the optical cavity and the large Brownian motion amplitude at room temperature produce strong intensity fluctuations above

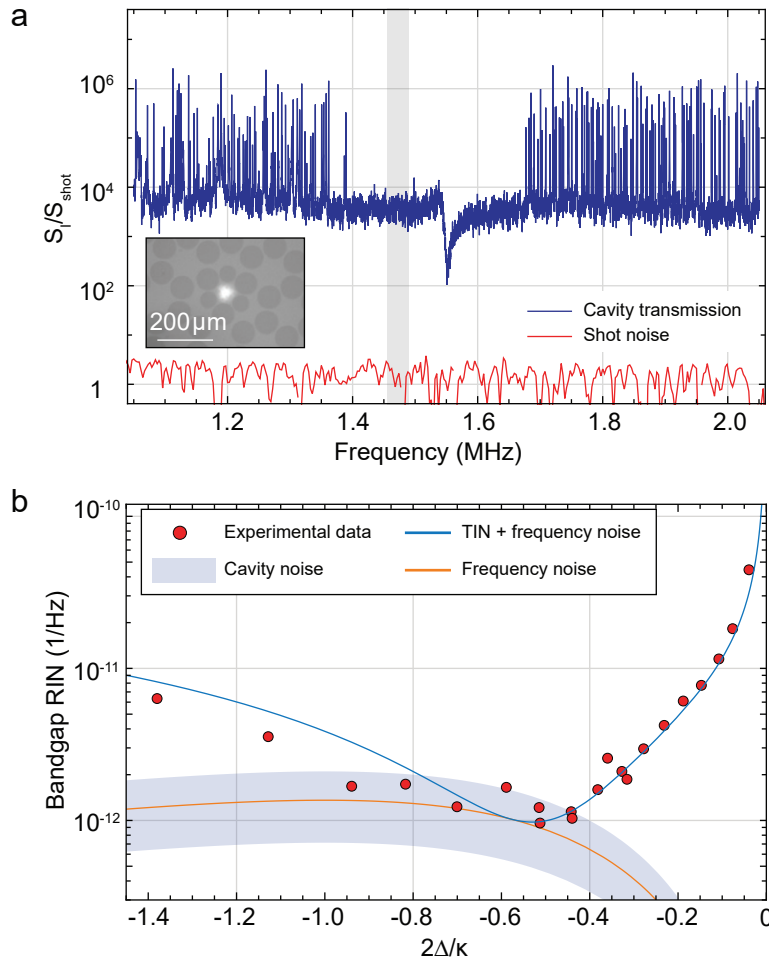


Figure 4.16: Measurement of the frequency spectrum and detuning dependence of TIN with a phononic crystal membrane. **a** Blue—photocurrent noise spectrum detected with the cavity-laser detuning set to  $2\Delta/\kappa \approx -0.3$ , red—shot noise level. The shaded region shows the noise averaging band for the plot in **b**. The inset shows an optical cavity mode (imaged at  $\lambda \approx 780$  nm) overlapping with the PnC membrane defect. **b** Variation of the relative intensity noise at bandgap frequencies with cavity-laser detuning. Red circles—experimental measurements, blue line—fit, orange line—cavity phase noise inferred from the fit, shaded blue region—independently calibrated cavity noise, with uncertainty given by the selection of the averaging band.

the quantum noise. For the measurements shown in this section, the pressure in the vacuum chamber was restored to  $\approx 5 \times 10^{-7}$  mbar, in order to operate at high vacuum cooperativity  $C_0$ . PnC membranes introduce slightly higher optical losses to MiM resonances, compared to unpatterned rectangular membranes, with a magnitude depending on the specific optical mode.

The phononic bandgap isolates soft clamped modes from the thermomechanical noise created by the rest of the membrane spectrum. Nevertheless, when a PnC membrane is incorporated in a MiM cavity the entire multitude of membrane modes contributes to the TIN even within bandgap frequencies, as TIN is produced by a nonlinear process. Figure 4.16a shows the spectrum of light transmitted through a resonance of a membrane-in-the-middle cavity with  $g_0/2\pi = 0.9$  kHz for the soft clamped mode,



$\kappa/2\pi = 34$  MHz and  $C_0 = 2.5$ . The noise at bandgap frequencies is dominated by TIN, which exceeds the shot noise by four orders of magnitude. The spectrum also shows a dispersive feature in the middle of the bandgap, which is a signature of classical correlations due to the intracavity TIN exciting the localized mechanical mode (the classical analogue of the ponderomotive squeezing described in section 4.1.3). The mechanical resonator in this case is a  $\approx 2$  mm, triangular-defect, square PnC membrane with the patterning shown in Fig. 4.11, but made of 40 nm-thick  $\text{Si}_3\text{N}_4$ . The membrane has a single soft clamped mode with  $Q = 4.1 \cdot 10^7$  at 1.55 MHz, as characterized immediately before inserting the membrane in the cavity assembly. The input power in the measurement was 100  $\mu\text{W}$  after correcting for spatial mode matching, which corresponds to a nominal  $C_q \approx 1$ . The shot noise level was calibrated in a separate measurement by directing an independent laser beam on the detector.

We then present in Figure 4.16b the dependence of the bandgap noise level on the laser detuning, measured on a different optical resonance of the same MiM cavity and at lower input power. The measurement shows that the in-bandgap excess noise is dominated by TIN at all detunings except for the immediate vicinity of the “magic” detuning  $\nu_0 = -1/\sqrt{3}$ . Around  $\nu_0 = -1/\sqrt{3}$  the excess noise is consistent with the mirror noise of an empty cavity. In the measurement in Figure 4.16b,  $g_0/2\pi = 360$  Hz for the localized mode,  $\kappa/2\pi = 24.8$  MHz and the input power was 30  $\mu\text{W}$ . The total noise level is well fitted by our model that includes both  $S_{\nu\nu}$  and  $S_{\nu\nu}^{(2)}$  contributions to the detected signal and accounts for the radiation pressure cooling (see section 4.1.1), as we now describe. From equation 4.45, the spectrum of intensity fluctuations of the output light is given by:

$$S_{II}[\omega] \propto \frac{4\nu_0^2}{(1 + \nu_0^2)^2} S_{\nu\nu}[\omega] + \frac{(3\nu_0^2 - 1)^2}{(1 + \nu_0^2)^4} S_{\nu\nu}^{(2)}[\omega]. \quad (4.59)$$

In an optomechanical cavity operated at high input power  $S_{\nu\nu}$  and  $S_{\nu\nu}^{(2)}$  in general are detuning-dependent because of the laser cooling/amplification of mechanical motion.

In order to find the precise dependence of  $S_{II}$  on  $\Delta$  some specific assumptions need to be made about the operating regime and the frequency of interest. In Fig. 4.16b, the noise level is estimated at the bandgap frequency (see the shaded gray band in Fig. 4.16a) and therefore only the mirror noise is expected to contribute to  $S_{\nu\nu}$ . The mechanical modes of the mirrors are relatively weakly coupled to the intracavity light and therefore the dynamical backaction for them can be neglected, resulting in detuning-independent  $S_{\nu\nu}$ . The intermodulation noise contribution, on the contrary, is significantly affected by laser cooling. It is natural to suggest (and it is advocated for by the very good agreement of our conclusions with experimental data) that TIN at bandgap frequencies is dominated by the mixing products of resonant and off-resonant parts of the membrane thermomechanical spectrum. Dynamical backaction reduces the mechanical spectral density on resonance  $\propto 1/\Gamma_{\text{DBA}}$ , where  $\Gamma_{\text{DBA}}$  is the optical damping rate (see equation 4.9) and  $\Gamma_{\text{DBA}} \gg \Gamma_m$  is assumed. On the other hand, DBA does not

affect the off-resonant spectral density. In the unresolved-sideband regime, which is typically well fulfilled in our measurements, the optical damping rate is given by<sup>12</sup>:

$$\Gamma_{\text{DBA}} = -32 \frac{\Omega_m}{\kappa} \left( \frac{2g_0}{\kappa} \right)^2 \frac{\nu_0}{(1 + \nu_0^2)^3} \eta_1 |s_{\text{in},1}|^2, \quad (4.60)$$

and under our assumptions the spectral density of quadratic frequency fluctuations at PnC bandgap frequencies follows the detuning dependence of  $1/\Gamma_{\text{DBA}}$ ,

$$S_{\nu\nu}^{(2)} \propto \frac{(1 + \nu_0^2)^3}{|\nu_0|}, \quad (4.61)$$

for  $\nu_0 < 0$ .

Motivated by this consideration, the experimental data in [Figure 4.16b](#) is fitted with the model:

$$S_{\text{II}} \propto \frac{4\nu_0^2}{(1 + \nu_0^2)^2} C_1 + \frac{1}{|\nu_0|} \frac{(3\nu_0^2 - 1)^2}{1 + \nu_0^2} C_2, \quad (4.62)$$

where  $C_1$  and  $C_2$  are free parameters. It should be stressed that although  $S_{\nu\nu}^{(2)}$  is globally related to  $S_{\nu\nu}$  via convolution, there is, in general, no relation between the two spectra at one given frequency, and therefore two independent parameters are required to reproduce the detuning dependence of  $S_{\text{II}}$ . As shown by the fit result, represented with the blue curve in [Figure 4.16b](#), the model very well reproduces the observed variation of output noise with detuning and the value of  $C_1$  found from the fit is indeed consistent with independently measured mirror noise, as shown in [Figure 4.17](#).

The intensity of the detected light in our measurement is proportional to the intensity of the intracavity field. Therefore, the suppression of TIN at the magic detuning necessarily implies the suppression of the corresponding radiation pressure noise, which otherwise can lead to classical heating of the mechanical oscillator and thereby limit the true quantum cooperativity, i.e. the contribution of radiation pressure shot noise to the oscillator heating.

#### 4.6 MEMBRANES WITH A SOFT CLAMPED FUNDAMENTAL MODE

PnC soft clamped membranes, by design, support a multitude of flexural modes below the bandgap frequencies: in order to provide a reasonable suppression of the displacement field before the clamped edges, the membrane must comprise at least several unit cells in each direction. In a MiM cavity, as we have seen, the low order flexural modes can display a frequency pull factor as high as the soft clamped mode, thus inducing strong intermodulation noise on the cavity field, at room temperature.

Alternative designs of the mechanical resonator can dramatically influence the magnitude of intermodulation noise, and even render it negligible at all relevant optical intensities. The PnC string resonators of [chapter 3](#), for example, exhibit a mode density

<sup>12</sup> This DBA damping rate expression can be obtained from [equation 4.9](#) by making explicit the detuning dependence of the photon number in  $g$ :  $g^2 = (2g_0^2/\kappa)^2 \eta_1 |s_{\text{in},1}|^2 / (1 + \nu^2)$ .

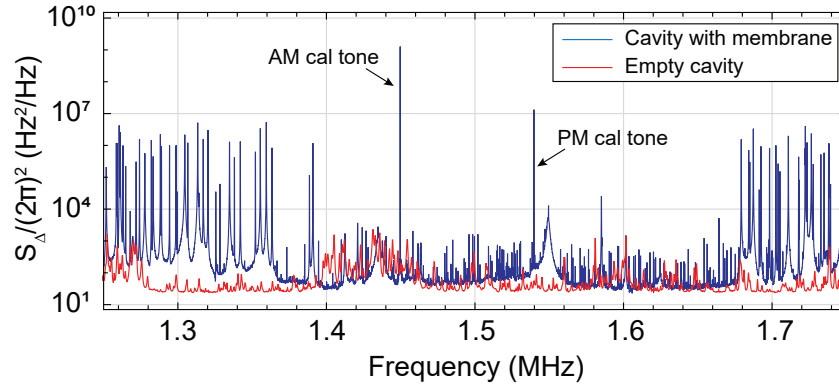


Figure 4.17: Red trace, spectrum of thermal detuning fluctuations at  $\sim 1.5$  MHz due to the mirror noise, measured for an empty Fabry-Pérot cavity with the same length (assembled with a perforated silicon chip as a spacer), but without a membrane. Blue trace, thermal detuning spectrum of the MiM cavity, corresponding to the  $2\Delta/\kappa \approx -0.51$  point in Figure 4.16.

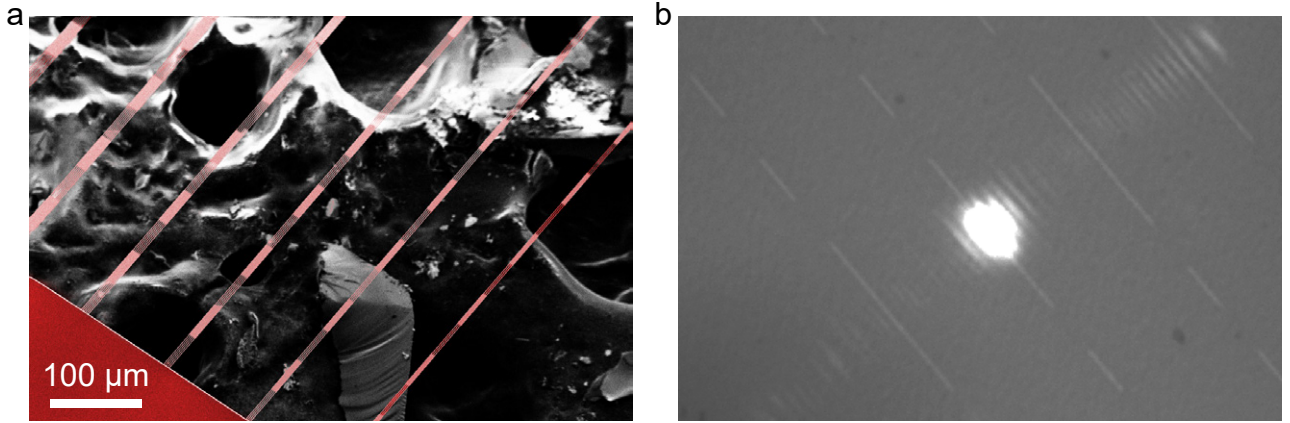


Figure 4.18: **a**, False-color SEM image of suspended PnC nanostrings, with the substrate completely removed. The string width increases from right to left in the image. Unit cell buckling (see Figure 3.16) is avoided by “joining” multiple strings in the width direction. The irregular surface visible below the strings in grayscale is carbon tape used for mounting the chip on the SEM sample holder. **b**, Imaging of an optical cavity mode centered on one of the nanostrings (courtesy of Sergey Fedorov). Significant optical losses are observed, which are clearly related to the diffraction from the string visible in the image.

linear with frequency, and are predicted not to generate significant intermodulation noise at room temperature. However, it is not trivial to integrate them in a Fabry-Pérot cavity, as the beam waist needs to be much smaller than their transverse width in order to retain a decent optomechanical coupling and not to introduce large optical dissipation. Our attempts at building this type of “string-in-the-middle” cavities (see Fig. 4.18) did not produce spectacular optomechanical parameters, and a sizeable dissipative coupling ( $d\kappa/dx$ ) was observed for the in-plane mode close in frequency to the localized out-of-plane mode. However, we did not dedicate an intense effort to the

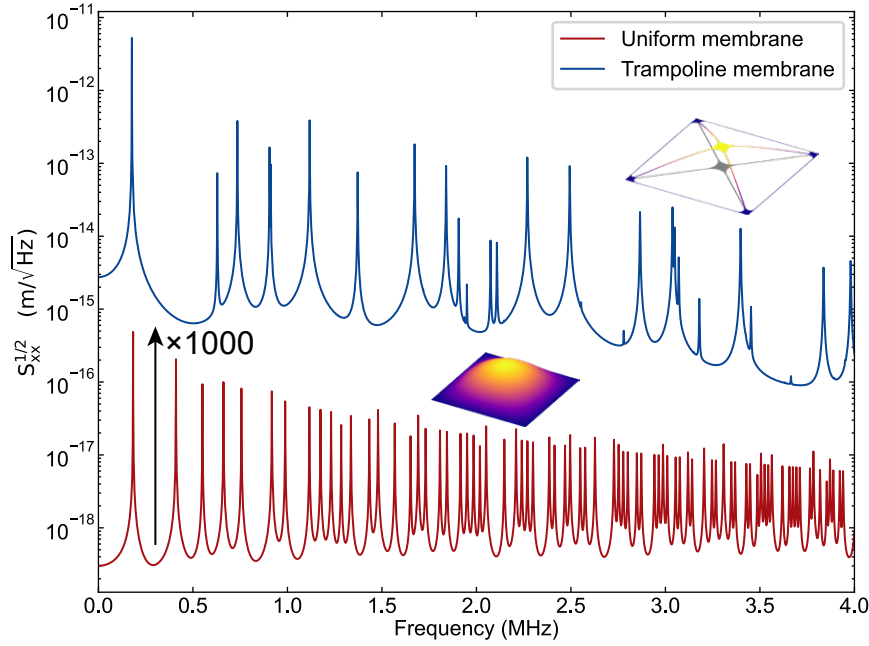


Figure 4.19: Simulated cavity-transduced (the mechanical peaks are weighted by  $\Theta_n^2$ ) thermo-mechanical displacement of a uniform membrane (red) and of a trampoline resonator (blue) with matched fundamental frequency. The uniform membrane spectrum has been shifted down by  $10^{-3}$  for clarity, and the  $Q$  of all the mechanical modes has been arbitrarily fixed to 2000 to facilitate the numerical evaluations.

development of this system, which remains, on paper, interesting. Other groups have achieved interesting regimes using similar optomechanical platforms [169]. Tensioned trampoline resonators [208, 209, 220, 221] are more interesting resonators for the MiM paradigm, as they possess a pad that facilitates integration with an optical cavity, and a vibrational spectrum that is very similar to that of a pair of crossed strings [126] (see the comparison between trampoline and square membrane thermomechanical spectra in Figure 4.19). In this type of devices, the highest-cooperativity mode is the fundamental out-of-plane oscillation, exhibiting a displacement extremum at the location of the pad. These modes possess high quality factors, roughly equivalent to the  $Q$  of the fundamental mode of a string whose length is equal to twice the trampoline tether's length. The fundamental mode, is also well-isolated in frequency from the higher order bending modes, without the need of an acoustic bandgap. However, these modes are not soft clamped, and there is room for optimization of their mechanical damping.

In the course of this thesis work, we have shown how to soft clamp the fundamental mode of a trampoline and significantly increase its quality factor, by constructing hierarchical networks of tethers. This builds on a previous theory work [222], where we showed that the displacement gradient of a flexural mode is suppressed over a three-beam joint and fractal-like strings can exhibit enhanced quality factors. I will present two trampoline designs with ultrahigh  $Q$  for the fundamental mode: a trampoline with branching tethers, a direct extension of the fractal-like string idea, and the “steering wheel” trampoline, that is easier to fabricate in practice. I will also discuss the pitfalls in their nanomechanical design. These resonators exhibit a clear interest for cavity optomechanics, but they are not straightforward to integrate in a high-performance

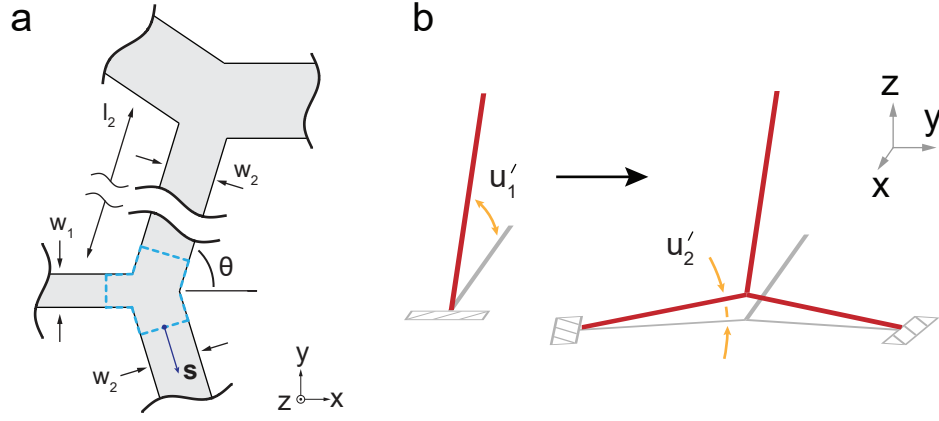


Figure 4.20: **a** Two branching points of a binary-tree resonator, with the branching angle  $\theta$ , the segment widths  $w_n$  and lengths  $l_n$  labelled. The dashed blue contour is employed to derive the transformation of the displacement derivative. **b**, Illustration of the effect of the three-beam branch on the displacement derivative when the structure is deformed out of the  $xy$  plane. The dashed rectangles indicate the structure anchoring pads.

MiM cavity. Their fundamental mode, in fact, is very susceptible to anchoring losses (see section 2.3.6.6), in contrast with PnC-localized resonances, that are intrinsically well-isolated from the substrate. Applying pressure to the chip boundaries in order to assemble a stable cavity will invariably result in mechanical  $Q$  degradation, and this needs to be overcome with appropriate assembly techniques or acoustic isolation structures in the membrane substrate [111, 112]. Recently, researchers at McGill university devised a method of clamping a trampoline resonator chip without spoiling its mechanical quality (at the level of  $Q \sim 2 \cdot 10^7$ ), by loading it using sapphire hemispheres that apply a point contact to appropriate locations on the chip surface [223].

#### 4.6.1 Displacement gradient suppression over a three-beam branch

As seen in section 2.3.2, the dissipation dilution of a tensioned membrane or string flexural mode crucially depends on the displacement gradient as the standing wave approaches the clamping points. The displacement gradient close to the clamping region determines the boundary curvature (see equation 2.85), which dominates the linear lossy energy, and soft clamping techniques suppress it by engineering the resonator shape. An interesting situation in which suppression of the flexural mode gradient occurs is when a string flexural mode propagates over a branch point. In order to show this, we consider a junction of three beams with rectangular cross section, highlighted by the blue contour in Figure 4.20a. The dynamic equation for the two-dimensional profile of out-of-plane vibrations  $u(x, y)$  is given by [33]:

$$-\frac{\partial}{\partial x_i} \left( \sigma_{ij} \frac{\partial u}{\partial x_j} \right) = \Omega^2 \rho u, \quad (4.63)$$

which generalizes equation 2.79 to the case of a strong but inhomogeneous stress field: the components of the stress tensor  $\sigma_{ij}$  are functions of  $x$  and  $y$ . By integrating both

sides of equation 4.63 over the infinitesimally small area of the contour and transforming the divergence into a boundary integral we find

$$\oint ds_i \left( \sigma_{ij} \frac{\partial u}{\partial x_j} \right) = 2 w_2 \sigma_2 u'_2 - w_1 \sigma_1 u'_1 = 0, \quad (4.64)$$

where  $u'_1$  and  $u'_2$  are the amplitude gradients in the directions of axes  $x_1$  and  $x_2$ , respectively. We assumed that the mode branches symmetrically and correspondingly doubled the contribution of  $u'_2$ . Next, the balance of static tensile forces requires

$$w_1 \sigma_1 = 2 w_2 \sigma_2 \cos(\theta). \quad (4.65)$$

Combining equations 4.64 and 4.65 we find

$$u'_2 = u'_1 \cos(\theta). \quad (4.66)$$

Equation 4.66 shows that the mode gradient is reduced by a factor of  $\cos(\theta)$  after propagating over a branch point. This is schematically illustrated in Fig. 4.20b. Although the reduction in principle can be arbitrarily large if  $\theta$  is close to  $\pi/2$ , the improvement in dissipation dilution provided by a single branch point is fairly limited. The reason is an associated increase in the distributed lossy energy caused by the torsional deformation of the beams. As seen in section 2.3.4, torsion carries a contribution to the linear elastic energy<sup>13</sup>:

$$\Delta W^{(\text{lin})} \approx \frac{E h^3 w}{12} \int dx \left( \frac{d\tau(x)}{dx} \right)^2, \quad (4.67)$$

where  $\tau(x)$  is the cross-section rotation angle and  $x$  is a longitudinal coordinate running along the beam segments. The equilibrium of force moments at the junctions define the boundary conditions for the torsion angles. At the beginning of the segment, the angle is set by the previous segment as  $\tau_n = u'_{n-1} (l_{n-1}) \sin(\theta)$ . If the aspect ratio of the segment is high (which we assume in the following), the transition from  $\tau_n$  to zero happens linearly and  $\tau' = \tau_n / l_n$ .

Nevertheless, cascading multiple branchings and forming a *binary-tree* structure can greatly reduce the overall lossy energy, and realize soft clamping for the low order flexural modes; an SEM image of such a nanomechanical resonator is shown in Figure 4.21. Exhaustive details on the modelling of dissipation in binary-tree strings are provided in [222].

#### 4.6.2 Trampoline membranes with branching tethers

The design concept of cascaded branching can be applied to the tethers of a trampoline resonator, to enhance the quality factor of its fundamental mode. We implemented two designs: the first one consists of two orthogonal binary trees combined with a pad, as

<sup>13</sup> The geometrically-nonlinear energy component can be neglected if the widths of the binary-tree string segments close to the antinodes is small enough.



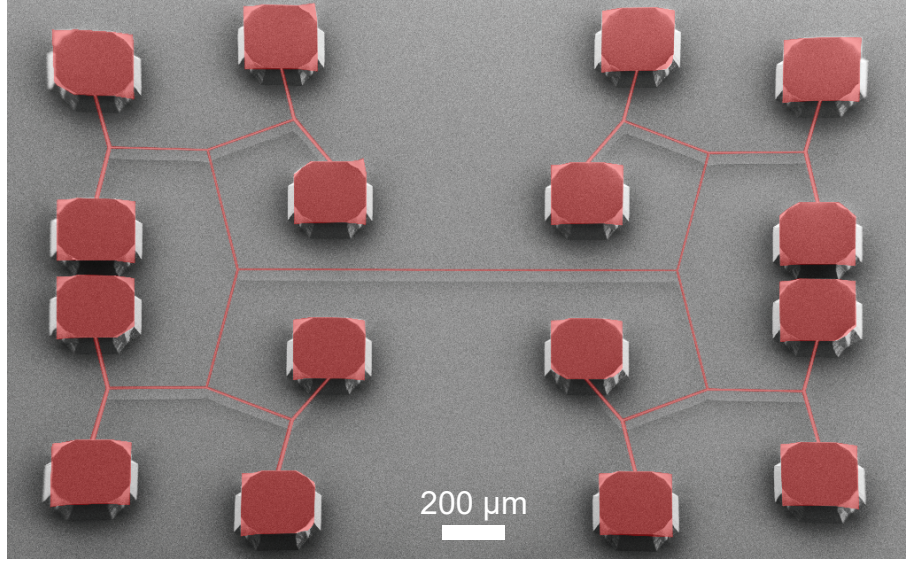


Figure 4.21: Scanning electron micrograph of a binary-tree beam with three branching levels, courtesy of Mohammad Bereyhi.

shown in Figure 4.22a; the second design, which we term a “steering wheel” membrane, can be produced from the first one by pairwise joining half of the segments at the 2<sup>nd</sup> branching generation (Figure 4.22b). Steering wheels are particularly simple to fabricate (their fabrication follows the process described in section 4.4.1), but have effectively only one generation of branchings, limiting the achievable dissipation dilution levels. Interestingly, similar geometries were obtained in [224] through a topology optimization algorithm, and experimentally demonstrated in [225]. Integration of the self-similar trampolines with a backside window is possible but makes the last steps of the fabrication process a little more sensitive; for this reason, in the device displayed in Figure 4.22a, the silicon substrate is still present below the trampoline. In both our membrane designs, the junctions are not exactly self-similar, and the width profiles of their segments are fine-tuned to optimize quality factors while maintaining constant stress. In the fabricated devices, the pad size varies between 35 and 85  $\mu\text{m}$ . We also show in Figure 4.22c a self-similar trampoline device with a backside window opened through the chip thickness. This requires a careful timing of the chip-scale KOH etching step in order not to create undesired overhang at the clamping points. The trampoline in Figure 4.22c exhibited a low quality factor: its particular design was formulated when we were not fully aware of the buckling constraints outlined in the next section, and exhibited pronounced static deformation in the largest branches. Correspondingly, the measured  $Q$  of  $\sim 9 \times 10^6$  was more than an order of magnitude lower than the numerical dissipation dilution prediction.

The fundamental modes of our trampolines are partially soft clamped, which can be seen from the suppression of mode gradients towards the peripheral clamping points in Figure 4.23c and d. The experimental results for devices with lateral extent between 0.5 mm and 2 mm are summarized in Figure 4.24. We observed quality factors of fundamental trampoline modes as high as  $Q = 2.3 \times 10^8$  at  $\Omega_m/2\pi = 100$  kHz and  $Q = 1.7 \times 10^7$  at  $\Omega_m/2\pi = 470$  kHz. We remark that the self-similar trampo-



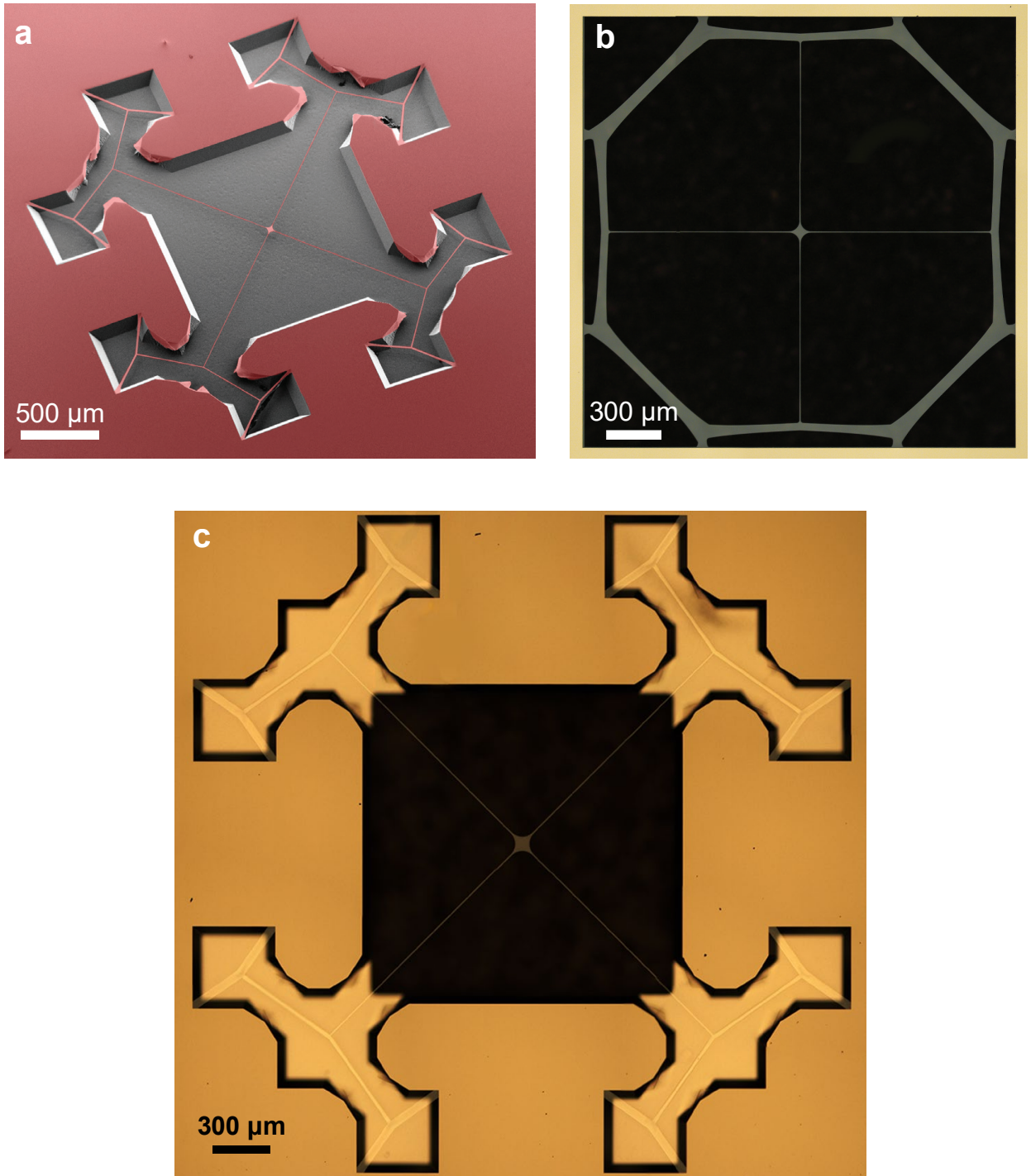


Figure 4.22: Trampoline membranes with partial soft clamping. **a**, Scanning electron micrograph of a trampoline resonator with branching tethers. The silicon substrate is recessed by about  $80\text{ }\mu\text{m}$  below the trampoline. **b**, Optical microscope image of a steering wheel membrane, enclosed in a square frame of about  $2.2\text{ mm}$  side length. The silicon substrate is completely removed below the sample. **c**, A trampoline resonator with branching tethers, with the underlying substrate removed by deep etching, to create an optical window. The membrane thickness is  $20\text{ nm}$ , while the chip is about  $200\text{ }\mu\text{m}$ -thick.

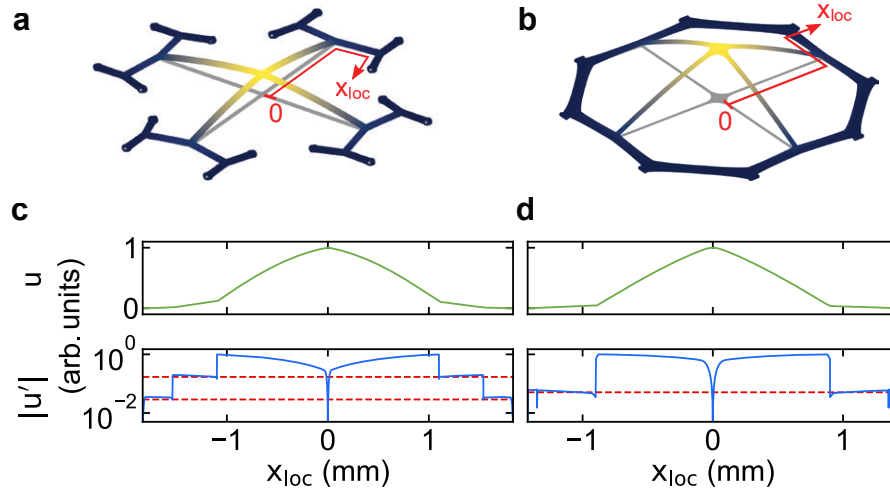


Figure 4.23: **a-b**, FEM-simulated displacement profiles of the trampoline and steering wheel fundamental modes. **c-d**, Displacement profile (green) and its first derivative (blue) evaluated along the red paths highlighted in **a** and **b**. The red dashed line indicates the step-like gradient suppression after a bifurcation, by a factor of  $\cos(\theta)$  (cfr. equation 4.66).

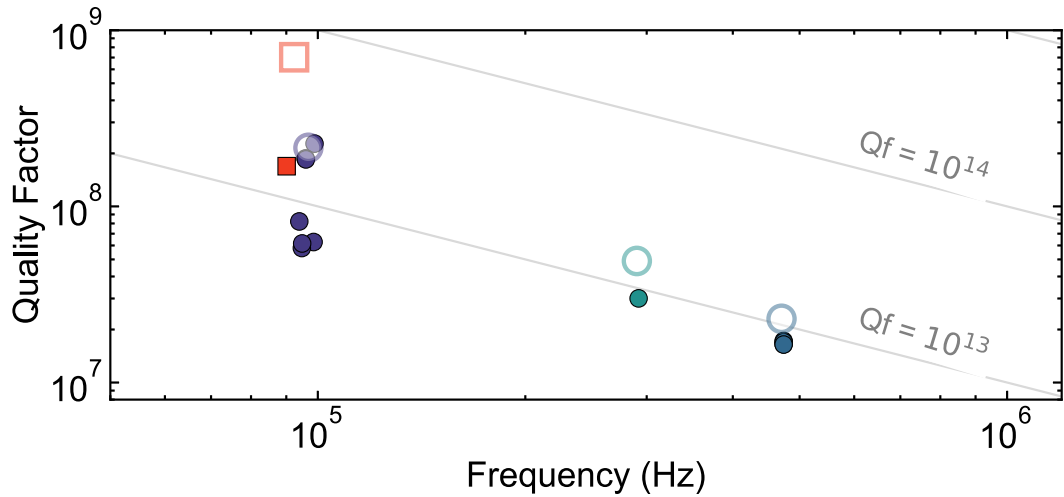


Figure 4.24: Measured quality factors of self-similar and steering wheel trampolines. Squares represent trampolines with branching tethers, while circles corresponds to steering wheels. Colors differentiate distinct designs. Measurements of individual devices are displayed with filled symbols, while open symbols portray the  $Q$  factors predicted with a finite element model.

line membrane exhibited a  $Q$  about 3.5 times lower than the finite element prediction (red symbols in Figure 4.24), potentially due to out-of-plane static deformations that we observed in the suspended device, as we will discuss in the next section. These dissipation dilution levels are a factor of three beyond those of the original trampoline designs [208] at the same frequencies. Trampolines with branching tethers, with a smaller pad (about  $35\mu\text{m}$ ) and lower effective mass (260 pg) than steering wheels, exhibit  $\sqrt{S_F} \approx 3.7\text{ aN/Hz}^{1/2}$  at room temperature.

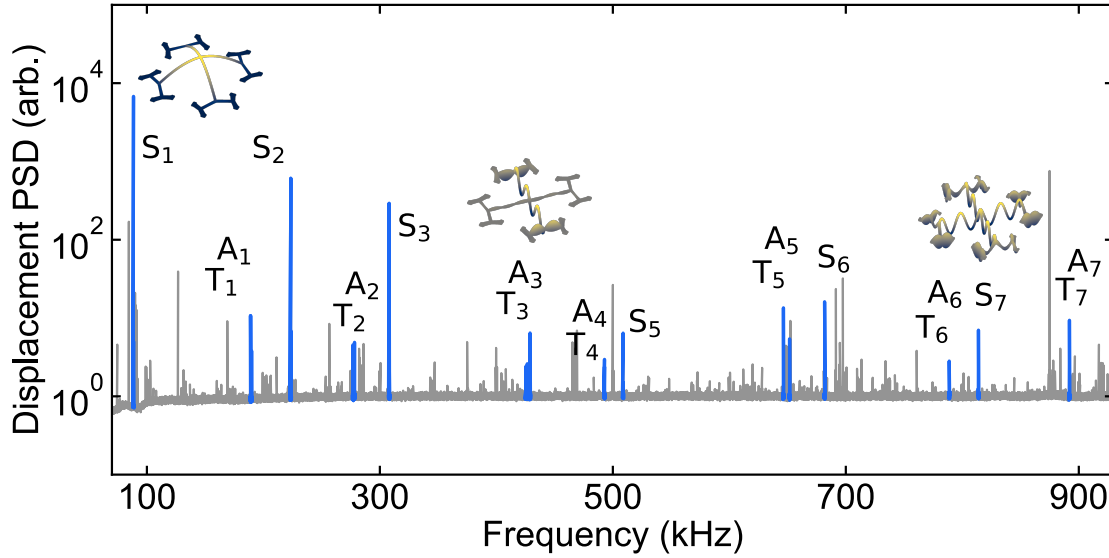


Figure 4.25: Thermomechanical noise spectrum of a trampoline with branching tethers. The gray line is the power spectral density of the homodyne record, where we highlight in blue the Brownian motion peaks of the trampoline resonator. The insets display the displacement patterns of modes  $S_1$ ,  $T_3$  and  $S_7$ .

In Figure 4.25 we display a thermomechanical noise spectrum recorded by shining the probe laser on the pad of a trampoline membrane with branching tethers. Resonance peaks were distinguished from spurious noise peaks by comparison with a similar spectrum obtained by reflecting the probe off the chip surface, and are highlighted in blue. The trace is normalized to the level of shot noise.

The low-frequency spectrum of the trampoline with branching tethers presents flexural mode families similar to those of regular trampoline membranes. We adopt the notation of [208]: ‘S’ indicates symmetric displacement patterns, with an antinode at the location of the pad, ‘T’, modes where one tether vibrates out of the plane, with a node at the pad, and the second undergoes torsion, and ‘A’, modes where the two tethers undergo flexural displacement with a  $\pi$  phase shift. ‘T’ modes always appear in degenerate pairs, and ‘A’ modes at a slightly higher frequency. The interferometer is most sensitive to out-of-plane motion, and purely torsional and in-plane flexural resonances could not be detected.

#### 4.6.2.1 Buckling and static deformations

As the structure of the tensioned trampoline membranes with branching tethers is quite complex, compressive stress along some directions can develop locally, especially close to the three-beam branches. This gives rise to the same buckling instability that was described for the sSi nanostring unit cells (see section 3.3.1), and we observed this phenomenon from the very first fabricated structures, that could develop wrinkles or out-of-plane twisting and deformation after the undercut process. In many cases, buckling can be avoided with judicious design of the tether profile, as we will discuss next.

In [Figure 4.26a](#), an example static deformation pattern is portrayed, which occurred in a steering wheel membrane close to its clamping point. A FEM simulation of the static stress distribution in the same structure is presented in [Figure 4.26b](#), which shows that the buckling is co-localized with regions of compressive principal stress. To obtain the color map in the figure, we decompose the simulated in-plane stress tensor into its principal components (i.e. its eigenvalues) and display the smallest one. Wherever one principal stress is negative, there is compression along some direction, which can trigger buckling. In the region where buckling is observed in the real device, the simulated minimum principal stress dips to  $\approx -30$  MPa.

Our strategies to avoid buckling in trampoline membranes were a) to ensure that the structures are stress-preserving [222], i.e. that the forces acting on each junction point are balanced prior to suspension, and b) to taper wide segments, which helped maintain their transverse stress above zero (compare the steering wheel trampoline tether profiles in [Fig. 4.26a-b](#) with those in [Fig. 4.22b](#)). Buckling is also expected to be less significant for films thicker than 20 nm.

Another type of static deformation that was observed in our tensile resonators is twisting of film segments. An example is portrayed in [Figure 4.26c](#) for the outer-most generation of segments of a trampoline membrane with branching tethers. The sample topography has been obtained through a confocal microscope profilometer. We conjecture that potential causes for this phenomenon could be the inhomogeneity of the film stress in the vertical direction, or the non-uniformity of the height of the silicon wafer. We expect that these undesired static deformations would also be reduced by increasing the film thickness.

#### 4.7 DENSITY-MODULATED PnC MEMBRANES

Since the integration of the hierarchical trampoline membranes in a Fabry-Pérot cavity is not trivial, we have devoted more energy to a second approach for room temperature quantum optomechanics. We decided to restrict operation of the MiM cavity to the magic detuning,  $\Delta \approx -0.29\kappa$ , where intermodulation noise is well-controlled, and develop the density modulated PnC membranes pioneered by the group of Ulrik Andersen at DTU [67] and described in the second chapter (see [section 2.3.3](#)). In these resonators, the  $\text{Si}_3\text{N}_4$  membrane film is not patterned, and rather the effective density is modulated by the fabrication of nanoscale pillars on top of it. These devices present a couple of important improvements on the stress-modulated PnC membranes introduced earlier in this chapter:

- The membrane stress is not relaxed from the initial value achieved with LPCVD, bringing a precious increase of a factor of 2-3 in the mechanical quality factors, and a corresponding optomechanical cooperativity improvement. The DTU group reports quality factors as high as  $9.1 \cdot 10^8$  at room temperature, that compare favourably with maximum  $Q \sim 2 - 3 \cdot 10^8$  achievable with stress modulation at similar frequencies.
- The 2D geometry, without the narrow features induced by the etch pattern, increases thermal conduction and heat dissipation. This could lead to better thermalization of the resonant modes in the presence of an intense laser field, and

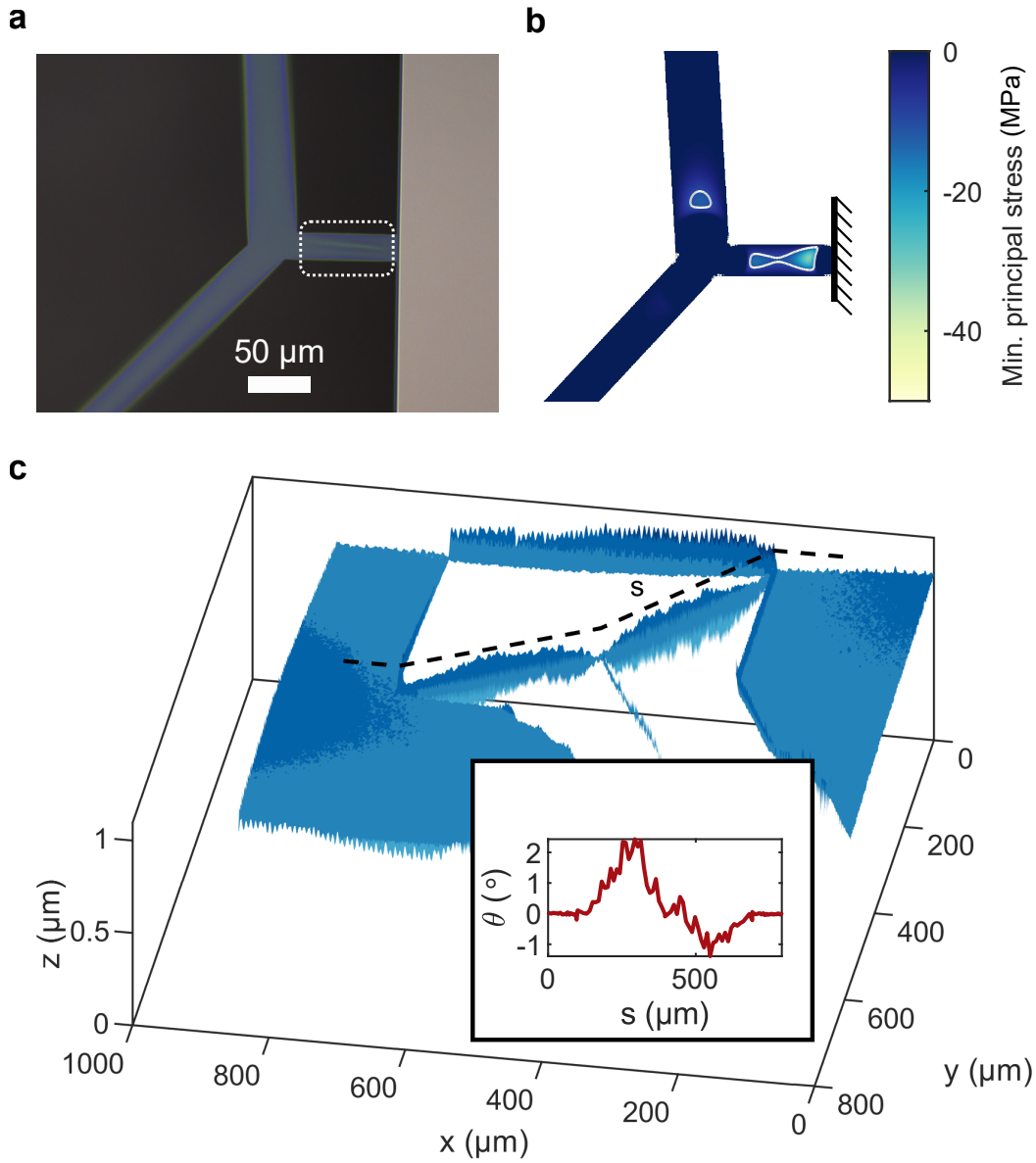


Figure 4.26: Buckling in a steering wheel resonator. **a**, The branch connecting the membrane to the silicon frame is visibly wrinkled (in the region circled with a dashed line), while wider tethers are bent in the transverse direction, as can be seen by the tether shifting out of the focal plane of the microscope. **b**, Minimal principal stress component from a FEM simulation of the membrane in **a**. The area where buckling is most prominent exhibits large compressive stress in the direction transverse to the branch. White contours encircle the regions with compressive stress below  $-10$  MPa. **c**, Profilometry of a trampoline membrane sample exhibiting static torsion in the branches closest to the clamping points. Inset: rotation of the beam surface normal along the black dashed path.



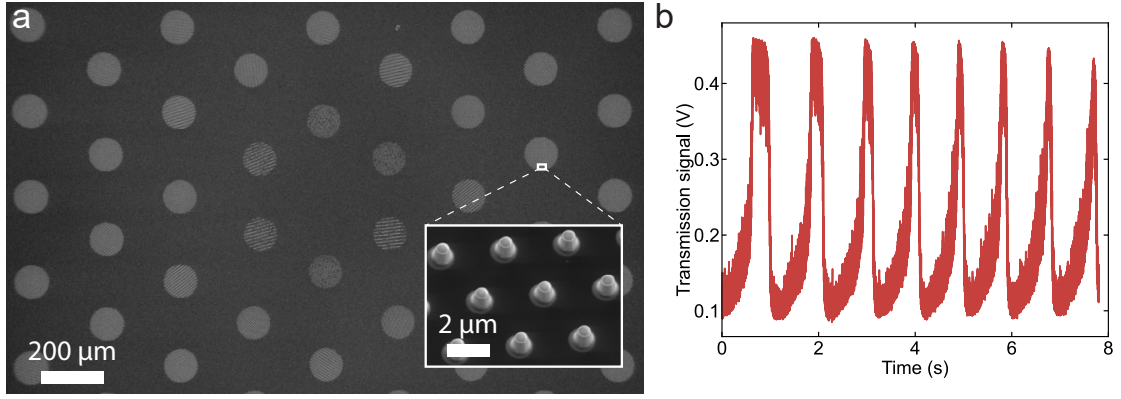


Figure 4.27: **a**, SEM micrograph of the defect region of a PnC membrane fabricated following the method of [67]. The inset shows the individual  $\text{Si}_x\text{N}_y$  pillars composing the high-density regions. **b**, Thermal instability of a MiM cavity built around a membrane fabricated using that method. The trace shows the transmission signal of the cavity when the laser wavelength is kept at a fixed detuning from the original resonance. The membrane temperature dynamics bring the cavity periodically on- and off-resonance, driving in turn the membrane temperature [226].

weaker photothermal effects [226, 227], that often limit optomechanics experiments.

- The acoustic bandgap width, governed by the density contrast, can be much larger than for stress-modulated PnC devices. This is advantageous for experiments such as feedback cooling, where spectral isolation of the high  $C_0$  mode from “spectator” membrane modes is important to avoid driving of the oscillator with uncorrelated thermal fluctuations.

In the last period of this thesis work, I developed a fabrication technique for density-modulated PnC devices. The method detailed in [67], with nanopillars made out  $\text{Si}_x\text{N}_y$ , is remarkably simple, but does not allow a fine control of the nanopillar dimensions, due to the pillars being subject to multiple isotropic etching steps. This hinders the experimental control on the effective density  $\rho_{\text{eff}}$ , and severely limits the fabrication of pillars of arbitrary shapes. Moreover, when we tried to reproduce the resonators in [67], we indeed measured high quality factors, but we observed photothermal bistability at low input power, when they were embedded in the MiM cavity (see Figure 4.27b), limiting the optical power that could be injected. From the measurement of different PnC membranes, we conjecture that the photothermal effect manifests when plasma-enhanced, chemical-vapor-deposited (PECVD)  $\text{Si}_x\text{N}_y$  is grown directly on the  $\text{Si}_3\text{N}_4$  membrane. PECVD  $\text{Si}_x\text{N}_y$  is known to have a larger optical absorption than LPCVD-grown  $\text{Si}_3\text{N}_4$  [228], and the absorption coefficient is related to the specific plasma generation parameters and to the substrate temperature during deposition. Apparently, our PECVD  $\text{Si}_x\text{N}_y$  (grown with the same recipe as in section 3.1) modifies the chemistry of the underlying  $\text{Si}_3\text{N}_4$  in such a way that it induces optical absorption even when the PECVD film is removed.

For these reasons, we have decided to pursue a different fabrication process, where amorphous silicon (aSi) pillars are grown and defined lithographically on the  $\text{Si}_3\text{N}_4$

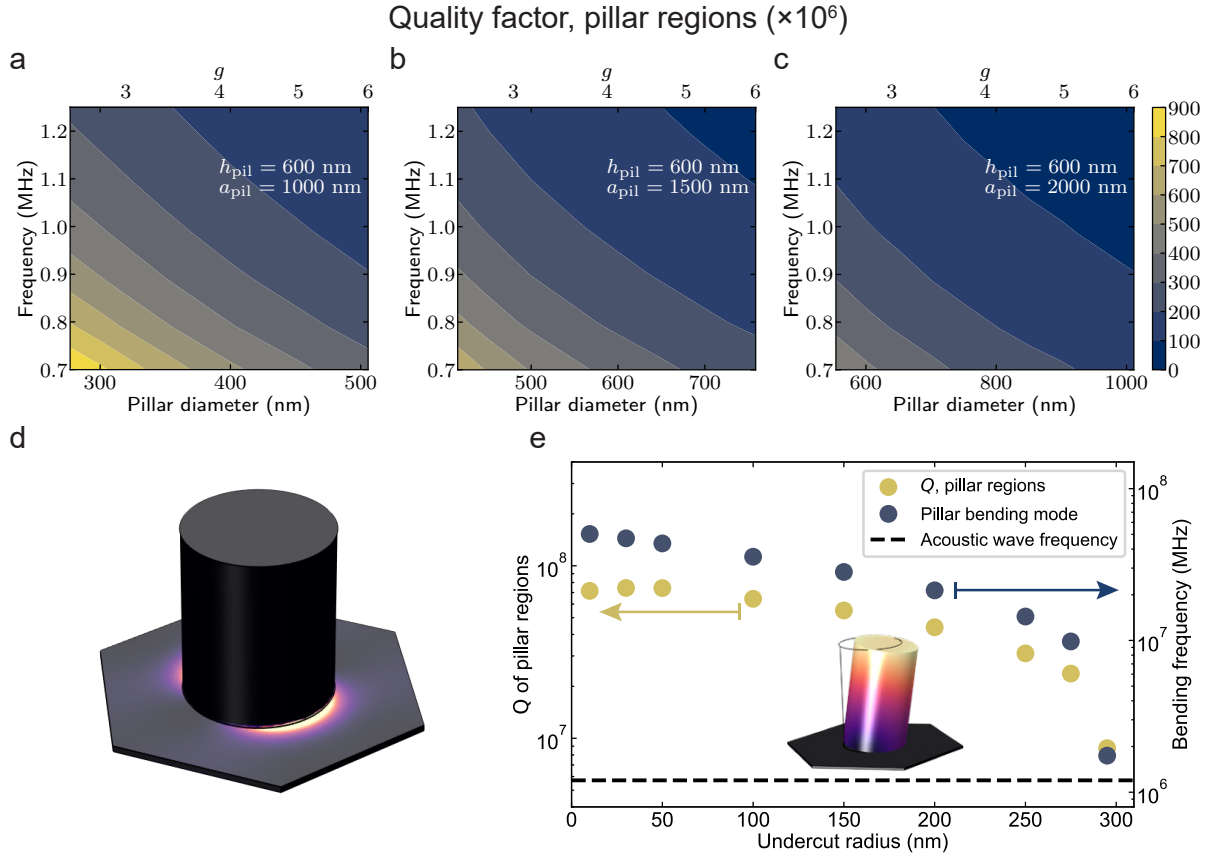


Figure 4.28: Losses induced by bending of nanopillars used to modulate  $\rho_{\text{eff}}$ . **a-c**, Q of a uniform pillar array with infinite extent, as a function of the frequency of the acoustic flexural wave and of the pillar diameter. The pillar separation  $a_{\text{pil}}$  is increased between the different panels, and the pillar thickness  $h_{\text{pil}}$  is kept constant. **d**, Visualization of the linear elastic energy density, that is associated with mechanical dissipation, close to the nanopillar. The largest contribution to dissipation is seen to occur close to the nanopillar base. **e**, Effect of an undercut at the pillar base on the pillar Q. For this simulation, the pillar has a diameter of 600 nm and a thickness of 1000 nm, and the separation between nearest-neighbours pillars is fixed to 1.5  $\mu\text{m}$ . The undercut layer is hardly visible in the illustration, as it is only 6 nm-thick. The pillar array's Q (ochre dots) is seen to drop sharply when the first flexural resonance frequency (blue dots, the inset illustrates the displacement field) of the nanopillar approaches the acoustic excitation frequency, marked by a horizontal dashed line.

membrane, and are not subject to isotropic etches. The complexity of this method is higher, but it appears to overcome the limitations of the original process. Although we have not yet reproduced the dissipation results of [67], our preliminary results are encouraging and we observed quality factors up to  $Q \sim 2 \cdot 10^8$ , on par with the best stress-modulated membranes.

#### 4.7.1 Design principles

The nanopillars can locally load the membrane to realize a density modulation, but they also introduce additional mechanical dissipation. When a bending wave impinges



on the pillar, it induces deformation carrying linear strain energy without a significant geometrically-nonlinear contribution. The pillars will thus reduce the dissipation dilution of the  $\text{Si}_3\text{N}_4$  membrane, of an amount that depends sensitively on the pillars' geometrical dimensions and on the elastic frequency of the flexural mode. The lower the elastic frequency and the smaller the pillars, the lower the susceptibility of the pillar displacement, and the lower will be the added dissipation induced by the individual pillars. The pillar damping contribution can be dominant, or sufficiently low that it is negligible compared to the finite dissipation dilution of the soft clamped mode, depending on the oscillation frequency and on the pillars' geometry [67].

We investigated this damping contribution with 3D finite element simulations of a single nanopillar. From now on, we assume that the pillars are arranged in a triangular lattice with a lattice constant  $a_{\text{pil}}$  (separation between the nearest neighbours), and we identify the pillar diameter and height (thickness) with  $d_{\text{pil}}$ ,  $h_{\text{pil}}$ . The effective density in the circular regions patterned with the nanopillars is then:

$$\rho_{\text{eff}} = \rho \left( 1 + \frac{\pi}{2\sqrt{3}} \frac{\rho_{\text{pil}} h_{\text{pil}}}{\rho h} \left( \frac{d_{\text{pil}}}{a_{\text{pil}}} \right)^2 \right), \quad (4.68)$$

where  $h$  and  $\rho$  are the thickness and density of the membrane film ( $\text{Si}_3\text{N}_4$ ). The periodicity of the pillar array is embedded in the simulation by restricting the domain to an hexagon-shaped unit cell (see Figure 4.28d) with Floquet boundary conditions ( $\vec{u}(\vec{x} + \vec{R}) = \vec{u}(\vec{x})e^{-i\vec{k} \cdot \vec{R}}$ ) on opposite sides of the hexagon. Due to the unit cell symmetry, the direction of the flexural wave is not important, but the magnitude of the elastic wavevector defining the boundary conditions,  $k$ , is chosen in order to produce a flexural eigenmode at the mechanical frequency of interest ( $ka_{\text{pil}} \ll 1$ ):

$$k \approx \Omega \sqrt{\frac{\rho_{\text{eff}}}{\sigma}}, \quad (4.69)$$

where  $\sigma$  is the membrane deposition stress. The model is then solved for its first eigenmode, which represents the pillar displacement upon the arrival of the flexural wave. The dissipation dilution of an infinite pillar lattice is evaluated as detailed in section 2.3.5, where the linear elastic energy is obtained either using its full expression (equation 2.11) [24] or the simplified plate formula 2.14<sup>14</sup>. The energy evaluated with the two methods differs by less than 10%, despite the nonuniform thickness in the pillar regions. The results of the computation of the infinitely-extended pillar lattice's quality factor are shown in Figure 4.28a-c, for a fixed pillar thickness of  $h_{\text{pil}} = 600$  nm and variable pillar separations, diameters and mechanical frequencies. The method was also benchmarked by verifying that when the pillar thickness is set to 0, the extracted quality factor is given by the "clamped" expression of equation 2.94. Note that the  $a\text{Si}$  loss angle is an unknown parameter in the FEM simulations, that we arbitrarily set by choosing  $Q_{\text{int},a\text{Si}} = 10000$ . The results in Fig. 4.28a-c do not depend sensitively on  $Q_{\text{int},a\text{Si}}$ ; nevertheless one should treat them as a rough estimation of the pillar damping contribution.

<sup>14</sup> Note that COMSOL does not properly calculate the linear elastic energy using equation 2.11, in case pre-stress is added to the pillar domain. The problem seems to be related with the evaluation of overlap integrals between the static and dynamic solution steps.

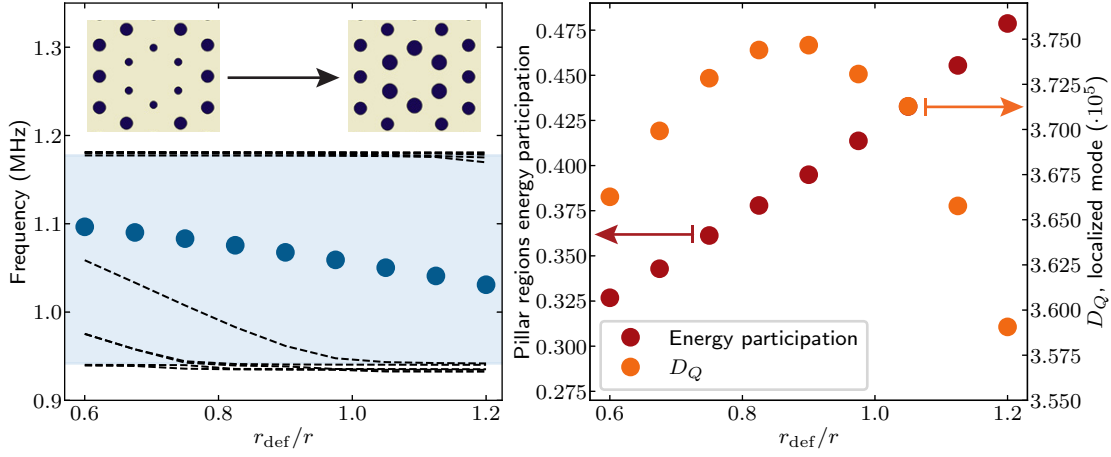


Figure 4.29: Effect of tuning the radius of the high density regions closest to the PnC defect. The density modulation is set to  $g = 4.2$  in all the circular regions for this simulation. Left graph: change of the soft clamped mode frequency (blue dots) as the radius is tuned. The 12 membrane modes closest in frequency are plotted with dashed black lines; as  $r_{\text{def}}$  decreases and the confinement is reduced, more localized modes are pulled in the bandgap (shaded in light blue). Right graph:  $D_Q$  (orange dots) and energy participation ratio (red dots) of the high- $\rho_{\text{eff}}$  pillar-containing regions for the soft clamped mode, as  $r_{\text{def}}$  is varied.

Another pillar geometry that is experimentally relevant is the case of a cylindrical pillar with a thin undercut layer formed at the base. As we will see, this is a possible outcome of the nanopillar microfabrication, in case the pillar is grown on top of an etch-stop layer with a different chemical identity. In this scenario, the frequency of the first bending mode of the nanopillars is decreased, as shown by the blue dots in Figure 4.28e, and the pillar motion can start to hybridize with the soft clamped membrane mode. This induces a large reduction in the overall quality factor when the undercut covers a significant portion of the pillar base (see the yellow dots in Figure 4.28e). Note that the undercut is not visible in the figure inset, as it is carved in a layer of only 6 nm at the pillar base, which is similar to the fabricated pillar geometrical parameters. A more striking example of undercut at the pillar base is portrayed in the nanopillar cross-section of Fig. 4.31.

In real density-modulated PnC devices, the nanopillar lattice does not cover the full membrane but is limited to the periodic circular regions of high density (see Fig. 2.6). To compute the actual damping contribution due to the pillars, it is then necessary to weigh the quality factor calculated as before with a *participation ratio* of the linear elastic energy developed in the high- $\rho_{\text{eff}}$  regions. The overall dissipation limit is then estimated using the following formula:

$$Q_{\text{pillar bend}} = Q_{\text{single pillar}} / p_{\text{hd}}$$

$$p_{\text{hd}} = \frac{\int_{\text{hd}} dS \left( \left( \frac{\partial^2 \psi}{\partial x^2} + \frac{\partial^2 \psi}{\partial y^2} \right)^2 + 2(1-\nu) \left( \left( \frac{\partial^2 \psi}{\partial x \partial y} \right)^2 - \frac{\partial^2 \psi}{\partial x^2} \frac{\partial^2 \psi}{\partial y^2} \right) \right)}{\int_{\Gamma} dS \left( \left( \frac{\partial^2 \psi}{\partial x^2} + \frac{\partial^2 \psi}{\partial y^2} \right)^2 + 2(1-\nu) \left( \left( \frac{\partial^2 \psi}{\partial x \partial y} \right)^2 - \frac{\partial^2 \psi}{\partial x^2} \frac{\partial^2 \psi}{\partial y^2} \right) \right)}, \quad (4.70)$$

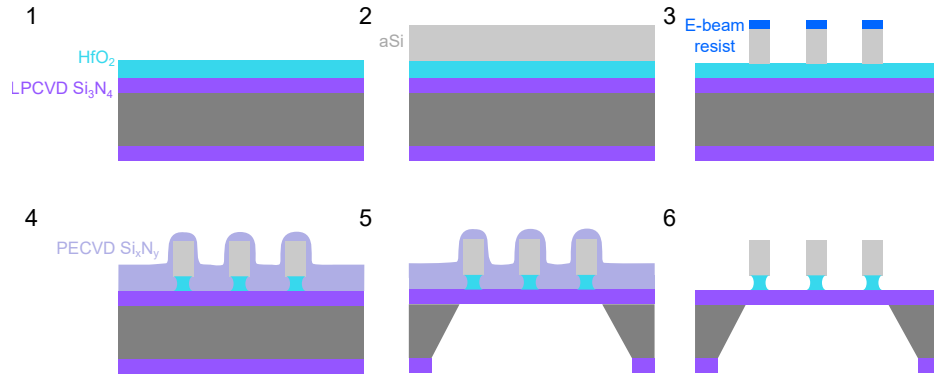


Figure 4.30: Simplified fabrication process for density-modulated membrane resonators. The features are not drawn to scale. 1 – Etch stop layer growth. 2 – aSi pillar layer growth. 3 – Electron beam lithography and pillar pattern transfer with RIE. 4 – Growth of PECVD nitride encapsulation layer. 5 – Chip separation and KOH membrane release. 6 – Removal of the encapsulation layer in buffered HF.

where the integral at the numerator of the participation ratio  $p_{hd}$  is computed only in the high-density regions, while the one at the denominator is extended to the whole membrane surface. The energy participation ratio depends sensitively on the defect geometry; an example is shown in Figure 4.29, where the soft clamped mode properties are tuned by changing the radius of the high-density regions closest to the defect (see the inset in the left graph). Shrinking the closest high-density regions reduces the participation ratio (as shown in the right graph), reducing the pillar bending contribution to  $Q$ , but it also has the effect of “pulling” further localized modes from the frequency bands below the bandgap, thus diminishing the spectral isolation of the target resonances. Interestingly, both the  $D_Q$  and  $m_{eff}$  are not significantly affected by the defect geometry tuning, varying by less than 5% and 10% respectively in the explored range of radii.

Finally, we note that if the membrane edges are terminated within the density modulation regions, edge modes will not appear at bandgap frequencies and the spectral isolation of the soft clamped modes will improve. This is more easily obtained than for stress-modulated PnC membranes, where the backside alignment tolerances are more demanding if the creation of an unpatterned membrane strip needs to be avoided.

#### 4.7.2 Microfabrication process

We detail here the fabrication process of amorphous silicon (aSi) nanopillars on a high aspect ratio  $\text{Si}_3\text{N}_4$  membrane. As previously mentioned, this method has some advantages over the original density-modulated PnC samples [67], where the pillars are made of PECVD silicon nitride. However, the process becomes a little more laborious, due to the need of protecting the pillars during the membrane undercut. The aSi pillars and the substrate have a very similar chemical composition, and they will be dissolved during the KOH undercut if left exposed to the etchant. Building on the expertise acquired in the fabrication of sSi nanostrings (see chapter 3), we devised a PECVD  $\text{Si}_x\text{N}_y$  encapsulation layer for the protection of aSi pillars, that can be removed selectively to the pillars and to the membrane as the last step of microfabrication.

#### 4.7.2.1 Nanopillars definition

In our PnC membranes, we target pillar diameters between  $d_{\text{pil}} = 300 \text{ nm}$  to  $800 \text{ nm}$  and nearest-neighbour distances between  $a_{\text{pil}} = 1.0 \mu\text{m}$  to  $2.0 \mu\text{m}$ . Features with such critical dimensions can be patterned in our cleanroom using deep ultraviolet (DUV) photolithography, with a KrF laser source at  $248 \text{ nm}$ , or using electron beam lithography. We chose to use electron beam lithography for the highest versatility in prototyping, as this technique does not require the prior fabrication of a photomask. In the future, we plan to switch to stepper DUV lithography, that would reduce substantially the exposure time. Dry etching is an excellent method to transfer the mask pattern to the underlying film, maintaining smooth and vertical sidewalls and keeping the pattern dimensions faithful to the original design. However, there are few dry etching recipes with a good selectivity between  $\text{Si}_3\text{N}_4$  and Si, with the exception of processes taking place at cryogenic conditions [229], which in our cleanroom are not supported. As soon as the  $\sim 20 \text{ nm}$   $\text{Si}_3\text{N}_4$  membrane is uncovered, it would rapidly get consumed by the etchants. One solution is to stop the dry etching step just short of uncovering the  $\text{Si}_3\text{N}_4$  layer, and finishing with a high-selectivity step such as wet etching [67]. Unfortunately, wet etching is typically isotropic, and would shrink the pillar dimensions from the design values, bringing forth issues in the reproducibility and control of the effective density and pillar damping. We decided instead to employ an etch-stop layer, much more selective to dry etching than  $\text{Si}_3\text{N}_4$ , on top of the membrane film, that allows for adequate overetching and process tolerances. Such an etch-stop material is not difficult to find: for  $\text{SF}_6$ -based processes, oxides such as  $\text{SiO}_2$ ,  $\text{Al}_2\text{O}_3$  or  $\text{HfO}_2$  (hafnium oxide) have been tested and found to provide a suitable selectivity. However, another important requirement is that no significant undercut in the etch-stop layer is created in subsequent steps of microfabrication (see the geometry of the pillar stem in Figure 4.31). As previously mentioned, undercut can reduce the frequency of the pillar bending resonances dramatically, thus increasing the pillar dissipation at MHz frequencies.  $\text{HfO}_2$  proved to satisfy this need, as a very thin layer with thickness  $< 5 \text{ nm}$  can completely block the dry etching step for a sufficient amount of time, and it is dissolved slowly in many acid and basic solutions. We measured an etch rate of atomic-layer-deposited  $\text{HfO}_2$  in HF 1% of  $\sim 2 \text{ nm/min}$ , comparable with that of stoichiometric  $\text{Si}_3\text{N}_4$ , and 1-2 orders of magnitude lower than that of  $\text{SiO}_2$  and  $\text{Al}_2\text{O}_3$ .

The process starts with (100)-oriented silicon wafers on which a  $\sim 20 \text{ nm}$  layer of stoichiometric, high stress  $\text{Si}_3\text{N}_4$  has been grown via LPCVD. After cleaning and dehydrating the wafer with an  $\text{O}_2$  plasma, we proceed with atomic layer deposition (ALD) of a  $\sim 6 \text{ nm}$   $\text{HfO}_2$  etch-stop film (step 1 in Figure 4.30). The growth takes place with a reactor temperature of  $200^\circ\text{C}$ , using  $\text{H}_2\text{O}$  and Tetrakis(ethylmethylamido)hafnium (TEMAHf) as precursors. TEMAHf is pre-heated to  $80^\circ\text{C}$  before starting the deposition process. About 60 precursor injection cycles are needed to grow a film of the desired thickness. After checking the thickness of the  $\text{HfO}_2$  layer with a spectroscopic ellipsometer, we proceed with the deposition of the aSi pillar layer. We employ a plasma-enhanced chemical vapor deposition (PECVD) tool (Oxford PlasmaLabSystem 100), where silane ( $\text{SiH}_4$ ) is the only precursor; at high temperatures and in the presence of a plasma, silane can decompose into silicon and volatile hydrogen, and deposit on the hot wafer (step 2 of Figure 4.30). The chamber temperature is set to  $300^\circ\text{C}$  during the deposition, and a 2%  $\text{SiH}_4:\text{N}_2$  mixture is flowed in the chamber at  $1000 \text{ sccm}$ ; plasma is generated

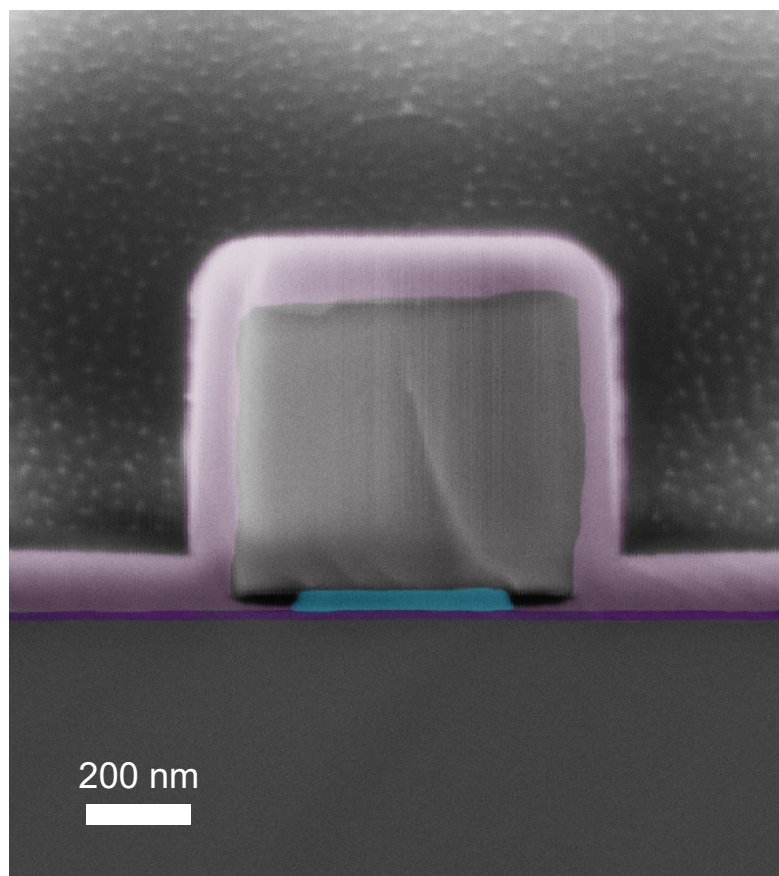


Figure 4.31: False-colored SEM micrograph of a nanopillar cross section. The different layers are color-coded as in Figure 4.30: violet –  $\text{Si}_3\text{N}_4$ , cyan –  $\text{SiO}_2$ , gray – amorphous Si, lavender – PECVD  $\text{Si}_x\text{N}_y$ . The pillar is covered by a layer of photoresist.

using 30 W of RF power. The pressure in the chamber is kept around 1500 mtorr during the process. The typical pillar thickness we target is  $\approx 600$  nm, that requires around 23 minutes of PECVD growth. We noticed that the aSi deposition process tends to greatly contaminate the chamber walls, and if the tool has been used many times without cleaning, the plasma ignition can fail during the process (easily noticeable by the fading of the plasma “glow”). Therefore, we usually run a chamber cleaning process just before starting the aSi growth, using a  $\text{CF}_4/\text{N}_2\text{O}$  plasma chemistry specifically tailored for etching the residues grown on the chamber walls.

We proceed then to define the nanopillars pattern with electron beam lithography. We spin-coat flowable oxide FOx16 resist (a formulation of HSQ) at 2000 RPM, resulting in a mask layer around 800 nm-thick. This thickness is more than sufficient to pattern the aSi layer, and in the future it could be slightly reduced in case the lithographic requirements become more demanding. FOx is exposed with a dose of about  $1400 \mu\text{C}/\text{cm}^2$  and developed with TMAH25% (2 minutes of immersion with agitation). Before the e-beam writing, the pattern is corrected for proximity effects in electron beam exposure (using the BEAMER software by GenISys), that would lead to nonuniformity within the pillar lattice regions. The pattern is transferred to the aSi layer with reactive ion etching (step 3 in Figure 4.30), using a recipe with  $\text{SF}_6$  and  $\text{C}_4\text{F}_8$  gases flowed simultaneously in the plasma chamber, where the wafer is kept at  $20^\circ\text{C}$ . The



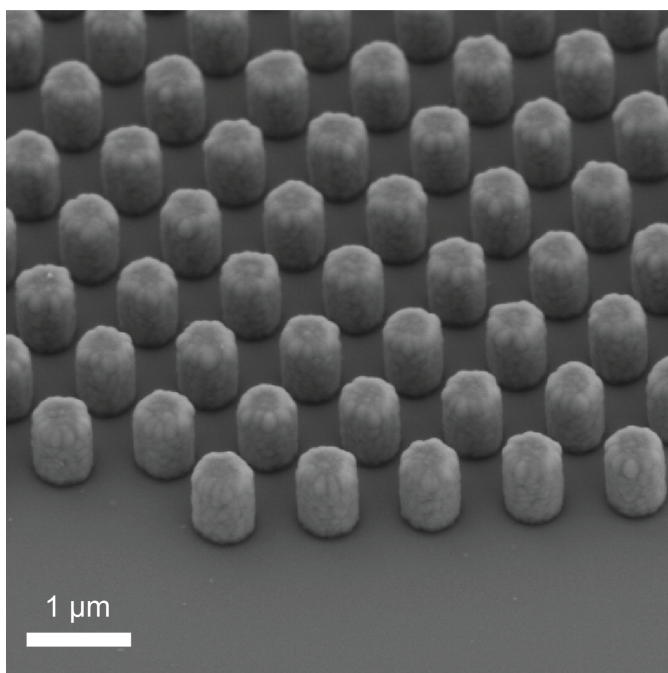


Figure 4.32: SEM micrograph of nanpillars covered with a PECVD  $\text{Si}_x\text{N}_y$  film.

etch is monitored *in situ* using a 670 nm laser beam reflected from the thin film stack: as the aSi layer is gradually thinned down, fringes are observed, due to thin film interference between the beams reflected from the top and bottom surfaces. For a starting thickness of  $\sim 600$  nm, about 5.5 - 6 interference fringes are observed before the  $\text{HfO}_2$  layer is exposed, which is clearly visible from the sudden dip of the interference signal slope. We let the dry etching process run for about 30 s after the endpoint to ensure that the pillars are fully defined on the whole wafer<sup>15</sup>, then we stop the process. Finally, we remove the FOx mask and the residual etch-stop layer by dipping the wafer in HF 1% for about 3.5 min, and confirm that the  $\text{Si}_3\text{N}_4$  membrane has been uncovered by recording ellipsometer traces.

#### 4.7.2.2 Nanopillars encapsulation

After patterning the pillars, we encapsulate them in a dielectric layer to protect them during the silicon deep etching step (step 4 in Figure 4.30). The requirements are similar as for the fabrication of sSi nanostrings (see section 3.1): we need a layer that can conformally cover the pillar topography, without defects or pinholes and with tensile deposition strain, such that it does not destructively buckle as it is suspended. Given our positive experience with sSi, we employed the same type of PECVD  $\text{Si}_x\text{N}_y$ . We first grow a thin ( $\sim 20$  nm), protective layer of  $\text{Al}_2\text{O}_3$  with ALD, to shield the membrane layer from plasma bombardment during PECVD. Then, approximately 125 nm of  $\text{Si}_x\text{N}_y$  are grown in our Oxford PlasmalabSystem100 PECVD with 2%  $\text{SiH}_4:\text{N}_2$  and  $\text{NH}_3$  as the precursors. The flow rates are set to 975 and 30 sccm. The chamber pressure is 800 mtorr and the reactor temperature is kept to 300 °C during the deposition).

<sup>15</sup> With some RIE recipes, overetching after reaching the etch-stop layer leads to “notching”, i.e. formation of an undercut at the pillar base as the plasma ions start to be deflected horizontally. Our selected dry etching process does not exhibit this behaviour.

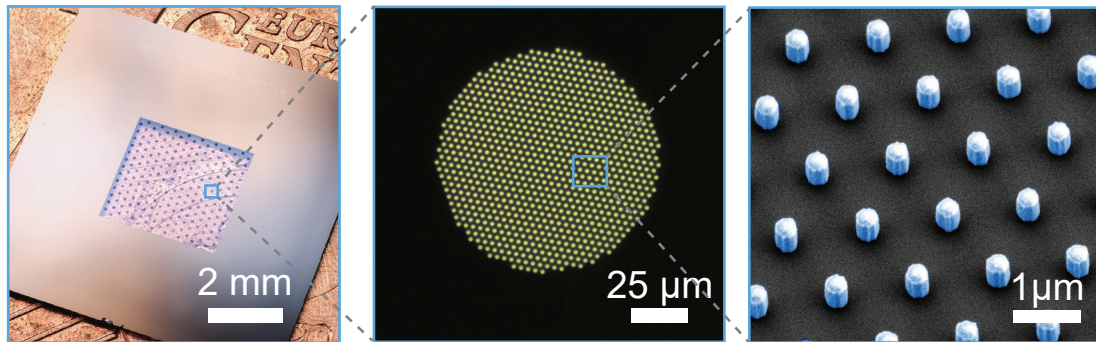


Figure 4.33: A density-modulated PnC membrane shown at different scales: full membrane chip, high- $\rho_{\text{eff}}$  region and single nanopillars. The three pictures were acquired respectively with a macro lens on a digital camera, with an optical microscope in dark field, and in a scanning electron microscope.

40 W of RF power excite the plasma during deposition, and the deposited layer has been characterized to have a tensile stress of  $\sim +300$  MPa at room temperature. The layer conformally covers the membrane and pillars, with a lower deposition rate on the sidewalls compared to the horizontal surfaces (see Figure 4.31). This PECVD layer has proved to perfectly seal the nanopillars and withstand several hours of immersion in hot KOH without significant consumption. An SEM image of the sealed nanopillars is shown in Fig. 4.32.

#### 4.7.2.3 Membrane release and encapsulation removal

At this point the process proceeds analogously to that of conventional stress-modulated PnC membranes (see section 4.4.1). A thick ( $\sim 3$   $\mu\text{m}$ ) layer of positive tone photoresist is spun on the frontside for protection during the backside lithography process, that we perform with an MLA150 laser writer. Membrane windows must be, once again, appropriately resized in order to account for the KOH slow-etching  $\langle 111 \rangle$  planes. After the resist mask and protection layer removal with NMP and  $\text{O}_2$  plasma, we deep-etch with KOH from the membrane windows while keeping the frontside protected, by installing the wafer in the watertight PEEK holder where only the backside is exposed. KOH40% at 70  $^\circ\text{C}$  is employed, and the etch is interrupted when about 30–40  $\mu\text{m}$  of silicon remains. The wafer is then rinsed and cleaned with hot HCl of the residues formed during KOH etching. Then, the wafer is separated into individual dies before concluding the process. A protective layer of positive-tone resist is coated on the frontside before cutting the wafer with a dicing saw, and the process continues chipwise. Chips are again cleaned with NMP and  $\text{O}_2$  plasma (paying attention not to use Piranha solution for organic cleaning, as it attacks the  $\text{Al}_2\text{O}_3$  layer), and the deep-etch is concluded with a second immersion in KOH 40% at a lower temperature of 55  $^\circ\text{C}$  (step 5 in Figure 4.30), followed as usual by cleaning in HCl. From the end of the KOH etching step, the composite membranes are suspended, and great care must be adopted in displacing and immersing the samples in liquid; nevertheless, the presence of a relatively thick PECVD nitride layer ensures that the survival yield is quite high after this step ( $> 90\%$ ). We dry the samples by moving them to an ultrapure isopropyl alcohol (IPA) bath after water rinsing. IPA has a low surface tension and a high vapour pressure,



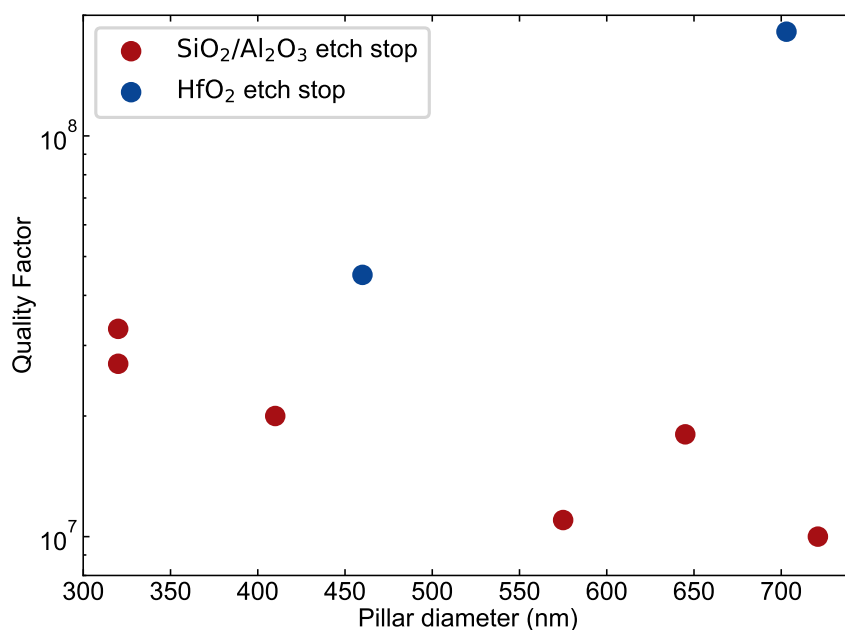


Figure 4.34: Density-modulated membranes characterization data. The quality factor is plotted against the nanopillar diameter, inferred from SEM-measurements or estimated.

therefore it can be easily dried off the membranes after a few minutes of immersion, with the help of a (cautiously operated) N<sub>2</sub> gun.

Finally, the PECVD nitride and Al<sub>2</sub>O<sub>3</sub> layers can be removed selectively with wet etching in buffered HF (BHF; step 6 in Figure 4.30). The etch rates of the encapsulation layers in BHF are orders of magnitude higher than the etch rate of stoichiometric Si<sub>3</sub>N<sub>4</sub> and HfO<sub>2</sub>, therefore even though the membrane backside is exposed, the membrane thinning during this step remains limited (few nanometers). In this step, a large or complete pillar undercut can be created, if the etch stop layer is not selected carefully (see Figure 4.31). Chips are loaded in a Teflon carrier where they are vertically mounted, and immersed for about 3 min 20 s in BHF 7:1. It is crucial not to overetch more than necessary to fully remove the encapsulation films: membranes become extremely fragile and the survival yield drops sharply when their thickness is reduced below ~ 15 nm. The etch rate of stoichiometric Si<sub>3</sub>N<sub>4</sub> in BHF 7:1 is around 1 nm/min. The membranes are then carefully rinsed, transferred in an ethanol bath and dried in a critical point dryer, where the liquids can be evacuated gently and with little contamination. The survival yield is slightly lower than for stress-modulated PnC membranes, probably due to the Si<sub>3</sub>N<sub>4</sub> thinning during the process. A photograph of a chip with a suspended density-modulated PnC membrane is shown in Fig. 4.33, where multiple close-ups at different scales show the regions of density modulation and the individual pillars.

#### 4.7.3 Mechanical characterization

The mechanical characterization of membrane resonators, before inserting the samples in the MiM assembly, was performed in the interferometric setup described in section

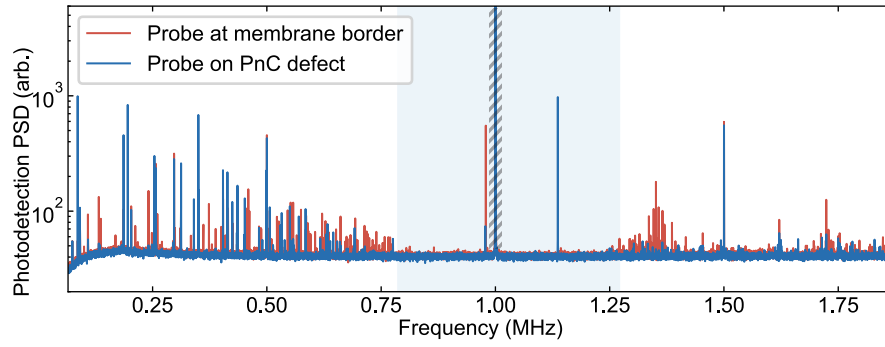


Figure 4.35: Thermomechanical spectrum of a density-modulated PnC membrane ( $a = 260 \mu\text{m}$ ,  $g \sim 5.0$ ). The data is acquired in the setup described in section 3.7 with the laser probe focused either close to the membrane edge (red trace) or at the PnC defect (blue trace). The localized mode coincides with the peak at 1.136 MHz, that is only visible in the trace acquired on the PnC defect. The peak at 1 MHz in both spectra (inside the hatched box) does not correspond to mechanical motion, but is phase noise associated with electromagnetic pickup. The acoustic bandgap is shaded in light blue.

3.7.2. A compilation of the measured quality factors is shown in Figure 4.34, where only data points with  $Q > 10^7$  are shown (in resonators with highly degraded  $Q$ , intrinsic dissipation is typically not dominant). The quality factor is displayed against the pillar diameter, that was measured directly by SEM imaging of the suspended samples (small differences from the design values can occur due to process drifts in e-beam lithography). The number of points is modest due to the limited amount of fabricated membrane wafers, for time constraints. Initially,  $\text{SiO}_2$  and  $\text{Al}_2\text{O}_3$  etch-stop layers were employed (red dots in Figure 4.34), and the measured quality factors were much lower than expected from naïve simulations of the pillar damping. We then formulated the hypothesis that a large pillar undercut, introduced in the last step of microfabrication, could increase sharply the pillar damping, and opted for ALD  $\text{HfO}_2$  as the etch-stop layer (blue dots in Figure 4.34), where undercut is generated much more slowly. Despite just a single wafer being fabricated, the change immediately brought a more than five-fold increase in the observed quality factors, confirming the hypothesis of the additional pillar dissipation being due to the undercut at the pillar base.

Note that it cannot be excluded that the  $Q$  improvement is associated with a lower intrinsic friction in the  $\text{HfO}_2$  film with respect to  $\text{SiO}_2$  and  $\text{Al}_2\text{O}_3$  (most of the linear strain energy is concentrated at the pillar base, see Figure 4.28d), but from the mechanical characterization of non-strained  $\text{HfO}_2$  resonators fabricated with our ALD tool, it appears that the intrinsic dissipation is comparable with that of  $\text{SiO}_2$  [230].

Thermomechanical spectra from one of the first fabricated membranes are shown in Figure 4.35. The soft clamped mode is visible at 1.136 MHz in the spectrum acquired on the PnC defect (blue trace). Note that the acoustic bandgap (shaded in light blue), with an extent of  $\sim 450 \text{ kHz}$ , is much larger than that created in stress-modulated PnC devices (cfr. Fig. 4.5).

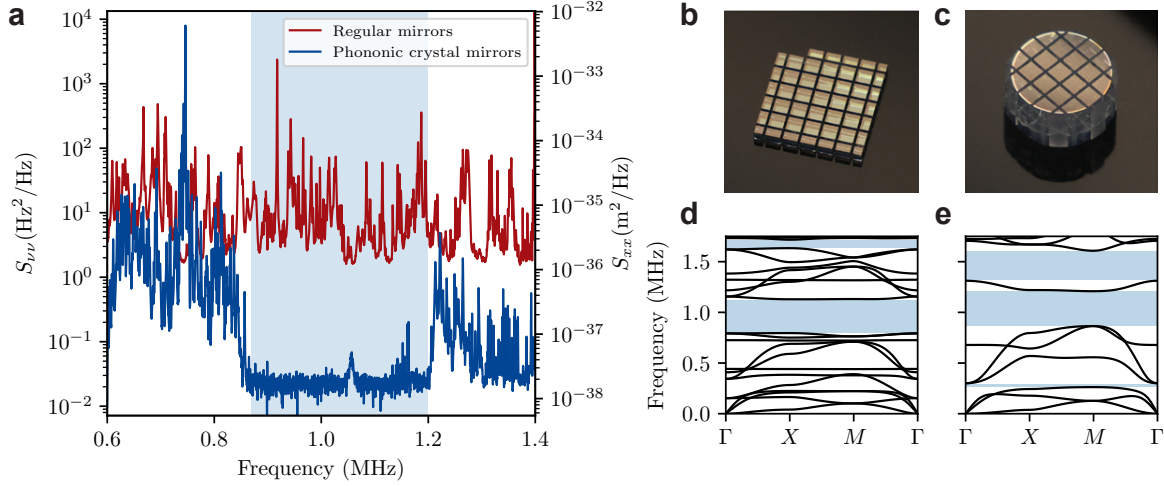


Figure 4.36: Vibrational noise of PnC cavity mirrors. **a**, Room temperature frequency noise observed at the output of an empty cavity (red line) compared with frequency noise of the cavity formed by PnC mirrors (blue trace). Shot noise of the output field has been subtracted by both traces. The conversion to mirror displacement is shown on the right vertical axis. The bandgap region common to both mirrors is shaded in light blue. **b** and **c**, Photographs of the PnC mirrors, showing the square arrangement of cut lines. The cuts extend approximately through 90% of the mirror thicknesses. **d** and **e**, Simulated band structures of the bottom and top mirrors. The acoustic bandgaps are shaded in light blue as in **a**.

## 4.8 OUTLOOK FOR MIM OPTOMECHANICS

In conclusion, I have reported in this chapter on the development of a MiM system based on ultracoherent  $\text{Si}_3\text{N}_4$  soft clamped membranes. I have described our novel membrane designs with a single localized mode within the acoustic bandgap and reduced effective mass, with quality factors up to  $\sim 3 \cdot 10^8$ . I presented as well different membrane designs we devised in order to mitigate some of the experimental challenges we faced, such as trampoline membranes with a soft clamped fundamental mode, and density-modulated PnC membranes. I discussed the main experimental challenge we faced during operation of the MiM cavity at room temperature, i.e. thermal intermodulation noise (TIN), a major deviation from the predictions of linearized optomechanics, and the strategy to reduce it, by operating the MiM cavity at a specific, ‘magic’ detuning. I will now shortly present some of the most recent developments in the experiment and some future related directions that could be explored.

### 4.8.1 Room temperature ponderomotive squeezing

Using a density-modulated PnC membrane and working at magic detuning for TIN suppression, we could recently observe ponderomotive squeezing at room temperature in our MiM system (see section 4.1.3). Since at the magic detuning the output spectrum was dominated by the mirror substrates’ vibrational noise (see Figure 4.16b), we had to devise a method to reduce it below the vacuum fluctuations. We did so by fabricating

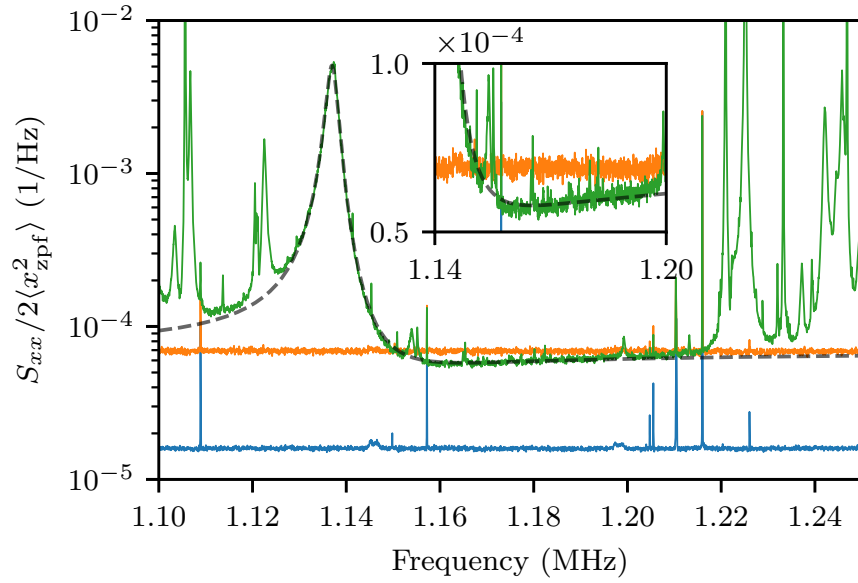


Figure 4.37: Room temperature ponderomotive squeezing observed at an angle  $\theta = 15.3^\circ$  from the amplitude quadrature. The green trace shows the homodyne spectrum: squeezing is generated at the right side of the soft clamped mode of a density-modulated membrane, and extends almost through the whole bandgap. The mode shows a noticeable optical damping due to the high intracavity power and operation at magic detuning ( $\Delta \approx -\kappa/2\sqrt{3}$ ). The orange trace is the shot noise level, and the blue trace shows the contribution of photodetector electronic noise (acquired with the laser beam blocked). The dashed black line is a fit to the predicted spectrum expression. The inset zooms on the region of maximum squeezing, displaying spectra in linear scale.

PnC structures directly within the cavity mirrors, by cutting lines through the glass substrates with a dicing saw, in a square lattice (see Figure 4.36). Surprisingly, this PnC was sufficient to open a bandgap for flexural vibrations at  $\sim 1$  MHz, and the cut lines did not degrade the cavity finesse (the cavity beam waist is much smaller than the PnC lattice constant). By performing homodyne detection with a single-detector scheme, we could cancel the majority of TIN from the photodetection record, and we observed squeezing down to  $\sim 1.1$  dB below the shot noise level, at a quadrature rotated of about  $\theta = 15^\circ$  from amplitude (see Figure 4.37). The experiment was mainly carried out by Guanhao Huang and me; more details will be provided in an upcoming article.

For the squeezing experiment we operated the MiM cavity at a quantum cooperativity  $C_q \approx 1.1$ , and we were even able to stably run the experiment with optical powers a few times higher (typically limited by the photothermal instability of some spectator membrane modes) without significant increase of the imprecision noise background. This suggests that we should be close to reaching the regime in which feedback cooling to the ground state of the membrane's soft clamped mode is possible (see 4.1.4), especially with a future density-modulated membrane device with higher  $Q$  and a larger acoustic bandgap. This will be required as the feedback-cooled linewidth approaches the bandgap extent, which will happen when cooling close to the ground state.

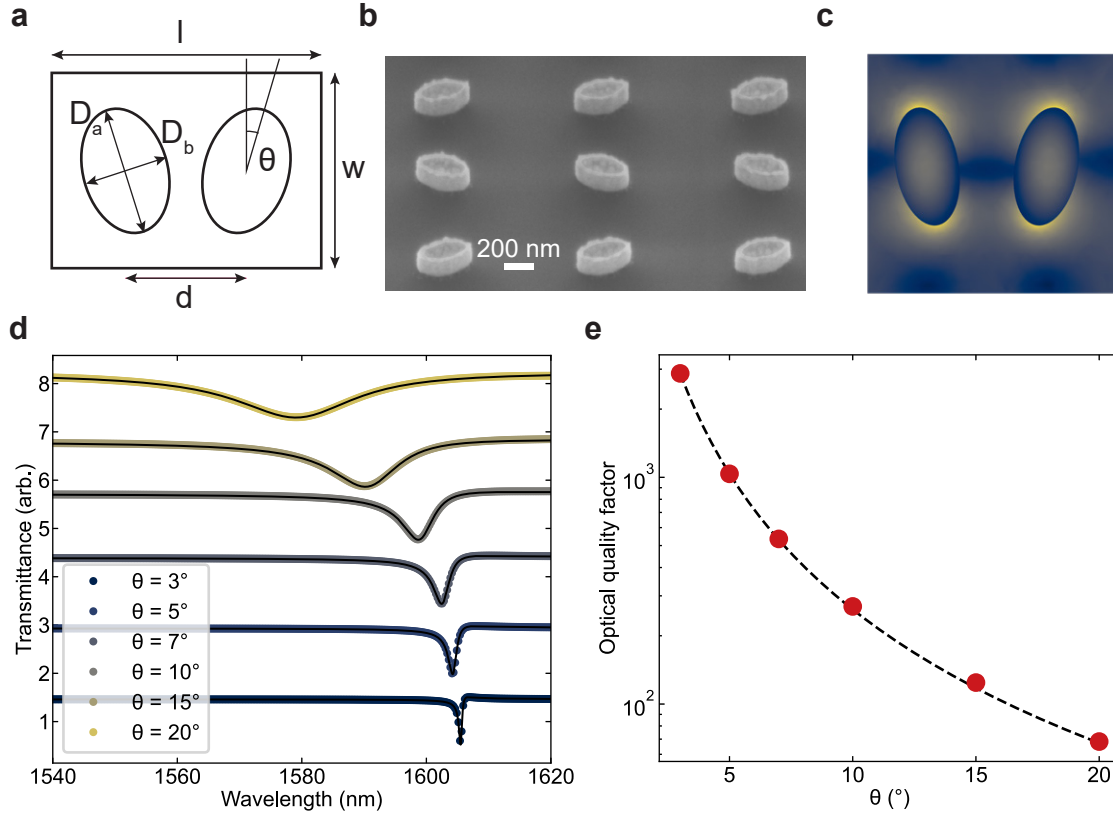


Figure 4.38: Optical resonance in nanopillar metasurfaces. **a**, Sketch of the ellipse-pair arrangement, with labels indicating the main geometrical parameters. **b**, SEM micrograph of a pillar lattice on top of a suspended membrane. **c**, FEM simulation of the electric field magnitude in the quasi-BIC state supported by the pillar lattice. **d**, Transmittance spectra (colored dots) of an infinitely-extended array of pillars, for different values of the axes tilt angle  $\theta$ . The different transmittance curves are offset by a constant amount, to improve clarity. The full black lines are fits with a Fano resonance model [234]. **e**, Extracted resonance quality factors from the fits of **d**. The dashed black line is a fit to the model  $Q_0/\sin^2\theta$ .

#### 4.8.2 Tailoring the optical properties of a PnC membrane with photonic structures

Even if the density modulation profile of a PnC membrane is fixed, the experimenter has a lot of freedom in the design of the single nanopillars that make up the high- $g$  regions at the nanoscale. The pillars are much smaller than the acoustic wavelength and roughly commensurate with optical or infrared wavelengths. This suggests the possibility of tailoring the membrane reflectivity by an appropriate choice of the pillar arrangement, with the goals of manipulating the radiation pressure backaction exerted on the membrane, enhancing its  $g_0$  when integrated in a cavity (see section 4.2), or inducing a particular light polarization response. These ideas are not new in the field of cavity optomechanics, where photonic crystals have been defined into  $\text{Si}_3\text{N}_4$  membranes to boost the optomechanical coupling rate in MiM experiments [209, 231, 232] or even to directly embed the cavity mirror onto the mechanical resonator [210, 233].

With density-modulated PnC membranes, the goal of tailoring the optical reflectance and creating photonic resonances may be obtained without compromising the mechan-

$D_a$ (nm)	$D_b$ (nm)	$d$ (nm)	$w$ (nm)	$l$ (nm)	$h_{\text{pil}}$ (nm)	$h$ (nm)	$\lambda$ (nm)
528	280	528	1056	1120	580	30	1580-1600

Table 2: Geometrical parameters of a periodic lattice of aSi elliptical pillars supporting a quasi-BIC resonance at  $\lambda \sim 1600$  nm.  $h$  is the thickness of the supporting  $\text{Si}_3\text{N}_4$  membrane.

ical quality factor. Dielectric pillars on a thin transparent slab are one of the most common geometries that realize metasurfaces with high-optical-Q resonances. A very common approach is starting with a periodic lattice of pillars that supports a symmetry-protected photonic *bound state in the continuum* (BIC) [235] and introducing a small geometrical asymmetry that induces a suitable coupling rate with free space [234]. The amorphous silicon elliptical pillar array shown in Figure 4.38 is an example of such a metasurface: when the adjacent ellipses axes are parallel, the structure supports a BIC at a wavelength of  $\sim 1600$  nm, which becomes a leaky Fano resonance as the axes are tilted by a small asymmetry angle  $\theta$ . Correspondingly, the simulated transmission from pillars with growing asymmetry angles becomes broader as the external coupling rate increases (see Figure 4.38d). The geometrical parameters of the pillar lattice supporting the quasi-BIC resonance are given in Table 2, and they correspond to a density modulation of  $g \approx 3.7$ . Note that silicon is transparent at wavelengths around  $\sim 1550$  nm, so that the intrinsic damping of the metasurface's optical resonances should be acceptable. Density-modulated PnC membranes with elliptical nanopillars (in the high- $g$  regions closest to the PnC defect) have been fabricated, as shown in Figure 4.38b, but we must still proceed to their experimental characterization.

## CONCLUDING REMARKS

---

During the past years, in our research team we exploited the effect of dissipation dilution to enhance the isolation from the thermal environment of high-aspect-ratio beam and membrane resonators. This led to record quality factors of MHz modes in crystalline silicon nanobeams, especially at liquid Helium temperatures, and supported the development of a state of the art membrane-in-the-middle cavity. Recent developments of the membrane resonator, of the cavity mirrors and of the homodyne detection configuration brought the experiment in the regime where quantum backaction influences the oscillator motion at room temperature, an experimental setting whose exploration has just recently started [54, 171].

Many open questions are being considered and investigated by researchers in the field. The dissipation dilution bound of 2.94 has been saturated by PnC structures [24], with lower frequency soft clamping approaches being limited instead by torsional losses [27]. Equation 2.94 predicts however a severe drop of the dilution factor as the mechanical frequency increases. For many experiments in the quantum regime, mechanical resonances at GHz frequencies are necessary [12, 13, 63, 236], in order to prepare the mechanical system in the ground state at the cryogenic temperatures of a dilution refrigerator (fulfilling  $k_B T \ll \hbar\Omega$ ), and to interact resonantly with superconducting qubits. Extending dissipation dilution to such GHz modes would present a breakthrough in the field, improving the performance of these hybrid quantum systems. One approach could be the implementation of dissipation-diluted resonators in single-layer or few-layers materials, such as graphene, with a naturally-increased aspect ratio. This endeavour seems challenging, due to technical difficulties in depositing high-quality layers on large surfaces, and to the lack of established microfabrication methods. In my opinion, a more interesting path could come from the field of acoustic metamaterials [237], where a manipulation of the elastic wave dispersion can be achieved with sub-wavelength structures. Fruitful investigations could include, for example, the suppression of the bending stiffness or the enhancement of the speed of sound (entailing reduced distributed curvature losses) in artificially-structured media [238].

Another open problem is the existence of bulk or surface acoustic waves with significant dissipation dilution. So far all of the known examples of dissipation dilution were demonstrated in high aspect ratio structures, but it would be greatly advantageous to enhance the mechanical quality factors of the natural vibrations of bulk materials. Sergey Fedorov proved in his thesis [70] that the only continuum mechanics displacement fields with vanishing linear strains are infinitesimal rotations, which do not seem practical to implement. This does not exclude, naturally, the existence of other acoustic wave solutions in bulk media with a sizeable geometrically-nonlinear strain energy, and a significant contribution of tension to the spring constant, especially when artificial dispersion engineering techniques are employed.





## APPENDIX: CAVITY-LESS LASER COOLING IN A CRYOGENIC ENVIRONMENT

---

Soft clamped perimeter modes of nanomechanical polygon resonators exhibited quality factors up to  $3.6 \cdot 10^9$  at room temperature and effective masses on the order of  $10 - 100$  pg, corresponding to zero-point displacement fluctuations around  $x_{zpf} \sim 10 - 100$  fm [27]. The remarkable thermal decoherence time and the large amplitude of zero-point motion offer a feasible path towards quantum control of perimeter modes with simple interferometric displacement detection techniques (described in chapter 3). An order-of-magnitude estimation of the displacement sensitivity at the standard quantum limit (see section 4.1) for such modes gives in fact a value around  $1 \text{ pm}/\sqrt{\text{Hz}}$ , which can easily be achieved and surpassed with common interferometric schemes and reasonable optical powers (see Fig. 3.23). The interaction of such beam-like mechanical resonators with an optical cavity is typically achieved by near-field coupling [172] or with the use of fiber cavities with tight optical confinement [239], but both methods incur into significant sample design, fabrication and experimental challenges, some of which were presented in chapter 4. Reaching the regime where quantum backaction of radiation pressure is a relevant agent of the mechanical displacement with simple interferometric detection would represent a major experimental advance. In the past, in fact, these displacement sensitivity levels were thought extremely challenging to approach without the finesse enhancement offered by an optical cavity [160].

As a proof-of-principle experiment, we plan to carry out feedback cooling of the perimeter mode of a polygon resonator starting from temperatures of  $\sim 8$  K, achievable in our cryostat. At such temperatures, the thermal phonon occupation of a 350 kHz mode would be around  $5 \cdot 10^5$  (assuming no excess optical heating takes place), implying that the interferometer sensitivity must be lower than that at the SQL by about 28 dB in displacement units to permit ground state cooling (see section 4.1.4). This sensitivity is almost achieved with the best imprecision levels that have been measured in our interferometric apparatus, and could be surpassed with future experimental improvements. We estimated displacement noise backgrounds down to approximately  $20 \text{ fm}/\sqrt{\text{Hz}}$  at 200 kHz for impinging powers of a few mW, using the scheme described in section 3.7.4 for the calibration. In Figure A.1a, I display the achievable phonon occupation with ideal feedback cooling against the imprecision noise limiting the interferometric displacement sensing. For the best imprecision levels that were characterized experimentally, cooling to occupations  $\bar{n}_{\text{th}} \sim 10^1$ , where sideband asymmetry is readily observable, should be possible. Further improvements of the cooling performance could arise due to the expected growth of mechanical quality factors at cryogenic temperatures.

There remain several experimental challenges to be overcome in order to demonstrate ground state cooling. The spurious reflection from the chip substrate underneath the polygon resonators contaminates the displacement record with additional phase noise, which can be significant when considering that the substrate reflection is much more intense than the reflection from the resonator. The magnitude of this reflection

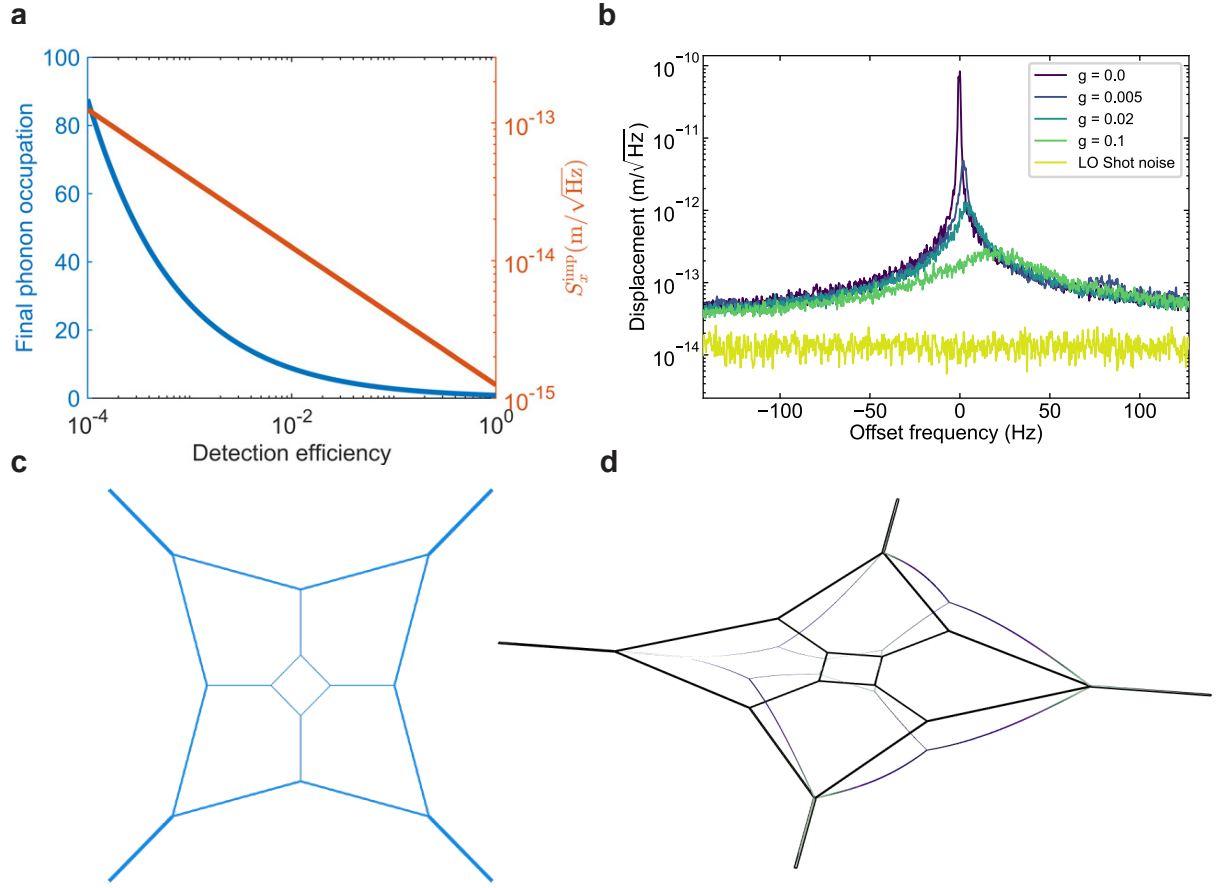


Figure A.1: **a**, Blue trace: estimated final occupation in a cavity-less feedback cooling experiment, assuming a beam of optical power 5 mW impinging on a polygon mechanical resonator, with a varying detection efficiency for the reflected light. The mechanical mode parameters are those characteristic of a polygon resonator, with temperature of 10 K, mechanical frequency of 250 kHz, quality factor of  $3 \cdot 10^9$  and effective mass of 150 pg. The orange trace represents the corresponding imprecision level of shot noise in the interferometer. **b**, Results of a feedback cooling trial conducted at room temperature, where the phonon occupation is reduced from about  $2 \cdot 10^7$  to 5300.  $g$  is an electronic gain parameter governing the strength of the piezoelectric feedback. **c**, Geometry of a modified polygon resonator with interior branches, with higher spectral isolation for the perimeter mode. **d**, Perimeter mode supported by the structure in **c**.

can be reduced by decreasing the depth of focus (increasing the numerical aperture) of the lens used to collect light from the resonator, or by removing the substrate below the resonator during the microfabrication process. Moreover, laser amplitude and phase noise at frequencies around 300 kHz could be reduced by exchanging our 850 nm ECDL for a 1064 nm Nd:YAG source or a 1550 nm fiber laser. Finally, perimeter modes in polygonal networks of strings are located very close in frequency to several other in-plane modes [27], which complicates the design of the feedback filter. Despite the very weak interaction with the laser probe, in-plane modes can easily become unstable by actuation with a naive filter, requiring a more cumbersome design that has to be implemented digitally, using e.g. an FPGA board [29], and can impose limitations to

the maximum applicable gain. The poor spectral isolation can be circumvented using a more advanced polygon resonator design. The structure shown in Fig A.1c, where the inclusion of additional branches inside the polygon increases greatly the effective stiffness of in-plane eigenmodes, exhibits a spectral isolation of about 14% of the mechanical frequency (519 kHz). This compares favourably against the thermal decoherence rate of a perimeter mode thermalized at 8 K, of about  $\Gamma_{\text{th}} \sim 2\pi \cdot 40 \text{ Hz}$ , and against the spectral isolation of the original polygons, of about 1 kHz [27].



## BIBLIOGRAPHY

---

1. Clotfelter, B. E. The Cavendish Experiment as Cavendish Knew It. *American Journal of Physics* **55**, 210–213. ISSN: 0002-9505, 1943-2909 (Mar. 1987).
2. Westphal, T., Hepach, H., Pfaff, J. & Aspelmeyer, M. Measurement of Gravitational Coupling between Millimetre-Sized Masses. *Nature* **591**, 225–228. ISSN: 1476-4687 (Mar. 2021).
3. Buikema, A. *et al.* Sensitivity and Performance of the Advanced LIGO Detectors in the Third Observing Run. *Physical Review D* **102**, 062003. ISSN: 2470-0010, 2470-0029 (Sept. 2020).
4. Weber, J. Detection and Generation of Gravitational Waves. *Physical Review* **117**, 306–313. ISSN: 0031-899X (Jan. 1960).
5. Whittle, C. *et al.* Approaching the Motional Ground State of a 10-Kg Object. *Science* **372**, 1333–1336. ISSN: 0036-8075, 1095-9203 (June 2021).
6. Saulson, P. R. Thermal Noise in Mechanical Experiments. *Physical Review D* **42**, 2437–2445. ISSN: 0556-2821 (Oct. 1990).
7. Gretz, D. J. Early History of Gravitational Wave Astronomy: The Weber Bar Antenna Development. *History of Physics Newsletters* **XIII** (2018).
8. Giessibl, F. J. Advances in Atomic Force Microscopy. *Rev. Mod. Phys.* **75**, 35 (2003).
9. Giessibl, F. J. & Binnig, G. True Atomic Resolution on KBr with a Low-Temperature Atomic Force Microscope in Ultrahigh Vacuum. *Ultramicroscopy* **42**, 281–286 (1992).
10. Rugar, D., Budakian, R., Mamin, H. J. & Chui, B. W. Single Spin Detection by Magnetic Resonance Force Microscopy. *Nature* **430**, 329–332. ISSN: 1476-4687 (July 2004).
11. Ido, S. *et al.* Beyond the Helix Pitch: Direct Visualization of Native DNA in Aqueous Solution. *ACS Nano* **7**, 1817–1822. ISSN: 1936-0851, 1936-086X (Feb. 2013).
12. Chu, Y. *et al.* Quantum Acoustics with Superconducting Qubits. *Science* **358**, 199–202. ISSN: 0036-8075, 1095-9203 (Oct. 2017).
13. Arrangoiz-Arriola, P. *et al.* Resolving the Energy Levels of a Nanomechanical Oscillator. *Nature* **571**, 537–540. ISSN: 1476-4687 (July 2019).
14. Karg, T. M. *et al.* Light-Mediated Strong Coupling between a Mechanical Oscillator and Atomic Spins 1 Meter Apart. *Science* **369**, 174–179. ISSN: 0036-8075, 1095-9203 (July 2020).
15. Møller, C. B. *et al.* Quantum Back-Action-Evading Measurement of Motion in a Negative Mass Reference Frame. *Nature* **547**, 191–195. ISSN: 0028-0836, 1476-4687 (July 2017).
16. Walschaers, M. Non-Gaussian Quantum States and Where to Find Them. *PRX Quantum* **2**, 030204 (Sept. 2021).
17. Zurek, W. H. *Decoherence and the Transition from Quantum to Classical – REVISITED* June 2003. arXiv: [quant-ph/0306072](https://arxiv.org/abs/quant-ph/0306072).

18. Braginsky, V. B., Mitrofanov, V. P. & Panov, V. I. *Systems with Small Dissipation* ISBN: 978-0-226-07073-5 (University of Chicago Press, 1985).
19. Braginsky, V. B., Vorontsov, Y. I. & Thorne, K. S. Quantum Nondemolition Measurements. *Science* **209**, 547–557 (Aug. 1980).
20. Aspelmeyer, M., Kippenberg, T. J. & Marquardt, F. Cavity Optomechanics. *Reviews of Modern Physics* **86**, 1391–1452. ISSN: 0034-6861, 1539-0756 (Dec. 2014).
21. Cumming, A. V. *et al.* Lowest Observed Surface and Weld Losses in Fused Silica Fibres for Gravitational Wave Detectors. *Classical and Quantum Gravity* **37**, 195019. ISSN: 0264-9381, 1361-6382 (Oct. 2020).
22. Phillips, W. A. Tunneling States in Amorphous Solids. *Journal of Low Temperature Physics* **7**, 351–360. ISSN: 0022-2291, 1573-7357 (May 1972).
23. González, G. I. & Saulson, P. R. Brownian Motion of a Mass Suspended by an Anelastic Wire. *The Journal of the Acoustical Society of America* **96**, 207–212. ISSN: 0001-4966 (July 1994).
24. Fedorov, S. A. *et al.* Generalized Dissipation Dilution in Strained Mechanical Resonators. *Physical Review B* **99**, 054107. ISSN: 2469-9950, 2469-9969 (Feb. 2019).
25. Tsaturyan, Y., Barg, A., Polzik, E. S. & Schliesser, A. Ultracoherent Nanomechanical Resonators via Soft Clamping and Dissipation Dilution. *Nature Nanotechnology* **12**, 776–783. ISSN: 1748-3387 (Aug. 2017).
26. Ghadimi, A. H. *et al.* Elastic Strain Engineering for Ultralow Mechanical Dissipation. *Science* **360**, 764–768. ISSN: 0036-8075, 1095-9203 (May 2018).
27. Bereyhi, M. J. *et al.* Perimeter Modes of Nanomechanical Resonators Exhibit Quality Factors Exceeding  $1e9$  at Room Temperature. *Physical Review X* **12**, 021036 (May 2022).
28. Beccari, A. *et al.* Strained Crystalline Nanomechanical Resonators with Quality Factors above 10 Billion. *Nature Physics* **18**, 436–441. ISSN: 1745-2481 (Apr. 2022).
29. Rossi, M., Mason, D., Chen, J., Tsaturyan, Y. & Schliesser, A. Measurement-Based Quantum Control of Mechanical Motion. *Nature* **563**, 53–58. ISSN: 0028-0836, 1476-4687 (Nov. 2018).
30. Delaney, R. D. *et al.* Superconducting-Qubit Readout via Low-Backaction Electro-Optic Transduction. *Nature* **606**, 489–493. ISSN: 1476-4687 (June 2022).
31. Manley, J., Chowdhury, M. D., Grin, D., Singh, S. & Wilson, D. J. Searching for Vector Dark Matter with an Optomechanical Accelerometer. *Physical Review Letters* **126**, 061301 (Feb. 2021).
32. Carlesso, M. *et al.* Present Status and Future Challenges of Non-Interferometric Tests of Collapse Models. *Nature Physics* **18**, 243–250. ISSN: 1745-2481 (Mar. 2022).
33. Landau, L. D., Lifshitz, E. M., Pitaevskii, L. P. & Kosevich, A. M. *Theory of Elasticity* (Pergamon Press, 1986).
34. Ogden, R. W. *Non-Linear Elastic Deformations* (Dover Publications, 1997).
35. Pinard, M., Hadjar, Y. & Heidmann, A. Effective Mass in Quantum Effects of Radiation Pressure. *The European Physical Journal D*, 10 (1999).



36. Sakurai, J. J. & Napolitano, J. *Modern Quantum Mechanics* 3rd ed. (Cambridge University Press, 2020).
37. Purdy, T. P., Grutter, K. E., Srinivasan, K. & Taylor, J. M. Quantum Correlations from a Room-Temperature Optomechanical Cavity. *Science* **356**, 1265–1268 (June 2017).
38. Clerk, A. A., Devoret, M. H., Girvin, S. M., Marquardt, F. & Schoelkopf, R. J. Introduction to Quantum Noise, Measurement, and Amplification. *Reviews of Modern Physics* **82**, 1155–1208 (Apr. 2010).
39. Kubo, R. The Fluctuation-Dissipation Theorem. *Reports on Progress in Physics* **29**, 255. ISSN: 0034-4885 (Jan. 1966).
40. Callen, H. B. & Greene, R. F. On a Theorem of Irreversible Thermodynamics. *Physical Review* **86**, 702–710. ISSN: 0031-899X (June 1952).
41. Nyquist, H. Thermal Agitation of Electric Charge in Conductors. *Physical Review* **32**, 110–113 (July 1928).
42. Einstein, A. Über die von der molekularkinetischen Theorie der Wärme geforderte Bewegung von in ruhenden Flüssigkeiten suspendierten Teilchen. *Annalen der Physik* **vol. 4, t. 17** (1905).
43. Nowick, A. S. *Anelastic Relaxation In Crystalline Solids* (Academic Press, 1972).
44. Verbridge, S. S., Parpia, J. M., Reichenbach, R. B., Bellan, L. M. & Craighead, H. G. High Quality Factor Resonance at Room Temperature with Nanostings under High Tensile Stress. *Journal of Applied Physics* **99**, 124304. ISSN: 0021-8979 (June 2006).
45. Verbridge, S. S., Craighead, H. G. & Parpia, J. M. A Megahertz Nanomechanical Resonator with Room Temperature Quality Factor over a Million. *Applied Physics Letters* **92**, 013112. ISSN: 0003-6951 (Jan. 2008).
46. Thompson, J. D. *et al.* Strong Dispersive Coupling of a High-Finesse Cavity to a Micromechanical Membrane. *Nature* **452**, 72–75. ISSN: 1476-4687 (Mar. 2008).
47. Southworth, D. R. *et al.* Stress and Silicon Nitride: A Crack in the Universal Dissipation of Glasses. *Physical Review Letters* **102**, 225503 (2009).
48. Unterreithmeier, Q. P., Faust, T. & Kotthaus, J. P. Damping of Nanomechanical Resonators. *Physical Review Letters* **105**, 027205 (July 2010).
49. Wu, J. & Yu, C. C. How Stress Can Reduce Dissipation in Glasses. *Physical Review B* **84**, 174109. ISSN: 1098-0121, 1550-235X (Nov. 2011).
50. Schmid, S., Jensen, K. D., Nielsen, K. H. & Boisen, A. Damping Mechanisms in High- Q Micro and Nanomechanical String Resonators. *Physical Review B* **84**. ISSN: 1098-0121, 1550-235X (Oct. 2011).
51. Yu, P.-L., Purdy, T. P. & Regal, C. A. Control of Material Damping in High-Q Membrane Microresonators. *Physical Review Letters* **108**, 083603 (Feb. 2012).
52. Kimball, A. L. & Lovell, D. E. Internal Friction in Solids. *Physical Review* **30**, 948–959. ISSN: 0031-899X (Dec. 1927).
53. Pohl, R. O., Liu, X. & Thompson, E. Low-Temperature Thermal Conductivity and Acoustic Attenuation in Amorphous Solids. *Reviews of Modern Physics* **74**, 991–1013. ISSN: 0034-6861, 1539-0756 (Oct. 2002).

54. Cripe, J. *et al.* Measurement of Quantum Back Action in the Audio Band at Room Temperature. *Nature* **568**, 364–367. ISSN: 1476-4687 (Apr. 2019).
55. Komori, K., Ďurovčíková, D. & Sudhir, V. Quantum Theory of Feedback Cooling of an Anelastic Macromechanical Oscillator. *Physical Review A* **105**, 043520 (Apr. 2022).
56. Fedorov, S. A. *et al.* Evidence for Structural Damping in a High-Stress Silicon Nitride Nanobeam and Its Implications for Quantum Optomechanics. *Physics Letters A. Special Issue in Memory of Professor V.B. Braginsky* **382**, 2251–2255. ISSN: 0375-9601 (Aug. 2018).
57. Villanueva, L. G. & Schmid, S. Evidence of Surface Loss as Ubiquitous Limiting Damping Mechanism in SiN Micro- and Nanomechanical Resonators. *Physical Review Letters* **113**, 227201 (Nov. 2014).
58. Bereyhi, M. J. *et al.* Hierarchical Tensile Structures with Ultralow Mechanical Dissipation. *Nature Communications* **13**, 1–9. ISSN: 2041-1723 (June 2022).
59. Kushwaha, M. S., Halevi, P., Dobrzynski, L. & Djafari-Rouhani, B. Acoustic Band Structure of Periodic Elastic Composites. *Physical Review Letters* **71**, 2022–2025. ISSN: 0031-9007 (Sept. 1993).
60. Martínez-Sala, R. *et al.* Sound Attenuation by Sculpture. *Nature* **378**, 241–241. ISSN: 1476-4687 (Nov. 1995).
61. Tsaturyan, Y. *et al.* Demonstration of Suppressed Phonon Tunneling Losses in Phononic Bandgap Shielded Membrane Resonators for High-Q Optomechanics. *Optics Express* **22**, 6810–6821. ISSN: 1094-4087 (Mar. 2014).
62. Chan, J. *et al.* Laser Cooling of a Nanomechanical Oscillator into Its Quantum Ground State. *Nature* **478**, 89–92. ISSN: 1476-4687 (Oct. 2011).
63. Mirhosseini, M., Sipahigil, A., Kalaei, M. & Painter, O. Superconducting Qubit to Optical Photon Transduction. *Nature* **588**, 599–603. ISSN: 1476-4687 (Dec. 2020).
64. Fiaschi, N. *et al.* Optomechanical Quantum Teleportation. *Nature Photonics* **15**, 817–821. ISSN: 1749-4893 (Nov. 2021).
65. Wallucks, A., Marinković, I., Hensen, B., Stockill, R. & Gröblacher, S. A Quantum Memory at Telecom Wavelengths. *Nature Physics* **16**, 772–777. ISSN: 1745-2481 (July 2020).
66. Ghadimi, A. H., Wilson, D. J. & Kippenberg, T. J. Radiation and Internal Loss Engineering of High-Stress Silicon Nitride Nanobeams. *Nano Letters* **17**, 3501–3505. ISSN: 1530-6984, 1530-6992 (June 2017).
67. Høj, D., Hoff, U. B. & Andersen, U. L. *Ultra-Coherent Nanomechanical Resonators Based on Density Phononic Crystal Engineering* July 2022. arXiv: [2207.06703 \[cond-mat\]](https://arxiv.org/abs/2207.06703).
68. Reetz, C. *et al.* Analysis of Membrane Phononic Crystals with Wide Band Gaps and Low-Mass Defects. *Physical Review Applied* **12**, 044027 (Oct. 2019).
69. Catalini, L., Tsaturyan, Y. & Schliesser, A. Soft-Clamped Phononic Dimers for Mechanical Sensing and Transduction. *Physical Review Applied* **14**, 014041 (July 2020).
70. Fedorov, S. *Mechanical Resonators with High Dissipation Dilution in Precision and Quantum Measurements* PhD thesis (EPFL, Lausanne, 2021).

71. Pratt, J. R. *et al.* Nanoscale Torsional Dissipation Dilution for Quantum Experiments and Precision Measurement. *Physical Review X* **13**, 011018. ISSN: 2160-3308 (Feb. 2023).
72. Zener, C. Internal Friction in Solids II. General Theory of Thermoelastic Internal Friction. *Physical Review* **53**, 90–99 (Jan. 1938).
73. Lifshitz, R. & Roukes, M. L. Thermoelastic Damping in Micro- and Nanomechanical Systems. *Physical Review B* **61**, 5600–5609 (Feb. 2000).
74. Tsaturyan, Y. *Ultrasoherent Soft-Clamped Mechanical Resonators for Quantum Cavity Optomechanics* PhD thesis (University of Copenhagen, 2019).
75. Cagnoli, G. & Willems, P. A. Effects of Nonlinear Thermoelastic Damping in Highly Stressed Fibers. *Physical Review B* **65**, 174111. ISSN: 0163-1829, 1095-3795 (Apr. 2002).
76. Hamdan, R., Trinastic, J. P. & Cheng, H. P. Molecular Dynamics Study of the Mechanical Loss in Amorphous Pure and Doped Silica. *The Journal of Chemical Physics* **141**, 054501. ISSN: 0021-9606 (Aug. 2014).
77. Phillips, W. A. Two-Level States in Glasses. *Reports on Progress in Physics* **50**, 1657–1708. ISSN: 0034-4885 (Dec. 1987).
78. Hauer, B. D., Kim, P. H., Doolin, C., Souris, F. & Davis, J. P. Two-Level System Damping in a Quasi-One-Dimensional Optomechanical Resonator. *Physical Review B* **98**, 214303 (Dec. 2018).
79. MacCabe, G. S. *et al.* Nano-Acoustic Resonator with Ultralong Phonon Lifetime. *Science* **370**, 840–843. ISSN: 0036-8075, 1095-9203 (Nov. 2020).
80. Behunin, R. O., Intravaia, F. & Rakich, P. T. Dimensional Transformation of Defect-Induced Noise, Dissipation, and Nonlinearity. *Physical Review B* **93**, 224110 (June 2016).
81. Tielbörger, D., Merz, R., Ehrenfels, R. & Hunklinger, S. Thermally Activated Relaxation Processes in Vitreous Silica: An Investigation by Brillouin Scattering at High Pressures. *Physical Review B* **45**, 2750–2760 (Feb. 1992).
82. Von Schickfus, M. & Hunklinger, S. Saturation of the Dielectric Absorption of Vitreous Silica at Low Temperatures. *Physics Letters A* **64**, 144–146. ISSN: 0375-9601 (Nov. 1977).
83. Gao, J. *et al.* Experimental Evidence for a Surface Distribution of Two-Level Systems in Superconducting Lithographed Microwave Resonators. *Applied Physics Letters* **92**, 152505. ISSN: 0003-6951 (Apr. 2008).
84. Grabovskij, G. J., Peichl, T., Lisenfeld, J., Weiss, G. & Ustinov, A. V. Strain Tuning of Individual Atomic Tunneling Systems Detected by a Superconducting Qubit. *Science* **338**, 232–234. ISSN: 0036-8075, 1095-9203 (Oct. 2012).
85. Faust, T., Rieger, J., Seitner, M. J., Kotthaus, J. P. & Weig, E. M. Signatures of Two-Level Defects in the Temperature-Dependent Damping of Nanomechanical Silicon Nitride Resonators. *Physical Review B* **89**, 100102 (Mar. 2014).
86. Vacher, R., Courtens, E. & Foret, M. Anharmonic versus Relaxational Sound Damping in Glasses. II. Vitreous Silica. *Physical Review B* **72**, 214205. ISSN: 1098-0121, 1550-235X (Dec. 2005).

87. Yuan, M., Cohen, M. A. & Steele, G. A. Silicon Nitride Membrane Resonators at Millikelvin Temperatures with Quality Factors Exceeding 108. *Applied Physics Letters* **107**, 263501. ISSN: 0003-6951 (Dec. 2015).
88. Gisler, T. *et al.* Soft-Clamped Silicon Nitride String Resonators at Millikelvin Temperatures. *Physical Review Letters* **129**, 104301 (Aug. 2022).
89. Ftouni, H. *et al.* Thermal Conductivity of Silicon Nitride Membranes Is Not Sensitive to Stress. *Physical Review B* **92**, 125439 (Sept. 2015).
90. Kleiman, R. N., Agnolet, G. & Bishop, D. J. Two-Level Systems Observed in the Mechanical Properties of Single-Crystal Silicon at Low Temperatures. *Physical Review Letters* **59**, 2079–2082. ISSN: 0031-9007 (Nov. 1987).
91. Wollack, E. A. *et al.* Loss Channels Affecting Lithium Niobate Phononic Crystal Resonators at Cryogenic Temperature. *Applied Physics Letters* **118**, 123501. ISSN: 0003-6951 (Mar. 2021).
92. Phillips, W. A. Comment on "Two-Level Systems Observed in the Mechanical Properties of Single-Crystal Silicon at Low Temperatures". *Physical Review Letters* **61**, 2632–2632 (Nov. 1988).
93. Galliou, S. *et al.* Extremely Low Loss Phonon-Trapping Cryogenic Acoustic Cavities for Future Physical Experiments. *Scientific Reports* **3**, 1–6. ISSN: 2045-2322 (July 2013).
94. Renninger, W. H., Kharel, P., Behunin, R. O. & Rakich, P. T. Bulk Crystalline Optomechanics. *Nature Physics* **14**, 601–607. ISSN: 1745-2473, 1745-2481 (June 2018).
95. Tao, Y. *et al.* Permanent Reduction of Dissipation in Nanomechanical Si Resonators by Chemical Surface Protection. *Nanotechnology* **26**, 465501. ISSN: 0957-4484, 1361-6528 (Nov. 2015).
96. Yasumura, K. Y. *et al.* Quality Factors in Micron- and Submicron-Thick Cantilevers. *Journal of Microelectromechanical Systems* **9**, 117–125. ISSN: 1057-7157 (Mar. 2000).
97. Luhmann, N. *et al.* Effect of Oxygen Plasma on Nanomechanical Silicon Nitride Resonators. *Applied Physics Letters* **111**, 063103. ISSN: 0003-6951 (Aug. 2017).
98. Sparks, D., Massoud-Ansari, S. & Najafi, N. Chip-Level Vacuum Packaging of Micromachines Using NanoGetters. *IEEE Transactions on Advanced Packaging* **26**, 277–282. ISSN: 1557-9980 (Aug. 2003).
99. Cho, Y.-H., Pisano, A. & Howe, R. Viscous Damping Model for Laterally Oscillating Microstructures. *Journal of Microelectromechanical Systems* **3**, 81–87. ISSN: 1941-0158 (June 1994).
100. Bao, M., Yang, H., Yin, H. & Sun, Y. Energy Transfer Model for Squeeze-Film Air Damping in Low Vacuum. *Journal of Micromechanics and Microengineering* **12**, 341–346. ISSN: 09601317 (May 2002).
101. Bao, M. & Yang, H. Squeeze Film Air Damping in MEMS. *Sensors and Actuators A: Physical. 25th Anniversary of Sensors and Actuators A: Physical* **136**, 3–27. ISSN: 0924-4247 (May 2007).
102. Photiadis, D. M. & Judge, J. A. Attachment Losses of High Q Oscillators. *Applied Physics Letters* **85**, 482–484. ISSN: 0003-6951, 1077-3118 (July 2004).

103. Cole, G. D., Wilson-Rae, I., Werbach, K., Vanner, M. R. & Aspelmeyer, M. Phonon-Tunnelling Dissipation in Mechanical Resonators. *Nature Communications* **2**, 231. ISSN: 2041-1723 (Sept. 2011).
104. Wilson-Rae, I. *et al.* High-Q Nanomechanics via Destructive Interference of Elastic Waves. *Physical Review Letters* **106**, 047205 (Jan. 2011).
105. Singh, R. & Purdy, T. P. Detecting Acoustic Blackbody Radiation with an Optomechanical Antenna. *Physical Review Letters* **125**, 120603 (Sept. 2020).
106. Huber, A. *Dispersion Calculator* German Aerospace Center (DLR). Jan. 2023.
107. Bermúdez, A., Hervella-Nieto, L., Prieto, A. & Rodríguez, R. An Optimal Perfectly Matched Layer with Unbounded Absorbing Function for Time-Harmonic Acoustic Scattering Problems. *Journal of Computational Physics* **223**, 469–488. ISSN: 0021-9991 (May 2007).
108. Bereyhi, M. J. *et al.* Clamp-Tapering Increases the Quality Factor of Stressed Nanobeams. *Nano Letters*. ISSN: 1530-6984, 1530-6992 (Feb. 2019).
109. Wilson, D. J., Regal, C. A., Papp, S. B. & Kimble, H. J. Cavity Optomechanics with Stoichiometric SiN Films. *Physical Review Letters* **103**, 207204 (Nov. 2009).
110. Jöckel, A. *et al.* Spectroscopy of Mechanical Dissipation in Micro-Mechanical Membranes. *Applied Physics Letters* **99**, 143109. ISSN: 0003-6951 (Oct. 2011).
111. Borrielli, A. *et al.* Control of Recoil Losses in Nanomechanical SiN Membrane Resonators. *Physical Review B* **94**, 121403. ISSN: 2469-9950, 2469-9969 (Sept. 2016).
112. Weaver, M. J. *et al.* Nested Trampoline Resonators for Optomechanics. *Applied Physics Letters* **108**, 033501. ISSN: 0003-6951, 1077-3118 (Jan. 2016).
113. Bachtold, A., Moser, J. & Dykman, M. I. Mesoscopic Physics of Nanomechanical Systems. *Reviews of Modern Physics* **94**, 045005. ISSN: 0034-6861, 1539-0756 (Dec. 2022).
114. Postma, H. W. C., Kozinsky, I., Husain, A. & Roukes, M. L. Dynamic Range of Nanotube- and Nanowire-Based Electromechanical Systems. *Applied Physics Letters* **86**, 223105. ISSN: 0003-6951 (May 2005).
115. Kozinsky, I., Postma, H. W. C., Kogan, O., Husain, A. & Roukes, M. L. Basins of Attraction of a Nonlinear Nanomechanical Resonator. *Physical Review Letters* **99**, 207201 (Nov. 2007).
116. Mishin, Y. & Hickman, J. Energy Spectrum of a Langevin Oscillator. *Physical Review E* **94**, 062151. ISSN: 2470-0045, 2470-0053 (Dec. 2016).
117. Gavartin, E., Verlot, P. & Kippenberg, T. J. Stabilization of a Linear Nanomechanical Oscillator to Its Thermodynamic Limit. *Nature Communications* **4**, 2860. ISSN: 2041-1723 (Dec. 2013).
118. Roy, S. K., Sauer, V. T. K., Westwood-Bachman, J. N., Venkatasubramanian, A. & Hiebert, W. K. Improving Mechanical Sensor Performance through Larger Damping. *Science* **360**, eaar5220 (June 2018).
119. Atalaya, J., Isacsson, A. & Dykman, M. I. Diffusion-Induced Dephasing in Nanomechanical Resonators. *Physical Review B* **83**, 045419 (Jan. 2011).

120. Fong, K. Y., Pernice, W. H. P. & Tang, H. X. Frequency and Phase Noise of Ultra-high Q Silicon Nitride Nanomechanical Resonators. *Physical Review B* **85**, 161410. ISSN: 1098-0121, 1550-235X (Apr. 2012).
121. Steele, G. A. *et al.* Strong Coupling Between Single-Electron Tunneling and Nanomechanical Motion. *Science* **325**, 1103–1107 (Aug. 2009).
122. Lassagne, B., Tarakanov, Y., Kinaret, J., Garcia-Sanchez, D. & Bachtold, A. Coupling Mechanics to Charge Transport in Carbon Nanotube Mechanical Resonators. *Science* **325**, 1107–1110 (Aug. 2009).
123. Bagdasarov, S., Braginsky, V. B. & Mitrofanov, V. P. Mechanical Dissipation in Single Crystal Sapphire. *Kristallografiya* **19**, 883 (1974).
124. McGuigan, D. F. *et al.* Measurements of the Mechanical Q of Single-Crystal Silicon at Low Temperatures. *Journal of Low Temperature Physics* **30**, 621–629. ISSN: 1573-7357 (Mar. 1978).
125. Liu, J. *et al.* High-Q Optomechanical GaAs Nanomembranes. *Applied Physics Letters* **99**, 243102. ISSN: 0003-6951 (Dec. 2011).
126. Romero, E. *et al.* Engineering the Dissipation of Crystalline Micromechanical Resonators. *Physical Review Applied* **13**, 044007 (Apr. 2020).
127. Kermany, A. R. *et al.* Microresonators with Q-factors over a Million from Highly Stressed Epitaxial Silicon Carbide on Silicon. *Applied Physics Letters* **104**, 081901. ISSN: 0003-6951 (Feb. 2014).
128. Cole, G. D. *et al.* Tensile-Strained In<sub>x</sub>Ga<sub>1-x</sub>P Membranes for Cavity Optomechanics. *Applied Physics Letters* **104**, 201908. ISSN: 0003-6951 (May 2014).
129. Bückle, M. *et al.* Stress Control of Tensile-Strained In<sub>1-x</sub>Ga<sub>x</sub>P Nanomechanical String Resonators. *Applied Physics Letters* **113**, 201903. ISSN: 0003-6951 (Nov. 2018).
130. Chu, M., Sun, Y., Aghoram, U. & Thompson, S. E. Strain: A Solution for Higher Carrier Mobility in Nanoscale MOSFETs. *Annual Review of Materials Research* **39**, 203–229 (2009).
131. Jacobsen, R. S. *et al.* Strained Silicon as a New Electro-Optic Material. *Nature* **441**, 199–202. ISSN: 0028-0836, 1476-4687 (May 2006).
132. Ghyselen, B. *et al.* Engineering Strained Silicon on Insulator Wafers with the Smart Cut (TM) Technology. *Solid-State Electronics* **48**, 1285–1296. ISSN: 0038-1101 (Aug. 2004).
133. Hopcroft, M. A., Nix, W. D. & Kenny, T. W. What Is the Young's Modulus of Silicon? *Journal of Microelectromechanical Systems* **19**, 229–238. ISSN: 1057-7157 (Apr. 2010).
134. Flinn, P., Gardner, D. & Nix, W. Measurement and Interpretation of Stress in Aluminum-Based Metallization as a Function of Thermal History. *IEEE Transactions on Electron Devices* **34**, 689–699. ISSN: 1557-9646 (Mar. 1987).

135. Chen, W. W., Sun, X. H., Wang, S. D., Lee, S. T. & Teo, B. K. Etching Behavior of Silicon Nanowires with HF and  $\text{NH}_4\text{F}$  and Surface Characterization by Attenuated Total Reflection Fourier Transform Infrared Spectroscopy: Similarities and Differences between One-Dimensional and Two-Dimensional Silicon Surfaces. *The Journal of Physical Chemistry B* **109**, 10871–10879. ISSN: 1520-6106, 1520-5207 (June 2005).
136. Norte, R. A. *Nanofabrication for On-Chip Optical Levitation, Atom-Trapping, and Superconducting Quantum Circuits* PhD thesis (California Institute of Technology, 2015).
137. Bereyhi, M. *Ultra Low Quantum Decoherence Nano-Optomechanical Systems* PhD thesis (EPFL, Lausanne, 2022).
138. Borselli, M., Johnson, T. J. & Painter, O. Measuring the Role of Surface Chemistry in Silicon Microphotonics. *Applied Physics Letters* **88**, 131114. ISSN: 0003-6951, 1077-3118 (Mar. 2006).
139. Boureau, V., Reboh, S., Benoit, D., Hÿtch, M. & Claverie, A. Strain Evolution of SiGe-on-insulator Obtained by the Ge-condensation Technique. *APL Materials* **7**, 041120 (Apr. 2019).
140. Hÿtch, M., Houdellier, F., Hÿe, F. & Snoeck, E. Nanoscale Holographic Interferometry for Strain Measurements in Electronic Devices. *Nature* **453**, 1086–1089. ISSN: 1476-4687 (June 2008).
141. De Wolf, I., Maes, H. E. & Jones, S. K. Stress Measurements in Silicon Devices through Raman Spectroscopy: Bridging the Gap between Theory and Experiment. *Journal of Applied Physics* **79**, 7148–7156. ISSN: 0021-8979 (May 1996).
142. Süess, M. J. *et al.* Power-Dependent Raman Analysis of Highly Strained Si Nanobridges. *Nano Letters* **14**, 1249–1254. ISSN: 1530-6984 (Mar. 2014).
143. Anastassakis, E., Pinczuk, A., Burstein, E., Pollak, F. H. & Cardona, M. Effect of Static Uniaxial Stress on the Raman Spectrum of Silicon. *Solid State Communications* **8**, 133–138. ISSN: 0038-1098 (Jan. 1970).
144. Ossikovski, R., Nguyen, Q., Picardi, G., Schreiber, J. & Morin, P. Theory and Experiment of Large Numerical Aperture Objective Raman Microscopy: Application to the Stress-Tensor Determination in Strained Cubic Materials. *Journal of Raman Spectroscopy* **39**, 661–672. ISSN: 1097-4555 (2008).
145. Hart, T. R., Aggarwal, R. L. & Lax, B. Temperature Dependence of Raman Scattering in Silicon. *Physical Review B* **1**, 638–642. ISSN: 0556-2805 (Jan. 1970).
146. Anastassakis, E., Cantarero, A. & Cardona, M. Piezo-Raman Measurements and Anharmonic Parameters in Silicon and Diamond. *Physical Review B* **41**, 7529–7535 (Apr. 1990).
147. Honig, R. E. & Hook, H. O. Vapor Pressure Data for Some Common Gases. *RCA Review* **21**, 360–368 (Jan. 1960).
148. Cannelli, G. *et al.* Reorientation of the B-H Complex in Silicon by Anelastic Relaxation Experiments. *Physical Review B* **44**, 11486–11489. ISSN: 0163-1829, 1095-3795 (Nov. 1991).
149. Gysin, U. *et al.* Temperature Dependence of the Force Sensitivity of Silicon Cantilevers. *Physical Review B* **69**, 045403. ISSN: 1098-0121, 1550-235X (Jan. 2004).



150. Anderson, O. L. Derivation of Wachtman's Equation for the Temperature Dependence of Elastic Moduli of Oxide Compounds. *Physical Review* **144**, 553–557. ISSN: 0031-899X (Apr. 1966).
151. Younis, M. I. *MEMS Linear and Nonlinear Statics and Dynamics* (Springer US, Boston, MA, 2011).
152. Aguilar Sandoval, F., Geitner, M., Bertin, É. & Bellon, L. Resonance Frequency Shift of Strongly Heated Micro-Cantilevers. *Journal of Applied Physics* **117**, 234503. ISSN: 0021-8979, 1089-7550 (June 2015).
153. Fogliano, F. *Ultrasensitive Nanowire Force Sensors in Extreme Conditions : From Dilution Temperature to Ultra-Strong Coupling in Cavity Nano-Optomechanics* PhD thesis (Université Grenoble Alpes, 2019).
154. Tebbenjohanns, F., Mattana, M. L., Rossi, M., Frimmer, M. & Novotny, L. Quantum Control of a Nanoparticle Optically Levitated in Cryogenic Free Space. *Nature* **595**, 378–382. ISSN: 1476-4687 (July 2021).
155. Wagner, J. W. & Spicer, J. B. Theoretical Noise-Limited Sensitivity of Classical Interferometry. *Journal of the Optical Society of America B* **4**, 1316. ISSN: 0740-3224, 1520-8540 (Aug. 1987).
156. Teufel, J. D., Donner, T., Castellanos-Beltran, M. A., Harlow, J. W. & Lehnert, K. W. Nanomechanical Motion Measured with an Imprecision below That at the Standard Quantum Limit. *Nature Nanotechnology* **4**, 820–823. ISSN: 1748-3395 (Dec. 2009).
157. Westphal, T. *et al.* Interferometer Readout Noise below the Standard Quantum Limit of a Membrane. *Physical Review A* **85**, 063806. ISSN: 1050-2947, 1094-1622 (June 2012).
158. Gallion, P. & Debarge, G. Quantum Phase Noise and Field Correlation in Single Frequency Semiconductor Laser Systems. *IEEE Journal of Quantum Electronics* **20**, 343–349. ISSN: 1558-1713 (Apr. 1984).
159. Ghadimi, A. H. *Ultra-Coherent Nano-Mechanical Resonators for Quantum Optomechanics at Room Temperature* PhD thesis (EPFL, Lausanne, 2018).
160. Barg, A. *et al.* Measuring and Imaging Nanomechanical Motion with Laser Light. *Applied Physics B* **123**, 8. ISSN: 1432-0649 (Dec. 2016).
161. Knuuttila, J. V., Tikka, P. T. & Salomaa, M. M. Scanning Michelson Interferometer for Imaging Surface Acoustic Wave Fields. *Optics Letters* **25**, 613–615. ISSN: 1539-4794 (May 2000).
162. Aubin, K. *et al.* Limit Cycle Oscillations in CW Laser-Driven NEMS. *Journal of Microelectromechanical Systems* **13**, 1018–1026. ISSN: 1941-0158 (Dec. 2004).
163. de Jong, M. H. J., Ganesan, A., Cupertino, A., Gröblacher, S. & Norte, R. A. Mechanical Overtone Frequency Combs. *Nature Communications* **14**, 1458. ISSN: 2041-1723 (Mar. 2023).
164. Metzger, C. H. & Karrai, K. Cavity Cooling of a Microlever. *Nature* **432**, 1002–1005. ISSN: 1476-4687 (Dec. 2004).

165. Gieseler, J., Deutsch, B., Quidant, R. & Novotny, L. Subkelvin Parametric Feedback Cooling of a Laser-Trapped Nanoparticle. *Physical Review Letters* **109**, 103603 (Sept. 2012).
166. Sementilli, L., Romero, E. & Bowen, W. P. Nanomechanical Dissipation and Strain Engineering. *Advanced Functional Materials*, 2105247. ISSN: 1616-3028 (Aug. 2021).
167. Carney, D. *et al.* Mechanical Quantum Sensing in the Search for Dark Matter. *Quantum Science and Technology* **6**, 024002. ISSN: 2058-9565 (Jan. 2021).
168. Tao, Y., Boss, J. M., Moores, B. A. & Degen, C. L. Single-Crystal Diamond Nanomechanical Resonators with Quality Factors Exceeding One Million. *Nature Communications* **5**, 3638. ISSN: 2041-1723 (Apr. 2014).
169. Fogliano, F. *et al.* Ultrasensitive Nano-Optomechanical Force Sensor Operated at Dilution Temperatures. *Nature Communications* **12**, 4124. ISSN: 2041-1723 (Dec. 2021).
170. Bild, M. *et al.* Schrödinger Cat States of a 16-Microgram Mechanical Oscillator. *Science* **380**, 274–278 (Apr. 2023).
171. Delić, U. *et al.* Cooling of a Levitated Nanoparticle to the Motional Quantum Ground State. *Science* **367**, 892–895 (Feb. 2020).
172. Guo, J., Norte, R. & Gröblacher, S. Feedback Cooling of a Room Temperature Mechanical Oscillator Close to Its Motional Ground State. *Physical Review Letters* **123**, 223602. ISSN: 0031-9007, 1079-7114 (Nov. 2019).
173. Saarinen, S. A., Kralj, N., Langman, E. C., Tsaturyan, Y. & Schliesser, A. Laser Cooling a Membrane-in-the-Middle System Close to the Quantum Ground State from Room Temperature. *Optica* **10**, 364–372. ISSN: 2334-2536 (Mar. 2023).
174. Bassi, A., Lochan, K., Satin, S., Singh, T. P. & Ulbricht, H. Models of Wave-Function Collapse, Underlying Theories, and Experimental Tests. *Reviews of Modern Physics* **85**, 471–527 (Apr. 2013).
175. Penrose, R. On Gravity's Role in Quantum State Reduction. *General Relativity and Gravitation* **28**, 581–600. ISSN: 1572-9532 (May 1996).
176. Marletto, C. & Vedral, V. Gravitationally Induced Entanglement between Two Massive Particles Is Sufficient Evidence of Quantum Effects in Gravity. *Physical Review Letters* **119**, 240402 (Dec. 2017).
177. Purdy, T. P., Yu, P.-L., Peterson, R. W., Kampel, N. S. & Regal, C. A. Strong Optomechanical Squeezing of Light. *Physical Review X* **3**, 031012 (Sept. 2013).
178. Fedorov, S. A. *et al.* Thermal Intermodulation Noise in Cavity-Based Measurements. *Optica* **7**, 1609–1616. ISSN: 2334-2536 (Nov. 2020).
179. *Quantum Optics* (eds Walls, D. & Milburn, G. J.) ISBN: 978-3-540-28573-1 (Springer, Berlin, Heidelberg, 2008).
180. Braginsky, V. B., Strigin, S. E. & Vyatchanin, S. P. Parametric Oscillatory Instability in Fabry–Perot Interferometer. *Physics Letters A* **287**, 331–338. ISSN: 0375-9601 (Sept. 2001).
181. Kippenberg, T. J., Rokhsari, H., Carmon, T., Scherer, A. & Vahala, K. J. Analysis of Radiation-Pressure Induced Mechanical Oscillation of an Optical Microcavity. *Physical Review Letters* **95**, 033901. ISSN: 0031-9007, 1079-7114 (July 2005).

182. Teufel, J. D. *et al.* Sideband Cooling of Micromechanical Motion to the Quantum Ground State. *Nature* **475**, 359–363. ISSN: 1476-4687 (July 2011).
183. Qiu, L., Shomroni, I., Seidler, P. & Kippenberg, T. J. Laser Cooling of a Nanomechanical Oscillator to Its Zero-Point Energy. *Physical Review Letters* **124**, 173601 (Apr. 2020).
184. Youssefi, A., Kono, S., Chegnizadeh, M. & Kippenberg, T. J. *A Squeezed Mechanical Oscillator with Milli-Second Quantum Decoherence* Aug. 2022. arXiv: [2208.13082 \[physics, physics:quant-ph\]](#).
185. Wilson, D. J. *et al.* Measurement-Based Control of a Mechanical Oscillator at Its Thermal Decoherence Rate. *Nature* **524**, 325–329. ISSN: 1476-4687 (Aug. 2015).
186. Purdy, T. P., Peterson, R. W. & Regal, C. A. Observation of Radiation Pressure Shot Noise on a Macroscopic Object. *Science* **339**, 801–804 (Feb. 2013).
187. Teufel, J. D., Lecocq, F. & Simmonds, R. W. Overwhelming Thermomechanical Motion with Microwave Radiation Pressure Shot Noise. *Physical Review Letters* **116**, 013602 (Jan. 2016).
188. Mason, D., Chen, J., Rossi, M., Tsaturyan, Y. & Schliesser, A. Continuous Force and Displacement Measurement below the Standard Quantum Limit. *Nature Physics* **15**, 745–749. ISSN: 1745-2481 (Aug. 2019).
189. Kampel, N. S. *et al.* Improving Broadband Displacement Detection with Quantum Correlations. *Physical Review X* **7**, 021008 (Apr. 2017).
190. Walls, D. F. Squeezed States of Light. *Nature* **306**, 141–146. ISSN: 1476-4687 (Nov. 1983).
191. Slusher, R. E., Hollberg, L. W., Yurke, B., Mertz, J. C. & Valley, J. F. Observation of Squeezed States Generated by Four-Wave Mixing in an Optical Cavity. *Physical Review Letters* **55**, 2409–2412 (Nov. 1985).
192. Safavi-Naeini, A. H. *et al.* Squeezed Light from a Silicon Micromechanical Resonator. *Nature* **500**, 185–189. ISSN: 1476-4687 (Aug. 2013).
193. Nielsen, W. H. P., Tsaturyan, Y., Möller, C. B., Polzik, E. S. & Schliesser, A. Multimode Optomechanical System in the Quantum Regime. *Proceedings of the National Academy of Sciences* **114**, 62–66 (Jan. 2017).
194. Aggarwal, N. *et al.* Room-Temperature Optomechanical Squeezing. *Nature Physics* **16**, 784–788. ISSN: 1745-2481 (July 2020).
195. Vyatchanin, S. P. & Zubova, E. A. Quantum Variation Measurement of a Force. *Physics Letters A* **201**, 269–274. ISSN: 0375-9601 (May 1995).
196. Cohadon, P. F., Heidmann, A. & Pinard, M. Cooling of a Mirror by Radiation Pressure. *Physical Review Letters* **83**, 3174–3177 (Oct. 1999).
197. Poggio, M., Degen, C. L., Mamin, H. J. & Rugar, D. Feedback Cooling of a Cantilever's Fundamental Mode below 5 mK. *Physical Review Letters* **99**, 017201 (July 2007).
198. Genes, C., Vitali, D., Tombesi, P., Gigan, S. & Aspelmeyer, M. Ground-State Cooling of a Micromechanical Oscillator: Comparing Cold Damping and Cavity-Assisted Cooling Schemes. *Physical Review A* **77**, 033804. ISSN: 1050-2947, 1094-1622 (Mar. 2008).

199. Wieczorek, W. *et al.* Optimal State Estimation for Cavity Optomechanical Systems. *Physical Review Letters* **114**, 223601. ISSN: 0031-9007, 1079-7114 (June 2015).
200. Magrini, L. *et al.* Real-Time Optimal Quantum Control of Mechanical Motion at Room Temperature. *Nature* **595**, 373–377. ISSN: 1476-4687 (July 2021).
201. Rossi, M. *Quantum Measurement and Control of a Mechanical Resonator* PhD thesis (University of Copenhagen, Copenhagen, 2020).
202. Biancofiore, C. *et al.* Quantum Dynamics of an Optical Cavity Coupled to a Thin Semitransparent Membrane: Effect of Membrane Absorption. *Physical Review A* **84**, 033814. ISSN: 1050-2947, 1094-1622 (Sept. 2011).
203. Wilson, D. J. *Cavity Optomechanics with High-Stress Silicon Nitride Films* PhD thesis (California Institute of Technology, 2012).
204. Dumont, V. *et al.* Flexure-Tuned Membrane-at-the-Edge Optomechanical System. *Optics Express* **27**, 25731–25748. ISSN: 1094-4087 (Sept. 2019).
205. Hecht, E. *Optics* 5th edition. ISBN: 978-0-13-397722-6 (Pearson, Boston, Dec. 2015).
206. Ivanov, E. *et al.* Edge Mode Engineering for Optimal Ultracoherent Silicon Nitride Membranes. *Applied Physics Letters* **117**, 254102. ISSN: 0003-6951 (Dec. 2020).
207. Beccari, A. *High Aspect Ratio Si<sub>3</sub>N<sub>4</sub> Nanomembranes* tech. rep. (Zenodo, June 2020).
208. Reinhardt, C., Müller, T., Bourassa, A. & Sankey, J. C. Ultralow-Noise SiN Trampoline Resonators for Sensing and Optomechanics. *Physical Review X* **6**, 021001 (Apr. 2016).
209. Norte, R. A., Moura, J. P. & Gröblacher, S. Mechanical Resonators for Quantum Optomechanics Experiments at Room Temperature. *Physical Review Letters* **116**, 147202 (Apr. 2016).
210. Gärtner, C., Moura, J. P., Haaxman, W., Norte, R. A. & Gröblacher, S. Integrated Optomechanical Arrays of Two High Reflectivity SiN Membranes. *Nano Letters* **18**, 7171–7175. ISSN: 1530-6984 (Nov. 2018).
211. Nielsen, C. B., Christensen, C., Pedersen, C. & Thomsen, E. V. Particle Precipitation in Connection with KOH Etching of Silicon. *Journal of The Electrochemical Society* **151**, G338–G342. ISSN: 0013-4651, 1945-7111 (May 2004).
212. Goldfarb, D. L. *Fabrication of a Full-Size EUV Pellicle Based on Silicon Nitride in Photomask Technology 2015* **9635** (International Society for Optics and Photonics, Oct. 2015), 96350A.
213. Brawley, G. A. *et al.* Nonlinear Optomechanical Measurement of Mechanical Motion. *Nature Communications* **7**, 10988. ISSN: 2041-1723 (Mar. 2016).
214. Leijssen, R., La Gala, G. R., Freisem, L., Muhonen, J. T. & Verhagen, E. Nonlinear Cavity Optomechanics with Nanomechanical Thermal Fluctuations. *Nature Communications* **8**, ncomms16024. ISSN: 2041-1723 (July 2017).
215. Vanner, M. R. Selective Linear or Quadratic Optomechanical Coupling via Measurement. *Physical Review X* **1**, 021011 (Nov. 2011).
216. Sudhir, V. *et al.* Quantum Correlations of Light from a Room-Temperature Mechanical Oscillator. *Physical Review X* **7**, 031055 (Sept. 2017).

217. Doolin, C. *et al.* Nonlinear Optomechanics in the Stationary Regime. *Physical Review A* **89**, 053838 (May 2014).
218. Gardiner, C. *Handbook of Stochastic Methods* 2nd ed. (Springer Berlin, Heidelberg, 1985).
219. Sudhir, V. *et al.* Appearance and Disappearance of Quantum Correlations in Measurement-Based Feedback Control of a Mechanical Oscillator. *Physical Review X* **7**, 011001 (Jan. 2017).
220. Fischer, R. *et al.* Spin Detection with a Micromechanical Trampoline: Towards Magnetic Resonance Microscopy Harnessing Cavity Optomechanics. *New Journal of Physics* **21**, 043049. ISSN: 1367-2630 (Apr. 2019).
221. Pluchar, C. M., Agrawal, A. R., Schenk, E. & Wilson, D. J. Towards Cavity-Free Ground-State Cooling of an Acoustic-Frequency Silicon Nitride Membrane. *Applied Optics* **59**, G107. ISSN: 1559-128X, 2155-3165 (Aug. 2020).
222. Fedorov, S. A., Beccari, A., Engelsen, N. J. & Kippenberg, T. J. Fractal-like Mechanical Resonators with a Soft-Clamped Fundamental Mode. *Physical Review Letters* **124**, 025502. ISSN: 0031-9007, 1079-7114 (Jan. 2020).
223. Dumont, V. *Quantum Noise and Mechanical Membranes in Microcavities* PhD thesis (McGill University, Montreal, 2022).
224. Gao, W., Wang, F. & Sigmund, O. Systematic Design of High-Q Prestressed Micro Membrane Resonators. *Computer Methods in Applied Mechanics and Engineering* **361**, 112692. ISSN: 0045-7825 (Apr. 2020).
225. Høj, D. *et al.* Ultra-Coherent Nanomechanical Resonators Based on Inverse Design. *Nature Communications* **12**, 5766. ISSN: 2041-1723 (Oct. 2021).
226. An, K., Sones, B. A., Fang-Yen, C., Dasari, R. R. & Feld, M. S. Optical Bistability Induced by Mirror Absorption: Measurement of Absorption Coefficients at the Sub-Ppm Level. *Optics Letters* **22**, 1433–1435. ISSN: 1539-4794 (Sept. 1997).
227. Metzger, C. *et al.* Self-Induced Oscillations in an Optomechanical System Driven by Bolometric Backaction. *Physical Review Letters* **101**, 133903 (Sept. 2008).
228. Gorin, A., Jaouad, A., Grondin, E., Aimez, V. & Charette, P. Fabrication of Silicon Nitride Waveguides for Visible-Light Using PECVD: A Study of the Effect of Plasma Frequency on Optical Properties. *Optics Express* **16**, 13509–13516. ISSN: 1094-4087 (Sept. 2008).
229. Simon, G. & Richard, N. NL2023917B1 (2021).
230. Howell, K. M. *Dielectric Actuation Techniques at the Nanoscale: Piezoelectricity and Flexoelectricity* PhD thesis (EPFL, Lausanne, 2019).
231. Chen, X. *et al.* High-Finesse Fabry–Perot Cavities with Bidimensional Si<sub>3</sub>N<sub>4</sub> Photonic-Crystal Slabs. *Light: Science & Applications* **6**, e16190. ISSN: 2047-7538 (Jan. 2017).
232. Enzian, G. *et al.* Phononically Shielded Photonic-Crystal Mirror Membranes for Cavity Quantum Optomechanics. *Optics Express* **31**, 13040–13052. ISSN: 1094-4087 (Apr. 2023).
233. Zhou, F., Bao, Y., Gorman, J. J. & Lawall, J. *Cavity Optomechanical Bistability with an Ultrahigh Reflectivity Photonic Crystal Membrane* Nov. 2022. arXiv: [2211.10485 \[physics\]](#).

234. Koshelev, K., Lepeshov, S., Liu, M., Bogdanov, A. & Kivshar, Y. Asymmetric Meta-surfaces with High- Q Resonances Governed by Bound States in the Continuum. *Physical Review Letters* **121**, 193903. ISSN: 0031-9007, 1079-7114 (Nov. 2018).
235. Hsu, C. W., Zhen, B., Stone, A. D., Joannopoulos, J. D. & Soljačić, M. Bound States in the Continuum. *Nature Reviews Materials* **1**, 1–13. ISSN: 2058-8437 (July 2016).
236. Satzinger, K. J. *et al.* Quantum Control of Surface Acoustic-Wave Phonons. *Nature* **563**, 661–665. ISSN: 1476-4687 (Nov. 2018).
237. Cummer, S. A., Christensen, J. & Alù, A. Controlling Sound with Acoustic Metamaterials. *Nature Reviews Materials* **1**, 1–13. ISSN: 2058-8437 (Feb. 2016).
238. Fleury, R. & Alù, A. Extraordinary Sound Transmission through Density-Near-Zero Ultranarrow Channels. *Physical Review Letters* **111**, 055501. ISSN: 0031-9007, 1079-7114 (July 2013).
239. Fogliano, F. *et al.* Mapping the Cavity Optomechanical Interaction with Subwavelength-Sized Ultrasensitive Nanomechanical Force Sensors. *Physical Review X* **11**, 021009 (Apr. 2021).

# Alberto BECCARI

Rue Couchirard 6 - 1004 Lausanne (CH)

✉ alb.beccari@gmail.com



## Education

---

### École Polytechnique Fédérale de Lausanne

Lausanne

Doctoral degree in Photonics,

April 2018 - ongoing

Thesis: Low-dissipation mechanical resonators for room temperature quantum optomechanics.

Anticipated defense date: 22/06/2023

### Politecnico di Milano

Milan

Master of Science in Engineering Physics,

October 2014 - October 2017

Thesis: Reconfigurable integrated photonic circuits for quantum machine learning.

Defense date: 03/10/2017

Final mark: 110L/110

### Friedrich-Schiller-Universität

Jena

Exchange Semester,

October 2015 - March 2016

ERASMUS scholarship in the Abbe School of Photonics.

### Politecnico di Milano

Milan

Bachelor of Engineering in Engineering Physics,

September 2011 - October 2014

Project: characterization of ultrashort coherent pulses in the visible and UV spectra (FROG).

Final mark: 110L/110

## Employment history

---

### Laboratory of Photonics and Quantum Measurements, EPFL

Lausanne

Graduate Researcher,

October 2017 - ongoing

Development of nanomechanical resonators with ultralow dissipation for quantum optomechanics and force sensing. Design of nanomechanical devices through numerical simulation and finite element methods, and their realization by the development of advanced top-down microfabrication processes. Construction of optical and infrared interferometers for the characterization of mechanical resonators. Operation of vacuum systems and a 4 K closed-cycle cryostat. Integration of mechanical resonators in high-finesse optical cavities, noise analysis of such optomechanical systems. Mentoring of master thesis students (Diego A. Visani, Robin Groth).

**Supervisor:** Prof. Tobias J. Kippenberg

### IBM Research Zürich

Rüschlikon

Research secondment,

June 2018 - October 2020

Finite elements simulations of superconducting electrodes for the design of microwave-to-optical piezoelectric transducers (GaP photonic crystal cavities). The research secondment was carried out for the most part remotely, in collaboration with Dr. Simon Hönl and Dr. Paul Seidler.

### Physics Department, Politecnico di Milano and IFN-CNR

Milan

Undergraduate Researcher,

September 2016 - October 2017



Design and fabrication of reconfigurable integrated photonic interferometers by *direct femtosecond laser writing* for implementing a machine learning algorithm (*Hamiltonian learning*) with quantum states of light. Numeric control of tools, fabrication and optical characterization of waveguides, integration of resistive phase-shifter elements, quantum information theory, numerical simulation and data analysis.

**Supervisors:** Dr. Roberto Osellame, Dr. Andrea Crespi

## Physics Department, Politecnico di Milano

Milan

*Undergraduate Researcher,*

June 2014 - October 2014

Design and construction of an optical and ultraviolet apparatus for the reconstruction of ultrashort laser pulses (FROG). Development of an algorithm for the temporal and spectral reconstruction of the pulses.

**Supervisor:** Prof. Salvatore Stagira

## Teaching experience

---

- 2021-2022: **Graduate teaching assistant** in General Physics: quanta (EPFL). Introductory quantum physics course taught by Prof. Vincenzo Savona for bachelor students of Life Sciences.
- 2020-2021: **Graduate teaching assistant** in General Physics: electromagnetism (EPFL). Introduction to electromagnetism taught by Prof. Hugo J. Dil for bachelor students of Computer Sciences.
- 2018-2020: **Graduate teaching assistant** in Optical laboratories I. Supervision of master students tasked with gain and noise characterization of an erbium-doped fiber amplifier (EDFA). Course organizers: Prof. Toralf Scharf and Dr. Ye Pu.
- 2017-2018: **Graduate teaching assistant** in Statistical Physics IV. Advanced statistical physics course taught by Prof. Tobias J. Kippenberg and attended by master and doctoral students of Physics.

## List of publications

---

- G. Huang\*, A. Beccari\*, N.J. Engelsen and T. J. Kippenberg, Room-temperature quantum optomechanics using an ultra-low noise cavity. In preparation.  
\* Indicates equal contributors.
- A. Beccari, N.J. Engelsen and T. J. Kippenberg, Dissipation dilution in nanomechanical resonators. Submitted to *Nature Nanotechnol.*
- M. J. Breyhi\*, A. Beccari\*, R. Groth\*, S. A. Fedorov\*, A. Arabmoheghi, N. J. Engelsen, and T. J. Kippenberg, Hierarchical tensile structures with ultralow mechanical dissipation, *Nature Communications* **13**, 3097 (2022).  
\* Indicates equal contributors.
- M. J. Breyhi\*, A. Arabmoheghi\*, A. Beccari, S. A. Fedorov, G. Huang, T. J. Kippenberg, and N. J. Engelsen, Perimeter modes of nanomechanical resonators exhibit quality factors exceeding  $10^9$  at room temperature, *Phys. Rev. X* **12**, 021036 (2022).  
\* Indicates equal contributors.
- S. Hönl, Y. Popoff, D. Caimi, A. Beccari, T. J. Kippenberg, and P. Seidler, Microwave-to-optical conversion with a gallium phosphide photonic crystal cavity, *Nature Commun.* **13**, 2065 (2022).
- A. Beccari, D. A. Visani, S. A. Fedorov, M. J. Breyhi, V. Boureau, N. J. Engelsen, and T. J. Kippenberg, Strained crystalline nanomechanical resonators with quality factors above 10 billion, *Nature Physics* **18**, 436-441 (2022).
- S. A. Fedorov\*, A. Beccari\*, A. Arabmoheghi, D. J. Wilson, N. J. Engelsen, and T. J. Kippenberg, Thermal intermodulation noise in cavity-based measurements, *Optica* **7**, 1609-1616 (2020).  
\* Indicates equal contributors.
- S. A. Fedorov, A. Beccari, N. J. Engelsen, and T. J. Kippenberg, Fractal-like Mechanical Resonators with a Soft-Clamped Fundamental Mode. *Phys. Rev. Lett.* **124**, 025502 (2020).
- M. J. Breyhi, A. Beccari, S. A. Fedorov, A. H. Ghadimi, R. Schilling, D. J. Wilson, N. J. Engelsen, and T. J. Kippenberg, Clamp-tapering increases the quality factor of stressed nanobeams, *Nano Lett.* **19**, 4, 2329-2333 (2019).

## Languages

---

Italian (native), English (full professional proficiency), French (intermediate knowledge), German (elementary knowledge)